EUROPEAN ORGANIZATION FOR NUCLEAR RESEARCH

CERN/AC/93-03(LHC)
8 November 1993

L H C

The Large Hadron Collider Accelerator Project

The LHC Study Group

Editors:

Y. Baconnier
G. Brianti
Ph. Lebrun
A. Mathewson
R. Perin

EUROPEAN ORGANIZATION FOR NUCLEAR RESEARCH

CERN/AC/93–03(LHC)
8 November 1993

L H C

The Large Hadron Collider Accelerator Project

The LHC Study Group

Editors:

Y. Baconnier
G. Brianti
Ph. Lebrun
A. Mathewson
R. Perin

Abstract

The Large Hadron Collider is a two-ring, superconducting accelerator and collider to be installed in the 27 km LEP tunnel. This 7 TeV proton–proton collider with a luminosity of 10^{34} cm^{-2} s^{-1} is the official next project of CERN. It will also provide ion–ion collisions at a centre-of-mass energy of 1148 TeV with a design luminosity of 10^{27} cm^{-2} s^{-1}, and could later be converted into an electron–proton collider with LEP.

The present project proposal (the baseline design) contains three parts. After an overall review of the main characteristics of the project, there follows a detailed technical description of the proposed machine. The third part concentrates on the most important technological aspects of the machine: superconducting magnets, cryogenics, and vacuum.

The LHC study and the R&D programme for the superconducting magnets and cryogenics are led by

G. Brianti

The Study Group wishes to thank Professor C. Rubbia, many CERN staff for their contribution to the project, and the members of ECFA for their encouragement and very effective work.

List of Contributors

E. Acerbi[1], B. Angerth, C. Arnaud, J.P. Bacher, G. Bachy, Y. Baconnier, J.L. Baldy, G. Barbuzzi, O. Bayard, E. Baynham[2], J.M. Baze[3], V. Benda, F. Bertinelli, A. Bézaguet, B. Bianchi, J. Billan, M. Bona, J. Bosser, D. Boussard, C. Bovet, D. Brandt, G. Brianti, E. Brouzet, J.C. Brunet, M. Buhler-Broglin, L. Burnod, D. Cacaut[3], R. Calder, D. Campi, R. Cappi, J. Casas-Cubillos, G. Claudet[4], L. Coull, C. Daum[5], N. Delruelle, J. Diaz-Montoya, G. Drouet, L. Ducimetière, K. Eggert, P. Faugeras, C. Ferigoule, G. Fernquist, J. Gareyte, R. Garoby, A. Gauthier[4], M. Genet, M. Giesch, P. Giovannoni[3], O. Gröbner, D. Hagedorn, M. Hatch, K.N. Henrichsen, W. Herr, A. Hilaire, H. Hirabayashi[6], J.J. Hirsbrunner, M. Höfert, A. Ijspeert, U. Jansson, J.B. Jeanneret, S. Kawabata[6], K.H. Kissler, A. Knezovic, T. Kurtyka, F. Le Coz[3], Ph. Lebrun, P. Lefèvre, L. Leistam, D. Leroy, C. Lyraud[3], R. Maleyran, M. Marquet, M. Martini, A.G. Mathewson, M. Mathieu, M. Mayer, M. Mayoud, V. Mazzone, Ch. Meuris[3], D. Möhl, A. Morsch, L. Oberli, G. Passardi, G. Patti, J. Pedersen, R. Perin, D. Perini, J. Perot[3], A. Perrot, J.G. Pett, S. Pichler, A. Poncet, K. Potter, F. Pouyat, P. Proudlock, J.P. Quesnel, M. Rabany, H.P. Reinhard, V. Remondino, C. Reymermier, G. Riddone, J.M. Rieubland, J.M. Rifflet[3], T. Risselada, J.P. Riunaud, V. Rödel, F. Rodriguez-Mateos, G. Rogner, P. Rohmig, L. Rossi[1], B. Rousset[4], C.E. Rufer, F. Ruggiero, S. Russenschuck, F. Savary, M. Savelainen, W. Scandale, K.H. Schindl, J. Schmid, F. Schmidt, M. Schmitt, G. Schröder, V. Sergo, P. Seyfert[4], G. Shering, N. Siegel, A. Siemko, P. Sievers, G. Spigo, G. Stevenson, B. Szeless, L. Tavian, T. Taylor, H.H.J. ten Kate[7], W. Thomi, T. Tortschanoff, T. Trenkler, R. Valbuena, R. van Weelderen, P. Védrine[3], A. Verweij, J. Vlogaert, G. Volpini[1], L. Vos, G. Vossenberg, B. Vullierme, L. Walckiers, E. Weisse, H. Wenninger, L. Williams, R. Wolf, A. Yamamoto[6], H. Yamaoka[6] and J. Zazula

[1] INFN Milano (Italy), [2] RAL (United Kingdom), [3] CEA-CEN Saclay (France), [4] CEA-CEN Grenoble (France), [5] NIKHEF (The Netherlands), [6] KEK Tsukuba (Japan), [7] University of Twente (The Netherlands)

The Study Group is indebted to many people who have contributed in various ways to this report and in particular to Isabelle Canon, Michèle Jouhet, and Susan Leech O'Neale who showed great patience in preparing the final layout.

Contents

List of Tables

List of Figures

Part I

Overview of the project

The Large Hadron Collider (LHC) Project will be a unique facility for particle physics research, while making maximum use of CERN's existing installations. Ion–ion and electron–proton collisions will naturally complement hadron physics, thanks to CERN's Heavy-Ion Facility, including LEAR for ion accumulation, and the LEP ring.

1 The quest of particle physics

CERN plans to build a machine to bring protons into head-on collision at higher energies than ever achieved before. This Large Hadron Collider (LHC) will penetrate still further into the structure of matter and will recreate the conditions prevailing in the Universe just 10^{-12} seconds after the 'Big Bang' when the temperature was 10^{16} degrees. It will reveal behaviour of the fundamental particles of matter that has never been studied before. The aim is to produce not only high energy but a higher luminosity, or probability of collision, than will be achieved in other existing or planned colliders.

Progressive mastery of the control of charged-particle beams since the beginning of the century has made it possible to construct particle accelerators and colliders of increasing energy. This has allowed matter to be analysed with greater and greater precision. For example, the LEP machine, which is the latest and largest of CERN's existing accelerators, takes the fine detail with which the structure of matter can be studied down to the level of 10^{-15} mm. The LHC will increase this magnification by a factor of ten.

Physics tells us that particles are also waves. An electron microscope exploits the short wavelength of an electron to reveal detail which cannot be seen with visible light. Accelerators and colliders make this wavelength much shorter. The higher the energy, the shorter the wavelength and the more massive the particle that can be created out of a collision. The price one must pay for revealing this fine detail is that the luminosity, or intensity, of the beam of colliding particles must rise in proportion to the square of the mass of the particle one wants to create. It is rather similar to the need to use a brighter light to illuminate the specimen on a microscope slide when a higher magnification is selected. Luminosity is as much a technical challenge as high energy for colliders and for their complex experimental detectors – a challenge which will promote technological advance in Europe's industry.

This addition to the impressive array of CERN accelerators will not be limited to colliding proton beams at an energy of up to 14 TeV, and could later diversify its programme to collide electrons from LEP with one of its proton beams up to a centre-of-mass energy of 1.3 TeV. This type of collision is being studied for the first time with the HERA collider in Hamburg, and the LEP/LHC combination could provide a logical next step with an energy which is five times higher.

The LHC can also collide heavy ions, such as lead, to produce a total energy of 1148 TeV. A large energy density can be obtained over a wide enough region in these collisions to cause phase transition of nuclear matter into quark–gluon plasma. Studies of such a state of matter are expected to yield important new results on subjects such as the collective effects of strong interactions, quark confinement as it occurred in the very early Universe around 10^{-6} s after the Big Bang, and the behaviour of matter in neutron stars. This will enable LHC to retain its unique place on the frontiers of physics research well into the next century.

As one of the world's leading accelerator laboratories, CERN is poised to start construction of the LHC. It has, in addition to its very experienced staff, a considerable infrastructure of laboratories, computing facilities, workshops, etc. It also already has two of the essential and costly ingredients of a collider project — the equipped LEP tunnel and the fully operational injector complex. It waits only for approval.

2 A brief history of colliders

In the mid-1960s, CERN constructed the 'Intersecting Storage Rings' with their two colliding proton beams of 30 GeV in two separate rings of magnets. This was the first in a series of colliders; machines which are really synchrotrons designed to accelerate and store intense particle beams so that they collide within large particle detectors which analyse their interactions. Like the LHC, the ISR's beams were made of protons, which belong to the family of heavier particles known as hadrons.

Up to that time, particle physics with proton beams had been carried out by firing beams from an accelerator onto fixed targets. This mode of operation has the disadvantage that most of the energy of the accelerated proton has to go into the continued forward motion of the particles which are produced and is not therefore available. This is avoided by colliding two protons of equal energy head-on; all the energy of acceleration is available for conversion into new particles or the transformation of the colliding protons.

When the ISR began operation in 1971, CERN launched construction of the last of its fixed-target proton machines, the Super Proton Synchrotron. This machine was also converted to a collider ten years later when a technique to produce intense, high-quality beams of antiprotons was invented at CERN. The SPS was then operated as a proton–antiproton collider and was the scene of the discovery of the W and Z particles, carriers of the weak force.

The latest CERN project to be completed returned again to colliding beams using electrons with their antiparticles, positrons, in a single collider ring. This is the LEP machine which came into operation in 1989. Its electron–positron collisions benefit from simplicity since the electron and positron are 'point-like' objects which can convert completely into energy, rather than the composite hadrons.

LEP is almost certainly the last in the line of circular machines of colliding leptons. Lepton beams emit energy while following a circular path. This synchrotron radiation, though it has extraordinarily useful properties for other applications, is a great drain in the operation of machines for particle physics. It increases dramatically as the beam energy rises and a machine like LEP would be extremely expensive to operate much above 100 GeV per beam.

Thus attention has turned again to proton–proton machines which do not have a significant synchrotron radiation problem; such beams can be accelerated to multi-TeV energies without unreasonable operating costs. (In fact the operating cost foreseen for the Large Hadron Collider is about the same as that of the Super Proton Synchrotron, thanks to the use of superconducting magnets.) With multi-TeV operation, the collision energies of the quark constituents within the protons will enter a fascinating energy domain which we hope will unlock the secret of the particles' mass.

3 The design concept of the LHC

The LHC is a synchrotron like LEP

The design principle of LHC is the same as that of LEP. Both machines are synchrotrons in which a stream of particles is accelerated and held in a circular orbit by thousands of electromagnets. The difference is that LEP collides electrons with their antiparticles, positrons, while both beams of particles which collide in the LHC are protons. The maximum energy of the leptons which collide in LEP is limited to about 100 GeV by the intense flux of synchrotron radiation which these light particles emit as they are bent into a circular path. The energy at which this happens to protons is much higher than for electrons, and they can circulate at the highest energy that the superconducting magnets which form the guide field allow, without the braking effect of this radiation. For a ring the size of LEP, a proton's energy, limited only by the field, may be a factor 80 larger than that of an electron of LEP.

A high guide field

The Large Hadron Collider must provide the maximum energy possible, since it is the energy that takes us deeper into matter and further back in time. Since the machine is to be installed in the existing LEP tunnel, the peak energy is dictated by the maximum strength of the magnetic field which will hold the protons on their orbit. Using superconducting magnets with fields as high as 8.65 T will allow proton beams to be stored at an energy of 7 TeV per beam. This gives a total collision energy of 14 million million electron volts. It should be stressed that magnets operating at 8.65 T must have a quench field of ~ 9.7 T in order to allow for adequate margins covering production scatter and possible heat deposit by lost particles. The LHC could have been designed to use lower fields, closer to the range of 4 to 6 tesla which has already proved possible in large-scale industrial production. However, the higher field seems to be a reasonable extrapolation of current development and promises a more interesting field of physics.

Antiprotons too scarce

It was already clear at the time that the 27 kilometre tunnel of LEP was being designed that this might well be the last new circular tunnel of large size constructed on the CERN site. It was argued that there should, if possible, be space for at least one more ring of magnets above those of the electron positron machine. LEP's designers therefore fixed the beam height and positioned services and cables in the tunnel to leave room for the ring that was to become the LHC.

At that time it was envisaged that a future hadron collider would have a single beam channel for protons to collide on antiprotons, like the SPS. The two beams, of particles and their antiparticles, can be guided by the same magnets because, although they travel in opposite directions, they have opposite charges. Although antiprotons are available at CERN, they are produced by a process with very low efficiency. It takes 300 000 protons to produce one antiproton. The antiprotons must be accumulated over many hours before injection into a collider is worth while. This process was pioneered at CERN in 1981 and perfected to operate the SPS as a proton–antiproton collider of 630 GeV in the centre of mass with a luminosity of 3×10^{30} cm^{-2} s^{-1}. However, although this enabled physicists at CERN to make discoveries of primary importance ($W^{\pm}$, Z) and other important contributions to particle physics, it would be several orders of magnitude too low to make discoveries at LHC energies.

It was therefore decided to use proton–proton collisions in the LHC instead of proton–antiproton collisions. Copious supplies of protons are available from the existing CERN accelerators which will be used as the injectors for LHC — enough to fill the LHC to maximum capacity in a few minutes.

Two beam channels in the same magnet

To collide two beams of equally charged particles, they must circulate in separate magnetic channels. There is hardly room for two separate rings of magnets above LEP but a novel solution has been found using a twin-bore magnet which consists of two sets of coils and beam channels within the same mechanical structure and cryostat. They lie side by side in the cold yokes of both the 1296 dipole bending magnets and 510 lattice quadrupoles. Moreover, in this arrangement a cost saving of 25% can be made with respect to two separate structures.

Use of straight sections

The LHC collider ring, like LEP below it, has eight-fold symmetry and the beam channels exchange and cross at each of the eight points of symmetry. The proton–proton collisions will take place in large underground detectors rather similar to those of LEP. Some of the existing four LEP areas could be converted to LHC use according to the needs of physics. Also one or other of the four odd-numbered points which are not used at present for LEP experiments could be enlarged by excavation for LHC detectors.

The LHC has ions and electrons at hand

The CERN injectors regularly provide a varied menagerie of particles to enrich the physics programme. It is also planned to use the LHC to collide ions. The two separate beam channels of the LHC can store relativistic ion beams instead of proton beams. The energy per ion is the energy reached for protons multiplied by the number of charges of the fully stripped ion. For heavy ions such as lead the total collision energy of the nuclei would reach 1148 TeV.

It will also be possible to collide the electrons of LEP with the protons of the LHC and to extend the work now starting at DESY. We are confident that this will ensure a long and fruitful research programme with the LHC. It was, after all, just such an ongoing development of the SPS, originally conceived for a much simpler purpose, that brought CERN into its pre-eminent position during the era of W and Z discovery.

No effect on the environment

Although the LHC accelerates and collides protons rather than electrons, the radiation level at ground level will be extremely low. Thanks to its deep underground tunnel the LHC will be sufficiently well shielded to ensure that there will be almost no detectable addition to the natural background radiation.

Power demand is no larger than for the SPS

It is also worth mentioning that both the electric power demand and the yearly energy consumption of the LHC are remarkably small, considering the enhancement it brings to physics. In fact, the LHC, with 22 times the collision energy and 10 000 times the luminosity of the SPS proton–antiproton collider, will only consume about the same amount of power as the SPS.

4 The performance of the LHC

4.1 Performance for proton–proton collisions

Luminosity determines the rate

Luminosity is as important a parameter as energy in the design of the LHC since it determines the number of events per second for a given particle interaction. As we build colliders of higher and higher energy, the luminosity should increase at least as E^2 in order to maintain an equally effective physics programme at a higher beam energy. This is due to the point-like nature of the quark–quark collisions which we wish to study. The exploration of those rare processes which are relatively easy to identify such as:

$$\text{Higgs} \rightarrow 2\text{Z} \rightarrow 4\mu\ ,$$

requires an even higher luminosity. Scaling from existing colliders, the LHC should therefore reach the highest usable luminosity which will be in the range of 10^{34} cm^{-2} s^{-1}. Luminosity is defined as:

$$L = N^2\, k\, f\, \gamma / 4\pi\, \epsilon_{\mathrm{n}}\, \beta^*$$

where N is the number of protons in each of the k circulating bunches, f is the revolution frequency, β^* is the value of the betatron function at the crossing point, and ϵ_{n} is the emittance corresponding to the 1 σ contour of the beam, normalized by multiplying by the Lorentz factor $\gamma = (E/m_0c^2)$.

Luminosity is limited by several effects

The main limit to luminosity comes from the beam–beam effect which tends to extract the periphery of the beam due to the influence of non-linear fields seen by the particles of one beam as it passes through the oncoming bunches of the other. The measure of this effect is the linear tune shift produced by these fields and it is generally accepted from the results of experiments with today's colliders that this quantity:

$$\xi = N\, r_{\mathrm{p}} / 4\pi\, \epsilon_{\mathrm{n}}$$

should not exceed 0.006, where r_{p} is the classical radius of the proton.

If we compare these two expressions we find the γ factor in the luminosity but not in the tune shift. This means that higher-energy colliders tend to have a higher luminosity but in proportion to their energy, and not the square of the energy as we would like.

We can also see from these two expressions that if luminosity is to be maximized, we should make β^* as small as possible. But it makes no sense to make it smaller than the length of the bunches themselves since β^* is also the characteristic length of the waist in the beam where they collide.

The number of bunches, k, has to be chosen in such a way as to maximize the luminosity for a given total current and to be acceptable for the data-taking of the experiments. The chosen bunch interval is 25 ns, or 40 MHz bunch frequency.

Clearly, the intensity per bunch must be as high as possible since luminosity depends on N^2, but for a constant tune shift the ratio N/ϵ_n must not change.

Synchrotron radiation heats the cold bore

Another practical limit comes from the total power delivered to the cold bore of the magnets by synchrotron radiation.

$$P_\mathrm{s} = \mathrm{Z}_0\, e^2\, c N\, k\, f\, \gamma^4/3\,\rho$$

where Z_0 is the impedance of free space and ρ is the magnetic bending radius. Although the synchrotron radiation power is modest in comparison with electron rings like LEP, it nevertheless is a problem because it must be absorbed at a temperature of a few kelvin. In fact it will be one of the main heat inputs to the cryogenic system. The strong energy dependence of P_s means that machines with a higher energy than LHC will have difficulty in reaching the same luminosity, at least within a reasonable refrigeration cost. Naturally, there are other limits to the beam intensity such as that due to the need to be able to safely dump the beam, and the usual catalogue of collective instabilities. However, these may be matched to the beam–beam limit by a judicious choice of parameters.

Luminosity

In choosing the parameters of LHC we have found a combination which gives the highest total luminosity for two experiments taking data at the same time. The maximum luminosity in this case and corresponding to the beam–beam limit is in excess of 2×10^{34} cm^{-2} s^{-1} for each experiment. As explained in Section 14 of Part II, Technical Description, the design luminosity of 10^{34} cm^{-2} s^{-1} has been selected well below the beam–beam limited value, in order to reduce the particle loss rate dangerous for superconducting elements. Another limiting effect is the large amount of energy deposited in the inner triplet of high-luminosity insertions by the secondaries produced in the interaction.

Stored energy in the beam

We have already mentioned that the total energy stored in the beam must be absorbed safely at the end of each run or in case of a malfunction or an emergency. At the maximum luminosity of the LHC the stored beam energy is approximately 550 MJ. This can be safely absorbed in a classical beam absorber made of a central graphite core surrounded by aluminium and iron blocks, provided the beam's cross-section is dilated. These absorbers must not be close to the sensitive elements of the ring and two fast extraction channels, one for each beam, will be built to lead to the beam dumps. The beam cross-section increases along these channels and fast, oscillating magnets cause the beam to describe a circular track on the front face of the beam dump to minimize thermal shock.

4.2 Performance as an ion–ion collider

CERN already accelerates sulphur and oxygen ions — lead is next

CERN has already operated the proton accelerator complex (linac–booster, PS, SPS and secondary beams) with sulphur ions and reinforced fixed-target experiments, and is currently building a lead-ion source together with a new pre-acceleration stage. Such a new front-end would enable the LHC to collide lead ions on lead ions with a total nuclei energy of 1148 TeV and a luminosity of approximately 10^{25} cm^{-2} s^{-1}.

Even higher ion luminosity

This luminosity might be improved by accumulating ions at low energy prior to injection into the LHC. It has been ascertained that LEAR, the existing Low Energy Antiproton Ring, can be made to accumulate lead ions so that luminosities of about 10^{27} cm^{-2} s^{-1} could then be obtained in the LHC — more than enough to carry out a very worthwhile physics programme.

4.3 Performance as an electron–proton collider

Energy and luminosity of electron–proton collisions

The LEP electron beam will reach an energy above 90 GeV well before the installation of the LHC. By colliding an electron beam at 60 GeV with one of the proton beams at 7 TeV, electron–proton collisions with a centre-of-mass energy of 1.3 TeV can be obtained with a high luminosity in excess of 10^{32} cm^{-2} s^{-1}.

To bring electrons to collide with protons

To obtain electron–proton collisions, the electron beam of LEP will have to be deflected upwards towards one of the proton beams at one collision region and returned to its normal path afterwards. Special precautions will have to be taken to protect the experiment against the synchrotron radiation generated by these deflections close to the interaction region, but by that time considerable expertise will have been built up as a result of the high-energy LEP and HERA operation.

5 The component systems of the LHC

5.1 The lattice

Matching up to LEP

The layout of the two beam channels is reminiscent of the ISR. They both lie in the same plane and cross at eight points, corresponding to the eight collision regions of LEP. The inner and outer beams are exchanged at each of these points so that both beams have precisely the same circumferential length. If this were not the case the bunches would not remain in synchronism. The crossing angle (200 μrad) is much smaller than in the ISR; large enough to ensure that the many bunches passing each other in the two beams do not influence each other too much outside the collision point, and small enough to be contained within the limited aperture of the common quadrupoles. In the eight arcs the bending and quadrupole magnets of the two rings are separated by 180 mm and the plane of the machine is exactly 1.21 m above LEP, both in the arcs and at the crossings.

These constraints, together with the practical issue of ensuring that LEP and the LHC remain mechanically in register for most of their circumference, essentially fix the shape of the bending structure of the ring. The regular FODO cells are 102 m long and there are 24 of them in each of the eight arcs of a ring. Each half-cell contains three twin-bore, bending magnets of 14 m overall length together with a twin-bore quadrupole, beam-position monitors, steering dipoles, tuning quadrupoles, and other multipole windings. The sagitta in the bending magnets is 8 mm (± 4 mm) but this will be compensated by a slight curvature of the cold mass of the magnet.

We shall see that in a machine as large as the LHC and with a strong non-linear perturbation at injection to cope with, it is not possible simply to correct for sextupole and decapole effects at each quadrupole. Small sextupole and decapole coils are therefore included at the ends of each main bending magnet, and powered separately for each ring.

Dispersion suppression and matching

The dispersion suppressor at the end of each arc consists of four quadrupoles interspersed with sets of two or three twin-bore dipoles. For low-beta insertions, this is followed by two quadrupole triplets which match the beam down to the low beta value required to maximize luminosity at the crossing point. The two beams merge in between the two triplets so that the triplet close to the crossing can be a single-bore quadrupole. The beam-merging system itself consists of a pair of dipoles. In these the beams see a common field and are therefore bent in opposite directions. Finally, the two beams are a few millimetres away from the LEP axis seen in plan view as they pass through the inner triplet. As they cross in the interaction region, they are essentially collinear and 1.21 m above LEP.

Insertions

Matching low-beta insertions is a routine problem in beam optics these days. There are three main configurations: a general-purpose low-beta insertion for experiments, an insertion specially adapted to the beam-cleaning system, and an insertion specially designed to allow the two beams to be extracted to the beam dumps, with a high beta at the kicker position.

The tuning range of the beta value in the general-purpose low-beta insertion is from 0.5 to 15 m and the free space between the triplets for the experiment extends 16 m on each side of the crossing point. The insertion for the electron–proton option has been fully worked out both for LEP and LHC including the method of bringing the LEP beam up to collide with the LHC.

Beam at injection

The r.m.s. alignment tolerance of 0.14 mm is standard for all magnets as is the relative field error of 5×10^{-4}. Steering magnets are sufficiently strong to correct the orbit distortion produced by these errors up to 7 TeV and separately for the two beams. The injection field is 0.58 T, about 15 times lower than the peak. This is quite close to the injection fields of the Tevatron and the SSC and roughly twice that of HERA. We expect the eddy currents, which persist in the windings of the dipoles and which produce sextupole fields, to be at least as important as in the Tevatron and the SSC and to dominate the correction strategy at injection. We are watching the experience of HERA closely for, in that machine, not only is the injection field lower but the filament diameter which determines the strength of these currents is more than twice that of the LHC.

Field errors

There are certain inevitable errors in the magnet construction which may be divided into two categories. The first, the systematic errors, stem essentially from the shape of the windings which, at best, can only be an approximation to the ideal current distribution (intersecting ellipses), from the persistent currents which tend to affect all magnets equally at low field, and from the twin-bore configuration whose yoke, when saturated, produces certain common asymmetries. One may hope to correct these systematic effects with a careful combination of prediction and experimental correction.

The second category, the random errors, are serious at injection energy because they excite non-linear stopbands which cause the beam to diffuse outwards during the few minutes one must wait to complete the filling sequence. It is one of the most challenging tasks of the magnet builder to keep these within bounds in the design and especially during the series production. A careful routine of magnetic field quality-control must be rigorously adhered to. The Technical Description gives full details of these tolerances, expressed as coefficients of the cylindrical harmonics of the field distribution.

Dynamic aperture

The simulation of the adverse effects of the magnet field errors could well keep the world's computers busy for many years. In practice, with runs of many hours on the CERN Cray, we have been able to identify the radial extent of the small central region of the magnet's aperture in which the beam can safely circulate.

All possible modes of beam disturbance must be built into these simulations since it is generally accepted that it is the combination of errors, rather than any one error, which causes the beam to leave this region.

The simulations so far show that this central region, or dynamic aperture, defined in terms of the stability over the several minutes of injection, is sufficient for the beam from the SPS which gives the design luminosity when an inner coil diameter of 56 mm is adopted.

5.2 The superconducting magnets

The superconducting magnets are the most technologically challenging components of the Large Hadron Collider. Superconductivity is a property that some materials acquire when they are cooled to a low temperature; their resistance to the passage of electrical current virtually disappears. Large currents can be passed through superconductors of small cross-section so that compact magnets can be built and operated for much lower cost than conventional magnets made with copper or aluminium conductor. The only energy that is used in producing the field in the superconducting magnet is that needed for the refrigeration of the conductor necessary for it to retain its superconducting property.

There are two large operational accelerators based on superconducting magnets, the Tevatron at Fermilab and HERA at DESY. Both make use of classical NbTi superconductors cooled with normal liquid helium at a temperature slightly above 4.2 K, and their operational fields are relatively low ($\sim$ 4 T for the Tevatron and 4.7 T for HERA). The HERA magnets were manufactured by industry.

More recently, the SSC decided to adopt a magnet design very similar to that of HERA but pushed to a high field (6.6 T), probably an upper limit with NbTi at 4.2 K. A number of magnets have been manufactured and tested successfully.

For the LHC, to be installed in the existing LEP tunnel, it is attractive to push the field significantly higher, still retaining the well-proven fabrication methods of cables and coils made of NbTi superconductors. The only way of obtaining fields around 9 T is to cool the magnets to a much lower temperature ($\leq$ 2 K). This technique has been applied successfully to the French tokamak TORE SUPRA in operation at Cadarache. Below 2.17 K, helium takes the so-called superfluid state, with much lower viscosity and much greater heat transmission capacity than normal helium. These properties can be used for the design of the cooling scheme, and in particular permit a drastic reduction of helium flow through a magnet.

On the other hand, the heat capacity of all metallic parts and in particular of the superconducting cables is reduced by almost an order of magnitude between 4.2 K and 1.9 K, with consequent faster temperature rise for a given deposit of energy. This feature calls for particular care in limiting conductor motion. It should be noted that the electromagnetic forces on the conductor increase with B^2 and so does the stored electromagnetic energy, calling for stronger force-retaining structures and more elaborate quench protection systems than for previous projects.

It was explained in a previous section how the two proton beams circulate in the opposite direction through a twin-bore magnet system with the same yoke and cryostat for both beams. Only the coil assembly and beam tubes are duplicated. They lie side by side in the cold yokes of the 1296 dipole bending magnets and the 510 two-in-one quadrupoles. In Figure 9 of Part II, Technical Description, which shows a dipole cross-section, we can clearly see these channels, their axes 180 mm apart.

Correction systems

The penalty one must pay for this compact cross-section is that the magnets of the two channels cannot be independently aligned, nor can individual magnets with small errors in one channel be easily paired off with others having the opposite errors. However, the LHC will be equipped with a sufficient number of correction magnets for beam steering and for optical tuning and will also have windings to produce fields corresponding to six-, eight- and ten-poled magnets. All magnets will be carefully inspected and measured and these correctors deployed to iron out any residual errors with tactics learned through many hours of supercomputer simulation and operational experience with the present CERN accelerators. There will also be time to embody the experience of building, measuring and operating the new HERA ring at DESY before the LHC embarks upon its own programme of construction.

Research and development

It is feasible today to build a magnet for an operational magnetic field as high as 8.65 T in a configuration suitable for a particle collider with long coils and a small aperture.

CERN has an ambitious programme of research and development in association with European industry to bring the peak field to at least 9.5 T.

New technology saves power and protects the environment

The use of superconducting magnets for particle colliders is an excellent example of how high technology brings cost savings yet, at the same time, has minimal environmental impact, in this case by providing a more advanced tool for research for a lower unit cost and with a lower energy consumption for a given performance.

5.3 Cryogenics

Refrigerators

The project LEP 200, aimed at almost doubling the present LEP beam energy, involves the installation of four large helium refrigerators in the even interaction points. These refrigerators are designed to produce a cooling power of up to 12 kW each at normal liquid-helium temperature. This happens to coincide with the requirements for the neighbouring two half-octants of the LHC magnet system, provided the compressor sets capable of 12 kW for LEP are increased to 18 kW capacity. In this way we plan to make double use of a considerable investment.

Extra refrigerators

To complete the cryogenic system for the LHC we shall also have to install refrigerators in the four odd LEP points. Obviously it would be preferable if all eight refrigerators were identical. Each will have an extension in order to lower the temperature to 1.8 K by means of multistage subatmospheric compressors operating with cryogenic helium.

5.4 Injectors

The existing complex of CERN accelerators is available as an injector. It has the highest reputation both for beam output and reliability. The only major additions required will be new RF systems for the PS and the SPS, and two new beamlines from the SPS to the LHC to allow protons to be fed to the new Collider in both the clockwise and anticlockwise directions.

Injection scheme

All the existing proton machines of CERN play their role in the injection scheme for the LHC. These include the 50 MeV proton Linac, the 1 GeV PS Booster, the 26 GeV PS itself, and finally the SPS which will inject into the LHC at 450 GeV — its top energy. The PS is filled with somewhat less than its peak current but within small transverse emittance. The combination for these two parameters is chosen to fill the dynamic acceptance of the LHC, but to be within the space-charge limit of the PS at injection and of its Booster at injection from the Linac. The PS will have new RF systems which form bunches at the 25 ns spacing that the LHC will need. It accelerates three times to deliver three batches of 81 bunches to the SPS. The SPS, at the limit of its beam handling capability, then accelerates these to inject into the LHC. This sequence is repeated 12 times for each ring of the LHC, taking a total of 400 seconds.

Injector performance

The PS must deliver a beam of 81 bunches to the SPS each containing up to 1.6×10^{11} protons. This is about 60% of the currently achieved peak intensity. However, at its peak intensity the normalized emittance[1] of the PS is typically 10 μm and is limited by space charge in both the PSB and the PS. To reduce this to the 3.0 μm required to achieve full design luminosity will impose some modifications, even at this reduced intensity. The proposal is to raise the PS space-charge limit by exploiting the possibility of raising the PSB energy at transfer to 1.4 GeV. This will allow a smaller but brighter beam to be accelerated. This entails an upgrading of the various transfer line elements and new RF systems accelerating one bunch per PSB ring.

With the newly installed RFQ, Linac II already provides a current pulse of sufficient intensity and length to fulfil the requirements of the LHC.

The SPS too will need new RF systems to capture the bunches at the 40 MHz frequency at 26 GeV and to compress them longitudinally prior to ejection towards the LHC. The existing travelling-wave cavities will provide the acceleration but their amplifiers must be upgraded to take care of the very strong transient beam loading. Naturally there must be new ejection systems in LSS4 and LSS5 to send the beams into the two new tunnels which connect with the LHC. These beam transfer lines will use superconducting magnets cooled with liquid helium at 4.5 K.

5.5 Protection against beam losses

The need for scraping

During high-energy collisions produced in the physics experiments, many elastic particles are emitted in the forward direction with the same momentum and a slight increase in transverse angle. The same effect occurs along the whole machine due to beam–gas interactions. Furthermore, non-linear effects also contribute to an amplitude increase of the transverse and longitudinal distributions. All these effects will progressively push some particles outside of the stable region, creating a systematic halo.

One of the most challenging problems we confront is the need to ensure that this halo be intercepted before it hits the cold inner bore of a magnet. Calculations have been made of the rate of dilation of this halo. It is clear that if only a few per mille of the diffusing flux were to end up in a superconducting magnet, it would cause it to quench. Transverse and longitudinal cleaning systems are then required.

---

[1] Normalized emittence: $\epsilon^* = (\beta\gamma)\sigma^2/\beta$.

Collimators and absorbers

The difficulty in cleaning a 7 TeV beam halo results from the fact that at those energies most particles will hit the primary collimator at a small distance from its edge, of the order of one micron. A large fraction of them will escape resulting in only a small increase in transverse distribution due to scattering. Secondary collimators, slightly retracted with respect to the primary collimator and set at optimum phase advances and betatronic values from it, are required to capture the escaping particles.

To be efficient the collimators must be well aligned with respect to each other and relative to the beam. Mounted on accurate mechanisms, they cannot be too heavy. Therefore, the particles entering into a secondary collimator will not be fully absorbed in it. The particles produced in the nuclear interactions escape from secondary collimators with a much lower momentum: they will be deflected by a warm magnet and absorbed in a region without superconducting magnets.

It has been shown that the momentum collimation can also use the same set of collimators by adjusting the dispersion by means of a dedicated optics.

The optical and radiation requirements of a cleaning area are clearly incompatible with an experiment in the same straight section.

Beam dumping

Beam dumping must work with a daunting reliability and we must find appropriate ways of detecting the onset of beam loss so that the beam can be safely extracted long before it causes a quench. It is not possible to envisage a beam-dump in the LHC ring itself. The density of the beam is so high that severe mechanical damage would result and the background radiation to nearby equipment would be unacceptable. The beam-dumps are at the end of tunnels excavated tangentially to the ring and we must take special measures to blow up the beam transversely before it hits the dump. The dump itself is an assembly of graphite and aluminium blocks buried in an iron shield. The whole assembly will be installed in a waterproof cavern to prevent underground water contamination. The radiation level at the surface will be undetectable.

Beam extraction

The two extraction lines leading to the dumps are conventional fast extraction systems. The scale of the equipment is impressive. For each beam 26 pulsed magnets and 26 power supplies must be held, charged and ready to fire. The rise time of 3 μs must match the gap in the beam left for this purpose.

Sinusoidal oscillation

The natural divergence of the beam is insufficient to ensure the spreading of the thermal shock of impact on the surface of the dump, and a pair of orthogonal kickers following a sine wave cause the beam to describe a circle as it is extracted.

5.6 The vacuum system

The vacuum system at cryogenic temperatures subjected to the effects of synchrotron radiation from the proton beam represents a novel challenge.

The pressure requirements for a 24-hour beam-gas lifetime do not seem difficult to meet in view of the effective cryo-pumping by the walls.

The stainless steel vacuum chamber, in contact with 1.9°K superfluid helium, is protected from the power deposited by the synchrotron radiation by a separate 'beam screen' cooled to a temperature between 4.5 and 20°K. The pumping capacity of the screen for hydrogren in this temperature range is insufficient to maintain the low operating pressure as the gas load by synchrotron radiation induced desorption accumulates on its surface. With a proper design of perforations in the beam screen, the excessive gas can be transferred to the 1.9°K surface of the surrounding cold bore which is protected from radiation or ion bombardment and where the capacity is practically unlimited.

5.7 The RF system

The choice of frequency for the LHC is a compromise between a low frequency, which would minimize the danger of particles leaving the bucket during storage due to intra-beam scattering, and a high frequency, which requires less RF voltage for a given bunch length, and for which modern technology offers economic hardware. Clearly the frequency must be a multiple of that used upstream in the injectors. Also the bucket must be larger than the bunch area which the SPS is to provide. The frequency chosen is 400.8 MHz.

The voltage required is 16 MV per beam — large enough to avoid RF noise diffusion in collision mode. Energy loss by synchrotron radiation is negligible compared to this.

The LHC has an unusually large number of intense bunches, separated by gaps for injection and ejection towards the beam dump. These gaps produce a strong transient beam-loading in the cavities. The result is a phase modulation among the bunches which can cause the collision point to be in a different longitudinal position depending on how far away from the gap the colliding bunches are.

The superconducting cavities proposed for the LHC greatly reduce this phase modulation because they have a lower R/Q and a higher voltage than ordinary copper cavities and the change in crossing-point position is greatly reduced.

For the very dense bunches and the very high average currents of the LHC, superconducting cavities with their large-diameter beam tube offer in addition the advantage of minimizing the parasitic impedances of the RF system.

The cavities must be located in a position where the two beams are essentially collinear and pass close to the cavity axis. Separate cavities for the two beams are excluded by the short distance of the two beam channels (180 mm). Eight cavities in total placed on either side of the interaction point dedicated to the ion experiments will fulfil this requirement. With sophisticated low-level controls the power demands are greatly reduced, the consequence being that windows, couplers and klystrons are within today's state-of-the-art technology.

To complement the main RF system a bunch-to-bunch longitudinal feedback is necessary to avoid any coupled-bunch instabilities. This system, based on broad-band cavities, separate for the two beams, will also quickly damp the phase injection errors in order to keep the highly undesired capture losses to an absolute minimum. Similarly, transverse feedback systems are necessary to minimize emittance blow-up due to horizontal and vertical errors at injection. The same systems will also prevent any coupled-bunch transverse instability from developing.

5.8 Other systems

Among the other machine systems, beam observation and monitoring, while not representing any major new technological challenge, are more delicate than the ones of LEP due to the much larger dynamic range of the intensity (from pilot to full beam) and to their location inside the cryostats. Some systems, such as electrical power distribution are relatively minor extensions of the LEP infrastructure. All these systems are described in the corresponding sections of the Technical Description but we shall not dwell upon them in this overview.

All the conventional facilities of LEP including electrical power distribution, ventilation, access shafts, handling equipment, telecommunications and computer networks will be used for the LHC. These represent considerable assets permitting corresponding savings in material and personnel expenditures for the project.

5.9 Survey and alignment

The initial positioning and alignment of LHC components will be ensured by using LEP as the reference geodetic network. A final smoothing will then be made directly on the LHC reference targets.

Particular attention will be paid to the alignment of the low-beta sections which may require direct sighting through the experimental equipment. Special cares and test measurements are intended for the inner metrology and stability control of the cold-mass inside cryostat, with respect to the fiducial points used for alignment.

6 The LEP and LHC programmes

In 1991, when the LHC Design Study was published [1], it was envisaged to continue the LEP programme after the installation of the LHC, for example alternating yearly running of the two colliders.

After a new thorough analysis and considering the delay in starting the LHC project, it is much more appropriate now to propose to bring the LEP 100 and LEP 200 programmes to an end prior to the commissioning of the LHC.

Indeed, an adequate time of the order of five years would normally be available to complete the LEP 200 programme prior to the LHC final installation. Of course, should exceptional results occur with LEP, demanding a prolongation of the programme, the LHC programme could be adjusted accordingly. Obviously, the LEP machine itself will be preserved in view of future electron–proton collisions.

The running of LEP and LHC in succession rather than in parallel has important positive repercussion on the total work to be carried out for the LHC, for both the machine and the experimental areas. Indeed, the considerable infrastructure in terms of underground areas and technical services existing in and around LEP can be used to a much larger extent with this new approach, resulting in significant overall savings.

7 Zones for experiments

7.1 Use of straight sections

Like LEP beneath it, the LHC has eight long straight sections symmetrically distributed around the ring. The two beam channels interlace in each of these and the opposing beams can be steered to collide at the mid-point. Four of these are now occupied by LEP experiments which will be removed to the garage position and could be dismounted prior to LHC operation. It should be stressed that the machine lattice has been kept very flexible and an insertion of a given type can be realized in any of the LHC straight sections independent of the neighbouring insertions.

Areas for LHC experiments

Out of the four remaining odd-numbered straight sections which are not used now for LEP experiments, two are reserved for machine utilities. Therefore LHC has potentially six possible locations for its detectors, the four even points and two odd points.

Two straight sections reserved for cleaning and dumping

There are two machine utilities which must find their place among the available straight sections: beam cleaning and beam dumping. LHC beams are so intense that we cannot risk their hitting magnets or other sensitive components. They may easily do severe mechanical damage if they hit anything other than a specially designed beam dump. At the first indication of beam instability, the beams will be ejected with a fast extraction system into 400 m long tunnels at the end of which is the dump. There are two such channels in opposite directions and their optics excludes a low-beta crossing region in the same long straight section.

At first sight it seemed desirable to locate this beam-dumping system in the inaccessible point 3 which is deep under the Jura. Closer examination exposes the severe civil engineering difficulties of making two new tunnels in the fragile water-bearing limestone in this region. We fear that excavation there might well put the whole project at risk. The final location of the beam-dumping system is in point 5 where excavation is easy, but where the alternative of a large new cavern for an experiment would be restricted by the shallow roof cover of the molasse.

The other machine utility is the beam clean-up system. This cannot be located in the same straight section as the dumping for reasons of equipment layout, beam parameters and trajectories. It therefore seems sensible to put it under the Jura in point 3 where we could not contemplate excavating a new experimental zone. Other machine utilities such as the injection of the two counter-rotating beams, are performed in straight sections 1 and 8, but they are compatible with an LHC experiment.

Beams and experiments for ions are as for protons

Ion–ion collisions can be achieved with exactly the same beam layout and equipment as proton–proton collisions. The proton injectors (PS and SPS) with the addition of the lead-ion source under construction and of LEAR, the existing low-energy antiproton ring, which can be converted into an ion accumulator with minor modifications, constitute an excellent injector complex for ion–ion collisions in the LHC with 2.76 TeV/nucleon and a luminosity of more than 10^{27} cm^{-2} s^{-1}.

Electron–proton collisions

Electron–proton collisions require a special insertion to raise and focus the electron beam into line with the proton beam at the interaction point. Such an insertion cannot be installed in the straight sections where the proton injections occur (1 and 8). It could be installed in straight section 7 without any limitations, or in straight sections 2, 4, or 6 once one-quarter of the LEP superconducting cavities are removed. Losing these cavities would not cause a loss of energy in the electron–proton mode since we expect 60 GeV to be the LEP top energy for the many electron bunches it will carry in the electron–proton configuration. The centre-of-mass energy of electron–proton collisions would be 1.3 TeV and the luminosity in excess of 10^{32} cm^{-2} s^{-1}.

7.2 Civil engineering of experimental areas

The dimensions and characteristics of the largest envisaged LHC experiment for proton–proton collisions (ATLAS), may call for the construction of a new experimental area, for example in points 1 or 7, or for a substantial modification of one of the LEP areas, for instance at point 6. The other proton experiment (CMS) can be housed in the existing area in point 2, with some modifications. The ion experiment (ALICE) can be housed in one of the other LEP areas, e.g. in point 4.

7.3 Other experiments

Some experimenters would like to use the LHC for other types of physics.

Examples are:

- Studies of beauty physics, using a gas jet on one LHC beam or on a slowly extracted beam (possibly by means of channelling in a bent crystal);
- Study of beauty particles from pp collisions;
- Experiments on neutrinos (from pp collisions).

These kinds of experiments are in most cases feasible, but precise technical solutions can only emerge from future studies.

8 Safety

It is perhaps not immediately self-evident that the radiation levels from the LHC will be as low as for LEP since protons do not behave in exactly the same way as electrons. On the one hand, protons do not emit significant synchrotron radiation like electrons, but on the other hand, they are strongly-interacting particles. These differences, together with the higher energy of the LHC beam prompted a workshop to review whether or not the LHC would have any impact on the local environment. This took place in May 1989, and was attended by scientists from several universities and national laboratories, as well as from CERN who studied the subject in depth.

They concluded that:

- At the surface above and around the LHC, radiation dose rates resulting from any possible process will be negligible, if not undetectable;
- The extra radioactivity induced in the rock around the tunnel will be negligible and will have no consequences on the environment;
- The quantities of radionuclides reaching the environment will be very small, and in any case well below national radiation regulations and CERN limits.

Host States will be consulted to ensure there is no impact from the LHC

A full and detailed environmental impact study will, of course, be an important early step in the project. It will then be submitted to the safety authorities of the Host States for approval. This procedure will fully guarantee that running the LHC will have no effect on the environment.

9 Steps towards completion

The R&D Programme (1990–1993)

The R&D programme of magnet and cryostat development is based on the active participation of Member-State institutes and industry for the fabrication of suitable cables, models (magnets of full cross-section but 1.3 m long) and prototypes (full-size magnets). At present industry is primarily involved in the production of full-size magnets. CERN also has facilities for the production of models with the aim of determining the final optimization of coils, particularly the ends, of insulation materials and systems, and of the mechanical structure.

A number of models and one long magnet have been made mainly by industry and tested so far. Seven full-size magnets are in production in industry and their delivery to CERN will start in a few months. The results, which are reported in detail in Part III, Superconducting Technology, can be summarized as follows:

- At 4.2 K the maximum field of 7.9 T, corresponding to the current-carrying capability of the cables as measured in short samples, was reached after one or few training quenches, confirming the soundness of the design according to the experience of previous projects;
- At 1.8 K the ultimate field of 9.8 T to 10 T was obtained, but in general after a relatively large number of training quenches above 9.5 T. The analysis of the results showed that most intermediate quenches occurred at the ends, where the field is lower than in the central part but where it is more difficult to prevent cable movements;

- A recent model using industrially made coils basically identical to all previous ones, but with more compact ends, and made with better-performing last-generation cables, was assembled at CERN, using an improved mechanical structure. This model showed a much improved behaviour. It reached 9.3 T in two quenches, 9.5 T in five quenches and finally attained the record field of 10.5 T. After full training and subsequent complete warm-up and cool-down all further quenches were above 9.75 T. In this magnet all training quenches started in the ends or in the splice between inner and outer coil layers. This makes us confident that long magnets will behave as short models;
- A magnet with a CERN twin structure, but coils identical to HERA, was built in industry and successfully tested at CEA-Saclay at the nominal temperature of 1.9 K. Its behaviour was excellent since at 4.2 K it reached the maximum field with no quenches and showed exactly the same properties as the single HERA magnets. When cooled down at 1.9 K, it was possible to increase the current from 6600 A to 9500 A thus reaching the conductor short sample limit of 8.3 T. It should be noted that the HERA coils have a much larger aperture (75 mm instead of 56 mm).

In addition, two full-size twin quadrupoles were designed and assembled by DAPNIA (CEA–Saclay) and their testing is about to start.

A lattice half-cell

A complete half-cell, comprising about 50 m of the magnetic structure of the collider and including four dipole and one quadrupole magnets, will be installed in the SM18 LEP assembly hall for system tests.

10 Conclusions

The design and experimental work carried out up to now, which is reported in more detail in Part II, Technical Description and in Part III, Superconducting Technology, indicate that the machine can be constructed to achieve the prescribed performance both in terms of energy (14 TeV in the centre of mass) and luminosity (10^{34} cm^{-2} s^{-1} for proton–proton collisions). It is now envisaged to also exploit lead-ion collisions soon after the beginning of operation (1148 TeV total centre-of-mass energy, 10^{27} cm^{-2} s^{-1} luminosity), taking advantage of the conversion of LEAR into an ion accumulator, while electron–proton collisions may be implemented later.

It should be noted that the first joint ECFA–CERN study on the feasibility of the LHC in the LEP tunnel took place in Lausanne in 1984, almost ten years ago. Since then, and in particular in the last two to three years, the design and the experimental work on both the accelerator and the detectors have progressed so much that CERN can now propose in full confidence a unique facility for particle physics research.

Part II

Technical description

1 Introduction

In May 1991 a design study of the Large Hadron Collider (LHC) was published in a document [1] with a pink cover, since called the 'Pink Book', which described the basic design and outlined the predicted performance for the three types of collisions, proton–proton, heavy-ion, electron–proton. In 1993 most of the arguments developed in this design study are still valid.

The present document gives a more detailed presentation of the machine, it being understood that the main choices presented in the Pink Book are maintained, but adapted to the progress in design and understanding:

- The LHC uses the LEP tunnel [2] with as little modification as possible for reasons of economy. The new time scale considered, where the LHC is installed after the completion of the LEP programme for e^+e^-physics, allows the use of the considerable LEP infrastructure. Obviously, the LEP machine itself will be preserved with a view to future electron–proton collisions;
- The two-in-one design of the main magnet and quadrupoles has been kept, the only change being an increase of the aperture by about 10% in order to enlarge the dynamic aperture and the physical aperture at injection, taking account of the beam screen. The magnet design itself has been slightly modified as explained in Part II, Superconducting Technology;
- The design field in the magnet has been lowered to 8.65 T, and the bending length around the circumference has been increased by 5% by inserting three magnets of 13.145 m in the half-cell instead of four magnets of 9 m. The number of cells per arc has also been reduced from 25 to 24. The design energy is 7.0 TeV.

The design luminosity has been fixed at 10^{34} cm^{-2} s^{-1}; the beam–beam limited value is 2.5×10^{34} cm^{-2} s^{-1}. It is limited by a number of effects detailed in the text. The machine will be designed such that if, given time and effort, the various limitations can be overcome, the hardware will not limit the luminosity to values lower than the beam–beam limit. As explained in Section 14.3 the high luminosity operation will only be achieved after several years of operation.

This Part describes the LHC equipment in clockwise order around the LHC rings. The machine parameters and the heavy-ion operation are reviewed in Sections 14 and 15. A series of annexes provides more detailed information:

- Table of parameters;
- List of equipment and equipment names as used for the cost estimate;
- Civil engineering at interaction points;

The text also makes reference to a number of related documents where more details and technical data are given. A list of LHC notes is available on request.

2 General layout of the LHC

The implantation of the LEP tunnel across the French–Swiss border is represented in Fig. 1. The LHC rings, installed in the same tunnel, must follow the same geometry. The description of the LHC is made easier by introducing the following definitions:

- **Rings**
  There are two rings, one per beam. Ring 1 refers to the beam circulating clockwise, ring 2 refers to the beam circulating anticlockwise.

- **Upstream/downstream**
  In the tunnel a downstream section refers to a machine section which follows a given point in the clockwise direction. This convention is also used for the numbering system.

- **Crossing points**
  The rings are interlaced and cross at eight points called crossing points or intersecting points referred to as IP1, IP2, ..., IP8. Crossing points where the two beams are made to collide are called interaction points or collision points, or experimental crossings. The area around an interaction point is called an interaction area or region.

- **Sector**
  That part of a ring between two consecutive crossing points is called a sector. Sector 1–2 is placed between crossing points 1 and 2. Ring 1 is the outer ring in the 'even' sectors 1–2, 3–4, 5–6, 7–8, and the inner ring in the 'odd' sectors 2–3, 4–5, 6–7, 8–1.

- **Arc**
  The part of the ring occupied by regular half-cells with three dipoles; does not contain the dispersion suppressor.

- **Octant**
  An octant starts in the middle of an arc and goes to the middle of the downstream arc. It is made of an upstream and a downstream half-octant. A half-octant and a half-sector cover the same part of the collider even though they may not have the same number.

- **Insertions**
  An insertion is the part of the ring between two arcs. It is made of one dispersion suppressor, one full straight section, and a second dispersion suppressor. There are different types of insertions called after their function: insertions 1, 2, 4 are experimental insertions, insertions 3 and 5 are, respectively, the cleaning and beam-dump insertions. It should be noted that the attribution of crossing points to experiments is tentative. Other possibilities exist. Insertions 1 and 8 are injection insertions. The other insertions are for the time being called empty or simple insertions. The attentive reader is warned that in the LHC, like in LEP, even-numbered insertions are 3 m longer than odd-numbered ones.

- **Straight sections**
  The term 'straight section' is reserved for the long straight sections of the insertions, including the separation magnets.

Geometry

The insertion straight sections are about 540 m long. The dispersion-suppressor arc measures 154 m and has a radius of curvature of about 4.7 km. The main arc is about 2.5 km long with a radius of curvature of about 3.5 km. The total circumference is about 26.7 km. The regular tunnel cross-section (Fig. 2) has a diameter of 3.8 m. The occupation of the straight sections is given in Table 1 and Fig. 3.

Table 1: Allocation of the straight sections

Intersecting Point	Tunnel		LEP 200	LHC
	Depth (m)	Slope (%)		
I (Meyrin)	82.0	1.23	Injection in arcs	p–p experiment Injection beam I
II (St Genis)	45.3	1.38	L3 RF	p–p experiment
III (Crozet)	97.5	0.72		Cleaning
IV (Echenevex)	137.5	0.36	Aleph RF	Ion experiment RF
V (Cessy)	86.6	1.23	Cleaning Dump	Dump
VI (Versonnex)	95.0	1.38	Opal RF	
VII (Ferney)	94.0	0.72		
VIII (Mategnin)	98.8	0.36	Delphi RF	Injection beam II

The LHC rings are, like LEP, in a plane tilted with respect to the horizontal. The LHC is placed 1.21 m above[2] LEP. The geometry of the LHC, represented schematically in Fig. 3, is strictly determined by the geometry of LEP. The tunnel is too small to allow the two rings of magnets (LEP and LHC) to differ in radial position by more than a few centimetres. The standardization of the tunnel infrastructure also requires a rather strict superposition of the two rings. Finally, the requirement of e–p collisions imposes a precisely equal revolution period of the beams in the two machines. The LHC lattice is designed to keep the axis of the LHC twin-aperture magnet centred on the central orbit of LEP. In the insertions, as well as in the arcs, the two orbits never differ by more that a few mm (Fig. 4). The interlacing of the two rings allows the circumferences of the LHC rings to be precisely equal to the LEP circumference.

Layout

It was not possible to adopt for the two machines (LEP and LHC) the same lattice cell in the arcs: LEP requires a strong focusing to reduce emittance, while the LHC requires as little focusing as possible in order to leave space for the dipole magnets. As a consequence, LEP has 31 cells, while the LHC has only 24 cells in the same arc. The design of the mechanical supports and of the auxiliary equipment (cable trays, connections etc.) of the LHC have to be adapted to the LEP environment. The corresponding mechanical design has been made easier by the attribution of well-defined areas for LEP and LHC in the tunnel cross-section (Fig. 2).

On each side of the arcs the dispersion suppressors reduce the dispersion to zero at the crossing point. They have to satisfy a number of constraints: the cell size and quadrupole strengths have to be as similar as possible to the standard LHC cells in order to maintain the beam size within the available aperture. The magnet cross-sections must be the same as the standard magnet and their length, if possible, identical in order to reduce the number of magnet types to be developed and produced. To match the LEP geometry the dispersion suppressors are slightly different in even and odd insertions.

Insertion straight sections

The eight insertion straight sections are divided into two sets: even straights and odd straights. The even insertion straight sections are all occupied with LEP experiments. The LEP experiments have been installed in caverns oriented perpendicularly to the machine tunnel (with the exception of SS 2 where the L3 experiment is installed in a 'longitudinal cavern', which can be used for an LHC experiment). These 'transverse caverns' may not be compatible with the larger LHC p–p experiments, so one of them has to be enlarged or a new cavern has to be created at an odd interaction point. The heavy-ion experiment can probably be installed in any of the LEP experimental caverns. In the present layout it has been assumed to be in SS 4.

Two straight sections have to be reserved for specific functions, namely beam dumping and beam cleaning, and cannot house any detector. These functions do not require large halls and are therefore installed in insertions where the civil engineering is more difficult and

---

[2] The LEP plane being tilted by about 1.42% with respect to the horizontal plane, 'above' implies a translation perpendicular to the plane of LEP and therefore not along the vertical direction.

should be minimized. For these reasons SS 3 and SS 5 have been attributed, respectively, to beam cleaning and beam dumping. One of the two remaining straight sections, SS 1 or SS 7, will be occupied in the present scenario by one LHC p–p experiment installed in a 'longitudinal cavern' (parallel to the beam orbit).

The injection of the clockwise and anticlockwise beams from the SPS will take place in SS 1 and SS 8, which are both compatible with an LHC experiment. The radiofrequency accelerating cavities must be placed around both beams, at a position where the two beams are not separated by more than a few millimetres. This situation occurs in experimental straight sections. A convenient place is SS 4, together with the ion experiment where the delicate RF hardware will not be irradiated by the heavy flux of secondaries from high-luminosity collisions. A detailed review of these installations is presented hereafter.

In the following sections arcs and dispersion suppressors are described first, followed by the successive straight section in the clockwise direction.

3 The arcs

The LHC circumference is made of eight arcs separated by insertions. Each arc is made of 24 cells (Figs. 5a and 5b). For reasons of beam optics each octant must be symmetrical with respect to the collision point, and the cells in an arc must be perfectly periodic. The consequence is that the half-cells of the arcs in even sectors (1–2, 3–4, 5–6, 7–8) have the short straight section downstream of the quadrupole, while in the odd sectors (2–3, 4–5, 6–7, 8–1) the short straight section is upstream of the quadrupoles. A short straight section is shown schematically in Fig. 6. In order to let the quadrupole Q10 belong to the insertion on both sides, the first cell of the even sectors and the last cell of the odd sectors do not contain a quadrupole.

In the middle of each arc the cryostat is interrupted and cold–warm transitions are installed together with a vacuum valve at room temperature. This separation decouples the installation and operation of half-octants. The valve, with cold–warm transitions on each side and return loops for both bus bars and cryogenic ducts, is installed in the space usually occupied, in the standard straight section, by the dipole and sextupole correctors.

With the exception mentioned above, all standard cells are made of two identical half-cells (Fig. 7). A half-cell contains three bending magnets and one straight section in which the quadrupole is placed, together with the various correcting elements. These elements are listed in Table 2. All main dipoles and quadrupoles are powered in series. This has the advantage of simplifying the bus bars and of reducing the effect of power supply ripple, but it requires the addition of tuning quadrupoles in the short straight section to allow a proper control of the betatron oscillation frequencies.

The optics functions in the arcs are perfectly periodic over the 24 cells and are represented in Fig. 8 for one half-cell. The exact values are given in the parameter list (see Annex I).

Table 2: Main elements in an arc half-cell

Name	MAD Length[1] (m)	Field[2] (T & m)	Reference name	Half aperture H/V (mm)	Power supply type
BPM-QSA			BPH/V		
Main quad.	3.05	220	MQF/D	21.5	1
Q-tuning	0.72	120	MOQF/D	21.5	2
Octupole	0.72	1.7×10^4	MOQF/D	21.5	3
Sextupole	1.14	1.5×10^3	MSBH/V	21.5	4
COD	1.07	1.5	MSBH/V	21.5	5
Sext. corr.	0.1	2850	MSC	21.5	4
MB	13.145	8.65	MB	21.5	1
Decap. corr.	0.028	1.9×10^6	MDC	21.5	4
Sext. corr.	0.1	2850	MSC	21.5	4
MB	13.145	8.65	MB	21.5	1
Decap. corr.	0.028	1.9×10^6	MDC	21.5	4
Sext. corr.	0.1	2850	MSC	21.5	4
MB	13.145	8.65	MB	21.5	1
Decap. corr.	0.028	1.9×10^6	MDC	21.5	4

[1] Magnetic length.

[2] Field strength B_n ($B_y = B_n x^{n-1}$).

3.1 The bending magnet

The main dipole magnet is of the two-in-one type, in which the two beams circulate in separate vacuum chambers and are subjected to opposite fields (the two beams have the same charge but opposite velocities). The coils are compressed by collars within a common yoke and cryostat operating at 1.9 K. The magnet cross-section is represented in Fig. 9. The magnetic length of the main bending magnet is 13.145 m. The design field is 8.65 T, corresponding to a beam energy of 7 TeV. As explained in Part II, Superconducting Technology, Section 1, the magnet will be designed for a much higher field. For reasons explained in Section 4, the coil inner diameter is 56 mm instead of the 50 mm in the Pink Book. The two beams are separated by 180 mm; each beam is housed in a vacuum tube, the cold bore. This vacuum tube, inner tube of the cryostat, is of 49 mm inner diameter.

- **The beam screen**

  Between the beam and the vacuum chamber a second tube (called the beam screen) is installed to absorb the 1.5 W/m (for the two beams at maximum energy and current) deposited by image currents and synchrotron radiation at a temperature up to 20 K rather than at the 1.9 K of the vacuum chamber. The space available for the beam is 43 mm horizontally and vertically. The beam screen, shown in Fig. 10, is an essential element in the vacuum and cryogenic design of the LHC. It is made of 1 mm thick stainless steel tube, has a quasi-square section and the inner surface is copperplated to reduce the beam coupling impedance. It is perforated over a few per cent of its surface to give access to the cryogenic pumping of the 1.9 K surface of the vacuum chamber. This technique, described in the Pink Book, combines the advantages of the low vapour pressure of the adsorbed gases at 1.9 K and the protection of the low-temperature pumping surface from synchrotron radiation. The holes must be small enough to prevent electromagnetic fields from penetrating the cavity between the screen and the vacuum chamber. The screen must be strong enough to withstand the forces due to the combined effects of eddy currents and magnetic field during a quench of the main dipole magnet.

- **Cold mass**

  The cold mass is the active part of the magnet made of the coils, the collars, the iron yoke, and the shrinking cylinder. The latter, the vacuum chamber, and the ends of the shrinking cylinder delimit the superfluid helium vessel. The magnet coil inner diameter is 56 mm, the shrinking cylinder outer diameter is 580 mm. The magnet cooling is done by means of a corrugated heat-exchanger tube (diameter 50 mm) passing though the magnetic yoke. In this heat-exchanger tube a two-phase (gas and liquid in equilibrium) circulation of helium II acts as a heat sink, cooling the pressurized superfluid helium of the cold mass. A number of superconducting bus bars and cables are installed in four slots placed on the periphery of the magnet yoke. They are listed in Table 4. The shrinking cylinder puts the whole magnetic assembly under compression.

- **Cryostat**

  The cold mass is inserted in a vacuum vessel and supported by thermally insulated feet. These support posts are also connected to two intermediate levels of thermal-insulation envelopes placed around the magnet.

  - A first envelope, the radiation shield, contains the cold mass and a set of four cryogenic ducts:
    - ∗ A 2.2 K liquid helium pipe at 1.3 bar;
    - ∗ A 1.8 K gaseous helium pipe at 16 mbar;
    - ∗ A 4.5 K helium pipe at 2.3 bar;
    - ∗ A 4.5–20 K gaseous helium pipe at 1.3 bar.

    These cryogenic pipes run all along the half-octant and have been placed in the cryostat for convenience. They are only connected to the half-cell cooling system at the level of the cryogenic service module (QSA) described below.
  - A second shield at 70 K combines a heat shield and a set of superinsulation layers. It includes a cooling channel for helium at 70 K .
  - The last envelope, at room temperature, is the vacuum vessel of the cryostat. It has a circular cross-section (diameter 980 mm).

  This cryostat is not specific to the magnets. The same structure is used all along the magnet string (dipole and quadrupole) and over the short straight sections so that the cryostat is continuous over a large part of a half-octant. It contains all the tubes distributing cryogenic fluids to the magnets.

- **Magnet instrumentation**

  The status of each magnet is measured by means of a number of probes, as detailed in Table 3.

  - Temperature probes: the temperature of a number of critical points of the dipole is measured using carbon or platinum resistors in order to monitor the cooling-down or warm-up procedures in each magnet.
  - Voltage taps: are used as quench detectors. They also allow analysis of the quench evolution and location.
  - Protection heaters: are triggered as soon as a quench is detected in order to dissipate the stored energy in the entire coil.
  - Cryo-heaters: allow the control of the warm-up procedure.
  - Beam-loss calorimeters: permanently monitor the circulating beam losses in the magnet. They trigger the beam-dump scheme so that catastrophic losses are prevented. They are also part of the essential beam-loss monitoring of the ring.

  The cables coming from all these probes leave the cryostat via instrumentation feedthroughs placed on each magnet.

- **Correctors**

  The magnet is equipped with two correctors: a decapole at one end and a sextupole at the other. Named Magnet Decapole Corrector (MDC) and Magnet Sextupole Corrector (MSC), these are aimed at correcting systematic imperfections due to persistent currents or to saturation, but are not used for the correction of lattice effects like chromaticity. Each type of corrector magnet is powered in series with one power supply per half-arc. The bus bars enter and exit the cryostat via the cryofeed box of the half-octant placed in the insertion.

- **Intermagnet connections**

  Connections between magnets include:

  - vacuum chamber connections with expansion bellows (the cold mass length of one magnet contracts by about 40 mm during cool down);
  - beam screen connections;
  - electrical connections of superconducting bus bars with their expansion loops;
  - flexible bellows connections of helium ducts;
  - flexible bellows connections of cryogenic shields;
  - the vacuum tanks of cryostats, with bellows for mechanical assembly.

  A model has been developed.

Table 3: Instrumentation in the arc

Instrument type	No. of probes	No. of wires
Bending magnet		
Temperature (resistor)	4	16
Voltage tap	13	13
Protection heaters	8	16
Cryo heaters	1	2
Beam-loss calorimeter	4	16
Total bending magnet		63
Short straight section[1]		
Temperature (resistor)	8	32
Voltage tap	22	22
Protection heaters	8	16
Cryo heaters	1	2
Beam-loss calorimeter	5	20
Beam-position monitor		4 Coax
Dipole correctors (±30 A, 104 V)		4
Total short straight section		96 + 4 Coax
Cryogenic service module (QSA)		
Temperature (resistor)	10	40
Cryo heaters	1	2
Total QSA		42
Total half-cell		327 + 4 Coax
Total half-arc[2]		7848 + 92 Coax

[1] Main quadrupole included.

[2] Q10 Straight section attached to insertion.

3.2 The quadrupole

The two-in-one quadrupole is part of the short straight section which will be installed as a single unit. Both apertures have the same field gradient and therefore, since the two beams circulate in opposite directions, one beam sees a focusing quadrupole in one aperture and the other beam sees a defocusing one of the same strength in the other aperture. Obviously the two beams have the same separation (180 mm) as in the bending magnets. The vacuum chamber and beam screen are also the same. The quadrupole magnetic length is 3.05 m, the maximum gradient 220 T/m.

The cold mass of the quadrupole (Fig. 11) is cooled by the same arrangement as for the dipoles, namely with a heat-exchanger channel passing through the cold mass. It also contains, in appropriate slots, the superconducting bus bars as detailed in Table 4. The instrumentation of the quadrupole is similar to that of the dipole, it is listed in Table 3, together with the straight section instrumentation.

Table 4: Bus bars in the arc cryostat

Name	No. of circuit	Magnet type	Max. current (kA)	Max. voltage (V)
Main bends and quadrupoles	1	MB+MQ	12	88
Protection bus bar	1	MB+MQ	12	88
Tuning quadrupoles	4	MOQ	±1.6	11
Straight section octupoles	4	MOQ	±0.2	12
Straight section sextupoles	4	MSBH(V)	±0.5	12
Bending magnet sextupoles	2	MSC	±0.5	19
Bending magnet decapoles	2	MDC	±0.5	19

3.3 The rest of the short straight section

The straight section of the half-cell (Fig. 6) contains, together with the main quadrupole, the following equipment:

- **Combined tuning quadrupole and octupole corrector**

  These quadrupoles of integrated strength 86 T are powered by four independent circuits, one for each of the focusing and defocusing quadrupoles of each ring. They are strong enough to vary the Q values at top energy within the range:

  $$\Delta Q_{\mathrm{H}} = \pm 2$$
  $$\Delta Q_{\mathrm{V}} = \pm 2\ .$$

  An octupole winding is inserted in the tuning quadrupole coil. Its integrated strength is 1.2×10^4 T·m^{-2} for a current of about 220 A. The bus bars are introduced in the cryostat in the half-octant cryofeed box.

- **Combined dipole and sextupole corrector**

  Two closed-orbit dipole correctors (one for each ring) one vertical, the other horizontal, are installed in the same cryostat. Their integrated strength is 1.5 T·m. They are independently powered and the corresponding feedthroughs are placed in the straight section cryostat. A sextupole is inserted into each of the dipole-corrector yokes for the correction of lattice chromaticities. These sextupoles are grouped in two families per ring, the corresponding cables are introduced into the cryostat at the arc cryofeed box. Their present integrated strength of 1600 T·m^{-1} is sufficient to compensate a chromaticity of 250 units at top energy.

- **Beam-position monitor**

  In the arcs the horizontal position of the beam is measured near a QF and the vertical position near a QD. The beam-position monitor currently being considered is of the directional-coupler type that requires two coaxial cables for a pair of plates. The cryogenic losses along these coaxial cables are under study.

- **Cryogenic service module**

  In the straight section of each half-cell, a technical service module (QSA) controls the cryogenic state of the half-cell cryostat. The QSA is an essential part of the cryogenic system organization. The two-phase saturated helium used in the heat transfer loop is generated there as explained in the cryogenics chapter of the Pink Book. The QSA also contains a number of heaters, and instrumentation to control and monitor the cool-down or warm-up procedures, the state of the insulation vacuum, as well as the beam vacuum. The beam-position monitor is also housed in this technical service module.

- **Quench protection**

  When a quench occurs in one of the magnets of the half-cell, the voltage taps detect the quench with a delay of about 10 ms. The protection heaters are then powered so that after a few tens of ms the whole string of magnets of the half-cell becomes normal-conducting, avoiding the destructive dissipation of the magnet string energy in the small volume of the quench. At this stage it is necessary to short-circuit the half-cell to avoid the dissipation of the whole half-arc stored energy in the quenched region. This is achieved automatically by a set of three diodes in series which, together with a return bus-bar, short-circuit the half-cell. In normal working conditions the diodes block the return current. When the half-cell becomes resistive a voltage of 3–4 V develops across the diodes which become conducting and thus bypass the main current. The de-excitation of the half-arc is triggered at the same time, for a total duration of about 100 s, corresponding to the time constant of the main magnet circuit, damping resistor included.

3.4 Cables

The information from the instrumentation listed above and the power to the closed-orbit dipoles are transported by a number of cables to be installed on the cable trays. A list of these can be found in Table 3.

4 Aperture

Apertures are discussed here and actual design values presented even though they concern equipment which will be described later. Two different types of aperture have to be considered, the mechanical aperture and the dynamic aperture. The LHC mechanical aperture is limited by collimators in order to localize the beam losses in a specially designed section, the beam-cleaning section. The efficiency of beam cleaning is, however, strongly related to the aperture available around the ring. Large-amplitude particles which escape from the cleaning system must circulate without hitting the beam enclosure anywhere in the cold part of the machine, before being captured by the collimators on a later turn.

The dynamic aperture is usually smaller than the mechanical aperture and is the maximum initial amplitude of particles which have to survive for millions of turns.

4.1 The mechanical aperture

Aperture considerations obviously occur when the beam size is limited by an object which protrudes into the ring. At a given place where the free space for the beam is A, the aperture is measured by different quantities.

- The mechanical aperture A is the distance between the vacuum chamber centre line and the innermost obstacle and may be different on the inner or outer side of the ring, or on the upper or lower side.
- The estimated available aperture n is usually expressed in number of r.m.s. beam size, σ. The number n is the result of a calculation using the following formula:

$$A = ((n\,\sigma)^2 + (\delta_p D_x)^2)^{1/2} * k_\beta + CO + \delta_{\mathrm{al}} + \delta_{\mathrm{tol}} + \delta_{\mathrm{sep}}\ ,$$

  where the result of the computation is n, the number of r.m.s. beam size (σ) which will be accepted taking into account the various effects or errors. The value of σ is deduced from the emittance ϵ and the local value of beta ($\sigma = \sqrt{\epsilon\beta}$). δ_p is the relative momentum spread considered (here the half-bucket size), D_x is the local value of the dispersion, k_β is a coefficient measuring the effect of the modulation of the beta function due to gradient errors (k_β=1.1), δ_{sep} is half the beam separation when the two beams are in the same vacuum chamber, CO is the expected local closed orbit amplitude, δ_{al} is the estimated alignment error, and δ_{tol} the mechanical tolerance of the object limiting the aperture.

The following principles have been used in the specification of apertures around the ring. The superconducting elements should all be designed such that at all energies the available aperture is 12 σ or more. Whenever possible the normal-conducting elements should be designed for this same available aperture of 12 σ. In specific cases like the extraction kickers where feasibility considerations impose a reduced aperture, one must ensure that particle losses in these specific points will not induce quenches in the neighbouring superconducting equipment. In all cases the primary collimator of the cleaning insertion must be the innermost limiting aperture.

Table 5: Superconducting elements aperture around the ring

Element	H/V	A (mm)	Energy	β (m)	δ_p (10^{-3})	D_x (m)	CO (mm)	$\Sigma\delta$[1] (mm)		Value of σ(mm)	Number of σ's
Arc											
QF	H	21.5	Inj.	172	1.3	2.0	4.0	0.7		1.16	13.0
MB (QF side)	H	21.5	Inj.	150	1.3	1.9	3.7	2.0		1.08	13.1
QD	V	21.5	Inj.	172	1.3	0.6	4.0	0.7		1.16	13.2
MB (QD side)	V	21.5	Inj.	151	1.3	0.6	3.7	2.0		1.08	13.7
Dispersion suppressor											
Q10	H	24.5	Inj.	179	1.3	2.1	4.0	0.7		1.18	15.1
MB (Q10 side)	H	21.5	Inj.	154	1.3	1.7	4.0	2.0		1.10	12.8
Q9	V	24.5	Inj.	173	1.3	0.6	4.0	0.7		1.16	15.5
Q8	H	24.5	Inj.	173	1.3	1.2	4.0	0.7		1.16	15.4
Q7	V	24.5	Inj.	175	1.3	0.6	4.0	0.7		1.17	15.4
MB (Q6 side)	H	24.5	Inj.	215	1.3	0.6	3.5	2.0		1.30	13.3
Q6	H	24.5	Inj.	274	1.3	0.6	4.0	0.7		1.46	12.3
Low-β and simple insertions											
Q5	V	24.5	Inj.	317	1.3	0.6	3.0	0.7		1.57	12.0
Q4	H	24.5	Inj.	316	1.3	0.6	3.0	0.7		1.57	12.0
Q3	V	31.5	Inj.	261	1.3	0.6	4.0	5.2		1.43	14.2
Q2	H	31.5	Inj.	249	1.3	0.6	4.0	3.7		1.40	15.5
Q1	H	31.5	Inj.	138	1.3	0.6	4.0	3.7		1.04	20.8
Beam cleaning insertion											
Q5	V	31.5	Inj.	436	1.3	0.6	4.0	0.7		1.85	13.2
Q4	H	31.5	Inj.	498	1.3	0.6	4.0	0.7		1.97	12.3
Q3	V	31.5	Inj.	629	1.3	0.6	1.5	0.7		2.22	12.0
Q2	H	31.5	Inj.	643	1.3	0.6	1.5	0.7		2.24	11.9
Q1a	H	31.5	Inj.	353	1.3	0.6	4.0	0.7		1.66	14.7
Beam dump insertion											
Q6	H	31.5	Inj.	368	1.3	0.6	4.0	0.7		1.70	14.4
Q4	H	31.5	Inj.	643	1.3	0.6	1.5	0.7		2.24	11.9
Q3	V	31.5	Inj.	569	1.3	0.6	1.5	0.7		2.11	12.4

[1] Addition of tolerances as defined in the text, very approximate at this stage.

The most restrictive apertures for superconducting equipment have been analysed for each section of the ring. The results are presented for the injection energy in Table 5 where the notation of the above formula has been used. The aperture in the arcs is everywhere larger than 13 σ. In the dispersion suppressor, the first quadrupole of the straight section, Q6 limits the aperture at 12 σ. The next aperture restriction is the nearby magnet. Two possibilities to enlarge the available aperture can be considered: suppression of the beam screen in that part of the magnet close to the quadrupole, which gives a mechanical aperture A of 24.5 mm and an available aperture of 13 σ, or keeping a standard magnet assembly but improving the alignment at the end of the magnet close to the quadrupole to obtain an available aperture larger than 12 σ. In the outer triplet, the two quadrupoles Q4 and Q5 also limit the aperture to 12 σ. The inner triplet quadrupoles, which are enlarged to cope with the requirements of collision optics, are far from the aperture limit.

In the beam-cleaning insertion SS 3 the situation is more difficult. The whole string of quadrupoles from Q5 to Q1 (six quadrupoles in total) must be enlarged to the same aperture as the low-beta quadrupoles. The difficulty is due to the fact that these are two-in-one quadrupoles, hence limited in lateral space. Preliminary studies indicate that such quadrupoles are feasible. In the case of the set of three quadrupoles (Q2a, Q2b, Q3) this is not sufficient, however, and must be complemented by a special local closed-orbit correction. This special attention to the closed-orbit correction will in any case be required for efficient operation of the beam-cleaning system.

The same problem is found in the dump straight section SS 5 where, because of the required very large beta functions, the two quadrupoles Q4 and Q3 must be enlarged and a special closed-orbit correction scheme applied.

With these precautions, all superconducting equipment apertures are large enough to leave an available aperture of 12 σ or more around the entire circumference.

At flat top energy, in collision, the vacuum chamber of the inner triplet quadrupoles is the mechanical aperture limitation in the absence of collimators, corresponding to about 15 σ of available aperture.

4.2 The dynamic aperture

In superconducting colliders the stable area in phase space is limited by the non-linear fields introduced by magnet imperfections or by the beam–beam effect. Above a certain amplitude of oscillation the particle motion becomes unstable. The dynamic aperture which is also measured in units of the r.m.s. beam size is only a limitation at injection where the non-linearities are large due to persistent currents and where the beam has a large emittance.

The non-linearities are measured in terms of the high-order coefficients a_n and b_n of the complex field expansion

$$B_y + iB_x = B_1 \sum_n (b_n + ia_n)\,(Z/R_r)^{n-1}$$

where B_1 is the nominal vertical magnetic field[3], B_y and B_x are the actual components of the field in the vertical and horizontal planes, $R_r = 1$ cm is the reference radius, and $Z = x + iy$. The values of the coefficients depend on the design and the size of the magnet coils, those considered for the evaluation of the LHC dynamic aperture are given in Table 6. With the same coil design it is possible to reduce the high-order coefficients by increasing the coil diameter. By doing so while keeping the value of the field on the inner coil surface constant, one reduces the coefficients a_n and b_n by the enlargement factor to the power $n-1$. This

---

[3] In the case of the quadrupole, the field B_1 is the value of the field at 1 cm from the axis.

holds for bending magnets, but can also be applied to quadrupoles provided their length is increased to keep the same integrated gradient.

Table 6: Field perturbations in the LHC magnet (at injection)

Perturbation type	Straight		Skew		Straight		Skew	
	Term	Strength[1]	Term	Strength	Term	Strength[1]	Term	Strength
Field errors in dipole magnets								
	Systematic field errors				**Random field errors**			
Dipole	b_1	0.0	a_1	0.0	b_1	0.0	a_1	0.0
Quadrupole	b_2	1.15	a_2	0.770	b_2	0.37	a_2	1.227
Sextupole	b_3	−2.19	a_3	0.086	b_3	0.882	a_3	0.186
Octupole	b_4	−0.11	a_4	0.023	b_4	0.055	a_4	0.186
Decapole	b_5	0.34	a_5	0.020	b_5	0.083	a_5	0.041
Dodecapole	b_6	−0.002	a_6	0.0	b_6	0.022	a_6	0.014
	b_7	0.035	a_7	0.00	b_7	0.012	a_7	0.011
	b_8	0.002	a_8	0.0	b_8	0.005	a_8	0.005
	b_9	0.007	a_9	0.0	b_9	0.003	a_9	0.004
	b_{10}	0.00	a_{10}	0.0	b_{10}	0.002	a_{10}	0.002
	b_{11}	0.004	a_{11}	0.0	b_{11}	0.001	a_{11}	0.001
Field errors in quadrupole magnets								
	Systematic field errors				**Random field errors**			
Quadrupole	b_2	0.0	a_2	0.0	b_2	0.0	a_2	0.0
Sextupole	b_3	0.02	a_3	0.280	b_3	0.454	a_3	0.478
Octupole	b_4	0.190	a_4	0.01	b_4	0.133	a_4	0.188
Decapole	b_5	0.05	a_5	0.01	b_5	0.065	a_5	0.093
Dodecapole	b_6	−0.60	a_6	0.0	b_6	0.053	a_6	0.069
	b_7	0.0	a_7	0.0	b_7	0.012	a_7	0.013
	b_8	0.0	a_8	0.0	b_8	0.006	a_8	0.007
	b_9	0.0	a_9	0.0	b_9	0.007	a_9	0.004
	b_{10}	0.02	a_{10}	0.0	b_{10}	0.005	a_{10}	0.003
	b_{11}	0.0	a_{11}	0.0	b_{11}	0.002	a_{11}	0.002

[1] In units of 10^{-4} $\Delta B/B_1$ at 1 cm, where B_1 is the dipole field for dipoles, and the field at 1 cm from axis for quadrupoles.

At the design stage the value of the dynamic aperture is evaluated by computer simulation. Errors from different sources are introduced in a tracking program in which particles launched with different initial amplitude and phase are followed over a large number of turns. Usually about 10^4 turns are sufficient to detect whether the particle motion is regular or chaotic. Chaotic particles will eventually be lost on the wall, but this may take a long time for weakly chaotic particles close to the dynamic-aperture limit. For some selected sets of parameters the tracking is pursued up to 10^5 or 10^6 turns, which is the maximum possible in practice with currently available computers. From this one obtains 'survival plots' showing the variation of the survival time as a function of the initial amplitude of the particles in the chaotic region. These plots can be extrapolated to evaluate the maximum amplitude of particles which are likely to survive for 10^7 or 10^8 turns. In the majority of cases this amplitude is only slightly above the chaotic boundary, which can therefore be taken as a safe value for the long-term dynamic aperture.

At the time of publication of the Pink Book an extensive campaign of computer tracking was in progress to evaluate the LHC long-term dynamic aperture at injection energy. This work was based on error coefficients assumed for the 50 mm inner coil diameter magnets then under design. It showed that when all known imperfections including residual closed-orbit deviations and coupling were taken into account, the available dynamic aperture was only 5.5 σ of the nominal injected beam. This was judged uncomfortably small for reliable operation of the machine. Since a computer model can never incorporate all possible imperfections of a real collider, some safety margin has to be provided. In line with the recommendation of the international LHC review committee of May 1991, a second simulation campaign was launched, this time with reduced errors corresponding to a magnet with a larger, 56 mm diameter coil of improved design. In these conditions the dynamic aperture increased to 6.5 σ, which is adequate. Detailed analysis of geometric aperture showed that a similar increase from 50 to 56 mm of the inner coil diameter was also required to assure a good collimation efficiency. Consequently, this new magnet design has been adopted for the LHC.

5 Dispersion suppressors

Between the arc and the straight section a length of 174 m of tunnel with a larger radius of curvature (4.7 km) than the normal arc is devoted to dispersion suppressors. The aim in the LHC as in LEP is to enter the straight section with a zero dispersion[4] as required by the collision optics. This is achieved within four non-standard half-cells. The schematic layout is given in Fig. 12 and the main items are listed in Table 7 in clockwise order from the crossing point to the arc.

The corresponding optics functions are plotted in Figs. 15 and 16 of Section 6 for the case of Interaction Region 1 (IR1), the minor differences (Table 8) between the dispersion suppressors in other insertions are the result of adaptations to the local matching conditions.

The aperture of the first bending magnet of the dispersion suppressor must be enlarged because the beta function at that point reaches a larger value than in the regular cell of the arc. The extra few mm required are provided by eliminating the synchrotron radiation screen. As a consequence the heat load increases in the channel exposed to synchrotron radiation from upstream magnets. The cryogenic system has been designed to accept this extra load. The danger of a quench associated with this irradiation is negligible because all the photons will be absorbed in the vacuum chamber.

In order to match the curvature of the tunnel in this region it is necessary to introduce a special magnet (MBS) which has the same cross-section as the main magnet, but a reduced length of 8.793 m (Table 7). It therefore requires no specific development work and can be manufactured using most of the main-magnet tooling.

---

[4] In the case of the LHC, the small dispersive effect of the two magnets D1 and D2 which separate/combine the beams in the straight section has to be taken into account.

Table 7: Main elements in a dispersion suppressor

MAD			Reference name	Half-aperture (mm)	Power supply type
Name	Length (m)	Field[1] (T & m)			
MB[2]	13.145	8.65	MB	24.5	1
MB	13.145	8.65	MB	21.5	1
BPM/QSA			BPC	24.5	
Q7	8.0	211	MQTC[3]	24.5	6
COR	0.65	3.85	MBVA	24.5	5
MB	13.145	8.65	MB	21.5	1
MB	13.145	8.65	MB	21.5	1
BPM/QSA			BPC	24.5	
Q8	4.6	220	MQTB		6
COR	0.65	3.85	MBHA	24.5	5
MB	13.145	8.65	MB	21.5	1
MB	13.145	8.65	MB	21.5	1
MBS	8.793	8.65	MBS	21.5	1
QS	0.72	120.0	MQS	24.5	2
QS	0.72	120.0	MQS	24.5	2
COR	0.65	3.85	MBVA	24.5	5
Q9	3.7	220	MQTA	24.5	6
BPM/QSA			BPC	24.5	
MB	13.145	8.65	MB	21.5	1
MB	13.145	8.65	MB	21.5	1
QS	0.72	120.0	MQS	24.5	2
QS	0.72	120.0	MQS	24.5	2
COR	0.65	3.85	MBHA	24.5	5
Q10	3.7	195.0	MQTA	24.5	6
BPM/QSA			BPC	24.5	

[1] Field or gradient.

[2] All bendings are equipped with sextupole and decapole correctors.

[3] Except in SS3 where Q_7 is a MQTA.

The beam observation and magnetic correctors are listed in Table 7. They are similar to those used in the arcs. Strong skew quadrupoles are required upstream of both Q9 and Q10. Together with another pair of skew quadrupoles in the straight section they form a set of four skew-quadrupole families used to compensate both the systematic and random skew quadrupolar errors of the LHC magnet (term a_2 in Table 6). The skew quadrupoles attached to Q9 and Q10 consist of two units powered in series for reasons of standardization.

A cryogenic technical service module (QSA) has been attached to each quadrupole of the pseudocell with the same function as in the regular arc cells.

The dispersion suppressor and straight section magnets are, as in the arc, equipped with a number of instrumental probes detailed in Table 3. The resulting number of wires are given in Table 9.

Table 8: Equipment in dispersion suppressors

Equipment name	Number per dispersion suppressor				Total ring
	Low-beta	Cleaning	Dump	Simple	
MB	8	8	8	8	128
MBS	1	1	1	1	16
BPC	8	8	8	8	128
QSA	4	4	4	4	64
MBVA	4	4	4	4	64
MBHA	4	4	4	4	64
MQTA	2	3	2	2	34
MQTB	1	1	1	1	16
MQTC	1	0	1	1	14

Table 9: Instrumentation in the dispersion suppressor

Equipment type	Quantity	No. of wires
Bending magnet	9	567
Quadrupoles	4	368
BPC	8	32 coax
QSA	4	168
Total dispersion suppressor		1103 + 32 Coax

6 SS 1: beam I injection and proton–proton collisions

The complete lattice is formed by a succession of modules. The straight sections, even though they are not all the same, are made by adapting basic modules to particular requirements. In the following, the modules are detailed one after the other going around the machine from straight section 1.

SS 1 combines an experiment with the injection of protons in the clockwise direction. The injection has to be made upstream of the experiment in order to avoid interference between the transfer tunnel and the experimental hall.

The experiment requires a low-beta section already described in some detail in the Pink Book [1]. The two beams cross at the collision point at a small angle of 200 μrad in order to limit the effect of parasitic collisions.

A basic layout using two triplets has been selected (instead of two doublets as in LEP) in order to obtain a low and equal value of beta ($\beta * = 0.5$ m) in both the horizontal and the vertical plane and to leave space for injection. This layout is schematically represented in Fig. 13 for the upstream part of the insertion and in Fig. 14 for the downstream part[5]. Starting from the interaction point one finds successively:

- A free space of 16 m for the experimental detector;
- The first triplet (the inner triplet) which adjusts the waist of the beta function at the interaction point. This triplet is protected from the collision radiation by a collimator;
- The pair of separation magnets which direct the two beams in separate channels;
- A long drift space of about 100 m where most of the injection equipment can be installed;
- The second triplet (the outer triplet) which provides the matching to the dispersion suppressor section.

In spite of its simplicity, this layout allows the 'detuning' of the low beta required at injection in order to reduce both the chromatic effects and the sensitivity of the lattice to magnetic or alignment errors. The optics functions for the 'tuned' and the 'detuned' low-beta are given in Figs. 15 and 16.

The two-in-one quadrupoles have gradients of equal amplitude and sign in both apertures. Therefore one beam sees a horizontally focusing quadrupole while the other, which goes in the opposite direction, sees a horizontally defocusing quadrupole. Two-in-one quadrupoles horizontally focusing for beam I are named QF. Combined with the requirement of equal horizontal and vertical betas at the interaction point this constraint imposes an optically antisymmetric lattice as can be seen on the various plots of the optics functions.

6.1 The inner triplet

At design luminosity (10^{34} cm^{-2} s^{-1}) the collision between the two beams will produce 8×10^8 events per second (60 mb inelastic and 20 mb diffractive cross-section). This corresponds to a stream of secondaries carrying a total power of 785 W to each side of the interaction

---

[5] A complete set of more detailed schematic drawings covering all insertions is available [3].

region. The flux of secondaries is strongly peaked forward, and the corresponding energy deposit will be distributed between the downstream equipment and the tunnel wall. A collimator is required in order to protect the superconducting quadrupoles which form the inner triplet. This collimator, made of copper and tungsten, will be 2 m long, with an inner aperture of 30 mm. Monte Carlo computations [4] show that approximately 140 W, which would otherwise be absorbed in the cold mass of the quadrupoles, will be dissipated in the collimator. On each side a total power of more than 640 W escapes through the aperture of the collimator.

Behind the collimator a space of about two metres will be used to house a number of components:

- A vacuum valve to separate the detector vacuum from the ring, together with a pumping station for the room-temperature section;
- The cold-to-warm transition between the room-temperature vacuum chamber of the detector and the 1.9 K quadrupole vacuum chamber;
- A beam-position monitor, working on both beams for both horizontal and vertical detection;
- A service module for the cryogenics of the inner triplet.

As indicated in Table 10, and on the schematic drawing of Figs. 13 and 14, the 30 m long inner triplet is made of four superconducting quadrupoles: Q1, Q2a, Q2b and Q3. Q2 has been divided into two units for reasons of standardization of the quadrupoles used in the straight sections.

Only a small part of the 640 W of the secondary particles which propagate through the inner aperture of the collimator will directly hit the quadrupoles of the inner triplet which have a much larger aperture (70 mm inside-coil diameter). Moreover, no beam screen will be installed inside these quadrupoles where the power deposition by synchrotron radiation is negligible. The power expected to be deposited by secondary particles in each of these quadrupoles is detailed in Fig. 17. The inner triplet quadrupoles are installed in the same cryostat as the first separation dipole D1. The specifications of the cryogenic system take into account the important additional heat load due to the secondary particles.

Table 10: Main machine elements in SS 1 (clockwise beam only)

Between the two D1 magnets the elements are common to both beams.

MAD			Reference	Aperture	Power supply
Name	Length (m)	Field (T & m)	name	(mm)	type
Q6	8.0	199	MQTC	24.5	6
Q5	8.0	196	MQTC	24.5	6
			Injection line dipole corrector		
			Injection line quadrupole		
			Injection line dipole		
			Injection line quadrupole		
Q4	3.7	194	MQTA	24.5	6
			Injection line quadrupole		
			Injection line dipole corrector		
			Injection bumper 1		
			Injection bumper 2		
			Injection line collimator		
			Injection septum		
			Injection beam stopper		
			Injection bumper 3		
			Injection kicker		
D2	27.0	1.8	MBSW		7
			Injection beam stopper		
BSN*	3.0		TDN		
D1	9.0	5.2	MBSH		6
Q3	6.9	236	MQIB	31.5	6
Q2b	6.1	220	MQIA	31.5	6
Q2a	6.1	220	MQIA	31.5	6
Q1	6.9	215	MQIB	31.5	6
C1	2.0		TDS		
IP	******	******	******	****	******
C2	2.0		TDS		
Q1	6.9	215	MQIB	31.5	6
Q2a	6.1	220	MQIA	31.5	6
Q2b	6.1	220	MQIA	31.5	6
Q3	6.9	226	MQIB	31.5	6
D1	9.0	5.2	MBSH		6
BSN*	3.0		TDN		
D2	27.0	1.7	MBSW		7
			Injection beam absorber		
			Injection beam absorber		
Q4	3.7	194	MQTA	24.5	6
Q5	8.0	196	MQTC	24.5	6
Q6	8.0	199	MQTC	24.5	6

* BSN: Neutral particle absorber (to stop neutral secondaries from collisions).

The danger of quenching of these quadrupoles under the heating effect of the power deposited by the secondary particles is linked more to the local energy deposition than to the overall power. A detailed analysis of the loss distribution in each quadrupole has been made and studies will continue. First results [5] suggest that the local power deposition is of the order of a few milliwatt per cubic centimetre. These extreme values will only be reached with the nominal luminosity (10^{34} cm^{-2} s^{-1}) which, as explained in Section 14, is not expected during the initial period of operation, so there will be ample time to adjust the protection before the risk of quenching due to secondaries becomes serious. This effect could however limit the luminosity before the beam–beam limit is reached. These quadrupoles are individually protected in case of quench by room-temperature circuits placed outside the cryostat.

The aperture of these quadrupoles must be large enough to cope with the requirements of:

- collision optics;
- injection trajectories and optics;
- power deposition from secondaries;
- field linearity.

The resulting apertures are shown in Table 10.

Special measures must be taken to protect the machine from the danger of spurious firing (or mistiming) of the injection kicker. When this happens the 450 GeV injected beam is swept across the horizontal aperture during the rise and fall time of the kicker. The fraction of beam which is swept has an energy of 3 MJ, sufficient to severely damage the machine and the detector. A first beam stopper TDI is installed to protect the inner triplet and the detector in case of kicker misfiring, while two other beam stoppers, placed 270° and 315° of betatron phase downstream of the kicker protect the rest of the machine.

A number of correctors and beam observation monitors are installed in between the inner triplet quadrupoles, all operate at cryogenic temperatures. They are listed in Table 11. The beam-position monitors will use directional couplers with two coaxial outputs per coupler in order to differentiate between the two beams. The correctors of integrated strength 1.75 T·m are only used to correct the local positioning errors of quadrupoles. Experience with LEP indicates that such correctors can be essential in the delicate tuning of the collision optics. The fitting of these correctors and beam monitors inside the very compact inner triplet will only be finalized after detailed design studies.

Table 11: Miscellaneous equipment in SS 1

Name	Reference name	Comments	
IP			WARM
Collimator	TDS	Protection from secondaries	
Vacuum valve	VVPE	Vacuum valve enlarged + pump	
CWT	QWTE	Cold–warm transition enlarged	COLD
BPM-QSA	BPCD	H & V beam pos. monitor, bidirectional	
Q1	MQIB		
COR	MBVI	Orbit corrector, vertical	
Q2a	MQIA		
BPM+QSA	BPCD	H & V beam pos. monitor, bidirectional	
Q2b	MQIA		
COR	MBHI	Orbit corrector, horizontal	
Q3	MQIB		
BPM-QSA	BPCD	H & V beam pos. monitor, bidirectional	
COR	MBVI	Orbit corrector, vertical	
D1	MBSH		
QFB-QSA	QFI	Cryofeed box	
CWT	QWTE	Cold–warm transition enlarged	
Vacuum valve	VVPE		WARM
Beam separation			
BSN	TDN	Beam stopper for neutral secondaries	
Vacuum valve	VVP		
D2	MBSW	Five magnet units	
COR	MBVW	Closed-orbit dipole, horizontal	
COR	MBHW	Closed-orbit dipole, vertical	
BPM	BPC	H & V beam pos. monitor	
Vacuum valve	VVP		
Vacuum valve	VVP		
CWT	QWT		COLD
QS	MQS	Skew quad.	
COR	MBHA	Closed-orbit dipole, horizontal	
COR	MBVA	Closed-orbit dipole, vertical	
Q4	MQTA		
BPM	BPC	H & V beam pos. monitor	
Q5	MQTC		
COR	MBHA	Closed-orbit dipole, horizontal	
BPM	BPC	H & V beam pos. monitor	
QFB-QSA	QFA	Cryofeed box, non-standard position[1]	
QS	MQS	Skew quad.	
COR	MBVA	Closed-orbit dipole, vertical	
Q6	MQTC		
BPM+QSA	BPC	H & V beam pos. monitor	

[1] To avoid interference with injection equipment.

6.2 The separation magnets

The two beams have to be separately guided in their respective vacuum chambers. This separation must be made as close as possible to the interaction point in order to avoid the parasitic tune shift and non-linearities induced by beam–beam effects in the so-called distant (or parasitic) crossings. In the part of the straight section where the two beams travel in the same vacuum chamber there is one such crossing per 3.75 m (for a bunch separation of 25 ns).

The separation is made using a pair of magnets named D1 and D2 in Table 10. In straight section 1, these magnets should be as close as possible in order to leave space for the injection equipment. The first magnet D1 is also submitted to an intense irradiation by secondaries from the collisions. Its own magnetic field deviates the charged secondaries onto its own coils, so that its aperture has to be enlarged to 75 mm in order to avoid excessive energy deposit. In the present version, this magnet is superconducting in order to limit its size and power consumption.

The D1 cryostat is the continuation of the triplet cryostat. The heavy heat load along the inner triplet and D1 magnet imposes a cryogenic service module (QSA) for each magnet. These magnets are fed by a feedbox placed downstream of D1.

The neutral secondaries are not deviated by D1 and will be stopped in a dedicated absorber (TDN) placed a few metres downstream of the Y-shaped junction of the two rings.

A detailed injection procedure will have to be prepared in order to avoid the catastrophic scenario where a full-intensity 450 GeV beam is injected with a very large oscillation amplitude and interacts in several places around the ring. From past experience it is known that such procedures can be installed and operate with a high degree of reliability. A set of three absorber blocks has been installed in the straight section to protect the machine against such injection trajectory errors. The first one will be used as a beam stopper in case of failure of the injection kicker or when the injection kicker is not energized.

The second magnet D2 is, in the present version, a normal-conducting magnet. This has the advantage of avoiding the installation of a new cryogenic system in the middle of the warm section between the inner and outer triplet cryostats. The D1, D2 pair of magnets has not been studied in great detail, other versions are possible which will be analysed in due course.

6.3 The outer triplet

The role of the outer triplet is to match the optical functions between the inner triplet and the dispersion suppressor. The quadrupoles are similar in cross-section to normal cell quadrupoles, but will not be equipped with synchrotron radiation screens.

Cables for feeding the dipoles, quadrupoles and a number of correctors are introduced via a cryofeed box (the main cryofeed box QFA) into the continuous cryostat which extends between Q4 and the middle of the adjacent arc. The same box also contains the feedthroughs for the cryogenic ducts. This cryofeed box is installed in the space between Q5 and Q6 in the upstream part of SS 1, in order to be out of the way of injection line equipment. In its standard position it is installed close to Q4. The list of bus bars entering this box is given in Annex II. All these bus bars are inserted in the Q4 quadrupole slots. The number of bus bars inserted in the magnet slots diminishes as one progresses along the half-octant, until one reaches the arc where the list of bus bars in the slots is as given in Table 4. A number of items are installed between the quadrupoles of the outer triplet, they are listed in Table 11.

6.4 Injection elements

The main injection elements are listed in Table 10 and shown in Figs. 13 and 14. Their characteristics are listed below:

- A horizontally deflecting kicker magnet
  - bending strength: 1.1 T·m
  - risetime: 0.94 μs
  - flat top length: 6.5 or 20 μs
  - overall length (in several modules): 10 m;
- A vertically deflecting iron septum magnet
  - bending strength, 18 T·m
  - overall length (in several modules): 20 m;
- Three horizontally deflecting 'bump magnets' with a bending strength of 1 to 2 T·m;
- A set of injection beam stoppers, used during adjustment of the injection trajectory, must be able to absorb a full SPS batch.

The beam coming from the SPS approaches the LHC from above. The transfer quadrupoles, dipole correctors, and vertically deflecting dipoles are interleaved with the superconducting main-ring quadrupoles of the outer triplet.

6.5 Auxiliary equipment

Each half-octant is fed by two cryofeed boxes (detailed in Annex II) where the cryogenic ducts and superconducting cables enter the ring cryostat. A number of other cables pass via cable trays to feed the equipment that requires individual power supplies, or to collect information from instrumentation. The cables coming from the half-octant are listed in Table 12. The first cryofeed box feeds only the inner triplet and the D1 magnet; the second feeds the outer triplet, the dispersion suppressor and the 12 arc cells of the half-octant.

In front of each cryofeed box a cavern is needed to play the role of an auxiliary building. The corresponding civil engineering works are schematically pictured in Annex III, where the caverns and liaison gallery dimensions are indicated. These caverns house the power supplies listed in Annex II and local controls, they will not be accessible during normal operation. Each cavern contains its own electrical and ventilation services. Local computer facilities are installed there together with a number of racks for the ring instrumentation, complementing the alcoves installed in the arcs.

Table 12: Instrumentation and cables in insertion 1

Equipment type	Quantity	No. of wires
Half-arc		
Bending magnet	72	4536
Quadrupoles	23	2208 + 92 Coax
QSA	23	966
Total half-arc		7710 + 92 Coax
Dispersion suppressor		
Bending magnet	9	567
Quadrupoles	4	384 + 32 Coax
QSA	4	168
Total dispersion suppressor		1119 + 32 Coax
Outer triplet		
Quadrupoles	3	288 + 24 Coax
QSA	1	42
Total outer triplet		330 + 12 Coax
Inner triplet		
Bending magnet	1	63
Quadrupoles	4	380 + 24 Coax
QSA	3	126
Total inner triplet		569 + 24 Coax

The following sets of service equipment are installed:

- *Cryogenics*

  Cryogenics in SS 1 is typical of the one installed in all the odd straight sections where no equipment from LEP 200 is available. This installation is separated into two levels:

  1. At ground level, compressors, upper cold box UCB (room temperature to 20 K) and utilities are installed in auxiliary buildings. Storage for gaseous helium is also provided.
  2. At tunnel level one finds the lower cold box LCB (20 K to 4.5 K) and the cold compressor box CCB (4.5 K to 1.8 K). These cold boxes are installed in a cavern excavated at the bottom of the existing shaft PX15.

  A total equivalent cooling power of about 18 kW at 4.5 K is required per octant.

- *Electrical installation*

  Electrical power at 18 kV is distributed to underground caverns and transformed there to user voltage level.

- *Cooling and ventilation*

  Each cavern is equipped with the required cooling and ventilation systems. The main tunnel ventilation is the existing one of the LEP machine.

7 SS 2: proton–proton collisions

Contrary to insertion 1 where LEP installations are very limited, the second insertion of the LHC is installed in a place where a number of underground works made for LEP are available:

- *The experimental cavern*
  This cavern is the only one of LEP with the main axis along the beam orbit and therefore suitable for an LHC experiment;

- *Service caverns*
  Also usable for the LHC.

7.1 Tunnel equipment

As indicated in Table 1, insertion 2 of the LHC will contain an LHC experimental straight section for proton–proton collisions, made of an inner triplet, a pair of separation magnets and an outer triplet, as described in Section 6. Contrary to SS 1, insertion 2 does not have to include injection equipment. For convenience, all items of the straight section are listed in Table 13. The equipment list is the same as for SS 1, with two exceptions; the vertical and horizontal correctors are interchanged since the defocusing and focusing quadrupoles are interchanged and the cryofeed box for feeding the arc is in its standard position.

Table 13: Miscellaneous equipment in SS 2

Name	Reference name	Comments	
IP			WARM
Collimator	TDS	Protection from secondaries	
Vacuum valve	VVPE	Vacuum valve enlarged + pump	
CWT	QWTE	Cold–warm transition enlarged	COLD
BPM-QSM	BPCD	H & V beam pos. monitor, bidirectional	
COR	MBVI	Orbit corrector, horizontal	
Q1	MQIB		
COR	MBHI	Orbit corrector, vertical	
Q2	MQIA		
BPM	BPCD	H & V beam pos. monitor, bidirectional	
Q2	MQIA		
COR	MBVI	Orbit corrector, horizontal	
Q3	MQIB		
BPM-QSM	BPCD	H & V beam pos. monitor, bidirectional	
COR	MBHI	Orbit corrector, horizontal	
COR	MBVI	Orbit corrector, vertical	
D1	MBSH		
QFB-QSM	QFI	Cryofeed box	
CWT	QWTE	Cold–warm transition enlarged	
Vacuum valve	VVPE		WARM
Beam separation			
BSN	TDN	Beam stopper for neutral secondaries	
Vacuum valve	VVP		
D2	MBSW	Five magnet units	
COR	MBHW	Closed-orbit dipole, horizontal	
COR	MBVW	Closed-orbit dipole, vertical	
BPM	BPC	H & V beam pos. monitor	
Vacuum valve	VVP		
Vacuum valve	VVP		
CWT	QWT		COLD
QFB-QSM	QFA	Cryofeed box, standard position	
QS	MQS	Skew quad.	
COR	MBVA	Closed-orbit dipole, horizontal	
COR	MBHA	Closed-orbit dipole, vertical	
Q4	MQTA		
BPM	BPC	H & V beam pos. monitor	
COR	MBVA	Closed-orbit dipole, horizontal	
Q5	MQTC		
BPM	BPC	H & V beam pos. monitor	
QS	MQS	Skew quad.	
COR	MBHA	Closed-orbit dipole, vertical	
Q6	MQTC		
BPM	BPC	H & V beam pos. monitor	

7.2 Auxiliary equipment

The general description of auxiliary equipment installed in straight sections has been given for SS 1 in Section 6.

The straight section 2 installation is typical of even insertions where LEP klystron galleries have been excavated; in SS 2 and SS 6 for LEP 100 and in SS 4 and SS 8 for the LEP 200 project. These galleries will be cleared of unused hardware and house power supplies, local control, and electrical and ventilation services for the LHC. Shaft PGC2, excavated during LEP civil engineering construction, will be used as the vertical link between surface facilities and underground enclosures for electricity and cryogenic lines and for the installation of underground cold boxes.

Cryogenics installed for LEP 200 and consisting of compressors and utilities for an equivalent cooling power of 12 kW at 4.5 K, helium storage, upper cold box UCB (room temperature to 20 K) and lower cold box LCB (20 K to 4.5 K) are available and will be reused for the LHC:

- *Cryogenics*

  The cryogenics installation is on two levels:

  1. At ground level, the complement of compressors to increase the cooling power from 12 kW to 18 kW equivalent in existing auxiliary buildings;
  2. At tunnel level the cold compressor box CCB (4.5 K to 1.8 K). This cold box will be installed in a cavern excavated at the bottom of the existing shaft PGC2.

  A total equivalent cooling power of about 18 kW at 4.5 K, as in SS 1, is required;

- *Electrical installation*

  Electrical power at 18 kV is distributed underground and transformed to user voltage level;

- *Cooling and ventilation*

  Some modifications are required to the existing cooling and ventilation systems, but the main tunnel ventilation is the existing one of the LEP machine.

8 SS 3: cleaning

During LEP construction the excavation of the straight section in the area around crossing point 3 required special precautions because of the presence of porous rock and water at high pressure. In this section, it is essential to limit the civil engineering work for the LHC to the minimum. For this reason it has been decided to install in this straight section the cleaning insertion which requires no additional excavation. The cleaning insertion is defined as the part of the ring where particle losses are concentrated in order to avoid beam losses in superconducting magnets and the resulting quenches. It is the place where the beam is 'cleaned' in the sense that the beam halo is suppressed by means of collimators.

The cleaning requirements can only be fulfilled by a dedicated insertion. The final optimization of the insertion and of the equipment to be installed will require several years of careful work. The studies presented here concentrate on feasibility and provide the basis for the cost estimate. Current analysis confirms that a satisfactory beam-cleaning system is feasible and that together with proper operational procedures it will ensure safe operation of the LHC.

8.1 Scenarios for beam losses

The cleaning specification results from the sensitivity of superconducting magnets to particle losses. The sensitivity is different if the losses take place at high or low energy, if they are instantaneous or continuous, so that all possible scenarios for beam losses have been reviewed [6] and [7].

All numbers quoted in this section correspond to the worst possible case where the machine works at the beam–beam limit luminosity.

A number of possible loss sources have been identified and described in the Pink Book; the latest study [8] provides the following list.

Systematic losses

Table 14 gives the estimated number of systematic particle losses in the extreme case of two high-luminosity insertions working at the beam–beam limit luminosity of 2.5×10^{34} cm^{-2} s^{-1} in each interaction point.

Table 14: Sources of systematic proton losses

	Events per beam			Power deposit per beam		
Type	Cross sect. (mbarn)	r.m.s. angle (μrad)	Rate (s^{-1})	Per m (mW)	Total (W)	Location
Beam–gas						
Nuclear elastic	146	15	0.6×10^9	–	670	Cleaning
Nuclear inelastic	319	–	1.4×10^9	57	1400	Whole ring
Beam–beam (per IP)						
Nuclear elastic	40	26	1.0×10^9	–	1200	Cleaning
Nuclear inelastic	60	–	1.6×10^9	–	1850	SS
Single diffractive	12	35	3.0×10^8	–	350	SS + clean
Non-linear fields						
Slow diffusion	–	–	2.1×10^9	–	2450	Cleaning

- Beam–gas interaction
  Proportional to the beam intensity, the beam–gas interaction induces a continuous loss of about 3×10^4 protons per sec and per metre, for the maximum intensity and the expected gas density [8], over the whole machine for the two beams.

- Beam–beam collisions
  The number of these interactions is proportional to the luminosity. They produce different types of events:

  - *Nuclear inelastic events*
    Already discussed in the SS 1 section, the losses will be localized in the collision straight sections. They amount to 1.6×10^9 events per second and per interaction point;
  - *Nuclear elastic events*
    About 1×10^9 events per second and per interaction point. The r.m.s. scattering angle is 26 μrad (the r.m.s. beam divergence at the IP is 31 μrad). Some of these particles will finally fall out of the dynamic aperture and slowly drift towards the collimators;
  - *Single diffractive events*
    The single diffractive events produce about 3×10^8 protons per interaction point, with scattering angles comparable to elastic collisions but with a non-negligible momentum deviation. Most of them will remain in the RF bucket and behave like elastic events; a small proportion ($\sim$ 10%) will have a larger momentum deviation (up to 15%) and will be absorbed in the pair of deflecting magnets (D_1, D_2) in the interaction region.

- Non-linear effects
  The beam–beam electromagnetic field non-linearities and the field non-linearities in superconducting magnets, combined with power supply or RF ripples, induce a diffusion of particles in transverse phase space. The expected flux of particles on the aperture limitation (the primary collimator) is 2×10^9 particles per second and per beam.

Accidental losses

- Injection mis-steering
  An asynchronous firing of the injection kicker will spray protons across the aperture. Errors in angle and position of a badly injected beam will produce the same effect. As already discussed in the injection section of SS 1, a set of absorbers in the injection straights SS 1 and SS 8 will prevent large-amplitude oscillating particles from entering the arc.

- Misfiring of the beam-dump kicker
  An asynchronous firing of the dump will also spray particles across the aperture. A set of absorbers in the dump straight section will reduce the number of large-amplitude oscillating particles to a non-destructive level. Some magnets might quench but none should be destroyed by this unlikely event.

- Magnet quench
  When a quench is detected, the beam dump is triggered in less than three turns, long before the beam reaches the aperture limit.

- Power converter trip
  As for a magnet quench, the dump is triggered after detection.

- Miscellaneous loss sources
  After RF capture loss, beam instabilities, or unpredictable mechanical failure it will take a number of milliseconds before the beam hits the aperture limit. Early loss of the halo will be detected and the beam dumped when the loss rate becomes excessive. In each case a number of particles will be absorbed by the collimation system whether the beam dump is triggered or not.

Obviously, all these scenarios will have to be analysed in detail, including the cases of several simultaneous faults. Present studies [7] indicate that cures can be proposed for each of them. Some detection and trigger systems will have to be duplicated for redundancy, and the control system must include protection against operational errors.

8.2 Energy deposit by beam losses

The analysis of the energy deposit in a dipole magnet by a lost proton has been presented in some detail in the Pink Book. The energy deposit is computed using nuclear cascade simulation programs, with reasonable assumptions on the angle of incidence of the particles and on their longitudinal distribution [6]. In these conditions the energy deposited in the most exposed part of the coil – the inner coil – by one incident proton is about 6 GeV/cm^3 at 7 TeV and 0.2 GeV/cm^3 at 0.45 TeV. The energy deposit is peaked in the first metre as indicated in Fig. 18.

- **Instantaneous loss**

  The energy deposit can be instantaneous at injection in the case, for example, of a mis-steered injected beam. The process is then adiabatic because heat exchange with the medium does not have time to develop. The temperature rise is calculated using $\mathrm{d}Q = C\ \mathrm{d}T$ where C is the specific heat of copper. The result is obtained by integration because at cryogenic temperatures the specific heat shows a strong dependence on temperature. A certain energy can be absorbed by the conductor before it reaches the temperature where NbTi becomes normal-conducting. At injection with a field of 0.58 T the temperature can be raised by 5 K before the quench develops. This instantaneous temperature of the conductor will be lowered as soon as some heat is transferred to the high heat conductivity helium bath so that the helium will not reach the boiling point. The corresponding energy absorption is called the enthalpy reserve of the conductor. In the case of the dipole inner coil the enthalpy reserve is about 16 mJ/cm^3. The admissible amount of localized instantaneous particle loss at injection is therefore about 1.4×10^9 protons [9].

- **Continuous loss**

  The situation is different once the beam has been correctly injected. Instantaneous losses, in the sense that they occur in a time that is short compared with the time constant of energy transfer to the helium bath, do not happen; the inertia of the beam is too high and any event will develop over several ms. The only imaginable case of an instantaneous loss would be a misfiring of the beam-dump kicker, this case is analysed in a separate note [7].

> These continuous losses are better analysed as a steady state for the heat transfer conditions. The temperature of the conductor is determined by the equilibrium between the power input by proton losses and the power evacuated by the cooling system. During a continuous loss, equilibrium temperatures are reached along the chain of thermal resistances separating the cable from the helium cold source (insulation layers, impregnated glass-fibre tapes, multiple helium channels up to the magnet heat-exchanger tube). These temperatures must be low enough to maintain the cable in the superconducting state. The helium temperature should not exceed the transition temperature T_λ of helium II (2.17 K) in order to keep the advantage of the high thermal conductivity of superfluid helium.

Recent experiments have shown that, with the present insulation, T_λ is reached for a power dissipated in an LHC cable of about 4 mW/cm^3, corresponding at 7 TeV to a localized loss of 4×10^6 protons per second or a distributed loss of about 1.3×10^6 protons per second and per metre. At injection energy the corresponding acceptable losses are about 30 times higher.

8.3 The cleaning process

The cleaning system uses a cascade of four collimators. The first one, the primary collimator, defines the aperture at which the cleaning system will suppress the halo. The cascade of secondary collimators is used to stop the secondary particles coming from the primary collimator.

The difficulty in cleaning the halo of a beam results from the fact that most particles will hit the primary collimator at a small distance from its edge; this 'impact parameter' in the LHC at high energy is of the order of a μm. The primary collimator (C1) must also be positioned with great accuracy with respect to the beam in order to define the maximum amplitude of oscillation or momentum deviation accepted by the cleaning system.

The particles escape from the primary collimator at a distance from the centre line equal to the collimator radius and with an angle in both the horizontal and vertical planes increased by the scattering angle in the first collimator. Some of them also have a momentum difference with respect to the central-momentum particle. Secondary collimators (C2), slightly retracted with respect to C1, are required to stop the flux of escaping particles. The system is fully efficient if the particles escaping these secondary collimators do not have a sufficient oscillation amplitude to reach the superconducting elements in the machine before they are absorbed by the cleaning system on subsequent turns.

The tracking of these particles through the cleaning insertion from one collimator to another and around the LHC can be made numerically, but the optimization of the lattice parameters and of the collimator positions requires some insight. A number of documents have been written on the subject [6, 10, 11]. An interesting approach [12] is to assume perfect rotational symmetry of the whole system in the transverse plane: the Twiss parameters in the cleaning section are the same in both planes and the collimators are round. In this way an analysis of what happens to particles placed e.g. in the horizontal plane at the first collimator C1 is sufficient, the behaviour of other particles can be deduced by a simple rotation. It can be demonstrated that this configuration is also the optimum one when the emittances, the Twiss parameters in the arcs, and the apertures are equal in both planes.

Secondary collimators must obviously have a larger aperture than primary ones, these apertures measured in units of r.m.s. beam size are referred to as n_1 and n_2. Secondary collimators at a phase advance μ and $\pi - \mu$ from the primary collimator have a symmetrical effect on the particles escaping from the primary collimator, they are paired so that the analysis is reduced to one collimator. The optimum phase advance between the secondary collimator and the primary one, that is the one which minimizes the number of secondaries (or their volume in phase space) which will escape the secondary collimator, can then be calculated to be $\mu_0 = \arccos(n_1/n_2)$. To further reduce the flux of secondaries which escape the collimator system a third set of collimators at 90° can be installed. The flux of escaping particles can then be plotted against their amplitude of oscillation (Fig. 19). The maximum amplitude of oscillation is $n = \sqrt{n_1^2 + n_2^2}$. At injection for example $n_1 = 6$, $n_2 = 7$ so that $n = 9.2$, well below the aperture of superconducting equipment around the ring: 12 σ. The margin of a few σ's will be reduced when the inevitable errors of a real system are introduced.

The momentum collimation will work on the same principle. It has been shown [13] that it can be done by adjusting the dispersion and its derivative at the primary collimator. This requires the solution of a difficult optics-matching problem which is still under study.

8.4 Lattice and layout

A special insertion with large beta functions at the first collimator, with equal horizontal and vertical Twiss parameters over the region of collimation and covering a phase advance of $\sim 180°$ has been adopted. The corresponding optics functions are given in Fig. 20.

The layout of quadrupoles in the straight section is based on the same principle as the low-beta insertions: after the dispersion suppressor a pair of triplets matches the arc functions to the specific requirements of the straight section. Here the aim is to leave the maximum space available for the installation of the warm equipment around collimators. The two triplets adjust both beta values and their derivatives to the same value in both planes. The value of beta at the crossing point allows the phase advance in the insertion to be tuned. The layout of machine elements in these two triplets is given in Table 15, a schematic representation is given in Fig. 21.

The triplets are made of two-in-one quadrupoles, so that the beam separation bending magnets are inserted in the collimation system. The bending magnets, placed after the primary collimator, eliminate, in a warm area, particles which have made a nuclear interaction in one of the collimator jaws. The collimators are isolated by vacuum valves in order to facilitate maintenance and repair work. A number of beam-position monitors are placed in the vicinity in order to help in the difficult alignment of the collimators with respect to the beam. The layout of elements in the cleaning section of SS 3 is given in Table 16. Proper shielding is required around the collimators and all along the cleaning section.

Table 15: Magnetic elements in SS 3, outside of cleaning section

MAD		Reference name	Aperture (mm)
Name	Length (m)		
BPM		BPC	24.5
Q6	4.6	MQTA	24.5
COR	0.65	MBHA	24.5
QS	0.72	MQS	24.5
Cryofeed box, half-arc		QFA	
Cryofeed box for Q1 to Q5		QFB	
BPM+QSB		BPCE	31.5
Q5	6.1	MQEB	31.5
COR		MBVC	31.5
Cryoline around the beam, from Q5 to Q4			
BPM		BPCE	
Q4	4.6	MQEA	31.5
COR		MBHC	31.5
COR		MBVC	31.5
QS		MQSB	31.5
COR		MBHC	31.5
BPM-QSB		BPCE-QSB	31.5
Q3	6.9	MQEC	31.5
COR		MBVC	31.5
COR		MBHC	31.5
Q2a	6.1	MQEB	31.5
BPM		BPCE	31.5
Q2b	6.1	MQEB	31.5
COR		MBVC	31.5
Q1	6.1	MQEB	31.5
BPM		BPCE	31.5
CWT-VVP		QWTE VVPE	

Table 16: Main elements in SS 3, cleaning section

Element name	Reference name
CWT-VVP-BPMH&V	
VVP	VVP
D2/1	MBSW
VVP	VVP
Primary collimator of beam I (6 jaws)	TCP
Secondary collimator of beam II (150°, 8 jaws)	TCC
VVP	VVP
D2/2	MBSW
D2/3	MBSW
D2/4	MBSW
D2/5	MBSW
D2/6	MBSW
BPMH&V	BPCE
VVP	VVP
Secondary collimator of beam I (30°, 8 jaws)	TCA
Secondary collimator of beam II (90°, 8 jaws)	TCB
Secondary collimator of beam I (90°, 8 jaws)	TCB
Secondary collimator of beam II (30°, 8 jaws)	TCA
VVP	VVP
BPMH&V	BPCE
D2/6	MBSW
D2/5	MBSW
D2/4	MBSW
D2/3	MBSW
D2/2	MBSW
VVP	VVP
Secondary collimator of beam I (150°, 8 jaws)	TCC
Primary collimator of beam II (6 jaws)	TCP
VVP	VVP
D2/1	MBSW
VVP	VVP
CWT-VVP-BPMH&V	

8.5 Collimator design

Ideal collimators have a circular aperture of variable radius to match the change of beam dimensions with energy. They can best be approximated in practice by diaphragms using a number of mobile jaws. The number of eight jaws per collimator has been chosen [12]. The centring of these collimators on the beam will require detailed operational procedures.

Primary collimator jaws will be made of a light material such as beryllium. The aim is to limit the heat deposition by nuclear interaction and to improve the necessary scattering, possibly using multiturn traversals [14]. Secondary collimators will consist of 450 mm long copper blocks. Copper presents the advantage of a short absorption length of 150 mm and a good heat conductivity. Both materials have good vacuum characteristics and are acceptable radiation absorbers. Magnetized collimators where the incident particles are deviated inside the block have been proposed [15]. The technology of collimators will have to be developed and final choices cannot be made at this stage.

8.6 Collimation efficiency

We have seen that to a first approximation (in the absence of errors in the collimator system) the particles escaping from the collimators will not hit the aperture of superconducting elements.

With a combination of errors a number of particles from the halo could escape the cleaning system with an amplitude large enough to hit a superconducting element. In the extreme case of operation at the beam–beam limit the diffusion rate of the halo corresponds to an estimated loss rate of 4×10^9 particles per second. The maximum acceptable loss of 4×10^6 particles per second at the highest energy in a localized spot indicates that the cleaning system must ensure that only one per mille of the halo reaches this localized loss point. If this loss rate is exceeded the beam dump will be triggered before the magnet quenches.

The evaluation of the cleaning efficiency, including all possible errors of position and angle of the various collimator jaws will result from detailed simulations. These tracking programs are currently in preparation, their result will obviously influence the final layout and specifications of the hardware. The present level of understanding indicates that the final version of the cleaning insertion should not be too different from the proposed one.

8.7 Auxiliary equipment

The general description of auxiliary equipment installed in straight sections has been given for SS 1 in Section 6.

Straight section 3 is situated right under the village of Crozet in the foothills of the Jura mountains and the quality of the rock is so bad that any new excavation must be severely limited. Consequently, there is only one cavern for the two half-octant cryofeed boxes as pictured in Annex III, this cavern being excavated at the bottom of a new 7 m diameter shaft. The two shafts, one for each half-octant, must be situated at locations compatible with existing houses and farms in the village of Crozet.

The following equipment is to be installed.

- *Cryogenics*

  The cryogenics for SS 3 is the standard one installed in all odd-numbered straight sections where no equipment from LEP 200 is available. This installation is separated into two levels:

  1. At ground level the compressors, utilities and upper cold box (room temperature to 20 K) are installed in auxiliary buildings. To avoid noise close to the village of Crozet the compressors will be installed in a technical area near the beginning of the LEP reconnaissance gallery. Cryogenic pipes installed in a small technical gallery will connect these compressors to the first cold box;
  2. At tunnel level one finds the lower cold box LCB (20 K to 4.5 K) and the cold compressor box CCB (4.5 K to 1.8 K). These cold boxes will be installed in the cavern described above.

  The same total equivalent cooling power of 18 kW at 4.5 K as at SS 1 is required.

- *Electrical installation*

  Electrical power at 18 kV is distributed to underground caverns and transformed to user voltage level.

- *Cooling and ventilation*

  Each cavern is equipped with the required cooling and ventilation systems. The main tunnel ventilation is the existing one of the LEP machine.

9 SS 4: ion collisions and RF

As indicated in Table 1 and Fig. 22 insertion 4 of the LHC contains an experimental straight section reserved for ion experiments. Contrary to SS 1 the low-beta arrangement does not have to include injection equipment. It houses instead the RF cavities and equipment for both proton and ion acceleration. The transverse and longitudinal dampers have also been installed in this insertion.

9.1 Low-beta insertion

Like other experimental insertions the low-beta insertion is made of an inner triplet, a pair of separation magnets and an outer triplet as described in the SS 1 or SS 2 Section. The two separation magnets have been moved away from the interaction point in order to leave space for the RF accelerating cavities. As can be seen in Fig. 23 the optics functions are not affected by this displacement.

The lower luminosity of the ion collisions means that no protection of the inner triplet is needed.

Table 17: RF hardware parameter list

RF system for protons		
400 MHz superconducting cavities	8	
Cavities per module	4	
Module length	6.5	m
Cell per cavity	1	
Peak RF voltage per cavity	2	MV
R/Q of a cavity cell	44	Ω
Klystron per cavity	1	
Klystron power	300	kW
HV converters	8	
Input power of HV converters	800	kW

Additional RF system for ions		
No. of Copper Cavities	16	
Frequency	200	MHz
Cell per cavity	1	
Cavity length	0.75	m
R/Q of a cavity cell	170	Ω
Peak RF voltage per cavity	1	MV
Tetrode per cavity	1	
Tetrode power	60	kW

9.2 Radiofrequency equipment

The RF system for proton operation has been described in the Pink Book and has not been modified since, the RF parameters are summarized in Table 17. It consists of two modules of four single-cell cavities (each module is 6.5 m long) [16]. These are superconducting cavities fed at 400 MHz by eight 300 kW klystrons (one per cavity) which must be placed close to the accelerating cavities, at not more than 10 m. The klystron power is essentially determined by the correction of injection transients. The problem of transient beam loading induced by the holes in the circulating beam has also been analysed in the Pink Book. Their detrimental effect is a periodic displacement of the collision points at the revolution frequency, which is minimized by choosing superconducting cavities. For reasons of symmetry, the collision points in the even insertions will not move; in the odd insertions, the maximum displacement, at full intensity, will be about 1 cm (to be compared with the r.m.s. collision length of 5.3 cm).

In order to match the bunch shape of the SPS, the RF voltage must be lowered at injection, thus enhancing the transient beam-loading effects. To keep capture losses as small as possible in the presence of phase injection errors, the SPS bunches will be adiabatically compressed prior to ejection with three 400 MHz single-cell superconducting cavities [17]. In this case the matching voltage in the LHC at injection will be 8 MV.

The RF system for ion acceleration will also be installed in this same straight section. It must provide a longitudinal acceptance twice as large as required for protons in order to keep intrabeam scattering effects at an acceptable level. This requires either an RF voltage four times larger, albeit with a negligible beam loading or an RF system working at a lower frequency. The RF system for ions will consist of additional cavities (to be removed from the beam line during proton operation): 200 MHz single-cell copper cavities to accept the longer bunches from the SPS at injection and provide a larger longitudinal acceptance.

Table 18: Main elements in SS 4 around the Interaction Point

MAD			Reference	Half-aperture
Name	Length (m)	Field (T & m)	name	H/V (mm)
IP				
VVP-CWT			VVPE-QWTE	31.5
BPMH&V-QSA			BPCD-QSA	31.5
COR	0.38	4.5	MBVI	31.5
Q1	6.9	214	MQIA	31.5
COR	0.38	4.5	MBHI	31.5
Q2a	6.1	224	MQIB	31.5
BPMH&V			BPCD	31.5
Q2b	6.1	225	MQIB	31.5
COR	0.38	4.5	MBVI	31.5
Q3	6.9	225	MQIA	31.5
COR	0.38	4.5	MBHI	31.5
BPMH&V			BPCD	31.5
QFB-CWT			QFI-QWTE	
VVP			VVPE	31.5
Copper cavities for ion acceleration			ACCI	
VVP			VVPE	31.5
CWT			QWTE	31.5
S.C. cavities for proton acceleration			ASCP	
CWT			QWTE	31.5
VVP			VVPE	31.5
CWT			QWTE	31.5
COR	0.38	4.5	MBHI	31.5
D1	9.0	5.2	MBSH	
QFB-QSA			QFI-QSA	
CWT-VVP			QWTE-VVPE	31.5

ACCI: accelerating copper cavities for ions.
ASCP: accelerating superconducting cavities for protons.

The cavities have been distributed symmetrically on both sides of the interaction point, as listed in Table 18 and indicated in the interaction area layout, Fig. 22. On each side one finds:

- **Superconducting cavities for proton acceleration**

  These cavities are schematically represented in Fig. 24. Their main characteristics are given in Table 17. These cavities are placed around both beams because the beam separation (180 mm) is, for obvious geometrical reasons, not compatible with 400 MHz cavities working on one beam only. The cavities are therefore placed in between the inner triplet and the D1 magnet, at a place where the two beams are very close to the machine centre line. The maximum separation of the two beams in the cavities is 7.5 mm for the maximum 100 μrad crossing angle of the ion experiment insertion. Four cavities are installed in a common cryostat. Each cavity is connected to its 300 kW klystron via a short waveguide feeder line and circulator. The klystrons are located in the access tunnel to the LEP klystron gallery in order to keep the amplifier-to-cavity delay within acceptable limits for the RF feedback. They will make use of the existing LEP power converters and auxiliary power supplies. The higher-order-mode couplers are installed in the large-bore beam tubes in between each cavity in which most of the higher-order modes propagate. It is expected that a combination of high-pass and tuned couplers will be needed (the latter for the lowest modes). The large tuning range needed for compensation of reactive beam loading may not be achievable with LEP2 type magnetostrictive tuners. In this case mechanical actuators will be considered;

- **Copper cavities for ion acceleration**

  Having twice the longitudinal emittance of the proton bunches, the ion bunches at injection are twice as long. This is in order not to increase their momentum spread, which is limited by the LHC and transfer line acceptance. Therefore they cannot be captured in the too short 400 MHz buckets, and additional 200 MHz cavities are needed. Two sets of these single-cell copper cavities common to both beams and installed on either side of the interaction point are used during ion operation. The 200 MHz 'standing-wave cavities' currently in use for lepton acceleration in the SPS can be used for this purpose. They provide a total voltage of 6 MV at 200 MHz with a 60 kW tetrode amplifier on each cavity. The high impedance 200 MHz cavities must be removed from the beam line during high intensity proton operation.

9.3 Dampers

The design of the dampers, both longitudinal and transverse, is dominated by the injection requirements: keep the capture losses as small as possible in the presence of phase injection errors, minimize the emittance blow-up resulting from decoherence induced by magnetic and space-charge non-linearities. Instability control, except for resistive wall at low frequency, is less demanding because superconducting cavities present small transverse impedance. In most cases, Landau damping should prevent coupled-bunch instabilities, longitudinal and transverse.

- **Longitudinal dampers**

  The longitudinal dampers (ADL) (the feedback cavities are shown in Fig. 25) are located in the drift space between the separation magnet D2 and the first quadrupole of the outer triplet as detailed in Table 19. There are four 'septum' cavities per beam, on one side only of the interaction point. These cavities work around 200 MHz, to be compatible with ion operation. Each cavity has a peak voltage capability of 90 kV, enough to damp a 15° phase error at injection in three synchrotron periods. The tetrode power amplifier (peak power 90 kW at 200 MHz) sits on top of the cavity in order to keep an approximately constant transformation ratio between anode voltage and cavity gap over the ±20 MHz operating range of the damper [18].

The impedance of the feedback cavities will be kept low with RF feedback for the fundamental mode and with a tuned higher-order-mode coupler for the only significant higher-order mode (HOM) at 580 MHz.

Table 19: Main elements around dampers in insertion 4

MAD			Reference	Half-aperture
Name	Length (m)	Field (T & m)	name	(mm)
D2 (5 elements)	5.2	1.8	MBSW	
COR			MBHW	
COR			MBVW	
BPMH&V			BPC	
Wideband pick-up for RF control			ABPW	
VVP			VVP	
*Longitudinal damper for beam I**			ADL	$\Phi = 60$
*Longitudinal damper for beam II**			ADL	$\Phi = 60$
VVP-CWT			VVP-QWT	
QFA-QSA			QFA-QSA	
QS	0.72	120	MQS	24.5
COR	0.65	3.9	MBHA	24.5
COR	0.65	3.9	MBVA	24.5
Q4	3.7	192	MQTA	24.5
BPMH&V			BPC	
QS	0.72	120	MQS	24.5
QS	0.72	120	MQS	24.5
COR	0.65	3.9	MBVA	24.5
Q9	3.7	220	MQTA	24.5
BPM/QSA			BPC	24.5
MB	13.145	9.0	MB	
MB	13.145	9.0	MB	
CWT-VVP			QWP-VVP	
Horizontal damper for beam I			ADT	22.5/35
Vertical damper for beam II			ADT	35/22.5
Pick-up for dampers and RF control			ABP	
VVP-CWT			VVP-QWT	
QS	0.72	120	MQS	24.5
QS	0.72	120	MQS	24.5
COR	0.65	3.9	MBHA	24.5
Q10	3.7	196	MQTA	24.5
BPM/QSA			BPC-QSA	

* On one side only of insertion.

- **Transverse dampers**

  The transverse dampers ADT are mainly aimed at reducing injection oscillations but should also reduce any emittance blow-up due to ground motion and to magnetic noise or ripple. At injection the gain should be large enough to keep emittance blow-up small (1%) in the presence of space-charge decoherence ($dQ = 10^{-3}$). The necessary deflections can be achieved by four kickers, each consisting of a pair of electrostatic plates 1.5 m long with a gap of 45 mm and a maximum voltage of 8 kV. These deflectors will be installed in the dispersion suppressors as indicated in Table 19. The electrostatic deflectors are excited by a pair of push-pull tetrodes driven by a broad-band (20 MHz) amplifier. The same deflectors are used, up to the highest frequency of the damper (20 MHz), at a reduced voltage capability, limited by the anode-deflector capacitance and the peak current of the tube. This is adequate for correcting the effect of the injection kicker ripple (2 mm oscillation on the newly injected batch at a frequency of about 1 MHz), the resistive wall instability, and the transverse instabilities induced by narrow-band parasitic impedances. A dedicated transverse beam monitor, working at room temperature and located in the same place, will provide the damper signals (horizontal for one beam, vertical for the other) and similarly on the other side of the IP. An additional signal, coming from one of the regular closed-orbit pick-ups may be used to correct for changes of the machine operating points.

9.4 Special beam instrumentation

A number of beam monitors will be installed in insertion 4 for emittance measurements, using synchrotron light or wire scanners, for beam intensity and bunch length measurements, etc. Most of them will be installed in the long warm sections available in insertion 4.

9.5 Auxiliary equipment

As explained for SS 2 the klystron galleries, once cleared of unused LEP hardware, will house power supplies, local controls, electrical and ventilation services, and existing LEP 200 cryogenic installations.

- *Cryogenics*

  Cryogenics in SS 4 will be similar to that of SS 2. The only minor difference is that the cold compressor box (CCB), instead of being installed in a new cavern, will be placed in the existing US45 at the bottom of existing shaft PM45.

- *Electrical installation*

  Electrical power at 18 kV is distributed to underground caverns and transformed to user voltage level.

- *Cooling and ventilation*

  Some modifications are required to the existing cooling and ventilation systems. The main tunnel ventilation is the existing one of the LEP machine.

10 SS 5: beam dump

A beam-dumping system, working reliably at all energies, is an essential element in the operation of a collider. Its reliable operation is even more important in a superconducting ring where, as soon as a small fraction of the beam is lost, quenches are induced, while larger losses lead to serious damage or destruction of components of the ring. In conventional storage rings the beam is usually dumped on an absorber block placed at the edge of the machine aperture. Such a solution is not possible in the LHC because the enormous amount of stored energy in the beam (up to 550 MJ) can only be absorbed after the beam cross-section has been greatly enlarged. As explained in the Pink Book and described schematically in Fig. 26, each beam must be extracted separately, diluted in phase space and then dumped in a dedicated area away from the machine where radiation will be contained under controlled conditions.

The principle adopted has not changed since the Pink Book: A specially designed insertion, shown in Figs. 26 and 27, allows the installation of a powerful kicker. A 3 μs gap will be left in the circulating beam in order to avoid spreading partially deflected beam particles around the machine while this kicker is rising to nominal field. The kicker deflection (0.7 mrad), increased to about 1 mrad by a 'kick enhancement' effect of the quadrupoles, removes the beam from the normal aperture at the entrance of the D2 separation magnet. Specially designed for this function, this separation magnet lets the beam pass outside the coil and hence without the 1.2 mrad deflection given to the circulating beam. The beam leaves the machine with a total deflection of 2.2 mrad, just sufficient to clear the specially reduced cryostat of the downstream quadrupole Q3. The extracted beam enters a new tunnel at the start of the main-ring bending magnets.

The dilution of the extracted beam must take place as far upstream as possible in order to ensure maximum cross-section enlargement at the dump block placed 850 m downstream of the crossing point. In the present layout the combined effects of dilution kickers and a quadrupole are used. Two pairs of orthogonally deflecting kicker magnets excited with 11 kHz sinusoidal currents produce a 20 cm diameter circular sweep at the front face of the absorber. The quadrupole has a focal length of about 50 m, so that it produces a net defocusing effect in both planes at the dump. Other techniques to reduce the energy density in the absorber, such as scatterers, have been studied and could be implemented if necessary.

The dump block, illustrated in Fig. 28 is placed at the end of an 850 m drift space, about 450 m being in a separate tunnel. Its central part is made of graphite, which has a low atomic weight and density to dilute the particle cascade, and also has excellent mechanical properties up to temperatures as high as 2500°C. An aluminium container surrounding the graphite core also absorbs part of the cascade. Finally, an important mass of iron (recovered from the CERN synchrocyclotron) provides effective shielding of the radioactive core. The whole assembly is made of blocks not heavier than the 25 tons that a small overhead crane can handle. The dump cavern has enough space to store additional blocks in case dismantling is required.

The lattice functions of the insertion required for the beam extraction system are plotted in Fig. 27 and the corresponding list of equipment given in Table 20. The larger than usual beta functions impose two-in-one quadrupoles of enlarged aperture. Even with this precaution a number of orbit correctors must also be installed in order to reduce the local closed-orbit amplitude and effectively increase the available aperture in Q3 and Q4. The resulting values of the available apertures are given in the last section of Table 5.

The technically most difficult and costly components are the kicker magnets for extraction. They must provide for each channel a total deflection of 0.7 mrad which at LHC peak energy corresponds to a required integral field of 17.05 T m. Given the available straight section length, this can only be achieved with very powerful magnets operating at a field level of 0.7 T which requires an unconventional design. A prototype of such a kicker magnet is under construction. It is made, as described in more detail in the Pink Book, of cores wound from 0.05 mm thick tapes of silicon steel and excitation bars insulated with epoxy-impregnated mica tapes, the whole assembled around a ceramic vacuum chamber. The magnet operates in air. Several types with different apertures will be built to match optimally to the available beam aperture. In total 26 kicker magnets, each with its own pulse generator, are required for each of the two extraction systems.

The generator must produce a 90 μs long current pulse of 30 kA with a risetime of 3 μs based on a capacitor discharge circuit with a diode stack parallel to the magnet to obtain the flat top length. The choice of the fast high-power switches must take into account the high reliability required with negligible prefiring rate, and the cost. Several solutions are under study using either multistage ceramic thyratrons, pseudospark switches, or semiconductor switches. Contrary to what has been assumed in the Pink Book, the pulse generators will now be installed in a parallel tunnel or in shielded alcoves to protect the diodes from the radiation present in the main tunnel.

It is clear that the design of the insertion and of the components of the beam-dumping system will be the result of a number of optimization cycles and the studies are continuing. The final result should however not be too different from the present ideas.

Table 20: Main elements in SS 5

MAD		Reference name	Half-aperture (mm)
Name	Length (m)		
MB	13.145	MB	24.5
BPM QSA		BPCE-QSA	31.5
Q6a	4.6	MQED	31.5
Q6b	4.6	MQED	31.5
COR	0.76	MBHEA	31.5
QS		MQSA	31.5
COR	0.65	MBVA	24.5
Q5a + Q5b	4.6	MQTB	24.5
BPM		BPC	24.5
QFB		QFA	
QWT VVP		QWT-VVP	24.5
*Blow-up quads, ejected beam II**			
Extraction kicker, beam I		MKE	
VVP QWT		VVPE-QWTE	31.5
QFB QSA		QFB-QSB	
QS		MQSB	31.5
COR		MBHD	31.5
Q4	6.1	MQEB	31.5
BPM		BPCE	31.5
QWT VVP		QWTE-VVPE	31.5
Extraction kicker, beam I		MKE	
VVP QWT		VVPE-QWTE	31.5
QFB QSA		QFB-QSB	
COR		MBVD	31.5
Q3	4.6	MQEA	31.5
BPM		BPCE	31.5
VVP QWT		VVPE-QWTE	31.5
Extraction kicker, beam I		MKE	
Dilution kicker, ejected beam II			
D2(3 modules)	5.5	MBSD	
Collimator, ejected beam II			
Beam monitor, beam II			
IP5			
Beam monitor, beam I			
Collimator, ejected beam I			
D2(3 modules)	5.5	MBSD	
Dilution kicker, ejected beam I			
Extraction kicker, beam II			
BPM		BPCE	31.5
QWT VVP		QWTE-VVPE	31.5
Q3	4.6	MQEA	31.5
COR		MBVD	31.5
VVP QWT		VVPE-QWTE	31.5
QFB QSA		QFB-QSB	
Extraction kicker, beam II			
BPM		BPCE	31.5
QWT VVP		QWTE-VVPE	31.5
Q4	6.1	MQEB	31.5
COR		MBHD	31.5
VVP QWT		VVPE-QWTE	31.5
QFB QSA		QFB-QSB	
Extraction kicker, beam II			
Blow-up quads, ejected beam I			
BPM		BPC	24.5
QFB QWT		QFA-QWT	24.5
VVP		VVP	24.5

* Elements not situated on ring 1

10.1 Auxiliary equipment

The general description of auxiliary equipment installed in straight sections has already been detailed in Section 6.

In addition to this technical equipment, the power supplies feeding extraction and dilution kickers of the beam-dumping system must be installed. For this, additional space underground is needed and the liaison gallery described in Section 6 will be widened from 3.8 m to 4.4 m (see Annex III).

- *Cryogenics*

  The cryogenics in SS 5 is similar to that installed in all odd-numbered straight sections where no equipment from LEP 200 is available. The compressors and upper cold boxes UCB (room temperature to 20 K) are installed in auxiliary buildings. Storage for gaseous helium is also provided at this level. The lower cold box LCB (20 K to 4.5 K) and the cold compressor box CCB (4.5 K to 1.8 K) will be installed in a cavern excavated at the bottom of a new 7 m diameter shaft. The same total equivalent cooling power of about 18 kW at 4.5 K is required, as for SS 1.

- *Electrical installation*

  Electrical power at 18 kV is distributed to underground caverns and transformed to user voltage level.

- *Cooling and ventilation*

  All underground enclosures are equipped with the required cooling and ventilation system, with the main tunnel ventilation being the existing one of the LEP machine.

11 SS 6 and SS 7

These two insertions are, at present, not used for physics or for special machine purposes. The lattice has therefore been simplified as much as possible in order to reduce costs. This has been achieved by suppressing the D1 magnet to leave a simple crossing, and reducing the inner triplet to a doublet. The outer triplet layout has been modified in order to match the new optics, but the dispersion suppressors are identical to those of the low-beta insertions. The corresponding layout is shown in Fig. 29 and the lattice functions are plotted in Fig. 30. Table 21 gives the list of equipment in the straight section. These simplified insertions do not require enlarged quadrupoles, and available apertures are everywhere larger than 12 σ.

11.1 Auxiliary equipment

Auxiliary equipment installed in SS 6 is identical to that described for SS 4, while auxiliary equipment in SS 7 is almost identical to that of SS 1. The main difference consists in the excavation of a new 7 m shaft to be used as a vertical link between the surface facilities and underground enclosures for electricity and cryogenic lines.

- *Cryogenics*

  At tunnel level the lower cold box LCB and the cold compressor box CCB are installed in a cavern excavated at the bottom of this new 7 m shaft. The same total equivalent cooling power of about 18 kW at 4.5 K, as at SS 1, is required.

- *Cooling and ventilation*

  Each cavern is equipped with the required cooling and ventilation system while the main tunnel ventilation is the existing one of the LEP machine.

Table 21: Main elements in SS 6 and SS 7

MAD		Reference name	Half-aperture (mm)
Name	Length (m)		
IP			
D2(6 modules)	5.2	MBSW	
VVP-QWT		VVP-QWT	24.5
COR	0.85	MBHB	24.5
Q2	8.0	MQTD	24.5
BPM		BPC	24.5
Q3	8.0	MQTD	24.5
COR	0.85	MBVB	24.5
COR	0.85	MBHB	24.5
BPM-QSA		BPC-QSA	24.5
QFB		QFB	
QWT-VVP		QWT-VVP	24.5
VVP-QWT		VVP-QWT	24.5
QFB		QFA	
QS	0.72	MQS	24.5
COR	0.65	MBVA	24.5
COR	0.65	MBHA	24.5
Q4	8.0	MQTC	24.5
COR	0.65	MBVA	24.5
Q5	8.0	MQTC	24.5
BPM-QSA		BPC-QSA	24.5
Cryoline from Q4 to Q5			
QS	0.72	MQS	24.5
COR	0.65	MBVA	24.5
Q6	8.0	MQTC	24.5
BPM		BPC	24.5
MB	13.145	MB	24.5

12 SS 8: beam II injection

The injection of the counterclockwise beam (beam II) is installed in straight section 8. The lattice has, for the time being, been selected as identical to the detuned low beta. This is the obvious solution if one wants to leave open the possibility of installing an experiment in this insertion at a later date. It is possible to inject into a 'simplified' insertion of the type selected for insertions 6 and 7, however, in this case the injection tunnel coming from the SPS would have to join the LHC at a slightly different position, making the conversion of SS 8 to an experimental insertion impossible at a later stage. The list of equipment required for SS 8 is similar to that of SS 1, Tables 10 and 11 of Section 6. The collimators (TDS and TDN) for stopping the secondaries coming from the interaction are not required. The fact that the detuned low beta is not squeezed to low-beta values does not modify in an appreciable way the requirements on the quadrupoles and their power converters. The lattice functions are given in Fig. 31. The injection matching takes into account the reversed polarity of the quadrupoles in SS 8 with respect to SS 1.

The layout drawings given in Fig. 32 are slightly modified with respect to SS 1 by the fact that even and odd insertions are not identical and that the collimators for stopping the secondaries from the interaction are not required.

12.1 Auxiliary equipment

Auxiliary equipment installed in SS 8 is identical to that described for SS 4.

13 Transfer lines from the SPS

The path chosen for the two beam lines to transfer the 450 GeV protons from the SPS to the LHC is still the same as proposed in the Pink Book [1], see Fig. 1.

The beam line TI13 to ring 1 of the LHC, where the protons circulate in the clockwise direction, starts in LSS5 of the SPS and ends in LHC straight section 1. The other one, TI87, which leads to the counterclockwise ring 2, starts in LSS4 of the SPS to end in LHC straight section 8. Their lengths, from the SPS ejection point to the LHC injection point, are 950 m and 2500 m respectively with required total horizontal deflections of 79° and 103°.

The beam line TI13 is the obvious choice for the transfer to ring 1. For the relatively long beam line TI87 to ring 2 an alternative has been considered. It consists in a beam line from LSS1 of the SPS to LHC straight section 1, which has about the same length and horizontal deflection as TI13, but which requires that the protons in the SPS circulate in reverse direction. Polarity reversal of the SPS is at present not possible. It requires a number of important modifications and additions and, moreover, the construction of a new beam line between the PS and the SPS to be able to inject in reverse direction. A detailed comparison resulted in a slight cost advantage of this alternative which, however, is considered to be too small to compensate for the extra operational complications and a lengthening of the total transfer time that this scheme implies.

The design constraints are most severe for TI13 where the horizontal and vertical deflections – to match the difference in height between the two machines – require the use of superconducting dipole magnets operating at a magnetic field of 5.5 T. These dipoles are inserted into a FODO lattice of 43 m period length which also makes use of superconducting quadrupoles and correctors. At the ends, close to SPS ejection and to LHC injection, individually powered normal-conducting quadrupoles and dipoles are used to ensure the optical and geometrical matching of the two machines. The maximum slope of the tunnel is 7.1%.

For TI87, because of its considerably longer distance, much more flexibility exists. A geometry with two strongly curved arcs separated by a 1 km long straight part has been chosen. The arcs use exactly the same lattice with superconducting magnets as TI13. In the 1 km long straight part classical warm quadrupoles are placed every 50 m. The maximum slope of the tunnel is 3.7%. The length available for TI87 also allows the use of classical warm magnets. This possibility could be selected if it leads to an overall cost saving, e.g. by using existing magnets free of charge.

No design of the superconducting magnets exists. The present layout and the cost estimate are based on HERA dipoles and quadrupoles reduced to 5.7 m and 1 m of magnetic length. These magnets would operate at 4.5 K and would have to be adapted for installation in a sloping tunnel. The UNK dipoles which have a magnetic length of 5.7 m could also fit into the lattice. Another interesting possibility would be to use a shortened single-bore variant of the LHC main dipoles operating at 4.5 K.

Table 22 gives the currently assumed types and quantities of magnets required for the two beam lines.

Power supplies and cryogenic plants for the whole of TI13 and for most of TI87 are installed in the existing equipment buildings at LSS4 and LSS5 of the SPS, which have become free since the dismantling of the $\bar{\mathrm{p}}$–p experiments. The downstream part of TI87 is supplied from the equipment cavern of LHC straight section 8.

14 Parameters and performance

The performance of the LHC presented here is not very different from that of the Pink Book version. However, some changes of parameters have occurred following the decision to base the design on two main experiments instead of three and to distribute the bunches every 25 ns instead of every 15 ns. The new parameter lists are given in Annex I, Tables 23–27.

14.1 Luminosity

The luminosity is given by

$$\mathcal{L} = \frac{N^2 k_\mathrm{b} f \gamma}{4\pi \varepsilon_\mathrm{n} \beta^*} F$$

where N is the number of protons per bunch, k_b the number of bunches, f the revolution frequency, γ the relativistic factor, ε_n the normalized transverse emittance, β^* the value of the betatron function at the interaction point, and F the reduction factor due to the crossing angle, which is about 0.9 in the LHC.

The most important limitation to luminosity comes from the beam–beam interaction. This effect has two components in the case of the LHC. There is the unavoidable head-on interaction of the colliding beams at the wanted interaction points and there is also the long-range interaction which occurs on either side of the interaction regions in the common

Table 22: Magnets required for beam lines TI13 and TI87

Magnet type	Integrated strength		Quantity	
	value	unit	TI13	TI87
Superconducting:				
Dipoles	31.4	T·m	69	99
Quadrupoles	120	T	28	46
Dipole correctors	0.5	T·m	15	26
Classical existing CERN types:				
Dipoles	5.13	T·m	9	9
Quadrupoles	72	T	6	30
Dipole corrector	1.0	T·m	3	13
Classical, special new:				
Slim dipoles	8.7	T·m	7	7
Slim quadrupoles	72	T	4	4

stretch of the beam pipe in which both beams run side by side. The importance of the head-on interaction is determined by the beam–beam tune shift parameter ξ

$$\xi = N r_p / 4\pi\varepsilon_n \ ,$$

where r_p is the classical proton radius, while the long-range interaction depends on the total beam current and the crossing geometry. The head-on interaction excites high-order betatron resonances and creates a tune spread across the beam distribution, while the long-range interaction essentially adds a contribution to the tune spread. Experience at the SPS proton–antiproton collider has shown that both the beam–beam parameter ξ and the total tune spread have to stay below certain limits.

With only two interaction regions instead of three a 50% higher beam–beam tune spread can be tolerated in each interaction region. Since the total beam current in the machine is limited by other effects, a better optimization of the LHC performance is obtained in this case by increasing the bunch population N and decreasing the bunch number k_b to keep the same beam current. This is approximately realized by changing the bunch distance from 15 ns to 25 ns, which is one of the few magic numbers allowing regular collisions at the centre of the eight LHC straight sections. Increasing N by the ratio 25/15 we obtain a beam–beam parameter $\xi = 0.0055$, a value which was achieved in the SPS collider operating at its maximum performance. The corresponding luminosity: the beam–beam limited luminosity is 2.5×10^{34} cm^{-2} s^{-1}.

However, theories which are well-established in the case of the SPS collider are extrapolated here to a machine of much larger dimension and complexity, and to a much higher luminosity. Moreover, other sources of limitation must be considered like the irradiation of low-beta quadrupoles by secondaries from the interaction (discussed in Section 6.1) or the chances of quenching superconducting magnets with the halo of a large circulating beam current (discussed in Section 8). In view of this, and considering that it is anyway recommended to operate somewhat below the beam–beam limit and the maximum attainable energy in order to ensure better stability and reliability, the design luminosity of the LHC has been fixed at

$$L = 10^{34}\ \mathrm{cm}^{-2}\ \mathrm{s}^{-1} \ .$$

Parameters corresponding to this luminosity at a beam energy of 7 TeV are given in Annex I, Table 24.

The machine will nevertheless be designed such that if, given time and effort, the various limitations can be overcome, the essential hardware will not limit the luminosity to values lower than the beam–beam limit.

14.2 Duration of data-taking runs

At the design luminosity of 10^{34} cm^{-2} s^{-1} the initial characteristic decay time of the beam current due to the collisions themselves is 40 hours. Neglecting all other sources of particle loss, this gives a luminosity half-life of 16 hours. Taking into account all sources of loss as detailed in Table 14, the beam lifetime is reduced to 22 hours and the luminosity lifetime to 10 hours, as indicated in Annex I, Table 24.

The optimum duration of an uninterrupted data-taking period depends both on the luminosity lifetime and on the time it takes to refill the machine. Although the beams can be injected into the two LHC rings in less than seven minutes, the overall interruption of data-taking is much longer. After the old beams have been dumped, one must lower the current in the magnetic systems to the injection values, tune the transfer and capture processes with pilot beams of small intensity, and, after the final transfers have been made, accelerate the beams to high energy and adjust collisions. When the operation of the LHC is well mastered this may take about two hours. In this case the ratio of average to initial luminosity reaches a maximum of 0.6 if the physics data-taking lasts about seven hours, and refilling of the LHC is required two to three times per 24 hours. In the first years of operation one may expect longer filling times, in which case it is advantageous to keep the beams in collision for longer periods.

14.3 Evolution of performance during the first years of operation

The LHC is the first superconducting collider foreseen to operate with a large value of the beam current. Superconducting magnets tolerate only extremely small beam losses. In order to prevent excessive quenching of the magnets, the particles in the beam halo which slowly diffuse out towards the beam-pipe walls have to be intercepted with a very high efficiency by collimators in a warm section of the machine. Although we do not yet know with precision the tolerance level of the LHC magnets to beam losses, we are confident, after careful studies, that a collimation system can be built with adequate performance, and a whole straight section has been reserved for this purpose.

However, learning how to operate the LHC in such conditions will take some time, and the initial commissioning of the machine will be done with beams of much smaller intensity than the nominal one. In order to avoid a dramatic reduction of luminosity in proportion to the square of the beam current, we have to operate in this case with a reduced transverse emittance. This is possible as long as the transverse beam density N/ε^* stays below its nominal value, which is limited by beam–beam effects in the LHC and space-charge problems in the injectors. Provided the transfer and inflection systems are suitably upgraded to preserve the required small emittance all along the injection chain, luminosity can be produced in proportion to the beam current.

After about one year of commissioning, it is reasonable to expect that the LHC could be operated with one tenth of the nominal beam current, providing in this case a luminosity of 10^{33} cm^{-2} s^{-1}.

In the following two to four years, the luminosity should then gradually increase towards the nominal value of 10^{34} cm^{-2} s^{-1} as a result of the improvement of systems and operational procedures.

14.4 Injectors

One of the big assets of the LHC project is the existence on the CERN site of a reliable chain of high-performance accelerators which are well-suited to providing the LHC with its supply of protons. The only major addition required will be new RF systems in the PS and the SPS, and two new beam lines from the SPS to the LHC to allow protons to be fed to the new collider in both the clockwise and anticlockwise directions.

The SPS will inject into the LHC at 450 GeV – its top energy. Twelve consecutive batches containing up to 4×10^{13} protons each will be accelerated in the SPS and transferred sequentially into each one of the two LHC rings. The bunch trains will be formed in the PS, with the right spacing between bunches required by the LHC (25 ns), by adiabatically capturing the beam at 26 GeV with the new 40 MHz RF system. Three such trains of 84 bunches will be transferred at 26 GeV into the SPS on three consecutive PS cycles. In the SPS the beam injected in this way fills about one-third of the circumference and corresponds to the maximum beam-handling capabilities of the machine.

The properties of the SPS beam suitable for injection in the LHC are given in Table 27 in Annex I. The normalized transverse emittance $\epsilon_n = 3.5 \times 10^{-6}$ m is such as to authorize the ultimate luminosity of 2.5×10^{34} cm^{-2} s^{-1} to be reached in the LHC at maximum beam current and energy, without exceeding the beam–beam limit.

The corresponding beam brightness, defined as the bunch intensity divided by the transverse emittance, has already been achieved in the SPS proton–antiproton collider and is therefore not a challenge for the SPS. However, in the PS it is necessary to increase the energy at which the beam is injected in this machine from 1 GeV to 1.4 GeV to prevent a dilution of the beam due to excessive space-charge forces. The value of the longitudinal emittance of the bunches, $\epsilon_l = 1$ eV/s, is determined by the necessity to maintain the growth rate of transverse emittances due to intrabeam scattering in the LHC below tolerable levels.

As explained previously, during its first years of operation the LHC will most probably use beams of reduced intensity. In this case the transverse emittance must also be reduced in order to optimize luminosity. Since the beam brightness is not increased, this poses no additional space-charge problems in the injectors. However, the conservation of emittances up to five times smaller than in the nominal case all along the injection chain considerably increases the demands on the quality of the beam-transfer elements.

The main parameters of the injector chain as described in the Pink Book, but updated to the present project definition, have been attached to the LHC parameter lists of Annex I Table 27.

15 The LHC as a lead-ion collider

The acceleration of ions in the LHC was already discussed in various chapters of the Pink Book. A number of modifications to the scheme and the progress made in the design justify a new description of the facility [19].

The acceleration of ions is a well-developed activity at CERN where the first ions were accelerated in the CPS in 1976 and the world energy record achieved (6.4 TeV for sulphur ions) in 1987. A Lead-Ion Acceleration Facility (LIAF) is currently under construction with the aim of making fixed-target ion physics with 177 GeV/u lead ions[6] extracted from the SPS. This programme should be operational in 1994.

The plans are to use this facility in order to achieve (after a moderate upgrading) lead-ion collisions at a centre-of-mass energy of 1148 TeV in the LHC. A list of parameters is given in Annex I.

Ions lighter than lead could also be accelerated in the CERN complex but, since at this stage no formal physics proposal has been discussed in CERN committees, the present document concentrates on lead ions.

---

[6] Throughout this section the energy per atomic mass unit has been used (1 a.m.u. = 931.502 MeV/c^2).

15.1 Lead ions in the LHC

The performance of the LHC as a lead-ion collider is characterized by a number of parameters:

- The energy of 1148 TeV in the centre of mass corresponds to the nominal LHC field of 8.65 T giving a total energy of 574 TeV to the lead ion (2.76 TeV/u and 7.0 TeV per charge);
- The transverse normalized emittances[7], have been fixed at $\epsilon^* = 1.5 \times 10^{-6}$ m, corresponding to the same size as the proton beam at the same field values in the SPS and the LHC. This represents a safe maximum operational value;
- The minimum luminosity half-life (the time after which the luminosity is halved), is fixed at 10 hours for obvious operational reasons;
- The initial luminosity per bunch collision is then, in the case of lead-ion collisions, determined by nuclear effects as explained below and detailed in a separate note [20];
- The number of particles per bunch is, like the initial luminosity, limited by nuclear effects as detailed in the next section;
- As explained below, the longitudinal emittance is blown up in a controlled way in order to limit the transverse blow-up induced by intrabeam scattering;
- The initial luminosity is obtained by multiplying the luminosity per bunch collision by the number of bunches. This number results from a detailed analysis of the generation of bunches in the injector chain as discussed below.

With 496 bunches circulating in the LHC, and with a luminosity per bunch of 3.6×10^{24} cm^{-2} s^{-1}, the initial luminosity of the lead-ion collisions is 1.8×10^{27} cm^{-2} s^{-1}.

Nuclear effects

Two effects (the Weizsacker–Williams effect where a nucleon is stripped from the nucleus, and electron capture by the ion after pair production), with a total cross-section of 277 b consume particles at a rate proportional to luminosity. Once the emittances have been given their maximum acceptable value and the luminosity half-life fixed to 10 hours, the initial luminosity per bunch is determined to be 3.6×10^{24} cm^{-2} s^{-1}. The number of particles per bunch is fixed by this same argument and can be calculated using the luminosity definition equation, in this case: 9.4×10^7 ions per bunch.

This limit is independent of the performance of injectors. Increasing the number of particles per bunch or decreasing the emittances would only lead to shorter luminosity half-life, and therefore to lower performance.

---

[7] All emittances quoted are r.m.s. emittances taken at 1 σ of the distribution.

In the case of two interaction regions working with equal luminosities the above argument shows that the initial luminosity of each experiment will be divided by four. Obviously if one of the experiments requires a much lower luminosity its effect is negligible.

The effect of intrabeam scattering

A second effect influences the variation of luminosity as a function of time: the intrabeam scattering (IBS) which is of particular importance with heavy ions. This multiple coulomb scattering inside the beam scales like the inverse product of emittances. The net effect of IBS is a blow-up of emittances in the six-dimensional phase space. In order to limit this effect the longitudinal emittance which does not enter in the formula for luminosity is artificially increased.

The remaining transverse emittance blow-up induces a progressive reduction of luminosity which combines with the effect of ion loss rate described above. The resulting luminosity decay is plotted in Fig. 33. The corresponding emittance growth times are given in the parameter list (Annex I, Table 26).

Hardware in the LHC

Apart from a low-beta section in SS 4, the main addition to the LHC hardware concerns the RF system. In order to contain the increased longitudinal emittance necessary to control intrabeam scattering (IBS), larger RF buckets than for protons have to be provided at all energies. This could be done at high energy either by providing more RF voltage to the 400 MHz system already used for protons, or by using a lower RF frequency. However, at injection energy the first solution is inadequate since it would increase the energy spead beyond the acceptance of the LHC and the transfer lines. It is therefore proposed to base the ion RF system on 200 MHz single-cell copper cavities. It is foreseen to re-use the lepton cavities currently installed in the SPS which will be available after the end of LEP. All additional RF cavities used for ions have to be withdrawn from the ring during the proton operation since their added impedance is not acceptable in the presence of the large circulating current with protons.

The bunch length during collision is somewhat longer than with protons.

15.2 Ions in the injector complex

As we have seen above, the LHC has very precise requirements for the performance of the injector chain which must also provide the maximum number of bunches compatible with an LHC filling scheme in a reasonable filling time. These bunches must have the correct emittance and number of lead ions. The facility (LIAF) currently under construction must be upgraded in order to reach the required level of performance.

The lead-ion acceleration facility (LIAF)

The facility [21] consists of a number of items with successive functions:

- An ECR source[8] produces 80 μA of $^{208}\mathrm{Pb}^{28+}$ at a kinetic energy of 2.7 keV/u;

---

[8] ECR source: electron cyclotron resonance source.

- A 100 MHz RFQ accelerates them to 250 keV/u;
- A new, specially built, interdigital-H (IH) linac with three tanks working at 100 and 200 MHz provides an output kinetic energy of 4.2 MeV/u;
- A stripper target followed by a magnetic filter delivers 22 μA of Pb^{53+} with a pulse length of 400 μs and a pulse rate of 1.2 s;
- The PS Booster (PSB) accelerates these ions in its four rings to a kinetic energy of 94 MeV/u;
- The PS accelerates them to 4.25 GeV/u;
- A stripper foil in the transfer line produces the final charge-state of Pb^{82+}, fully stripped ions;
- The beam is transferred to the SPS where it is debunched and recaptured at 200 MHz;
- The procedure is repeated three times before the SPS accelerates the bunches to the final energy of 177 GeV/u.

Taking into account the expected losses in the chain, the nominal intensity the LIAF will deliver to fixed-target experiments will be 4×10^8 lead ions per SPS cycle of 14.4 s. The overall efficiency (SPS output/source output) is only 1.4%.

The LHC injection scheme

A detailed analysis of the bunch cog-wheeling in the injector chain led to the conclusion that the optimum bunch separation compatible with all machines was about 40 m corresponding to 134.7 ns at the LHC collision energy.

The LIAF chain working with direct bunch-to-bucket transfer can only provide a bunch population of 3.4×10^6 ions per bunch, a factor 30 lower than the number of ions specified above for optimum LHC luminosity, leading to a luminosity reduced by a factor of 1000.

Several schemes were considered [22] to reach LHC requirements. The basic idea [23] of the one selected is to use LEAR as an accumulation ring to accumulate 20 linac3 batches during one PS cycle, making extensive use of the powerful electron-cooling system. The injector chain is then modified (see Fig. 34) as follows:

- The lead linac delivers a 60 μs, 22 μA pulse of Pb^{53+} at 4.2 MeV/u within a normalized emittance of 0.25 μm and a momentum spread of 1×10^{-3}. The pulse rate is 10 Hz;
- The pulse is injected in LEAR via existing channels using multiturn injection (efficiency 50%). This accumulated beam is then cooled in LEAR in 0.1 s using electron cooling until a new linac pulse can be accepted. After the accumulation of 20 such batches the beam is captured on harmonic number 4. The beam contains 1.2×10^9 ions captured in four buckets with normalized transverse emittances $\epsilon_x = 1.0$ μm and $\epsilon_y = 0.5$ μm. The four bunches are then accelerated to 14.8 MeV/u and transferred directly into the PS without passing through the PSB;

- The PS, tuned to harmonic number 32, receives the LEAR bunches by direct bunch-to-bucket transfer and accelerates the bunches to a flat top of 258 MeV/u. This rapid acceleration is required in order to limit the losses due to the residual gas to the already large figure of 30–40%. The spacing between bunches is then about 20 m;

- The correct bunch spacing is achieved by a stepwise change of the harmonic number on the PS flat top, successively $h = 28$, 24, 20 and finally 16. The four consecutive bunches occupy a quarter of the PS circumference. After a controlled blow-up of their longitudinal emittance to avoid excessive intrabeam scattering blow-up, the four bunches are accelerated in the PS to a momentum of 3.9 GeV/c/u;

- A bunch compression operation reduces their length to 4 ns, compatible with the SPS 200 MHz RF bucket, and the bunches are transferred to the SPS;

- The SPS receives four bunches, with 1.6×10^8 ions per bunch. Thirty-two such batches are successively transferred into the SPS and stored in succession, leaving a gap equivalent to one empty bunch in order to accommodate the risetime of the SPS injection kicker. These bunches are then accelerated using a fixed frequency RF system;

- Three such SPS batches, separated by five empty bunch places for the LHC injection kicker risetime, are transferred to the LHC followed by a fourth SPS batch containing only 28 PS batches in order to leave room for the LHC beam-dump extraction kickers' risetime. If b denotes an occupied bunch place and e an empty one the LHC circumference contains:

  $$3 \times (32 \times (4b + 1e) + 5e) + 28 \times (4b + 1e) + 25e\ ,$$

  that is 496 bunches in 660 bunch places.

The injector cycle uses 124 PS cycles for a total filling time of 8 min per LHC ring.

Hardware in the injectors

- The ECR source and linac must be upgraded to 10 Hz.

- The requirement to reduce the beam emittances by electron cooling in LEAR in less than 100 ms imposes a major upgrade. At present the cooling time of antiprotons is several seconds, but fortunately it scales like Q^2/A. An R&D programme including a high-perveance gun and some adaptation of the LEAR lattice is required. Part of it is already under way.

- The transfer scheme between machines is indicated in Fig. 34. The same line will be used to transfer ions from the linac into LEAR and from LEAR to the PS. This implies polarity changes of the line every cycle of 3.6 s. Some magnets will have to be changed to laminated magnets. The injection/extraction equipment will have to be upgraded and rearranged.

- Power converters must be adapted to obtain the necessary fast acceleration in LEAR and polarity reversal in the transfer line.

- Several improvements to beam diagnostics, dampers and controls are required.
- No major improvements are required in the PS and SPS which are already adapted to LIAF specifications.
- If, by the time ions are requested, LEAR is still involved in antiproton physics, a dedicated accumulator–cooler ring would have to be built, with a better performance potential, but at a much higher cost.

15.3 The case of light ions

The use of the LHC for collisions of lighter ions, only recently investigated, presents significantly different characteristics from all points of view: nuclear effects are less pronounced and limitations come mainly from IBS; the injectors would probably require a different, more elaborate scheme; a higher luminosity in LHC would become possible.

Annex I

Parameter lists

Table 23: The LHC list of parameters

Ring parameters			
Circumference	$2\pi R$	m	26658.87
Revolution frequency ($\beta = 1$)	$f_{\rm rev}$	kHz	11.24551
Revolution period	$T_{\rm rev}$	μs	88.924
Dipole bending radius	ρ	m	2700.27
Orbit separation		mm	180
Free space for detectors		m	32
Cell length		m	102.042
Number of cells per arc			24
Horizontal tune	$Q_{\rm h}$		68.28
Vertical tune	$Q_{\rm v}$		68.31
Phase advance per cell	ϕ_β	°	90
Max. beta value	$\beta_{\rm max}$	m	172.8
Min. beta value	$\beta_{\rm min}$	m	30.3
Max. dipersion	$D_{\rm max}$	m	2.02
Min Dispersion	$D_{\rm min}$	m	0.98
Ramping time		s	1200
RF frequency	$f_{\rm rf}$	MHz	400.8
Harmonic number	$h_{\rm rf}$		35640
Number of single-cell cavities			8
Number of klystrons			8
Cavity R/Q		Ω	44
External Q	$Q_{\rm ext}$		6.6×10^4
Momentum compaction factor	α_p		2.94×10^{-4}

Table 24: The LHC list of parameters: proton–proton collider design parameters

Proton collider
(Design parameters)

Energy	E	TeV	7.0
Dipole field	B	T	8.65
Luminosity	$\mathcal{L}$	$\mathrm{cm}^{-2}\mathrm{s}^{-1}$	10^{34}
Beam–beam parameter	ξ		0.0032
Total beam–beam tune spread*			0.01
Injection energy	E_i	GeV	450
Circulating current/beam	I_beam	A	0.53
Number of bunches	k_b		2835
Harmonic number	h_rf		35640
Bunch spacing	τ_b	ns	25
Particles per bunch	n_b		1×10^{11}
Stored beam energy	E_s	MJ	332
Normalized transverse emittance: $(\beta\gamma)\sigma^2/\beta$	ϵ^*	mrad	3.75×10^{-6}
R.m.s bunch length	σ_s	m	0.075
Collisions			
Beta-value at I.P.	β^*	m	0.5
R.m.s. beam radius at I.P.	σ^*	μm	16
R.m.s. divergence at I.P.	σ'^*	μrad	32
Luminosity per bunch collision	$\mathcal{L}_\mathrm{b}$	cm^{-2}	3.2×10^{26}
Crossing angle	ϕ	μrad	200
Number of events per crossing	n_e		19
Beam lifetime	τ_b	h	22
Luminosity lifetime	τ_l	h	10
Nuclear events per IP per s	n_nucl	s^{-1}	1.0×10^9
Inelastic events per IP per s	n_inel	s^{-1}	6.0×10^8
Elastic events per IP per s	n_elst	s^{-1}	4.0×10^8
Synchrotron radiation (top energy)			
Energy loss per turn	U_0	keV	6.9
Critical photon energy	u_c	eV	45.6
Total radiated power per beam	P_s	kW	3.7
Power per unit length for two beams	P_m	Wm^{-1}	0.44
Transverse damping time	τ_x	h	24.9
Longitudinal damping time	τ_s	h	12.5

*With two high-luminosity IP + distant crossings.

Table 25: The LHC list of parameters: proton–proton collider design parameters (cont.)

Proton collider (Design parameters cont.)			Injection	Collision
Intrabeam scattering				
Horizontal growth time	τ_h	h	45	100
Longitudinal growth time	τ_p	h	33	60
Radiofrequency				
RF voltage	V_{rf}	MV	8	16
RF power (peak)	P_{rf}	MW	1.65	1
Beam-loading-induced detuning		kHz	13.7	8.6
Synchrotron tune	Q_s		5.5×10^{-3}	1.9×10^{-3}
Bunch area (2σ)	A_b	eV/s	1	2.5
Bucket area	A_{rf}	eV/s	1.46	8.7
Bucket half-height	$\Delta p/p$		1×10^{-3}	3.6×10^{-4}
R.m.s bunch length	σ_s	m	0.13	7.5×10^{-2}
R.m.s energy spread	σ_e		4.5×10^{-4}	1.0×10^{-4}

Table 26: The LHC list of parameters: lead-ion collider (one I.P.)

Lead-ion collider

Atomic number of lead	Z		82
Number of nucleons in lead ion	A		208
Lead rest mass	E_{208}	GeV/c^2	193.73
Maximum lead-ion energy		TeV	574
Maximum γ			2963
Injection γ			190.5
LHC filling time (per ring)	τ_{fill}	min	8
Collision centre-of-mass energy	E_{max}	TeV	1148
Collision dipole field	B_{max}	T	8.65
Luminosity	$\mathcal{L}$	$\text{cm}^{-2}\text{s}^{-1}$	1.8×10^{27}
Number of bunches	k_{b}		496
Number of bunch places			660
Bunch spacing		ns	134.7
Number of ions per beam			4.7×10^{10}
Number of ions per bunch			9.4×10^{7}
Ion intensity per beam		mA	6.9
Transverse normalized emittance: $(\beta\gamma)\sigma^2/\beta$	ϵ^*	m	1.5×10^{-6}
Beta at IP	β^*	m	0.5
R.m.s. beam radius at IP	σ^*	μm	15
Crossing angle		μrad	≤ 100
Longitudinal emittance/charge (inj.)		eV/s	2
Longitudinal emittance/charge (coll.)		eV/s	5
R.m.s. bunch length at collision	σ_s	cm	12.5
R.m.s. energy spread at collision	σ_E/E		1.3×10^{-4}
RF voltage (200 MHz)		MV	16
Emittance growth time (inj.)	τ_{h}	h	14.5
Emittance growth time (coll.)	τ_{h}	h	22
Luminosity half-life*		h	10

*Weizsacker–Williams effect + electron capture.

Table 27: The LHC injectors' main parameters

		RFQ	Linac2	PSB	PS	SPS
Design parameters						
Energy (kinetic)	GeV	0.00075	0.05	1.4	25	450
Repetition time	s	1.2	1.2	1.2	3.6	16.8
Number of pulses[1]		1	1	2	3	2×12
Intensity	mA	200	$\leq$180			
Pulse length	μs	25	25			
Particles/pulse	10^{12}			4.3	8.4	24.3
Particles/bunch	10^{11}				1.0	1.0
Number of bunches/pulse					84	243
Bunch spacing	ns				25	25
Transverse emittance[2]	μm	0.5	1.2	2.5	3.0	3.5[3]
Longitudinal emittance 2σ	eV/s				0.7	1.0
RF systems parameters						
Main system frequency	MHz	200	200	0.6–1.7	3.5–7.6[4]	200
harmonic number				1	8/16	$\sim$ 4620
Second harmonic	MHz			1.2–3.4		
LHC bunch generation	MHz				40	
harmonic number					84	
PS/SPS transfer matching	MHz				40, 80	80
SPS/LHC transfer matching	MHz					400

[1] To fill the downstream machine.

[2] Normalized emittance: $\epsilon^* = (\beta\gamma)\sigma^2/\beta$.

[3] Emittance reduced during commissioning to 0.7 μm for 1.7×10^{10} protons per bunch.

[4] Including a bunch-splitting operation on a 3.5 Gev/c flat top.

Annex II

Equipment names and lists

Service [illegible]

Table 28: Equipment names for LHC magnets

Equipment name	Description
MB	Main bending magnet
MBS	Main bending magnet Short
MQF(D)	Main quadrupole focusing (defocusing)[1]
MSC	Magnet sextupole corrector (spool piece)
MDC	Magnet decapole corrector (spool piece)
MSBH(V)	Combined sextupole and dipole H. (resp. V)
MOQF(D)	Combined octupole and quadrupole
MBSH	Separator dipole superconducting (D1)
MBSW	Separator dipole normal-conducting (D2)
MBSD	Separator dipole normal-conducting (dump insertion)
MQIA	Insertion quad single-bore (6.1 m)
MQIB	Insertion quad single-bore (6.9 m)
MQTA	Insertion quad (3.7 m)
MQTB	Insertion quad (4.6 m)
MQTC	Insertion quad (8.0 m, 1.9 K)
MQTD	Insertion quad (8.0 m, 4.7 K)
MQEA	Insertion quad enlarged (4.6 m, 4.7 K)
MQEB	Insertion quad enlarged (6.1 m, 4.7 K)
MQEC	Insertion quad enlarged (6.9 m, 4.7 K)
MQED	Insertion quad enlarged (4.6 m, 1.9 K)
MQS	Magnet quadrupole skew
MQSA	Magnet quadrupole skew enlarged (1.9 K)
MQSB	Magnet quadrupole skew enlarged (4.7 K)
MBHA(V)	Magnet dipole corrector (1.9 K) H. (resp. V)
MBHC(V)	Magnet dipole corrector enlarged (1.9 K) H (resp. V)
MBHD(V)	Magnet dipole corrector enlarged (4.7 K) H (resp. V)
MBHW(V)	Magnet dipole corrector warm H (resp. V)
MBHI(V)	Magnet dipole corrector inner triplet H (resp. V)

[1] The F(focusing) or D or H (horizontal) or V always apply to beam I.

Table 29: Equipment names for LHC (second table)

Equipment name	Description
BPH(V)	Beam-position monitor H (resp. V) (arc)
BPC	Beam-pos. monitor combined H and V (insertions)
BPCE	Beam-pos. mon. H and V, enlarged (insertions)
BPCD	Beam-pos. mon. H and V, bidirectional (inner triplet)
BWC	Wall-current monitor
BCT	Beam-current transformer
BSH	Horizontal Schottky monitor
BSV	Vertical Schottky monitor
BSL	Longitudinal Schottky monitor
BRL	Synchrotron radiation monitor (low energy)
BRT	Synchrotron radiation monitor (top energy)
BGH(V)	SEM grid horizontal (vertical)
BFH(V)	Wire scanner (flying wire) horizontal (vertical)
ACCI	Copper cavities for ion acceleration
ACSP	Superconducting cavities for proton acceleration
ADT	Transverse damper
ADL	Longitudinal damper
ABW	Wideband pick-up for RF control
ABD	Beam pick-up for dampers and RF control
QFA	Cryofeed box for the arcs
QFI	Cryofeed box for the insertion
QFJ	Cryofeed box for the insertion (4.5 K)
QBM	Cryobox in mid-arcs for octant separation
QSA	Cryogenic service module
QSB	Cryogenic service module (4.5 K)
QWT	Cold-warm transition
QWTE	Cold-warm transition enlarged
TDN	Beam stopper (dump) for neutral secondaries
TDI	Beam stopper for injected protons
TCP	Primary collimator in cleaning
TCA	30° secondary collimator in cleaning
TCB	90° secondary collimator in cleaning
TCC	150° secondary collimator in cleaning
TDS	Beam absorber for secondaries (inner triplet)
VVP	Vacuum valve and pumping station
VVPE	Vacuum valve and pumping station enlarged

Table 30: Bending magnet parameters

Equipment Name	 Type	Field (T)	Length (m)	Inner coil Φ (mm)	Temp. (K)	Number
MB	Main dipole	8.65	13.145	56	1.9	1280
MBS	Dipole short	8.65	8.793	56	1.9	16
MBSH	Separ. S.C. (D1)	5.2	9.0	75	4.7	8
MBSW	Separ. dipole (D2)	1.8	5.2	50 × 240	warm	76
MBSD	Separ. (D2 SS5)	1.5	5.5	50 × 260	warm	6

Table 31: Quadrupole parameters

Equipment Name	 Type	Gradient (T/m)	Length (m)	Inner coil Φ (mm)	Temp. (K)	Number
MQF(D)	Main quad	220	3.05	56	1.9	376
MQIA*	Inner triplet	220	6.1	70	1.9	16
MQIB*	Inner triplet	226	6.9	70	1.9	16
MQTA	Normal	220	3.7	56	1.9	42
MQTB	quads	220	4.6	56	1.9	22
MQTC	of	211	8.0	56	1.9	42
MQTD	insertions	165	8.0	56	4.7	8
MQEA	Enlarged	185	4.6	70	4.7	4
MQEB	quads	190	6.1	70	4.7	10
MQEC	of	195	6.9	70	4.7	2
MQED	insertions	170	4.6	70	1.9	4

* Single-aperture quadrupoles.

Table 32: Corrector magnet parameters

Equipment Name	 Type	Field[1] (T & m)	Length (m)	Inner coil Φ (mm)	Temp. (K)	Number	Comments
MSC	Sextupole	1.9×10^3	0.1	56	1.9	2592	'Spool piece'
MDC	Decapole	1.9×10^6	0.028	56	1.9	2592	'Spool piece'
MSBH(V)	Dipole	1.5	1.07	56	1.9	768	Combined
	Sextupole	1.5×10^3	1.14	56	1.9		elements
MOQF(D)	Quadrupole	120	0.72	56	1.9	768	Combined
	Octupole	1.7×10^4	0.72	56	1.9		elements
MQS	Skew quad.	120	0.72	56	1.9	180	
MQSA	Skew quad.	75	1.15	70	1.9	4	
MQSB	Skew quad.	75	1.15	70	4.7	8	
MBHI(V)	Dipole	4.50	0.38	70	1.9	36	Inner triplet
MBHA(V)	Dipole	3.85	0.65	56	1.9	256	
MBHC (V)	Dipole	3.30	0.76	70	1.9	4	
MBHD (V)	Dipole	1.0	1.5	70	4.7	28	
MBHW(V)	Dipole	1.0	1.5		warm	40	

[1] The 'field' value is B_n from ($B_y = B_n x^{n-1}$), ($n = 2$ Quad., $n = 3$ Sext., $n = 4$ Oct.), units tesla and metre.

Table 33: Power converters in low-beta insertions

Magnet	No. of circuits per 1/2 octant	Max. current (kA)	Max. voltage (V)	Converter type
Arc cryofeed box				
Main bends and quads	1	12	88	1
Sextupoles (Spool pieces)	1	±0.5	19	7
Decapoles (Spool pieces)	1	±0.5	19	7
Tuning quads	4	±1.6	11	6
Lattice sextupoles	4	±0.5	12	9
Lattice octupoles	4	±0.2	12	9
Disp. supp. Q7	1	10	6	2
Disp. supp. Q8 to Q10	1	10	6	2
Disp. supp. Q8 trim	1	0.6	6	8
Disp. supp. Q10 trim	1	0.6	6	8
Outer triplet Q4	1	10	6	2
Outer triplet Q5	1	10	6	2
Outer triplet Q6	1	10	6	2
Skew quads	8	±1.6	11	6
Arc direct feed				
Closed-orbit correctors	48	±0.030	110	11
Dipole correctors	16	±0.05	32	10
Inner triplet cryofeed box				
Inner triplet Q1 to Q3	1	5	7	4
Inner triplet Q1 trim	1	0.6	6	8
Inner triplet Q3 trim	1	0.6	6	8
D1 separator magnet	1	8	8	3
Inner triplet direct feed				
D2 separator magnet	1	5	68	5
Dipole correctors (cold)	4	±0.05	32	10
Dipole correctors (warm)	4	±0.05	32	10

Table 34: Power converters in cleaning insertion

Magnet	No. of circuits per 1/2 octant	Max. current (kA)	Max. voltage (V)	Converter type
Cryofeed box				
Main bends and quads	1	12	88	1
Sextupoles (Spool pieces)	1	±0.5	19	7
Decapoles (Spool pieces)	1	±0.5	19	7
Tuning quads	4	±1.6	11	6
Lattice sextupoles	4	±0.5	12	9
Lattice octupoles	4	±0.2	12	9
Disp. supp. Q8 to Q10	1	10	6	2
Disp. supp. Q8 trim	1	0.6	6	8
Disp. supp. Q10 trim	1	0.6	6	8
Outer triplet Q4	1	5	6	4
Outer triplet Q5 to Q7	1	10	6	2
Outer triplet Q5 trim	1	0.6	6	8
Outer triplet Q7 trim	1	0.6	6	8
Skew quads	8	±1.6	11	6
Inner triplet Q1 to Q3	1	5	7	4
Inner triplet Q1 trim	1	0.6	6	8
Inner triplet Q3 trim	1	0.6	6	8
Direct feed				
Closed-orbit correctors	48	±0.03	110	11
Dipole correctors	24	±0.05	32	10
D2 separator magnet	1	5	105	12

Table 35: Power converters in beam-dump insertion

Magnet	No. of circuits per 1/2 octant	Max. current (kA)	Max. voltage (V)	Converter type
Arc cryofeed box				
Main bends and quads	1	12	88	1
Sextupoles (Spool pieces)	1	±0.5	19	7
Decapoles (Spool pieces)	1	±0.5	19	7
Tuning quads	4	±1.6	11	6
Lattice sextupoles	4	±0.5	12	9
Lattice octupoles	4	±0.2	12	9
Disp. supp. Q8 to Q10	1	10	6	2
Disp. supp. Q8 trim	1	0.6	6	8
Disp. supp. Q10 trim	1	0.6	6	8
Outer doublet Q6	1	5	7	4
Outer doublet Q5-Q7	1	10	6	2
Outer doublet Q5 trim	1	0.6	6	8
Skew quads	8	±1.6	11	6
Arc direct feed				
Closed-orbit correctors	48	±0.03	110	11
Dipole correctors	16	±0.05	32	10
Inner doublet cryofeed boxes				
Inner doublet Q3-Q4	1	5	7	4
Inner doublet Q3 trim	1	0.6	6	8
Inner doublet direct feed				
D2 separator magnet	1	5	68	5
Dipole correctors (warm)	4	±0.05	32	10

Table 36: Power converters in simple insertions

Magnet	No. of circuits per 1/2 octant	Max. current (kA)	Max. voltage (V)	Converter type
Arc cryofeed box				
Main bends and quads	1	12	88	1
Sextupoles (Spool pieces)	1	±0.5	19	7
Decapoles (Spool pieces)	1	±0.5	19	7
Tuning quads	4	±1.6	11	6
Lattice sextupoles	4	±0.5	12	9
Lattice octupoles	4	±0.2	12	9
Disp. supp. Q8 to Q10	1	10	6	2
Disp. supp. Q8 trim	1	0.6	6	8
Disp. supp. Q10 trim	1	0.6	6	8
Outer triplet Q4	1	10	6	2
Outer triplet Q5-Q7	1	10	6	2
Outer triplet Q5 trim	1	0.6	6	8
Outer triplet Q7 trim	1	0.6	6	8
Skew quads	8	±1.6	11	6
Arc direct feed				
Closed-orbit correctors	48	±0.03	110	11
Dipole correctors	16	±0.05	32	10
Inner doublet cryofeed box				
Inner doublet Q2-Q3	1	5	7	4
Inner doublet Q3 trim	1	0.6	6	8
Inner triplet direct feed				
D2 separator magnet	1	5	68	5
Dipole correctors (cold)	4	±0.05	32	10
Dipole correctors (warm)	4	±0.05	32	10

Table 37: Power converter characteristics

Type	Current (kA)	Voltage (V)		Power (kW)		Number of units
	Coast	Coast	Peak	Coast	Peak	
1	12	8	88	96	1060	16
2	10	5	6	50	60	60
3	8	6	8	48	60	8
4	5	6	7	30	33	20
5	5	68	68	340	340	14
6	±1.6	8	11	13	18	192
7	±0.5	8	19	6	13	32
8	0.6	6	6	4	4	72
9	±0.5	8	12	4	6	128
10	±0.05	12	32	1	2	376
11	±0.03	100	100	3	3	768
12	5	105	105	525	525	2

Annex III

Civil engineering views

These views describe the civil engineering modifications (thick lines) of the existing LEP installations (thin lines) for the LHC collider. Additional modifications will be required for experimental halls.

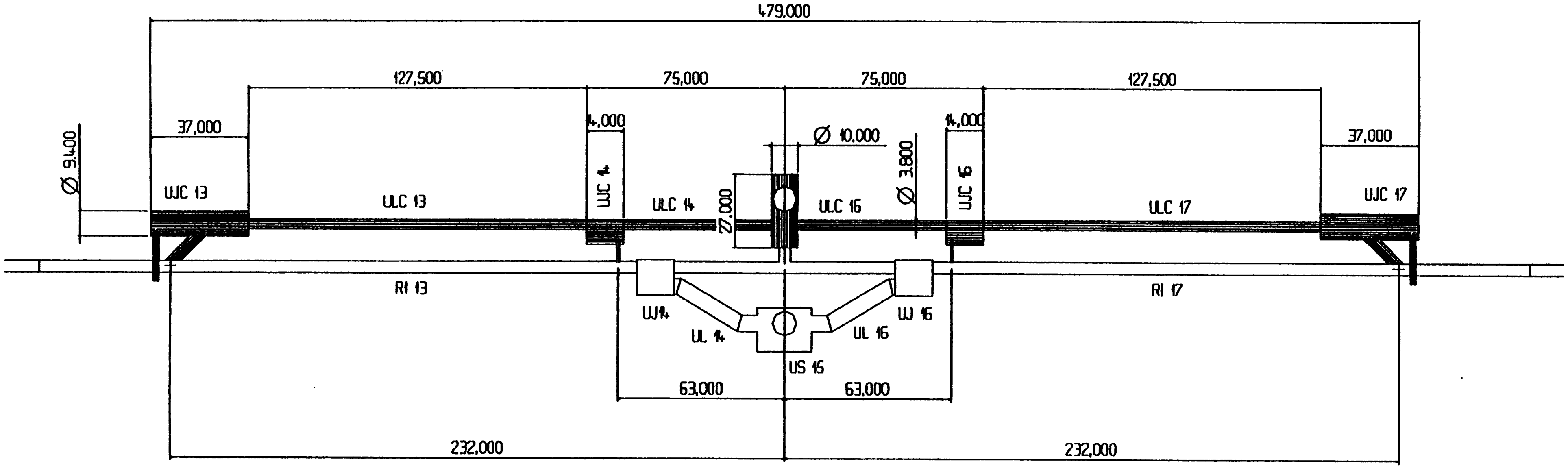

SS1

ADDITIONAL CIVIL ENGINEERING WORKS FOR LHC AT POINT 1
(DARK AREAS)

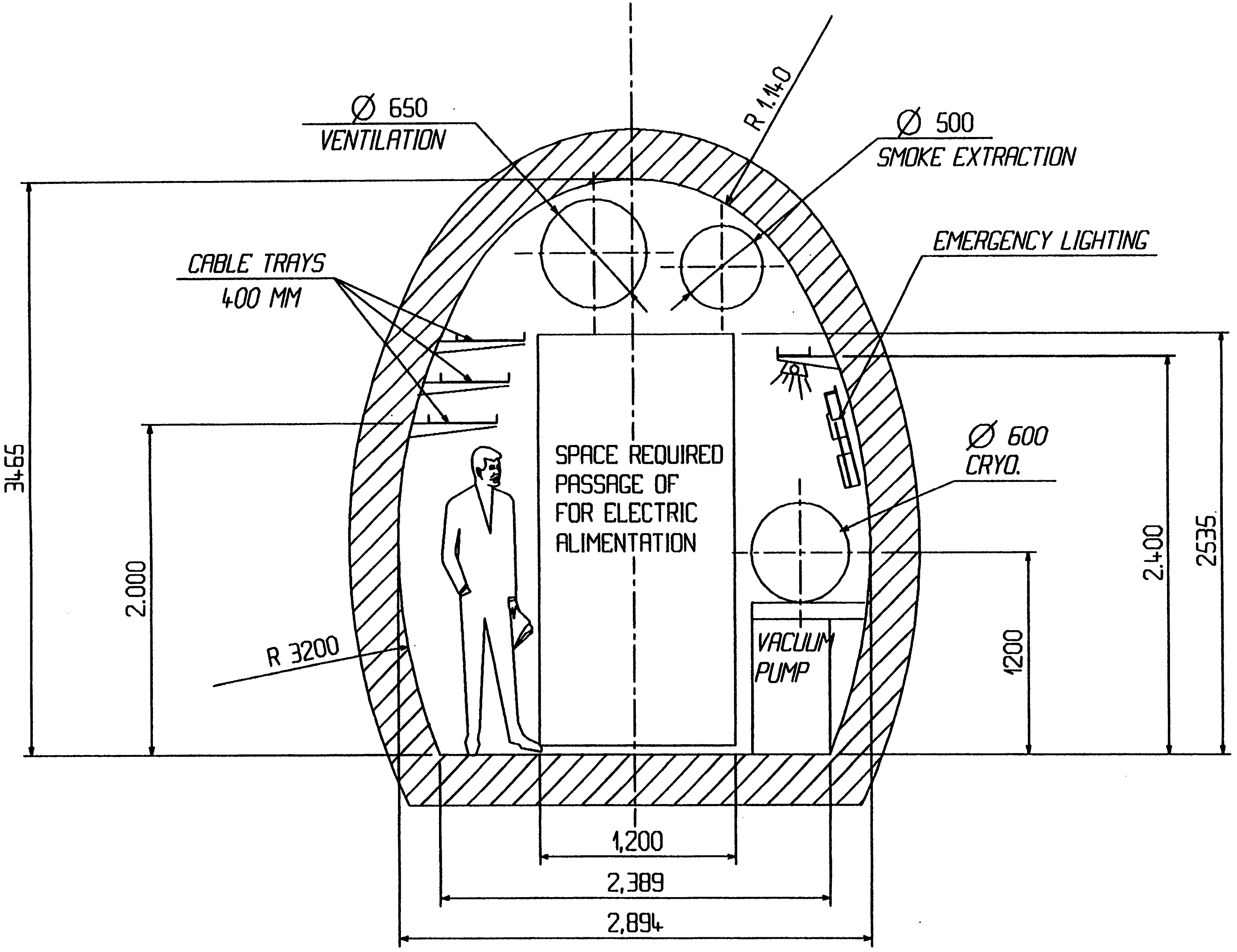

SS1

CROSS SECTION OF LIAISON GALLERY ULC 13-17
(POINT 1 NEW SERVICE CAVERNS)

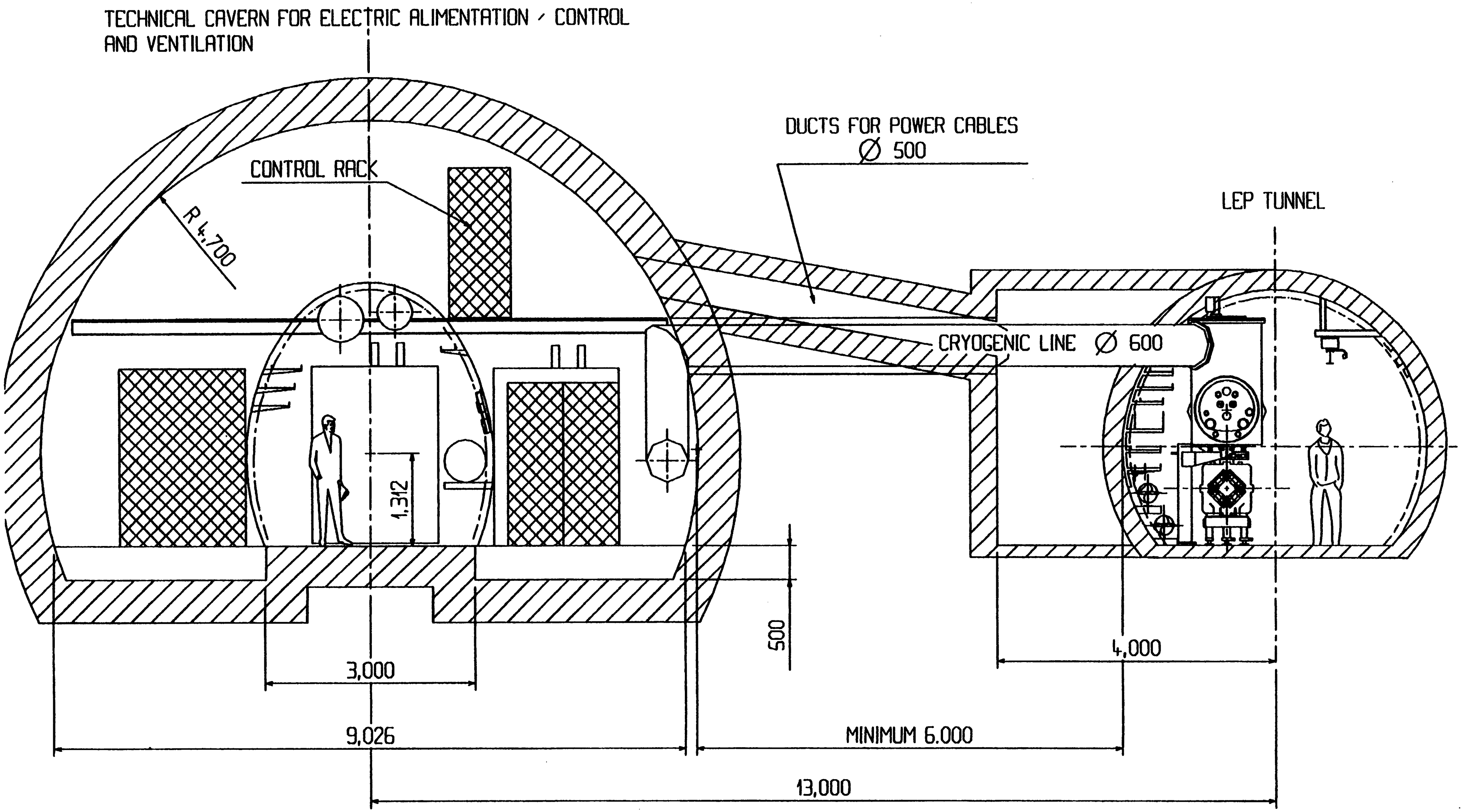

SS1

CROSS SECTION OF TECHNICAL CAVERN UJC 13-17

(NEW TECHNICAL CAVERNS FOR PC & CRYO SERVICES)

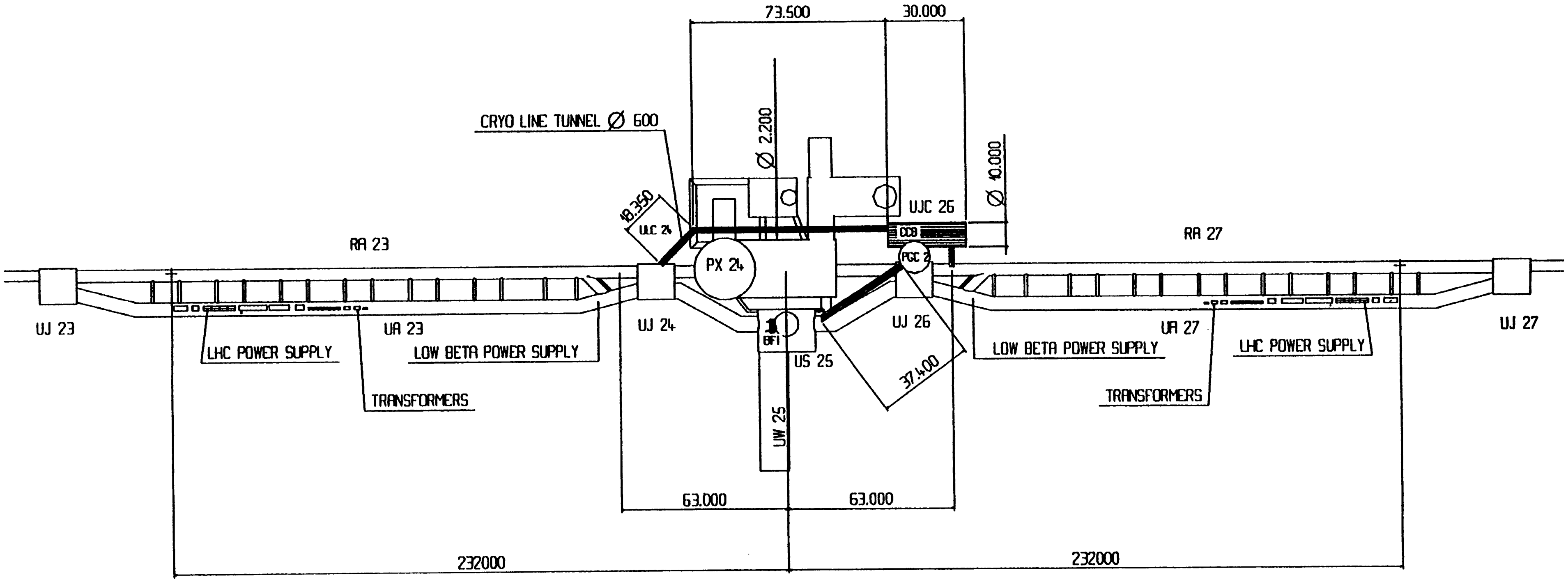

SS2

ADDITIONAL CIVIL ENGINEERING WORKS FOR LHC POINT 2

(DARK AREAS)

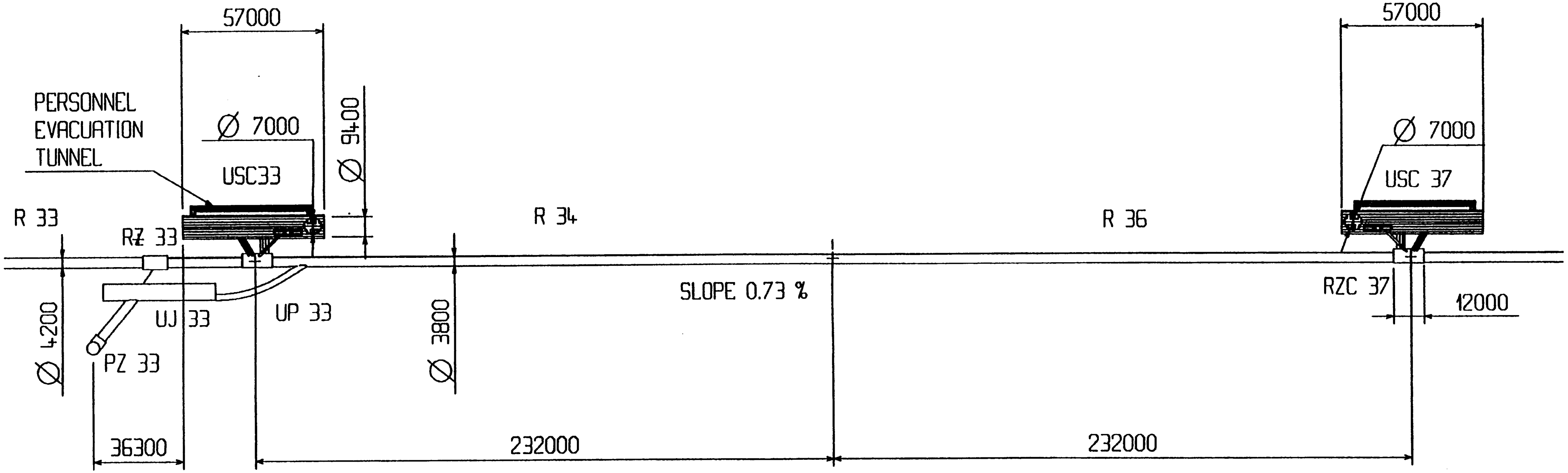

SS3

ADDITIONAL CIVIL ENGINEERING WORKS FOR LHC POINT 3

(DARK AREAS)

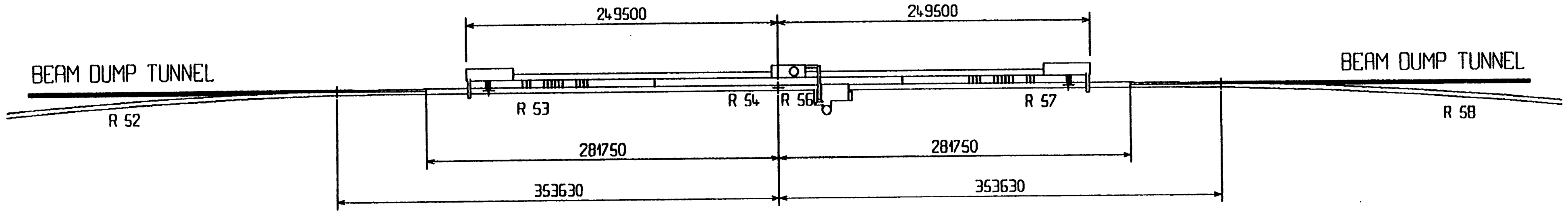

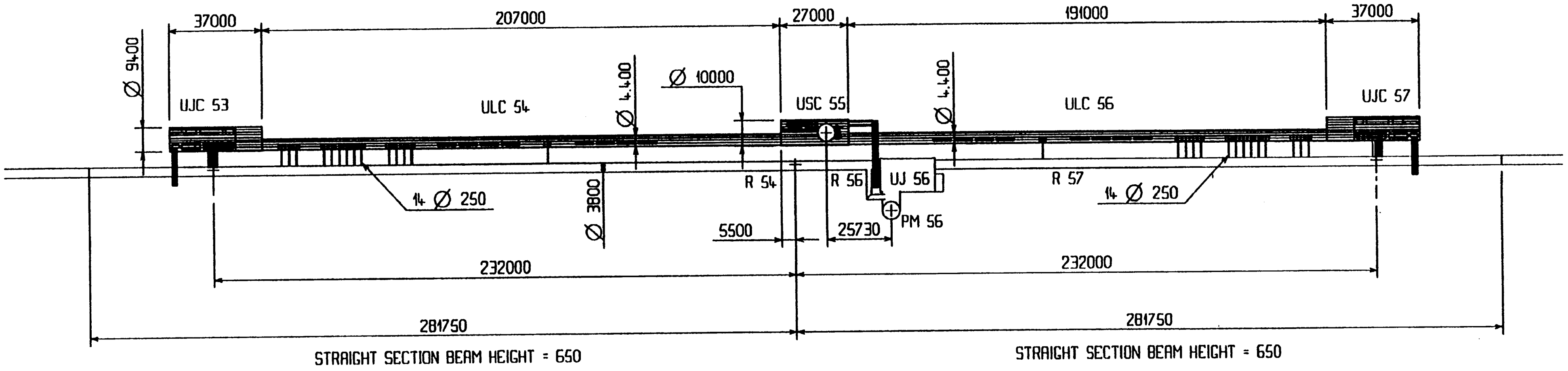

SS5

ADDITIONAL CIVIL ENGINEERING WORKS FOR LHC POINT 5

[DARK AREAS]

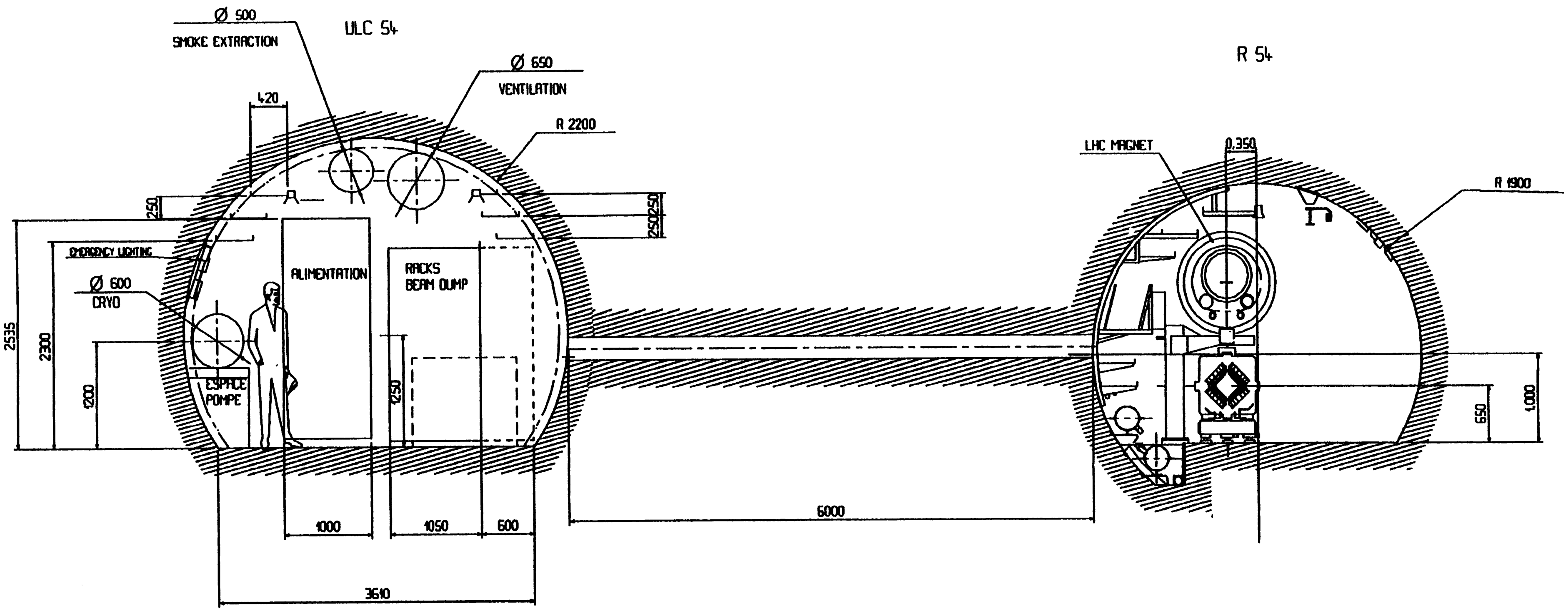

SS5

CROSS SECTION OF GALLERY ULC 54-56 AND LEP TUNNEL

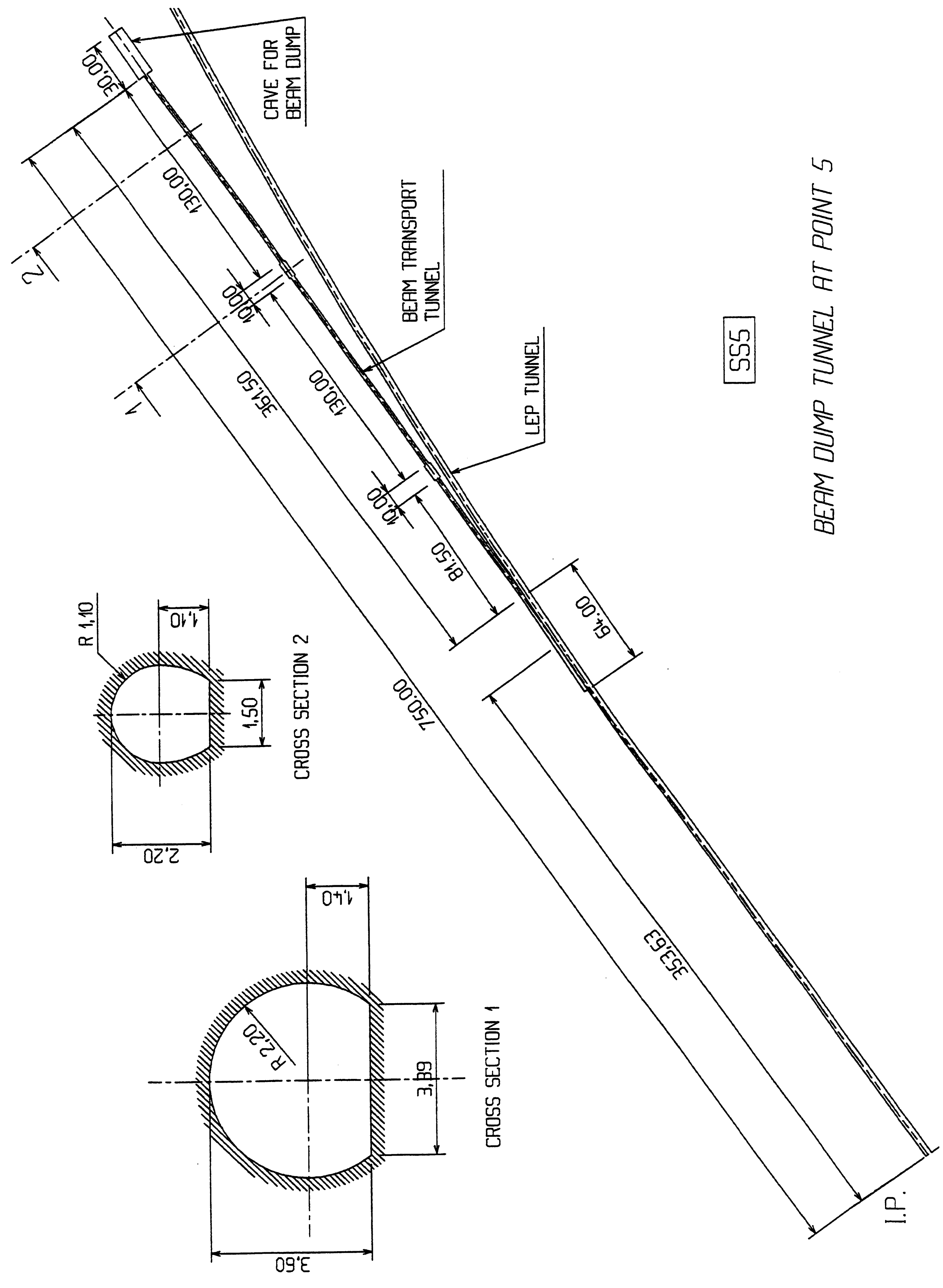

BEAM DUMP TUNNEL AT POINT 5

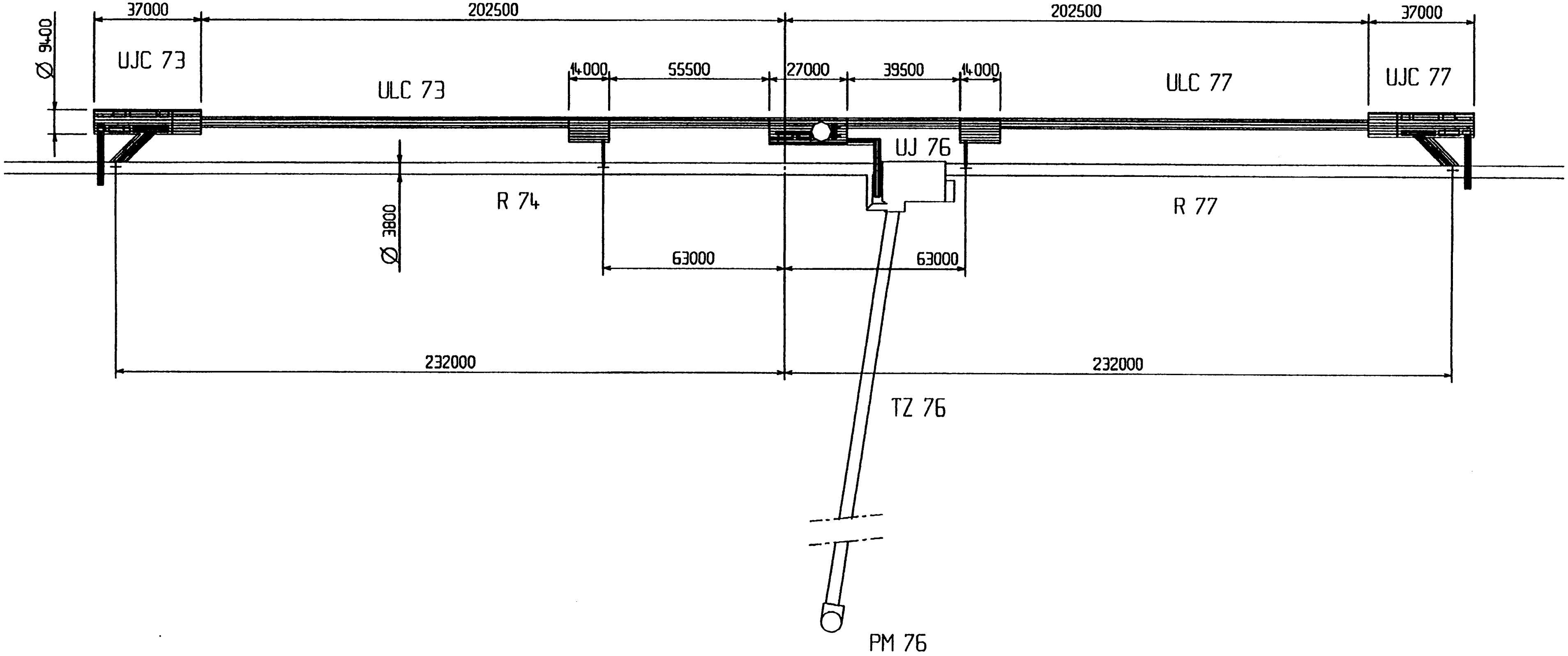

SS7

ADDITIONAL CIVIL ENGINEERING WORKS FOR LHC AT POINT 7

(DARK AREAS)

Part III

Superconducting technology

1 Magnets

1.1 Superconducting technology for accelerator magnets

There are two large operational accelerators based on superconducting magnets, the Tevatron (Fermilab) and HERA (DESY). Both make use of classical NbTi superconductors cooled with normal liquid helium at a temperature slightly above 4.2 K, and their operational fields are relatively low (~4 T for the Tevatron and 4.7 T for HERA). The HERA magnets were manufactured in industry.

More recently the SSC decided to adopt a magnet design very similar to that of HERA but pushed to a high field (6.6 T), probably an upper limit with NbTi at 4.2 K. A number of magnets have been manufactured and tested successfully.

For the LHC, to be installed in the existing LEP tunnel, it is attractive to push the field significantly higher, still retaining the well-proven fabrication methods of cables and coils made of NbTi superconductors. The only way of obtaining fields of 9 T or above is to cool the magnets at a much lower temperature ($\leq$ 2 K). This technique has been applied successfully to the French Tokamak TORESUPRA in operation at Cadarache. Below 2.17 K, helium takes the so-called superfluid state, with much lower viscosity and much greater heat transmission capacity than normal helium. These properties can be used for the design of the cooling scheme, and in particular permit the drastic reduction of the helium flow through magnets.

On the other hand, the enthalpy of all metallic parts and in particular of the superconducting cables is reduced by almost an order of magnitude between 4.2 K and 1.8 K, with consequent faster temperature rise for a given deposit of energy. This feature calls for particular care in limiting conductor motion. It should be noted that the electromagnetic forces on the conductor increase with B^2 and so does the stored electromagnetic energy, calling for stronger force-retaining structures and more elaborate quench protection systems than for previous projects.

Proton–proton colliders require two separate beam channels with fields equal in strength but of opposite directions. In the case of the SSC this is obtained with two completely separate magnet systems in separate cryostats.

For the LHC, the more compact 'two-in-one' design is adopted whereby the two beam channels and their corresponding sets of coils are inserted in a unique structure and in a single cryostat.

In summary, the novel features of the LHC magnets, namely high forces and stored energy, lower temperatures and 'two-in-one' structure justified the undertaking of a substantial R&D programme, in close cooperation with industry, for both the magnets themselves and the cryogenic system.

1.2 Results of the R&D programme

1.2.1 The cables

Satisfactory and economical magnets depend on superconducting cables showing well-defined properties, the main ones being (specifically for the LHC):

1. A current density as high as possible.

2. Superconducting NbTi filaments of about 6 μm, the lowest technical limit, in order to minimize persistent current effects at low field.
3. Good mechanical properties (stability and ease of winding over small radii).
4. Uniformity of properties during production.
5. Possibility of making wide cables (up to 17 mm instead of 10–12 mm as previously).

The development of such wires and cables was entrusted to five European manufacturers from 1986 onwards, and cables satisfying the main criteria have been produced by all of them [24] (Table 38).

The total quantity produced is now 14 tons, a very significant amount (for reference, the total for HERA was ~100 tons, and for RHIC is 45 tons). These cables have been used for ten magnet models and for the 10-metre-long coils which are being inserted in the seven prototypes.

Table 38: Characteristics of developed LHC dipole strands

Firm	Strand diameter (mm)	Number of filaments	Filament diameter (μm)	J_c (A/mm^2) at 10^{-14} Ω m	
				6 T 4.2 K	8 T 4.2 K
1	1.29	21780	5.4	2104	1087
1	0.84	9438	5.1	2195	1032
2	0.84	9438	5.1	2113	1060
3	1.29	28158	4.7	–	1025
4	1.29	27954	4.8	1885	937
4	0.84	10164	5.0	1970	992
5	1.29		7.8	–	1005
5	0.84		7.8	2185	–

1.2.2 The models

As the fabrication of the 2000 twin main magnetic elements and of the 7000 single-aperture corrector magnets will be carried out in industry, it was decided to undertake their development, including models (full cross-section, 1.3 metre long), in close collaboration with interested firms.

About ten models of the main dipoles (see Tables 39 and 40), the most important elements of the machine, were made in industry and tested at CERN [25]–[30]. The results can be summarized as follows:

- At 4.2 K the maximum field of 7.9 T, corresponding to the current-carrying capability of the cables as measured in short samples, was reached after one or few training quenches, confirming the soundness of the design according to the experience of previous projects.

- At 1.8–2 K the ultimate field of 9.8 T was obtained but in general after a relatively large number of training quenches above 9.5 T. The analysis of the results showed that most intermediate quenches occurred at the ends, where the field is lower than in the central part, but where it is more difficult to prevent cable movements.

- A recent model using industrially made coils basically identical to all other ones, but with more compact ends, and made with better performing last generation cables, was assembled at CERN, using a modified mechanical structure. This model exhibited improved behaviour: it reached 9.3 T in two quenches, 9.5 T in five quenches, and finally attained the record field of **10.5 T**. After full training and subsequent complete warm-up and cool-down all further quenches were above 9.75 T [31, 32]. In this magnet all training quenches started in the ends or near the transition between inner and outer coil layers. This makes us confident that long magnets will behave as short models. If these results were to be confirmed in the long prototype magnets, their operational field could be about 9 T, with a margin of about 10% with respect to the maximum field.

Since industry is engaged in the fabrication of seven long magnets, design optimization with models (coil ends, insulation, details of the mechanical structure, etc.) is now continuing at CERN.

The programme is the following:

- One model with SSC cables. Aperture ø 56 mm, intra-beam distance 180 mm, overall cold mass diameter 580 mm, $B_{ss} = 9.34$ T;

- One model with the same mechanical structure but cables with optimized strands for the new design (see Sections 1.3.1 and 1.3.2);

- A number of tests for improved cable support in the ramp and splice region and in the coil ends, by using structures of existing models;

- A number of tests for studying mechanical structures, coil/structure interference, alternative insulation systems, etc.

Table 39: Characteristics of LHC magnet models (l = 1.3 m)

Name	Aperture	Inner cable			Outer cable			Collar material	B_{ss}
	ϕ (mm)	Strand No.	Strand ϕ (mm)	Width (mm)	Strand No.	Strand ϕ (mm)	Width (mm)		(T)
Single-aperture models									
8 TM1	50	30	0.84	13	30	0.84	13	Al	9.3
8 TM2	50	30	0.84	13	30	0.84	13	Al	9.3
MSA 1E	50	26	1.29	17	40	0.84	17	Al	10.0
MSA 2 KEK	50	22	1.39	15	37	0.79	15	Mn/Al	10.2
Double-aperture models									
MTA1/E	50	26	1.29	17	40	0.84	17	Al (S)	9.8
MTA1/A	50	26	1.29	17	40	0.84	17	Al (C)	9.8
MTA1/H	50	26	1.29	17	40	0.84	17	Al (C)	10.0
MTA1/JS	50	26	1.29	17	40	0.84	17	Al (C)	10.0
MTA2/KEK	50	22	1.39	15	37	0.79	15	MnAl	10.2
MTA3/CERN*	50	26	1.29	17	40	0.84	17	SS (S)	10.5
MBTRA**	56	30	0.808	12.4	36	0.648	11.7	SS (S)	9.4
MFISC**	56	30	1.10	16.7	38	0.87	16.7	SS (S)	9.9

B_{ss} = Field in the aperture centre at which the conductor placed in the magnet peak-field position reached the short sample limit.

* With industrially-made coils.

** Under construction.

(S): Separate collars; (C): Combined collars.

Al: Aluminium alloy; SS: Austenitic steel; Mn: Mn steel.

Table 40: Performance of LHC magnet models (l = 1.3 m)

Name	B_{ss} (T)	B_0 reached (T)	No. of quenches to pass 9 T	First quench field after thermal cycle
Single-aperture models				
8 TM1	9.3	9.3	3	8.9
8 TM2	9.3	9.4	3	8.9
MSA 1E	10.0	9.7	11	not tested
MSA 2 KEK	10.2	9.8	4	9.5
Double-aperture models				
MTA1/E	9.8	9.0	12	not tested
MTA1/A	9.8	9.7	9	8.3
MTA1/H	10.0	10.0	5	8.9
MTA1/JS	10.0	10.0	10	8.4
MTA2/KEK	10.2	under test		
MTA3/CERN*	10.5	10.5	0	9.7
MBTRA**	9.4	under construction		
MFISC**	9.9	under construction		

B_{ss} = Field in the aperture centre at which the conductor placed in the magnet peak-field position reached the short sample limit.
B_0 = Field in the centre of the aperture.
* With industrially-made coils.
** Under construction.

1.2.3 *Ten-metre-long dipole magnets*

A magnet with a CERN twin structure but coils identical to HERA was built in industry and successfully tested at CEA–Saclay at the nominal temperature of 1.9 K [33]. This magnet, called TAP, had an excellent behaviour since at 4.2 K it reached the maximum field with no quenches and showed exactly the same properties as the single HERA magnets. When cooled down to 1.9 K, it was possible to increase the current from 6600 A to 9500 A thus reaching the conductor short sample limit of 8.3 T. It should be noted that the HERA coils have a much larger aperture (75 mm instead of 56 mm).

Subsequently, the construction of seven higher field (cable width 17 mm), 10 m long magnets was launched in four firms or consortia. All these magnets have the same type of coils, but three slightly different mechanical structures (Table 41).

Table 41: Characteristics of LHC magnet prototypes (l = 10.0 m)

Name	No. of units	Aperture	Inner Cable			Outer Cable			Collar	B_{ss}	B_0 reached
		ø (mm)	Strand (No.)	Strand ø (mm)	Width (mm)	Strand (No.)	Strand ø (mm)	Width (mm)	material	(T)	(T)
Double-aperture prototypes											
TAP	1	75	24	0.84	10	24	0.84	10	Al (C)	8.3	8.3
MTP 1/A	3	50	26	1.29	17	40	0.84	17	Al (C)	10.0	Under construction
MTP 1/N	2	50	26	1.29	17	40	0.84	17	Al (C)	10.0	
MTP 2/AJS	1	50	26	1.29	17	40	0.84	17	Al (S)	10.0	
MTP 3/EH	1	50	26	1.29	17	40	0.84	17	SS (S)	10.0	

B_{ss} = Field in the aperture centre at which the conductor placed in the magnet peak-field position reaches the short sample limit.

B_0 = Field in the centre of the aperture.

(C): Combined collars; (S): Separate collars.

Al: Aluminium alloy; SS: Austenitic steel.

The present status is as follows:

- Several sets of coils have been made and precompressed in their collars; all mechanical components are nearing completion.
- The first fully assembled cold mass was finished in September 1993, and the magnet inserted in its cryostats should be delivered to CERN before the end of the year.

The magnets will be individually tested and measured. Four of them will then be used with one quadrupole to constitute a full half-cell (the basic unit of LHC lattice and cryogenics) installed in the hall SM18 for system testing with particular regard to cryogenic distribution, powering and quench protection.

Although these magnets do not yet fully incorporate the improvements already introduced in models, the experience with them will be very important for the final production.

1.2.4 Quadrupoles

Two full-size prototype quadrupole magnets of final aperture (56 mm) and length (3.05 m) have been designed and built by CEA–Saclay, using superconducting cables and structural parts made in industry [34]. The first one is under test at CEA–Saclay and will be installed as an important element of the string test.

1.2.5 Other magnets

- Combined tuning quadrupoles and octupoles.
  A prototype magnet of the combined tuning quadrupole ($\partial B/\partial r = \pm 120$ T/m, ± 1600 A, 0.8 m yoke length) and octupole corrector ($\partial^3 B/\partial r^3 = \pm 10^5$ T/m^3, 430 A) has been designed in collaboration with industry [35]. The tuning quadrupole was delivered and successfully tested in Summer 1993.
- Combined dipole and sextupole.
  A prototype 1.3 m long combined dipole (± 1.5 T, ± 47 A) and sextupole ($\partial^2 B/\partial r^2 = \pm 8000$ T/m^2, $I = \pm$ 458 A) corrector was made in industry and tested successfully at RAL at 4.5 K and at CERN at 1.8 K. The magnet can be operated over the full range of specified currents with adequate margin [36]–[38].
- 'Spool pieces'.
  The local sextupole and decapole correctors placed at the ends of the main dipoles are being developed by a RAL/CERN Collaboration, prototypes are being built in industry [39].
- Enlarged single-aperture quadrupoles for the low-β insertions.
  A 1.3 m long, single-aperture model quadrupole with ø 70 mm aperture is being developed by a CERN/Industry Collaboration [40].

1.2.6 The string test

As mentioned above, one quadrupole and four dipole magnets will be installed in hall SM18, after their individual test, to form one half-cell (~50 m long), which is the basic lattice and cryogenic unit of the machine. The purpose is to test the complete functional system combining cryogenics, powering and quench protection.

While the test of individual magnets is essential for assessing the technical foundation of the design and judging the soundness of the magnet construction methods, the string test is aimed more at acquiring experience with the operation of the machine structure.

It is envisaged to pursue the operation of the string over a period of time sufficient to settle a number of details relevant for the machine installation.

1.2.7 Main results of the R&D programme

The R&D has already answered a number of fundamental questions on the basic technical solutions for the LHC magnets:

- The superfluid helium, 1.9 K cooling of magnets in long horizontal cryostats has been proved feasible and less difficult than expected;
- It is now demonstrated for both short and long magnets that twin-aperture ('two-in-one') magnets behave as well as single-aperture magnets with respect to quench and training performance;
- It has been verified by measurements on model magnets that the required field quality can be achieved;
- It has been proved in short models, in particular by the last one, that an adequate margin with respect to the 8.65 T design field can be obtained;
- Since in the last model there was no training quench in the straight part of the magnet, there is confidence that long magnets of the same cross-section design will behave in a satisfactory way;
- The industrialization of magnet manufacture is well under way.

1.3 Dipole magnets

1.3.1 Main features and parameters

The main parameters of the dipoles are listed in Table 42; Fig. 9 shows their transverse cross-section, and Fig. 35 their longitudinal cross-section. The design is based on:

- design field: 8.65 T;
- twin apertures in a common force-retaining structure/flux return yoke and cryostat;
- coil inner diameter: 56 mm;
- distance between the axes of the apertures: 180 mm;

- NbTi superconductor operating in superfluid helium at 1.9 K;
- two-shell coils with graded current density supported by collars and iron yoke surrounded and compressed by a shrinking cylinder.

The coils are formed of two winding layers made with keystoned cables of the same width but of different thickness, resulting from the wanted grading of current density for optimum use of the superconducting material. The copper to superconductor ratios in the strands, different in the two layers, result from stability and protection considerations. Wedge-shaped copper spacers are inserted between blocks of conductors to produce the desired field quality and to approximate a quasi-circular coil geometry, compensating for the insufficient keystoning of the cables. These spacers are continued at the coil ends by saddle-shaped pieces which allow the winding and the mechanical confinement of the cables. The cables are insulated by two half-overlapped wraps of polyimide tape and a wrap of B-stage epoxy impregnated fibreglass spaced by 2 mm. After winding, the epoxy is cured by heating each coil layer in a curing mould, which at the same time gives the final shape and size to the coil. Between the inner and the outer coil shells a so-called 'fish-bone' spacer is placed to provide channels for circulation of the cooling helium. The insulation to ground is composed of superposed polyimide film layers and includes the quench protection heaters.

The force containment structure consists of coil clamping elements, the collars, the iron yoke, and the shrinking cylinder which all contribute to producing the necessary azimuthal precompression in the coils and to preventing tensile stresses from arising under the action of the electromagnetic forces.

The shrinking cylinder is at the same time the outer shell of the helium tank, while the inner wall forms the beam vacuum chamber. The assembly between these two cylindrical walls (the cold mass), is kept at 1.9 K. In order to reduce the heat load on the low-temperature cryogenic system, the heat generated by the proton beams from their synchrotron radiation and the effect of beam-induced currents in the resistive wall is intercepted by a shield. This is inserted within the vacuum chamber and is cooled by helium circulating at 5–20 K.

The cold mass is closed at the ends by covers, welded to the shrinking cylinder, which leave passages for the beam vacuum chambers, the heat exchanger tube, two pipes containing the main and the auxiliary electrical connections, respectively. The cover on the magnet electrical connections side also leaves a passage for a pipe leading to a pressure relief valve located in the junction space between magnet units. All these pipes are welded to the end covers. Small sextupole and decapole magnets for the correction of systematic errors in the dipoles are placed around the beam pipes inside the end caps at the connection end and at the opposite end, respectively.

Main and auxiliary bus-bars to feed the magnets of the arcs and the dispersion suppressors are located in grooves in the iron yokes (Fig. 9).

Table 42: Dipole parameters

Operational field	8.65	T
Coil aperture	56	mm
Magnetic length	13.145	m
Operating current	11 470	A
Operating temperature	1.9	K
Coils (two-shell construction)		
Coil inner diameter	56	mm
Coil outer diameter (incl. insulation to ground)	120.5	mm
Coil length (incl. end pieces)	13 445	mm
Inner shell		
No. of turns per beam channel	30	
Cable width	15	mm
Thickness	1.71/2.07	mm
No. of strands	28	
Strand diameter	1.065	mm
Filament diameter	7	µm
Copper to superconductor ratio	1.6	
Outer shell		
No. of turns per beam channel	52	
Cable width	15	mm
Thickness	1.34/1.60	mm
No. of strands	36	
Strand diameter	0.825	mm
Filament diameter	6	µm
Copper to superconductor ratio	1.9	
Conductor insulation		
Thickness of 1st tape (50% overlapped)	2 × 0.025	mm
Thickness of 2nd tape (50% overlapped)	2 × 0.0125	mm
Thickness of glass pre-preg tape	0.125	mm
Compressed ins. azimuth. thickness	0.12	mm
Thickness of 'fish-bone' spacer	0.5	mm
Thickness of insulation to ground	0.75	mm
Structure		
Distance between aperture axes	180	mm
Collar outer diameter	170	mm
Yoke outer diameter	540	mm
Shrinking cylinder outer diameter	560	mm
Length of active part (incl. end plates)	13 585	mm
Overall length of cold mass	14 085	mm
Mass of cold mass	24.5	t
Outer diameter of cryostat	980	mm
Overall mass of cryomagnet	29	t
Other characteristics		
Stored energy for both channels (550 kJ/m)	7.2	MJ
Self-inductance for both channels (8.3 mH/m)	110	mH
Resultant of e.m. forces in the first coil quadrant		
ΣF_x	1.80	MN/m
ΣF_y (inner layer)	–0.15	MN/m
ΣF_y (outer layer)	–0.62	MN/m
Axial e.m. force on magnet ends (for both channels)	0.55	MN

The cold mass is installed inside a cryostat (see Section 1.3.6) whose main components are a radiation shield at 5 K, a thermal screen at 70 K, and the outer cylindrical wall of the vacuum vessel. The cold mass is supported by three feet made of composite material and having their cold end bolted to it. The foot nearest to the connection side is fixed to the vacuum vessel while the other two can move on rollers to follow the thermal contraction/expansion of the cold mass. All parts between beam vacuum-chamber walls and shrinking cylinder are immersed in superfluid helium at atmospheric pressure and cooled by means of a corrugated heat-exchanger tube, in which two-phase low-pressure helium is circulated and acts as a heat sink. The cold mass will be bent to a 2700 m radius of curvature, with a horizontal sagitta of 8 mm in the centre, to match the beam paths. This will be done in one of the last phases of the magnet assembly, before welding together the two halves of the shrinking cylinder, which will be suitably pre-bent. As shown in the more difficult case of the HERA magnets, this operation did not present any problem.

1.3.2 The cables

The transverse cross-section of the coils for the LHC 56 mm aperture dipole magnet shows two layers of different cables distributed in five blocks (Fig. 36). The cable used in the inner layer has 28 strands of 1.065 mm diameter and the cable of the outer layer 36 strands of 0.825 mm diameter.

The basic parameters of the two cables are given in Table 43.

The proposed filament size (7 μm for inner layer and 6 μm for outer layer) allows the fabrication of superconducting wires by a single stacking process. The persistent current sextupole component (expressed in relative field error at 10 mm) is -3.56×10^{-4} and the decapole component is 0.18×10^{-4} for these filament diameters. These error components, discussed in Section 1.3.3, are however corrected by small sextupole and decapole magnets located at each dipole end.

Critical current densities in the superconductor

Considerable experience has been obtained during the manufacture of cables for the 10 m long dipole prototype for the R&D phase of the LHC programme. Twenty-four kilometres (6.75 tons) of cable made of 26 strands of 1.29 mm diameter, and 42 km (7.35 tons) of cable using 40 strands of 0.84 mm diameter have been qualified. The process of fabrication of the wires and cables with NbTi filaments of 5 μm has been optimized for high fields. The current densities in the non-copper part of the strand cross-section used in the present definition of the cables correspond to the critical current densities measured on strands extracted from the finished cables at the 3 σ limit in the distribution curve of production. They are 980 A/mm^2 at 8 T, 4.2 K, for the inner layer and 2000 A/mm^2 at 6 T, 4.2 K, for the outer layer. Any further gain in the current densities during mass production will improve the temperature margin of the magnet.

The results of the models show that the short-sample quenching field of the dipole (B_{ss}) is close (within $\sim$ 2%) to the cable short-sample limit determined from strands extracted from the cables.

Table 43: Strand and cable characteristics

	Inner layer	Outer layer
Strand		
Diameter (mm)	1.065	0.825
Copper to superconductor ratio	1.6	1.9
Filament size (μm)	7	6
Number of filaments	8900	6500
RRR	≥ 70	≥ 70
Twist pitch (after cabling) (mm)	25	25
Critical current (A)		
10 T, 1.9 K	≥ 515	
9 T, 1.9 K		≥ 380
Cable		
Number of strands	28	36
Cable dimension		
thin edge (mm)	1.72	1.34
thick edge (mm)	2.06	1.60
width (mm)	15.0	15.0
Transposition pitch (mm)	110	100
Keystone angle (°)	1.30	1.0
Cabling angle (°)	15.95	15.95
Aspect ratio	7.93	10.20
MIITs (300 K) (10^6 A^2 s)	45 (8 T)	30 (6 T)
Critical current I_c (A)		
10 T, 1.9 K	≥ 13750	
9 T, 1.9 K		≥ 12950
dI_c/dB	> 4800	> 3650

Expected quench characteristics and temperature margin

Table 44 shows the peak fields on the conductor (B_p), the field margin and the temperature margin when the magnet operates at 8.65 T for the two layers of cable described in Section 1.3.2. The field margin is defined as the ratio of the operating field to the expected quenching field at the short-sample limit (B_{ss}). The reference temperature of the bath is 1.9 K (He between coil inner radius and cold bore). The current density in the copper at 8.65 T in case of a quench is also given, with the expected hot-spot temperature in the outer layer and the maximum voltage across the outer layer. The maximum voltage of 425 V corresponds to 17 V between turns (the interturn insulation is tested at room temperature with a voltage of 75 V). These two values have been calculated with a 80 ms delay for the quench detection plus the active initiation of the quench over the volume of the outer layer triggered by the quench heaters. This time delay produces 10.5 'MIITs' (MA^2 s), corresponding to a hot-spot temperature of 60 K for a quench in the inner layer or 80 K if the quench starts in the outer layer. Experience has shown that it would be difficult to reduce this time delay. The hot-spot temperature, and consequently the maximum voltage are related to the current density in copper by the approximate formula:

$$\int_{\Delta t_{\mathrm{delay}}}^{\infty} J_{\mathrm{cu}}^2\, \mathrm{d}t + J_{\mathrm{cu},0}^2\, \Delta t_{\mathrm{delay}} \cong 1.40 \times 10^5 \left(\frac{T}{300}\right)^{1/2} \left(1 + \frac{1}{\alpha}\right)$$

where α is the copper to superconductor ratio, T is the temperature of the hot spot, $\Delta t_{\mathrm{delay}}$ is the time delay of firing the outer layer, and J_{cu} is expressed in $\mathrm{A/mm}^2$.

Table 44: Expected quench performance and temperature margin
($B_0 = 8.65$ T, $I_0 = 11470$ A, $T_{\mathrm{bath}} = 1.9$ K)

Layer	B_{p} (T)	B_{margin} (%)	ΔT (K) margin	J_{cu} ($\mathrm{A/mm}^2$)	T_{max} quench (K)	V_{max} (V)
Inner layer	9.07	89.2	1.20	747	295	425
Outer layer	7.59	85.3	1.50	910		

AC losses

During ramping and discharge of the current in the dipole magnet, losses occur due to hysteresis in the filaments, interfilament coupling through the Cu matrix, and interstrand coupling.

The losses due to interstrand coupling depend strongly on the final resistivity of the copper, the coating on the strands, and the compression of the coils at low temperature.

Losses for a twin-aperture dipole have been estimated at 325 mW/m for a charging time of 1200 s, corresponding to an energy of 400 J/m transmitted to the helium bath and to specific power dissipation in the cables of $0.14\ \mathrm{mW/cm}^3$.

In the case of discharge of the machine, the upper limit of the time constant is given by the characteristics of the diode heat sink of the quench protection system and the quench propagation to other magnets via bus-bars (see Section 1.8.3). In the models, a linear discharge $\mathrm{d}B/\mathrm{d}t$ of 0.11 T/s does not initiate a quench. An exponential discharge with a time constant of 100 s leads to a load of 2800 J/m.

Discussion on temperature margin

A superconductor stays in the superconducting state when the temperature, the magnetic field, and the current density are below their critical value. The temperature margin calculated in Table 44 is the difference between the bath temperature and the critical temperature at the design field and current.

During the ramping tests on the MTA models, we have seen that the temperature of the superconductor can stay at 4 K in steady-state conditions above the λ point, without perturbations of the helium II bath. Experiments made by CEA–Saclay show that, with the existing insulation, the temperature difference between the conductor and the superfluid helium bath is 1 K for a power of 4 mW/cm^3 [41]. Encouraging results have been obtained in the laboratory with porous insulations, which show a very small ΔT because the heat is carried away by the superfluid helium.

Table 45 illustrates the distribution of the ΔT margin of 1.20 K for the inner layer. The main part of the temperature margin will be used for beam losses (4 mW/cm^3 corresponds to a loss of 4×10^6 protons/s in the inner layer of the dipole, see Section 8.2 of Part II, Technical Description).

Table 45: Use of temperature margin

Phenomenon	Limits	ΔT
J_c measurement precision	±2.5%	±0.05 K
Dissipation*	< 0.5 mW/cm^3	0.20 K
Beam losses (3.6×10^6 p/s)	3.6 mW/cm^3	0.92 K
Ramping losses	0.14 mW/cm^2	0.035 K
TOTAL		~1.2 K

* The short-sample critical-current density is defined as the value at which the sample resistivity is $\rho = 10^{-14}$ Ω m.

1.3.3 The electromagnetic design

The coil must be shaped to make the best use of a superconducting cable whose current is limited by the peak field to which it is subjected. It must also produce a dipole field of the best homogeneity possible over the whole range of its operational excitation. The contribution of the iron yoke enhances the strength of the magnet but must contain the magnetic flux in such a way that the field quality is maintained.

The constraints for the magnet design are numerous and contradictory. For achieving best field quality a cable with a small cross-section appears desirable. This allows for an easier approach to the ideal coil geometry where all higher unwanted multipoles are eliminated. A small cross-section cable facilitates the construction of the coil ends which is a particularly difficult part of the coil fabrication and has turned out to be the location of a high fraction of all quenches in the models tested so far. A larger cable cross-section improves the filling factor in the coils, thus providing a greater safety margin on the load line, which is equivalent to a higher margin in temperature. The larger cable cross-section also means fewer turns in the magnet and hence a lower self-inductance. This reduction of self-inductance, together with a higher thermal capacity of the conductor, reduces the maximum temperature and voltages developed in the magnet at quench.

In addition, persistent currents have to be taken into account [42]. They appear in the superconducting filaments and their effects diminish with increasing field. They produce most pronounced field errors at low magnet excitation, at injection, which is a critical phase in machine operation and where one would like to have the minimal field perturbations. The persistent currents depend on the critical current density in the filaments and on the filament diameter. This explains the search for conductor material with the thinnest possible filaments. To complicate matters, these persistent current effects can be time-dependent as has been shown in the HERA magnets.

The above points are all addressed in the electromagnetic design [43]. The iron yoke enhances the strength of the magnet and influences the field quality. Both are subject to the saturation of the iron. The two-in-one nature of these magnets makes the design more difficult since it introduces multipoles of quadrupole and octupole symmetry. These appear in addition to the multipoles, compatible with the normal dipole symmetry, namely the sextupole, the decapole, and so on, which are primarily due to saturation.

For defining the field quality we use the standard notation of harmonic multipole analysis, namely:

$$B_y + iB_x = B_1 \Sigma_{\mathrm{n}} (b_{\mathrm{n}} + i a_{\mathrm{n}})(Z/R_{\mathrm{r}})^{\mathrm{n}-1}$$

where B_1 = magnitude of dipole field in the y (vertical) direction;
b_{n} = normal multipole coefficient;
a_{n} = skew multipole coefficient;
Z = $x + iy$;
R_{r} = reference radius.

The index n = 1 describes the dipole field, n = 2 the quadrupole one, n = 3 the sextupole and so on.

Compared to the earlier design report [1], stricter limits have been imposed on the dipoles for the fourteen- and eighteen-pole components, n = 7 and n = 9. These must not exceed relative field error values of 3.5×10^{-6} and 7×10^{-7} at 10 mm radius respectively. While for some other multipole components correction magnets or windings are foreseen, these multipoles must be kept below these small values by design, taking into account all possible effects and tolerances.

The dipole magnet parameters (Table 42) are the result of all the above considerations. They take into account the outcome of the measured model dipole magnets and include the experience in construction of the prototype dipoles. Numerous additional case studies were performed by means of optimization routines, specially developed for this purpose.

The resulting conductor distribution in one coil quadrant is shown in Fig. 36. The increase of conductor peak field with respect to the field in the aperture centre B_0 is 4.5% and the equivalent of 4.8% of the ampere-turns are lost by saturation in the iron yoke for $B_0 = 8.65$ T.

Expected multipole fields at injection and at top field operation

The multipolar components, describing the perturbations with respect to the ideal dipole field, can be classified as those which are inherent in the design of the geometry, those generated by persistent currents in the superconductor filaments, and those which are due to fabrication tolerances of the different components and of the tooling used to assemble them. While the former are multipoles which respect at least the symmetry given by the horizontal mid plane, the latter may present components which do not respect any symmetry. These are responsible for any skew components appearing in the apertures. They may, moreover, be systematic, although in a series fabrication all effort will be made to keep them as small as possible. For this purpose thorough analysis of the measured magnetic field errors and their relation to the fabrication methods and tooling will be done in the production phase of the magnet pre-series. In addition to this, a certain spread must be expected for all systematic multipoles.

The lower order multipoles tend to change with varying excitation. At low excitation these variations concern the multipoles created by the persistent currents in the filaments, mainly sextupole, b_3, and decapole, b_5, components. When raising the current these perturbations will die away. Above the second half of the excitation, multipoles caused by iron yoke saturation will appear. These consist again of sextupole and decapole components but also of a quadrupole and octupole component induced by the two-in-one geometry.

It is the objective of the yoke magnetic design to keep these multipoles, and especially their variation over the whole range of excitation, to a minimum. The parameters on which one can act are the inner and outer yoke diameters, and the positioning of additional holes into the yoke. This must be balanced, however, with the aim of reaching the highest possible dipole field while maintaining the margin on the load line. Figure 37 shows the flux plot as computed for the coil collar yoke assembly.

Table 46 gives the multipoles, expressed in relative field errors in 10^{-4} at 10 mm, at magnet excitation corresponding to beam injection and that of nominal operation. Table 46 also shows the spreads expected for each component expressed in one σ. These latter values were obtained by scaling the random errors of the measured multipoles of the HERA magnets to the dimensions of the LHC dipoles.

1.3.4 Coils and insulation to ground

During operation, the primary source of heat to the coils is from lost particles, the synchrotron radiation and the beam image current being intercepted by the beam screen. An additional dynamic heat load results from losses when ramping the magnet current. This heat increases the superconductor temperature which reduces the magnet operating margin. Particular care has therefore to be taken to provide a cable insulation which should not only withstand the voltage between turns but also be sufficiently porous to let the superfluid helium carry away the heat. To avoid short-circuits, this insulation has also to be robust in order not to break during winding (especially in the coil end region) and curing. The

Table 46: Expected multipole fields, at injection and at 8.65 T
(In units of 10^{-4} relative field error at 10 mm)

	At injection, 0.58 T				At nominal operation, 8.65 T			
	Systematic		Random		Systematic		Random	
n	norm. b_n	skew a_n	norm. $\sigma(b_n)$	skew $\sigma(a_n)$	norm. b_n	skew a_n	norm. $\sigma(b_n)$	skew (a_n)
2	0.029	±0.76*	0.372	1.227	–0.080	±0.76*	0.366	1.125
3	-3.32**	±0.086	0.882	0.186	2.510**	±0.086	0.877	0.129
4	–0.019	±0.023	0.055	0.186	–0.015	±0.023	0.043	0.173
5	0.206**	±0.020	0.083	0.041	0.044**	±0.020	0.092	0.019
6	–0.004	0.000	0.022	0.014	–0.005	0.000	0.006	0.013
7	–0.026	0.000	0.012	0.011	0.006	0.000	0.009	0.003
8	0.000	0.000	0.005	0.005	0.000	0.000	0.001	0.002
9	0.006	0.000	0.003	0.004	–0.001	0.000	0.001	0.001
10	0.000	0.000	0.002	0.002	0.000	0.000	0.000	0.000
11	0.008	0.000	0.001	0.001	0.008	0.000	0.000	0.000

* It is hoped to reduce the value of the systematic a_2 during series production.
** Systematic b_3 and b_5 will be compensated by correctors at each dipole end. The b_3 values in this table indicate the magnitude of the persistent current effect at injection and of the yoke saturation at maximum operational conditions, the coil geometry being designed for $b_3 = 0$. For the final design the coils can be modified with only minor conductor block displacements to provide a negative b_3 offset. This would diminish the required strength of the sextupole correction spool pieces.

basic cable insulation, which must safely withstand a turn-to-turn test voltage of 75 V, is composed of two polyimide layers wrapped around the cable with 50% overlapping and a fibreglass pre-impregnated epoxy tape wrapped onto the cable and spaced by 2 mm (Fig. 38). The resulting gap makes the coil porous by setting up channels for superfluid helium, without affecting the mechanical support between turns. Different options are under test, while other materials and designs, which may give both better coil porosity and higher thermal conductivity, are being examined.

Integrated field harmonics are kept low by careful location and spacing of the conductors in the magnet straight part and in the ends. Compared with earlier superconducting magnets, the ratio between conductor width and bore diameter is high. Special insulating fillers (end spacers) were therefore designed to confine the conductor to a consistent shape, close to a constant perimeter profile for each individual turn. Satisfactory shapes were determined using the approach of the minimum strain energy, in combination with empirical methods. Several manufacturing options are being pursued, such as die-casting, moulding and machining, to produce these end spacers at the lowest possible cost.

Coils composed of two constant thickness layers with graded current density have been chosen. The two layers are joined together in the part of the inner cable that crosses over from the inner to the outer layer (ramp-splice) and soldered to the outer layer cable. A strip of OFHC copper is soldered to this cable in order to thermally stabilize and mechanically stiffen the ramp and its curved portion. Different ways of making the ramp-splice are under investigation and are being tested in models. At the moment, a revision of the solution already used in early LHC models and HERA dipoles is favoured because it appears to be the best compromise with respect to magnet length, current margin, manufacturing simplicity, reliability, and clamping of the soldered joint.

To stabilize and reinforce the coil leads, copper strips or copper braids are soldered to the superconducting cable. The amount of copper depends on the permitted maximum temperature and on the discharge time constant of the system.

Multipole components are generated by manufacturing errors which are related to tooling (winding mandrels, centre posts, sizing bars, curing moulds, liners etc.) and process. Very precise tooling (with tolerances of 20 μm on critical dimensions) is required and the process (curing temperatures and times, placement of the conductors) must be carefully checked and trimmed.

The coil layers are separated radially by an insulating material which has to withstand a voltage estimated at 400–500 V. A slotted fibreglass epoxy layer (called fish-bone) is the current solution, but other solutions are being studied and tested.

The coils require additional insulation between poles and with respect to the collars sitting at ground potential (Fig. 39). The ground insulation is composed of several layers which are cut azimuthally and longitudinally for reasons of assembly. Besides its electrical scope of preventing shorts from coil to coil (test at 3 kV in dry air) and from coil to ground (test at 5 kV in dry air), it also has the mechanical role of providing good slip surfaces during collaring, and a smooth surface over which both azimuthal and radial preloads are adequately distributed to avoid the deterioration of the insulation. Quench heaters are placed between the outer coil layers and the insulation to ground. They consist of stainless-steel strips, with about half of the length intermittently copper-clad (0.5 m with copper cladding alternating with 0.5 m without copper cladding). In case of a quench, they rapidly heat up the conductors through the thermal barrier of the insulation. Collaring shims, which are located at the layer poles, and collaring shoes, located between the outer layer ground insulation and the inner collar surface, prevent damage due to contact with the serrated edges of collars. Moreover, the collaring shoes help to avoid wrap breakdown and provide a continuous support to the conductors. A good slip plane between collars and collaring shoes is provided by coating the collaring shoe facing the collars with dry lubricant. The current solution is to use polyimide film layers for the insulation to ground, but experiments are under way to determine the most suitable and economical materials for the ground insulation and whether or not collaring shoes are needed to serve the above-mentioned functions.

1.3.5 Mechanical structure

Description of the structure

The mechanical structure of the dipoles must be able to withstand the high forces generated in the magnet and limit as much as possible the coil deformation over the range of operation. The materials used for the most highly stressed components must, therefore, have a high load-bearing capacity, high elastic moduli, good fatigue endurance and good behaviour at cryogenic temperatures down to 1.9 K.

Figure 40 shows the cross-section of the magnet cold mass. The coil support structure is formed by:

- Two separate collars made of high-strength non-magnetic steel. The coils are assembled inside the collars and precompressed at room temperature;
- An iron yoke split in two parts at the vertical symmetry plane of the twin-aperture magnet. The gap is needed to compensate for the difference of the thermal contraction of iron and stainless steel during the cooling from room temperature to 1.9 K. The yoke is made of 6 mm thick low-carbon-steel laminations.
  The iron insert keeps the collars separated and is optimized to reduce the quadrupole component due to the iron saturation;
- A stainless-steel outer cylinder. This part is welded with interference around the iron yoke in such a way that the iron yoke gap is already closed at the outer edge at room temperature.

When current is flowing in the cables, the coils must be under compressive stress in order to avoid the appearance of sudden cracks. Displacements and deformations of the coils must be limited as much as possible. A necessarily stiff structure can be realized fulfilling the following conditions:

a) the gap between the two iron yoke halves must be closed before and during excitation;

b) there has to be a good contact between the iron yoke and the collars for all design conditions.

The parameters to be optimized to satisfy these conditions are the relative dimensions of the components of the structure, the choice of materials, the prestress in the outer shrinking cylinder, and the dimension of the gap between the two half-yokes. Furthermore, except for a short time during the collaring operation, the compressive stress in the coils at room temperature must be limited to about 100 N/mm^2, a maximum to avoid creep of the insulation and of the copper.

The structural behaviour of a dipole, through the sequence of the assembly and excitation of the magnet, is given below.

Collaring

The collars are pressed around the coils to obtain a compression of about 90 N/mm^2 for the inner layer and 70 N/mm^2 for the outer layer at the end of the process. Before the collaring, the dimensions and the modulus of elasticity of the coils are measured. The shim to impose the wanted prestress can therefore be computed. In doing this, it is necessary to consider the difference between the measuring device, which is very rigid, and the real collars which deform due to the prestress in the coils. During the collaring process, the compression of the coils can be 30–40% higher than the final wanted value depending on the method used to apply the load of the press. Once the press force is released, the compressed coils expand the collars and part of the prestress is therefore lost. In the case of collars which are too soft, if they are not already elastically deformed under the press, one has to expect large deformations and perhaps dangerous overstress of the coils under the press, only to provide a poor remaining prestress after collaring. The collaring is also critical for the collar resistance as well. Around the locking rods, the concentration of stress could reach excessive tensile values if particular care is not taken in defining the shape and dimension of the holes and in the choice of materials. The deformation of the locking sites contributes in a considerable way to the global deformation of the collars and consequently to the loss of prestress at the end of the process. Thus it is important to use high-strength materials for the collars in order to avoid or limit the plastic deformation.

Welding of the shrinking cylinder

The shrinking cylinder is welded with interference around the iron yoke. The interference generates a tensile stress of about 150 N/mm^2 in the cylinder. The prestress starts to close the iron yoke gap such that the two iron yoke halves are just in contact at their external radius. The greatest part of the force exerted by the shrinking cylinder is therefore applied to the collars. The horizontal interference at room temperature will maintain a good contact between the collars and the iron yoke at cryogenic temperature. It will also deform the collars and the coils increasing the compression at the top of the inner coil. To avoid a dangerous overcompression of the cables, a slot has been foreseen in the collar post. Such a slot makes the post behave as a spring; it releases the pressure at room temperature and follows the coil deformation and shrinking during cooling and energizing.

Cooling from 293 K to 1.9 K

During the cooling, the iron yoke closes also in its inner part. At 1.9 K the mating force between the two iron halves is around 3000 N per mm length and per quadrant of magnet.

Thanks to the interference at room temperature, there is still a good contact between the iron and the collars at 1.8 K. A loss of prestress of about 15–30 N/mm^2 is however expected in the coils, as they contract more than the austenitic steel collars.

Excitation at nominal field

At excitation, the iron gap stays closed and there is practically no change in the outer cylinder stress.

The outward electromagnetic force (1800 N per mm length, per quadrant for a field $B_0 = 8.65$ T) is shared between the iron structure and the collars. The radial deformation in the median plane of the collared coils at this field excitation is about 0.06 mm. The coils reach minimum compression at their top (between 10 N/mm^2 and 30 N/mm^2) and the maximum at the mid-plane (130–150 N/mm^2).

Ends

In the ends, the bend of the blocks of cables and, consequently, the different direction of the electromagnetic forces make the situation very different from that in the straight part.

The coil ends are mounted inside the collars with much lower prestress (around 20–30 N/mm^2 in the azimuthal direction). In this region, part of the iron yoke is replaced by non-magnetic material in order to decrease the field. The choice of this material is largely dictated by its thermal contraction which must be as close as possible to that of iron. In this way, the external cylinder perfectly matches the inside structure in all conditions. The longitudinal, resultant electromagnetic force is partly transmitted from the coils to the collars, yoke and cylinder by friction. The remaining part directly loads the thick end plate. Studies are under way to determine the sharing between these two parts. Measurements performed on model magnets indicate that the end plate takes 15–20% of the axial load.

Alternative configurations

Aluminium-alloy collars

Collars made of aluminium alloy can be used instead of austenitic steel collars. One advantage is the cost per unit of volume of the raw material. Furthermore, the aluminium thermal contraction between ambient and 1.9 K temperatures is larger than that of austenitic steels. This allows the coils to be less prestressed at room temperature since they do not lose prestress during cool-down. An important drawback is, however, the stiffness of the collars, which, for the same dimension, is a factor 3 lower than for austenitic steel. Therefore, to keep the same dimensions, it is necessary to have a different distribution of loads between collars and the yoke/shrinking cylinder complex.

The interference necessary to close the gap at room temperature would be too dangerous for the coils. The gap has, therefore, to remain open at room temperature and close during the cool-down.

Horizontally split iron yoke

A horizontal split of the yoke (Fig. 41), could reduce the number of pieces necessary for the yoke from three to two. A complication comes from the fact that the gap is placed exactly where the ion is submitted to the electromagnetic forces. The gap must be safely closed on both sides when the magnet is energized; a 0.1 mm opening on one side may cause a ΔB between the two apertures of the order of 1×10^{-3}, which is unacceptable. An increase of shrinking cylinder thickness may therefore be necessary. Studies and tests on model magnets are under way to assess technically this economically interesting possibility.

Twin collars combined for both apertures

Versions with common collars to both apertures have been successfully tested in short models and on a 10 m long prototype (TAP) in which the yoke was composed of only two parts with a split in the vertical symmetry plane. The TAP [33] style structure is in fact the most natural and economical configuration with twin collars, whether they are made of austenitic steel or of aluminium alloy. The iron yoke inserts, two additional pieces used in the first models and in some of the long high-field prototype magnets to improve the field quality, could be advantageously replaced by two iron bars passing through holes in the central part of the collars. These bars would not require high precision in size and positioning. In the case of collars made from aluminium alloys, particular care must be taken in the design of the central pinhole area, as this part is highly stressed and could be affected by fatigue problems. Advantages of the twin-collar configuration are:

- Lower cost, more compact construction;
- Better control of the parallelism of the field direction in the two apertures. This might be an important asset, since the twin-aperture magnet is aligned as a whole.

The disadvantages are that sorting of the magnets becomes more difficult and that more powerful tooling is needed for punching the collars and for collaring the coils.

Five long (10 m) prototype magnets are being built with combined aluminium-alloy collars, one with separated austenitic steel collars and one with separated aluminium-alloy collars.

The final configuration will be chosen after testing of the models and prototypes which are at present in the assembly phase.

1.3.6 Dipole cold mass and cryostat

The cross-section of the dipole cryomagnet is shown in Fig. 9. Figure 35 shows the longitudinal view of the magnet.

The cryostat dimensions are largely dictated by the size of the largest magnet, the dipole, and the very limited space in the tunnel above the LEP machine. Similar arguments lead us to place all the cryogenic piping within the cryostat. The dipole cryostat [44] runs at three low temperature levels, 1.9 K for the cold mass and at 5–20 K and 50–70 K for the two intermediate heat intercept levels.

The dipole magnet, its connections, main and auxiliary bus-bars, both copper-stabilized, and bus-bar thermal expansion loops are enclosed in a stainless steel skin, the shrinking cylinder, which closed at its ends forms the dipole cold mass and becomes a containment vessel filled with static pressurized superfluid helium at 1.9 K. Furthermore, the cold mass contains correction sextupoles and decapoles mounted on either end of the dipole. A heat-exchanger tube, made out of corrugated copper, and the cold bores pass through the cold mass and are welded to close it at its extremities. The superfluid-helium cooling scheme is described in Part III, Section 2, Cryogenics.

A dipole cryomagnet consists of a dipole cold mass assembled into its cryostat comprising a support system, cryogenic piping, radiative insulation and thermal shield, all contained within a vacuum vessel. The cryostat provides a stable, mechanical support for its cold mass whilst limiting heat inleaks to a level matching the strict heat-load budget of the LHC. The steady-state operational heat loads are estimated to be: 6.55 W/m at 50–70 K, 1.76 W/m at 5 K, and 0.35 W/m at 1.9 K. A detailed summary is given in Table 38 of Part III, Section 2, Cryogenics. The beam screen, a thermal interceptor for beam-induced heat losses cooled to 5–20 K is mounted inside the cold bores of the cold mass. Each unit is interchangeable together with its electrical, cryogenic and vacuum connections with units up- and downstream.

The dipole cold mass weighing roughly 24 t is linked to the cryostat via three support posts [45] each consisting of a low thermal conductivity composite tubular column mechanically interfaced via metallic top and bottom flanges and equipped with two intermediate thermal intercept plates supporting thermal shields. These intercept plates are connected to the 5 K and 50 K cryogenic tubes. The support post closest to the magnet connection side is blocked to the vacuum vessel, the two others slide longitudinally.

Two thermal shields are installed to minimize heat inleaks to the cold mass at 1.9 K. The inner radiation screen uses multilayer superinsulation operating at 5–10 K enclosing both the cold mass and cryogenic piping. The outer thermal shield which intercepts the largest fraction of incoming heat at 50–70 K consists of a self-supporting aluminium screen covered with multilayer superinsulation. A helium-gas-cooled aluminium pipe, which is the return line of the 50–70 K system, forms part of the screen which is divided into several segments to decrease movements during cool-down and warm-up.

The vacuum vessel contains insulation vacuum below 10^{-6} mbar and is made in construction steel with stainless steel flanges to reduce costs and shield stray magnetic flux. The vacuum vessel is equipped with a safety lid which opens at less than 0.5 bar over pressure, all seals are radiation-resistant Viton$^{\mathrm{TM}}$ 'O-rings'. The mechanically rigid vacuum vessel will itself be supported at two points, non-coincident with the support posts. Two alignment targets, at the position of the first and third support post, and one spirit level are mounted on the vacuum vessel. These outside references to the cold mass are established mechanically and verified on the magnet measurement bench with respect to the magnetic centres. The stability of the relationship between the targets and the magnetic centres will be checked with internal sensors. A series of tests made on prototype magnets will confirm or invalidate the necessity of such a system [46].

The safety valve actuator and diagnostics feedthroughs are grouped close to the end flange at the electrical connections side. The passive safety valve mounted onto the cold mass end-flange discharges into the 5–10 K pipe in a case of quench. The diagnostic and control cables also emerging from the cold mass end-flange are brought to the vacuum vessel via instrumentation capillaries.

A retractable sliding sleeve with flexible bellow elements encloses the interconnect region between two cryomagnets ensuring the continuity of the insulation vacuum; the radiative insulation and thermal shield are also continued across the interconnection region. All hydraulic connections and beam vacuum connections in the interconnect are welded.

1.4 Lattice quadrupole magnets

1.4.1 Main parameters

In the present layout, the lattice quadrupoles are connected electrically in series with the main dipoles. Thus, the main parameters of the lattice quadrupole magnets (Table 47) are governed by the design of the dipole magnets. The nominal operational current and the integrated gradient are, therefore, design constraints as is the distance of 180 mm between aperture axes.

Table 47: Parameter list for LHC lattice quadrupole magnets

Operating quadrupole gradient value	220 T/m
Peak quench field in conductor	8.9 T
Operating current	11470 A
Magnetic length	3.05 m
Distance between centres of apertures	180 mm
Inner coil aperture	56 mm
Outer coil diameter	105.7 mm
Outer collar diameter	164 mm
Inner yoke aperture diameter	168 mm
Outer yoke diameter	444 mm
Collar material	Stainless steel
Yoke material	Low carbon steel
Insulation thickness (azimuthally)	0.120 mm
No. of turns per coil inner layer	4+6
outer layer	10
No. of turns per aperture (both layers)	40
Stored energy (both apertures)	580 kj
Self-inductance (both apertures)	8.8 mH
Resultant of the e.m. forces in the first octant	
ΣF_x	0.37 MN/m
ΣF_y	-0.57 MN/m

Although its strength is slightly reduced with respect to the Pink Book design [1], the quadrupole will not be significantly different from the quadrupole prototypes already built in collaboration with CEA–Saclay. The quadrupoles are paired in a F–D combination. The previous quadrupole coil of 56 mm inner diameter was kept after it was decided to eliminate the dodecapole coils which limited the aperture to 50 mm, the design value of the Pink

Book. This 56 mm aperture of the quadrupole is now in line with the new design value of the dipole.

1.4.2 *The cable*

The lattice quadrupole magnets have two layer coils with the same superconducting cable. The same type of strand as in the dipole outer cable will be used for the quadrupole cable. The basic parameters of the quadrupole cable are shown in Table 48.

Table 48: Cable characteristics of the lattice quadrupole

Number of strands	28
Strand diameter (mm)	0.825
Copper to superconductor ratio	1.9
Cable dimension	
thin edge (mm)	1.338
thick edge (mm)	1.602
width (μm)	11.60
Transposition pitch	95
Keystone angle (°)	1.3
Aspect ratio	7.89
Critical current I_c (A)	
at 9 T, 1.9 K	$\geq$10060
dI_c/dB (A T^{-1})	$\geq$3040

1.4.3 *The electromagnetic design*

The design is governed by similar considerations as for the dipoles. However, the saturation effects are much less pronounced. The two-in-one arrangement will mainly induce a dipole component at saturation. This is equivalent to a displacement of the magnet centre and has been evaluated to be not more than 0.006 mm at nominal excitation. Table 49 shows the expected multipoles and their spreads at injection and at nominal operation. At low excitation a dodecapole and a small twenty-pole due to the persistent currents in the filaments will appear and behave similarly to the sextupole and the decapole in the dipole magnets.

At present it is not foreseen to include 12-pole correction windings.

The cross-section of the coil is shown in Fig. 42. Figure 43 shows the flux plot in the coil collar yoke assembly of the two-in-one quadrupole.

Table 49: Expected multipole performance, at injection and at 220 T/m
(In units of 10^{-4} relative field error at 10 mm)

	At injection, 14.5 T/m				At nominal operation, 220 T/m			
	Systematic		Random		Systematic		Random	
	norm.	skew	norm.	skew	norm.	skew	norm.	skew
n	b_n	a_n	$\sigma(b_n)$	$\sigma(a_n)$	b_n	a_n	$\sigma(b_n)$	$\sigma(a_n)$
3	±0.02	±0.28	0.454	0.478	±0.03	±0.30	0.373	0.376
4	±0.19	±0.01	0.133	0.188	±0.07	±0.03	0.099	0.144
5	±0.05	±0.01	0.065	0.093	±0.11	±0.06	0.047	0.038
6	-0.72	0.00	0.053	0.069	-0.06	±0.07	0.045	0.023
7	0.00	0.00	0.012	0.013	0.00	0.00	0.006	0.005
8	0.00	0.00	0.006	0.007	0.00	0.00	0.004	0.004
9	0.00	0.00	0.007	0.004	0.00	0.00	0.004	0.003
10	-0.01	0.00	0.005	0.003	-0.01	0.00	0.002	0.002
11			0.002	0.002			0.001	0.001

1.4.4 Coil design

In contrast with the dipole coil design, the lattice quadrupole coils are not graded in current density. The winding of the two layers of each coil is made out of the same stretch of cable in the double-pancake style: before starting the winding operation for the first layer, the amount of conductor needed for the second layer is stored on an intermediate storage bobbin. Once the inner layer is finished and cured, the winding of the second layer is performed on top of it, after placing the fish-bone and after putting into place the joggle of the conductor for its passage between the two layers. This technique avoids the interlayer splices which, being numerous in the quadrupole, would be a significant load to the cryogenic system.

The turns of the inner block of conductors in the inner layer are spaced with respect to each other over the end region. This technique of diluting the cables avoids too-high peak fields in this mechanically sensitive part of the coils. The end-spacers, machined out of glass-epoxy composite or copper have warped surfaces which are difficult to define theoretically but may be produced using numerically controlled machines, after a certain number of prototype fittings. In fact, the critical point here is to find the shape of the end-spacers around which the rather stiff conductor bends naturally. The bending radius for this conductor is considerably smaller than that in the corresponding location in the dipole coils. Great care has to be taken not to damage the insulation when forcing the conductor into the required position.

1.4.5 Mechanical structure

The structure of the quadrupole (Fig. 11) is similar to the dipole structure. The electromagnetic forces in the quadrupoles are considerably smaller than those in the dipoles. It is thus possible to contain the forces by the collar structure alone. The collars are made out of austenitic steel laminations of 2.5 mm thickness. The pairs of half-collars are alternately turned by 90 degrees and they are completed by two separate pole pieces.

As for the dipoles, the selection of the collar austenitic steel material is of utmost importance. The permeability of this material, which can vary according to the basic quality of the steel and to details of its composition, must be low and homogeneous over the whole range of production.

The keying and prestressing of the assembly is done by eight lines of wedge-shaped stainless steel keys which are progressively inserted in grooves on the outside of the collars. Between the coils and the collars a multilayer, polyimide film ground insulation is placed which also accommodates the 25 μm thick stainless steel quench heater strips.

Once the coil-collar assemblies are completed and the coil interconnections done, the yoke is put around the two units. The yoke laminations are punched out of 6 mm thick low-carbon-steel plates. They are in one piece and are symmetric, with the exception that one side, top or bottom, is cut flat. They are placed around the pair of coil-collar assemblies and turned alternately by 180 degrees. The mechanical linkage between the collars and the yoke is done by four lines of keys placed in additional grooves on the outside of the collars and on the inner faces of the yoke laminations. Once a package of these laminations is in place, they are compressed from top and bottom and locked with the keying rods. This centres and fixes the two coil-collar assemblies in place.

In order to have the whole yoke assembly stiffened, a so-called inertia tube is placed around the yoke. This tube, made of stainless steel of 15 mm wall thickness, serves also as the helium vessel. The mechanical connection to the yoke laminations is done by keys fitting into grooves on the yoke outer surface. Lines of holes and flat surfaces, machined to a good precision along the inertia tube, serve as references. The keys are bolted to these surfaces and the yoke is centred inside the inertia tube straight and without twist.

The inertia tube is about twice as long as the quadrupole magnet since it also houses the tuning quadrupoles as well as dipole and sextupole correction magnets (see Section 1.6 below). The tightness is ensured by endplates and by specially formed caps welded over the mounting holes. This technique of using an inertia tube has already been used for the HERA quadrupoles and, more recently, for the prototype magnets constructed by CEA–Saclay.

1.5 Correctors

1.5.1 Tuning quadrupoles and octupole corrector magnets

Strength and function

The tuning quadrupoles operate between +120 T/m and –120 T/m. They allow the separate variation of the tune of each ring by ± 2 units, the compensation of the tracking differences between main dipoles and quadrupoles, and the correction of the quadrupole error in the dipoles due to iron saturation at high field.

The octupole correctors operate between $\partial^3 B/\partial r^3 = +10^5$ T/m^3 and -10^5 T/m^3. In the LHC [1] baseline design, a nested construction (Fig. 44) of these two magnets is foreseen with a same magnetic length of 0.72 m.

Nested construction

In this design [35], the octupole correction windings are placed on the vacuum chamber of the tuning quadrupole which has sufficient aperture to accommodate them, thus saving some longitudinal space in the lattice. Both magnets have separate mechanical structures and are assembled into units installed side by side near to the main quadrupoles in the regular lattice. Each unit has a separate magnetic circuit to suppress cross-talk. This unit is shaped cylindrically, but slimmed down horizontally to fit into the available distance of 180 mm between beams. A cross-section of a pair of such units is shown in Fig. 44. The main parameters of the tuning quadrupole and octupole magnets for the nested version are shown respectively in Tables 50 and 51, column I.

A prototype tuning quadrupole with an inner coil diameter of 56 mm has been built and tested successfully up to nominal operating current without training quenches.

Table 50: Main parameters of the tuning quadrupole magnets

		I Nested construction	II Separate unit
Nominal strength (B_2)	T/m	±120	±120
Magnetic length	m	0.72	0.72*
Current	A	±1600	±1050
Turns per coil		77	96
Peak field in coil	T	4.2	3.8
Current density in NbTi	A/mm^2	1520	1500
Inner diameter of coil	mm	62	56
Outer diameter of collared coil	mm	125	110.4
Stored energy	kJ	21.8	12.8
Self inductance	mH	17	23.2
Conductor dimensions bare	mm^2	1.35 x 2.3	1.15 x 1.75
Filament diameter	μm	10	10
Twist pitch	mm	25	25
Cu/Sc ratio		1.9	1.8

* Length to be defined.

Table 51: Main parameters of the octupole corrector magnet

		I Nested construction	II Separate units	
			Superferric	Spool piece
Nominal strength ($B_4 = B'''/6$)	T/m	1.67×10^4	4.8×10^4	6.7×10^4
Magnetic length	m	0.72	0.25	0.18
Overall length	m	0.88	0.29	0.26
Current	A	430	500	500
Turns per coil		8	12	53
Peak field in coil	T	3.6	1.5	1.5
Current density in NbTi	A/mm^2	2570	1330	1330
Inner diameter of vacuum pipe	mm	49	–	–
Average diameter of coil	mm	54.7	–	–
Coil inner diameter	mm	–	56	56
Coil outer diameter	mm	–	–	76
Self inductance	mH	0.4	1.6	4.2
Conductor cross-section	mm^2	0.50	1.14	0.98
Filament diameter	μm	10	10	10
Twist pitch	mm	20	20	20
Cu/Sc ratio		2	2	1.6

Variant construction tuning quadrupole integrated in main quadrupole

From the parameters of the main dipole described in this document, it has been shown that the integrated strength of the tuning quadrupole needed to fulfil the requirements defined in Section 1.5.1 could be reduced [47] with the magnet becoming shorter if the same nominal gradient were maintained. However, in this case nesting the octupole inside the tuning quadrupole is not practical, since mechanical limitations arise due to the increased forces on the octupole windings. Separating the magnets will have several advantages: ease the fabrication and mounting of the vacuum tube, increase the operating margin of the octupole and allow separate testing of these magnets, suppress magnetic coupling and thus facilitate operation, reduce the inner diameter of the tuning quadrupole coils, etc. A compact and economically interesting design is to integrate the tuning quadrupole in the yoke of the main quadrupole and to adopt for the octupole a superferric or spool-piece type design.

In this variant, the collared coils of the tuning quadrupole are placed in continuation of the main quadrupole coils and are assembled into a common two-in-one yoke using the same laminations as for the main quadrupole but with a smaller inner aperture, adapted to the diameter of the tuning quadrupole coils. Since the field in the iron is low, the two tuning quadrupoles are magnetically decoupled. The longitudinal spacing between main and tuning quadrupole can be kept relatively small, about one aperture diameter, sufficient to avoid magnetic interference.

The main parameters of the tuning quadrupole and octupole magnets for this variant are shown respectively in Tables 50 and 51, column II. For the tuning quadrupole, a lower current version is foreseen. For the octupole, both the superferric and spool-piece design parameters are shown.

1.5.2 Combined sextupole and correction dipole MSBH/V in the short straight sections

These sextupoles operating between - 1500 and + 1500 T/m^2 allow the correction of the lattice chromaticity. The correction dipoles operating between - 1.5 and + 1.5 T are used for orbit corrections. Figure 45 shows a transverse cross-section of a pair of these magnets, one will correct the horizontal orbit in one ring, and the other the vertical orbit in the other ring. A gap between the magnets suppresses the cross-talk. The coil of the sextupole magnet is mounted inside the coil of the dipole corrector magnet. Placing the sextupole close to the axis of the magnet minimizes the necessary excitation and the peak fields in the coils. The dipole is designed for a very low current and therefore wound with many turns of a thin wire. As it is difficult to make a regular winding with such a small wire, the wires are preassembled in a 20-wire ribbon and the coil is wound from this ribbon. At the end of the ribbon the wires are connected in series [37]. The package of sextupole and dipole windings is surrounded by aluminium shrink rings which prestress the coils. The iron yokes have a rectangular shape which allows the absorption of the return flux of the dipoles while still maintaining the intra-beam distance of 180 mm. The design parameters are given in Table 52. A prototype has been tested [38] and the results showed that this magnet can cover the desired combinations of sextupole and dipole field.

Table 52: Design parameters of MSBH/V correction magnets

	Sextupole coil		Dipole coil	
Nominal strength	$B_3 = 1\ 500$	T/m^2	$B_1 = 1.5$	T
Peak field in coil	2.8	T	2.5	T
Current	230	A	29	A
Number of turns/coil	112		2480	
Stored energy/magnet	2	kJ	7.8	kJ
Coil inner diameter	56	mm	80	mm
Coil outer diameter	76	mm	96	mm
Magnetic length	1.14	m	1.07	m
Conductor				
Cross-section	0.61×1.13	mm^2	ϕ 0.31	mm
Filament diameter	9.1	μm	8.5	μm
Twist pitch	14	mm	14	mm
Copper/NbTi ratio	1.6		4	
Current density NbTi	870	A/mm^2	1920	A/mm^2

The sextupoles of each ring will be connected in series through the machine cryostat forming two families; a family of focusing sextupoles containing those placed close to the focusing quadrupoles, and a family of defocusing sextupoles which are close to the defocusing quadrupoles. The dipoles will each be powered individually and therefore need local current leads between ambient and 1.9 K.

A study has been made [48] to see how much the heat inleak can be reduced if the cold part of these leads is made of high Tc superconductors. In Table 53 the performance of such leads is compared with that of conventional leads. A prototype lead will be built to test the thermal behaviour and the reliability of a lead where the cold part is made of high Tc material and the conventional copper part is cooled by a forced helium gas flow.

Table 53: Comparison of conventional lead with leads containing a high Tc superconducting cold part

Type of lead	Ratio to type a
Conventional lead	
Self-cooled copper lead	1
Leads with copper from 300 K to 77 K and YBCO from 77 K to 1.8 K	
Copper cooled with He gas	0.24
Copper cooled by conduction to heat sink at 77 K	0.36

1.5.3 Sextupole and decapole correctors of the main dipoles

The main dipole magnets will be equipped with small sextupole and decapole corrector magnets [39] to compensate for the systematic sextupolar and decapolar field errors of the dipoles. Each bore will carry a sextupole corrector of 300 Tm/m^2 on one end and a decapole corrector of 81 200 Tm/m^4 on the opposite end. The sextupoles of one machine will all be connected in series through the cryostats to form one family, and the same is true for the decapoles which form another family. Figures 46 and 47 show the cross-sections of these magnets. The design parameters are given in Table 54.

Table 54: Design parameters of MS and MD correction magnets

	Sextupole coil		Decapole coil	
Nominal strength	$B_3 = 2850$	$\mathrm{T/m^2}$	$B_5 = 1.9 \times 10^6$	$\mathrm{T/m^4}$
Peak field in coil	2.7	T	1.6	T
Current	405	A	346	A
Number of turns/coil	112		48	
Stored energy/magnet	607	J	48.7	J
Inner diameter coil	56	mm	56	mm
Outer diameter coil	76	mm	71	mm
Magnetic length	105.5	mm	42.8	mm
Conductor				
Cross-section	0.61 × 1.13	$\mathrm{mm^2}$	0.61 × 1.13	$\mathrm{mm^2}$
Filament diameter	9.1	μm	9.1	μm
Twist pitch	14	mm	14	mm
Copper/NbTi ratio	1.6		1.6	
Current density NbTi	1625	$\mathrm{A/mm^2}$	2075	$\mathrm{A/mm^2}$

1.6 Short straight section cold mass and cryostat

The Short Straight Section (SSS) cryostats [49] of the standard arcs house the twin-aperture quadrupole MQD/F, two tuning quadrupoles MOQD/F, two combined dipole–sextupole–decapole correctors MSBH/V, and the quench protection diodes. The magnets and diodes are mounted in a common inertia tube with end covers, forming the cold mass and thus the helium vessel, filled with pressurized helium II at 1.9 K. The cross-section of the whole assembly is shown in Fig. 6.

Furthermore, separated from the standard section of the cryomagnet by a vacuum barrier, a cryogenic Technical Service Module (QSA) is placed between the cold mass and the interconnection region of the next half-cell dipole. Vacuum manifolds, located on the rear side of the SSS cryostat, permit the pumping of the beam pipes every half-cell

The inertia tube of the quadrupole provides mechanical support and reference for the corrector magnets. The alignment of these corrector magnets with reference to the quadrupole is obtained by supporting plates with a fitted key system, similar to that of the quadrupole, and which position the corrector magnets in the inertia tube. Held in place by longitudinal spacer rods, the support plates also define the position of the bus bars with their expansion loops, mounted in insulating covers.

The protection diodes of the half-cell are mounted such that their replacement without dismounting the SSS is possible (access to the cold mass by the interconnection region).

The QSA consists of the half-cell cryogenic control valves, the helium phase separator, the instrumentation capillaries, the electrical feedthroughs for the correction dipole, magnet and a pair of Beam Position Monitors (BPM). The function of the cryogenic controls are described in more detail in Part III, Section 2, Cryogenics.

For measurement of the beam's position and the diagnostics of its dynamic behaviour, transverse BPMs are mounted close to the quadrupole magnet on the outside of the cold mass. One vertical and one horizontal 0.3 m long BPM, pre-aligned in a common fixture, are positioned by alignment jigs with reference to the inertia tube plugs and thus to the mechanical axis of the quadrupole. Welded into the beam pipes, they form part of the LHC beam vacuum system. Held in position by an adjustable support, the BPMs are thermalized to 4.5 K.

A vacuum barrier permits separation of the insulating vacuum of each half-cell.

The basic SSS cryostat design has been conceived together with the LHC dipole cryostat [44], with which it forms part of the LHC half-cell, sharing the piping for refrigeration distribution.

The cold mass is assembled in the cryostat which consists of a support system, the cryogenic piping, the radiative insulation, the thermal shield, and the vacuum vessel. Together they form the standard section of the cryomagnet.

Two support posts, essentially filament-wound, epoxy glass columns glued between stainless-steel plates [44], transfer the magnet and helium vessel load onto cylindrical seats of the vacuum vessel. As well as the cold mass load, the front support post will also restrain the 4000 daN axial force of the vacuum barrier during half-cell vacuum testing. To allow for the differential thermal contraction between the cold mass at 1.9 K and the vacuum vessel at ambient temperature, the rear support post slides longitudinally on a low-friction polyethylene plate while the front one is fixed.

Reference targets, adjusted on the vacuum vessel support points, and a level gauge enable alignment of the cryomagnet in the half-cell.

1.7 Insertion magnets

As shown in Table 55, there are a total of 166 special quadrupoles in the LHC insertions and straight sections differing in type, length, and integrated gradient. Of this total, 114 magnets are of the lattice quadrupole type having the same cross-section, but with three different lengths. The inner triplet (Q1–Q3) is comprised of special magnets, based on a 70 mm aperture coil which is being developed for the low-beta quadrupoles. In the experimental insertions, these are single-aperture units, while for the cleaning insertion a two-in-one version is being designed, which may, however, operate at 4.5 K. These large-aperture, twin-bore magnets are also required in the dump insertion.

Table 55: Quadrupole magnets for the LHC insertions

Quadrupole magnet	Name	Gradient (T/m)	Length (m)	Number
Low-β quadrupoles	MQ IA	220	6.1	16
(Single 70 mm aperture)	MQ IB	226	6.9	16
Enlarged quadrupoles	MQ EA	183	4.6	4
(Twin 70 mm aperture)	MQ EB	187	6.1	10
	MQ EC	192	6.9	2
	MQ ED	168	4.6	4
Lattice-type quadrupoles	MQ TA	220	3.7	42
(Twin 56 mm aperture)	MQ TB	220	4.6	22
	MQ TC	211	8.0	42
	MQ TD	163	8.0	8

Other magnets in the straight sections and insertions include short dipoles described elsewhere in this document, the separation/recombination dipoles, skew quadrupoles, dipole correction magnets, and special dipoles for the dump insertion. Whereas most of the correcting elements are of the same design as that used for the lattice, 12 of the 192 skew quadrupoles require a 70 mm aperture, as do 40 correcting dipoles. The remaining skew quadrupoles are regular tuning quadrupoles rotated through 45°. All of these magnets are based on current technology.

1.7.1 Separation/recombination dipoles

In the interaction regions the two beams must be brought into almost head-on collision. This is achieved with the separation/recombination dipoles designated type D1 and D2.

Type D1 dipoles are superconducting of 75 mm aperture with a field of 5.2 T and 9 m length. The HERA type dipoles have characteristics very close to these, and it is currently foreseen to use a magnet of this design.

Type D2 dipoles are classical magnets with normal copper coils. A cross-section of these dipoles is shown in Fig. 48. They are a scaled-up version of the SPS MBB dipoles. The main parameters are given in Table 56; a total of 76 units of length 5.2 m are required.

For the beam-dump insertion, the D2 (MBSO) dipoles are of similar design, with, however, a modified cross-section to take into account the opening in the coil window for the passage of the ejected beam. The maximum operating field is 1.5 T; six units, of length 5.5 m, are required.

The total power consumption of these classical dipoles is about 5 MW, so a superconducting alternative is also being studied. Except for the cleaning and beam-dump insertions, where the high radiation environment imposes the use of classical magnets, such a solution

Table 56: Main parameters of recombination dipoles D2

Nominal field	1.8	T
Magnetic length	5.2	m
Excitation current	3750	A
Losses	60	kW
Total mass	30	t

may be preferable. First investigations have shown that the twin-aperture main dipoles with a special single-layer coil could provide the necessary aperture (inner coil radius 42 mm) and a reasonable field homogeneity at a field level of 4 T. The collars, steel yoke and cryostat could be similar to those used for the main dipoles, development work being confined to the coil design.

1.7.2 Low-β quadrupoles

The low-beta quadrupoles are single-bore units 6.1 and 6.9 m long. Owing to the very large betatron amplitudes occurring in these magnets, the LHC performance depends critically on their field quality, especially on the higher order, random, multipole errors at low field. In order to obtain this field quality and to provide additional space for the cone of secondaries emanating from the interaction, a novel design based on a graded coil with an aperture of 70 mm wound from NbTi keystoned cables cooled at 1.9 K, has been proposed. The design gradient of the magnet is 250 T/m for an excitation current of 5200 A.

The cross-section of the LHC low-β quadrupole is shown in Fig. 49. It features a four-layer coil [50] wound from two keystoned cables 8.20 mm wide with their current-carrying capacities graded by a factor of 1.5. The coils are assembled with the aid of thin quadrupole-type, stainless-steel collars locked with rods. A four-fold symmetric yoke is assembled around the collared coils and compressed with a tight fitting outer shell. Because of their small width, the collars act as spacers, transferring the compressive forces from the tight fitting ring to the coil. The yoke thus has both important magnetic and structural functions, since the magnetic forces are taken by the rigidity of the iron lamination pack. This design concept is currently being verified on a 1.3 m model magnet which is being developed in collaboration with an industrial firm [40].

1.7.3 Large-bore, twin-aperture quadrupoles

For the two-in-one enlarged aperture (70 mm) quadrupoles for the cleaning and dump insertions, we propose to use the coil and collar design of the low-β quadrupoles to take advantage of that development (and to increase the statistical basis for coil selection). In this case, with a beam-to-beam separation of 180 mm, a yoke diameter of 500 mm is sufficient to guarantee low saturation and cross-talk effects. The mechanical structure follows the same approach as in the low-β magnets, as the collars have no supportive strength. The yoke laminations may need to be split into six sections, which, by relative movement, generate compression of the two magnets. The exact interface location and values depend strongly on the beam-to-beam distance and the elastic properties of the coils.

It should be noted that the large-bore, twin-aperture quadrupole magnets are required to provide a maximum gradient of 200 T/m, which allows operation at 4.5 K, and facilitates yoke design, as the forces are 35% lower than in the low-β magnet. Moreover, should the minimal distance between the magnets (14 mm for 180 mm beam-to-beam separation) turn out to be too small for structural reasons, it would be possible to choose slightly smaller conductor dimensions, while retaining (or even increasing) the coil aperture, which is especially important for the cleaning insertion from the point of view of both field quality and radiation losses. These and other design options will be specified in detail following the results of the low-β model magnet.

1.8 Powering and quench protection

1.8.1 Powering scheme

More so than for any previous machine, the powering scheme of the LHC must be closely integrated with the needs of the magnets, cryogenics, and quench protection. Already the discontinuity of the cryostat at mid-arc means that power cannot easily be fed from one intersection point through to the next. Furthermore, when one considers the horizontal and vertical distance of about 700 m across to the start of each main cryostat and up to the surface, it then becomes apparent that the power converters need to be located underground, close to the feed box of the main cryostat. (These feed boxes are located at the start of each arc, about 230 m from the intersection points.) Doing this divides the machine into 16 units for powering in the same way as for cryogenics and vacuum (Fig. 50). This has certain advantages:

- the steady-state power consumption is reduced from over 100 MW to about 24 MW for the magnet powering system;
- likewise, the installed power of the power converters is reduced by a similar amount even though their number increases. However, their overall cost is halved;
- the complication, cost and volume required to install between 100 and 170 kA of warm connections down to and across each intersection is avoided. Short straight connections of a few metres from the power converters to the feed boxes are all that is required. This reduces the cost of the D.C. connections by a factor of 6;
- only one-sixteenth of the machine needs to be discharged rapidly in the event of a quench (see Section 1.8.3);
- testing, commissioning, operation and fault-finding are broken down into more manageable pieces;
- galvanic isolation and the ability to earth each sub-unit reduces the voltage stresses.

As far as the main magnet is concerned, the disadvantage is that their power converters must track very precisely ($< 10^{-5}$) so that it appears that the magnets are connected in series. (The corollary is that half-octant trimming is possible if, for instance, there exist slight variations in the magnetic field, for one reason or another, from sector to sector.) The other disadvantage is that underground civil engineering is needed to create caverns to locate the power converters, rather than cheaper surface buildings. (The necessary access galleries replace what would have been warm bus-bar or cable galleries.) However, the overall cost of the system is lower.

The situation has eased somewhat with the use of the klystron galleries of LEP in the even points. Since these galleries run in parallel to the straight sections between the intersections and the start of the arcs, they are ideal for locating the power converters. The power converters for the main lattice, dispersion quadrupoles, outer triplets and correctors can all be placed at the far end of the galleries near to the main feed box. Those for the inner triplet (or doublet) and separators can be placed at the beginning of the galleries near to their respective feed points. The existing cooling and ventilation systems can be adapted to cool the power converters and short warm connections. The odd points still need the excavation of caverns. Again the nearby LEP cooling water will be used.

The alternative to underground caverns at the start of the arcs is to effectively move the feed boxes to the intersection points or even to the surface by using cold current feeds. This is technically more difficult and may prove more expensive but is being looked into.

Each circuit is individually fed and has galvanic isolation. However, certain quadrupoles have been placed in series and use trim power converters to adjust their settings (e.g. Q_8, Q_9, Q_{10}). It is also possible to group families with a common return, alternating the polarity of each power converter, so that only n + 1 feedthroughs and bus-bars need to be used instead of 2 n.

1.8.2 The power converters

The list of power converters is given in Table 57. In all, there are 1688 power converters having a total installed power of 50 MVA and taking a steady-state input power of 24 MW. They are characterized, in general, by a low voltage and high current. The 16 power converters for the main magnet circuit must produce 80 V at 12 kA during their charging phase, then reduce to approximately 8 V when on flat-top. Novel topologies will be investigated for these power converters.

High-frequency, switch-mode power converters will be used for most of the other power converters. The reduced volume, light weight and high efficiency of this type of power converter are ideal characteristics for underground location. Their superior dynamic response will be necessary if the very tight performance parameters required by the machine are to be met. Collaboration and development with industry and universities will be undertaken in order to optimize the designs. Special attention will be needed for the many bipolar converters for the corrector magnets.

The acceleration and previously mentioned tracking precision required by LHC will need an order of magnitude increase in the present levels of precision of power converters. Investigations are already under way with a view to using high-speed digital control techniques. Likewise, work will be needed to produce economic precision current monitors (DCCTs) in the 10 kA region.

Table 57: Power converter characteristics

Type	Current (kA)	Voltage (V)		Output power (kW)		Number of units
	Coast	Coast	Peak	Coast	Peak	
1	12	8	88	96	1060	16
2	10	5	6		60	60
3	8	6	8	48	60	8
4	5	6	7	30	33	20
5	5	68	68	340	340	14
6	±1.6	8	11	13	18	192
7	±0.5	8	19	4	10	32
8	0.6	6	6	4	4	72
9	±0.5	8	12	4	6	128
10	±0.05	12	32	1	2	376
11	±0.030	100	100	3	3	768
12	5	105	105	525	525	2

1.8.3 Quench protection

The quench protection of the LHC machine is based on the so-called ‘cold diode’ concept.

In a group of series-connected magnets, if one magnet quenches, then, unless precautions are taken, the magnetic energy of **all** the magnets will be dissipated in the quenched magnet, so destroying it. The solution to this problem is to bypass the quenched magnet and then de-excite the remaining series-connected unquenched magnets. In this case, only the magnetic energy of the quenched magnet itself will be dissipated as heat internally in the magnet. For the LHC machine it is foreseen to use silicon diodes situated inside the cryostat, so-called ‘cold diodes’ as bypass elements. These cold diodes will be located in the helium II vessel at a temperature of 1.9 K, and will be exposed to a radiation of about 50 kGy over a 10-year operation period [51]. Newly developed thin-base epitaxial diodes of 75 mm diameter, which can absorb the integral current load of about 10^{10} A^2 s, have been tested in an accelerator environment at liquid nitrogen temperature and seem to be sufficiently radiation-hard for this application. Radiation tests are continuing in a nuclear reactor at 4.2 K. In order to simplify the mechanical layout, it was decided that the cold diodes would be connected across each half-cell of the machine and be situated in the quadrupole cryostat. If one magnet in the half-cell, composed of three bending magnets and one quadrupole magnet, then quenches, the complete half-cell will be force-quenched by heaters (see below), thus causing the current to commutate from the half-cell over to the diodes. The diode packet will consist of four series-connected diodes with each diode connected across each of the four magnets of the half-cell by interconnecting copper bus-bars (Fig. 51). The bus-bars to the internal connection points of the four-diode stack can be of small cross-section, since they carry current only for a short transient time caused by differences in the heater delays and in the resistances of the four magnets in the half-cell before the current is fully commutated over to the diode stack.

The extremely high energy density of the LHC magnets, coupled with the relatively slow propagation speed of a 'natural' quench, can lead to excessive heating at the zone where a quench starts. It is therefore necessary to detect very quickly the incipient quench, using sensitive radiation-hard isolation amplifiers, and then fire strip heaters which provoke quenching along the outer layer of the magnet coil. This spreads the energy out through a large volume of the winding, and so limits the maximum temperature rise and maximum internal voltages.

In order to avoid that the quench spreads to other magnets and that the cold diode overheats, a fast de-excitation of the magnet chain must be initiated whenever a quench is detected. This fast de-excitation is achieved by switching high-power energy-dump resistors in series with the magnets giving a de-excitation time constant of about 100 seconds. Figure 50 shows the proposed power circuit of the LHC main ring magnet. The machine is divided into 16 sub-units (half-octants of both machines together), powered separately and so electrically independent [52]. This scheme, also proposed for the SSC, has several important advantages compared with a series connection of all magnets (see also Section 1.8.1).

- During fast de-excitation, since there is only one switched resistor per circuit, there is no risk of a build-up of voltage to earth due to differences in switch timing and resonances.
- The earthing of the ring is much more efficient since it is effectively at 16 points around the ring.
- If quenches occur in only one limited region (one or more magnets in the same half-octant) then only this sixteenth of the total machine has to be rapidly de-excited. This reduces the total eddy current losses during de-excitation, decreases the risk of false quench detection and quench provocation, and gives less wear on the switches.
- The 16 'small' autonomous sub-units, which correspond to the vacuum and cryogenic sub-divisions of the machine, give easier testing and setting-up possibilities.

The above advantages of a sub-divided system, compared with a series connection of all magnets, are sufficiently important to more or less impose this choice. However, this whole system stands or falls on how well the 16 separate power converters can maintain the required tracking and precision.

1.9 Tests and measurements

The LHC will have a large number of dipoles, quadrupoles and correction elements (see Part II, Technical Description). The time, effort and infrastructure required for the testing of several thousand of these magnets may be extrapolated to a certain extent from the experience gained recently at DESY. The total amount of magnetic measurements, assuming two per twin-aperture magnet, is about seven times that handled during the construction of HERA.

The procedure applied to each of the dipole and quadrupole main magnets consists of:

- Magnetic field measurement of all collared coils at room temperature at the factory followed, if necessary, by shimming;
- Final overall acceptance tests of each magnet and its cryostat at CERN. These include dimensional and electrical tests, checks of instrumentation, vacuum, etc.;
- Installation of the magnet on the measuring bench and connection to cryogenics and current supply;
- Cryogenic tests;
- Power test and quench behaviour;
- Quench analysis;
- Magnetic field measurements and alignment;
- Storage of magnets in batches according to their field quality.

A series of test benches will be provided for the magnet tests at CERN. Each of them will be equipped, among other things, with a reference support and the necessary vacuum, cryogenic and electrical connections to energize the magnets. They will also include all the associated safety devices and controls. Each bench will be fitted with a series of magnetic field detectors, together with their electronics and controls, to allow the measurements to be made in a semi- or completely automated way, independently from the other benches.

However, for economic reasons, one power supply will serve several test benches. Since the actual time over which a magnet is energized is much less than the overall duration of a magnet test, including cool-down and warm-up, one power supply for three or four test stations might be acceptable. This is consistent with HERA experience.

Assuming for LHC magnets a turnround time per test bench and per twin magnet of about 150 hours, about 16 test stands must be operated around the clock in order to accomplish the total LHC test programme within about 4 years.

In order to allow high field measurements of the cold magnet an auxiliary stainless steel pipe is inserted into the cold magnet vacuum chamber [53]. The annular vacuum gap filled with several layers of superinsulation provides adequate thermal insulation to keep the auxiliary inner pipe at room temperature. The magnetic measurements can readily be performed inside this room-temperature pipe. However, this reduces the diameter of the aperture accessible during the measurement to about 35 mm, which is still adequate for high-precision field measurements.

After initial checks and cool-down, the excitation curves will be measured, and the quench behaviour will be investigated. For the purpose of quench localization measurements it is proposed to use a dedicated system of pick-up coils built in the form of a long shaft placed into both warm aperture pipes of the magnet [54].

Thereafter, rotating coils driven from the outside through a long, high-precision shaft will be used to measure the field quality, strength and field integrals of dipoles and quadrupoles [55]. Field orientation with respect to the vertical of dipoles and quadrupoles will also be measured by this unit employing high-precision encoders and inclinometers. In addition, the position of the axis of quadrupoles will be measured by localizing the lateral position of the coil by a laser-beam system which will also serve to refer this axis to the outside fiducials. Calibration of the measuring coils will be made by NMR as well as in normal-conducting, high-precision reference dipoles and quadrupoles.

These techniques may be backed up or complemented for cross-checks by others like the stretched wire technique, as used extensively for HERA.

The measurement of the magnetic axis of quadrupoles and the field orientation of both dipoles and quadrupoles are of particular importance for these double-aperture magnets. Errors can no longer be taken care of by aligning the magnet accordingly, but only by combining 'faulty' magnets in order to compensate errors in a magnet shuffling procedure.

Each measuring bench is connected to its own analog conditioning and acquisition electronics. This is in turn connected to a workstation used as an operator console to monitor the data acquisition and storage. All the other equipment (motorization, cryogenics, power supplies) is controlled by programmable logic controllers connected via an industrial network to the operator workstations. A particular effort is made to use readily available equipment and keep to a minimum the in-house developments both for hardware and software.

1.10 General list of LHC magnets

The list of magnets and their parameters are presented in Tables 58, 59 and 60.

Table 58: Main parameters of dipole magnets

Equipment Name	 Type	Operational field $B(r)$ (T, m)	$\partial B/\partial r$ (T/m)	Length (m)	Inner coil aperture ø (mm)	Temp. K	No.	Comments
MB	Main dipole	8.65	-	13.145	56	1.9	1280	Twin-aperture
MBS	Dipole short	8.65	-	8.793	56	1.9	16	Twin-aperture
MBSH	Separ. S.C.(D1)	5.2	-	9.0	75	4.7	8	Single-aperture
MBSW	Separ. dipole(D2)	1.8	-	5.2	50 × 240	warm	76	Single-aperture
MBSD	Separ. (D2 SS5)	1.5	-	5.5	50 × 260	warm	6	Single-aperture

Table 59: Main parameters of quadrupole magnets

Equipment Name	 Type	Operational field $B(r)$ (T, m)	$\partial B/\partial r$ (T/m)	Length (m)	Inner coil aperture ø (mm)	Temp. K	No.	Comments
MQF(D)	Main quad.	$220 \times r$	220	3.05	56	1.9	376	Twin-aperture
MQIA	Inner triplet	$220 \times r$	220	6.1	70	1.9	16	Single-aperture
MQIB	Inner triplet	$226 \times r$	226	6.9	70	1.9	16	Single-aperture
MQTA	Normal	$220 \times r$	220	3.7	56	1.9	42	Twin-aperture
MQTB	quads	$220 \times r$	220	4.6	56	1.9	22	Twin-aperture
MQTC	of	$211 \times r$	211	8.0	56	1.9	42	Twin-aperture
MQTD	insertions	$163 \times r$	163	8.0	56	4.7	8	Twin-aperture
MQEA	Enlarged	$183 \times r$	183	4.6	70	4.7	4	Twin-aperture
MQEB	quads	$187 \times r$	187	6.1	70	4.7	10	Twin-aperture
MQEC	of	$192 \times r$	192	6.9	70	4.7	2	Twin-aperture
MQED	insertions	$168 \times r$	168	4.6	70	1.9	4	Twin-aperture

Table 60: Main parameters of corrector magnets

Equipment Name	 Type	Operational field $B(r)$ (T, m)	$\partial^{n-1}B/\partial r^{n-1}$ (T/m)	Length (m)	Inner coil aperture ø (mm)	Temp. K	No.	Comments
MSC	Sextupole	$1850 \times r^2$	5700	0.1	56	1.9	2592	'Spool piece'
MDC	Decapole	$1.9 \times 10^6 \times r^4$	45.6×10^6	0.028	56	1.9	2592	'Spool piece'
MSBH	Dipole	1.5	–	1.07	56	1.9	384	Combined elements
	Sextupole	$1500 \times r^2$	3000		56	1.9		
MSBV	Dipole	1.5	–	1.07	56	1.9	384	Combined elements
	Sextupole	$1500 \times r^2$	3000		56	1.9		
MOQF(D)	Quadrupole	$120 \times r$	120	0.72	56	1.9	768	Combined elements
	Octupole	$1.7 \times 10^4 \times r^3$	1.0×10^5	0.72	56	1.9		
MQS	Skew quad.	$120 \times r$	120	0.72	56	1.9	180	
MQSA	Skew quad.	$75 \times r$	75	1.15	70	1.9	4	
MQSB	Skew quad.	$75 \times r$	75	1.15	70	4.7	8	
MBHI(V)	Dipole	4.50	–	0.38	70	1.9	36	Inner triplet
MBHA(V)	Dipole	3.85	–	0.65	56	1.9	256	
MBHC(V)	Dipole	3.30	–	0.76	70	1.9	4	
MBHD(V)	Dipole	1.0	–	1.5	70	4.7	28	
MBHW(V)	Dipole	1.0	–	1.5		warm	40	

2 Cryogenics

The basic design criteria and constraints, as well as the main technical choices for the LHC cryogenic system, remain those described in Chapter 6 of the 'Pink Book' [1]. In this document we shall only cover the specific aspects of LHC cryogenics which have undergone important changes, or in which our knowledge has made significant progress, either through more detailed design or experimental verification by prototypes and models. Hereafter we follow a similar line of presentation to that of the Pink Book.

2.1 Temperature levels and heat loads

The set of temperature levels envisaged for the LHC cryogenic system has been essentially maintained, with some minor adaptations in order to match the thermodynamic cycles of the now existing LEP 200 cryogenic plants [56], supplied by two different manufacturers, which will be used for LHC refrigeration after suitable modification and upgrade. These temperature levels are:

- Thermal shielding between 50 K and 75 K as a first major heat intercept sheltering the cold mass from the bulk of heat inleaks from ambient temperature;
- Distribution of supercritical helium at 4.5 K for initial filling of the cryomagnets and lower temperature heat interception in operation; as previously, this circuit is used for non-isothermal cooling of the beam screens between 4.5 K and 20 K (instead of 10 K), a change which preserves the vacuum performance of the cold bore and beam screen cryopumping system and better matches the cryogenic plants, while reducing the entropic load resulting from beam-induced losses (synchrotron radiation and image currents) falling on the beam screens;
- Quasi-isothermal superfluid helium cooling the magnet cold mass at a maximum temperature of 1.9 K and transporting the applied heat loads across the length of half-octants (1670 m) to the cryogenic refrigerators operating at 1.8 K, thus allowing an overall temperature drop of 0.1 K [57];
- Normal helium cooling special superconducting magnets in insertion regions at a saturation temperature between 4.5 K and 4.7 K due to hydrostatic head between machine tunnel and refrigerator level;
- Liquefaction at 4.5 K for current-lead cooling.

The implementation of the first three temperature levels in the standard LHC dipole cryomagnet is shown in the cross-section of Fig. 9. Although the basic design concepts of the cryostat have shown little evolution with respect to the Pink Book version, the expected thermal performance has been assessed with better confidence through several independent, yet converging approaches:

- Thermal calculations, conducted on the basis of the detailed construction drawings established for industrial manufacturing of full-scale prototypes, have allowed us to refine heat inleak estimates and perform parametric sensitivity studies concerning the prototype dipole [44] and short straight section [49] cryostats, including auxiliaries and interconnection regions [58];

- Critical components of the cryostat thermal insulation system, e.g. radiative insulation [59] and cold-mass support posts [45, 60], have been developed, investigated and thermally validated by precision heat-inleak measurements;
- Global measurements performed on the quasi full-scale Twin-Aperture Prototype (TAP) cryomagnet [33, 61, 62] have confirmed the technical feasibility of efficient cryostats housing 10 m-long superconducting magnets operating with superfluid helium.

Besides heat inleaks from the ambient temperature environment, the cryogenic components of the LHC will be subject to heat loads of two other kinds.

Resistive dissipation in the non-superconducting sections of the magnet excitation circuits (essentially current feedthroughs and splices in the superconducting cables) has been reduced to an average of 0.064 W/m, as a result of the change to 12 kA in the maximum excitation current of the main magnets, and assuming a residual resistance per splice of 6×10^{-10} Ω [63].

Heat loads deposited in the magnet cold mass, through several processes, by the circulating and colliding proton beams have also been re-evaluated:

- Synchrotron radiation from the bending magnets, mostly absorbed by the beam screens, amounts to a maximum average power of 0.81 W/m for the two beams [63], in the arcs and dispersion suppressors;
- Resistive heating due to image currents induced in the conducting walls of the beam channels has scaled down to 0.68 W/m for the two beams [63], all around the circumference of the machine;
- Continuous loss of particles from the circulating beams, produced by nuclear inelastic beam-gas scattering, results in a distributed heat load of 0.115 W/m all around the circumference of the machine;
- Continuous loss of particles due to collimator inefficiency results in a locally deposited heat load estimated to be about 30 W in each arc over a length of a few tens of metres corresponding to the region of aperture restriction;
- Absorption of secondaries in the cold mass of the superconducting magnets located close to the high-luminosity experimental areas (inner triplet of low-beta quadrupoles and beam recombination dipole) will deposit large heat loads at the 1.9 K level [5].

The heat load estimates based on the above assumptions are given in Tables 61 and 62 for standard-cell dipoles and short straight sections, respectively, and include auxiliaries and one interconnection region per cryostat. From these data, the heat loads corresponding to a standard half-cell (Table 63) and an arc (Table 64) have been assessed in three cases of interest for the cryogenic operation of the machine, namely:

- 'Normal operation' at full beam energy and luminosity;

- 'Low beam intensity operation', still with full beam energy and thus full excitation current in the magnets;
- 'Injection standby', characterized by negligible resistive dissipation and beam-induced heat loads in the magnets.

For the purpose of comparison with the Pink Book estimates, the average distributed heat loads in nominal operation in an arc of the LHC are presented in Table 65, showing marked decrease at the 4.5–20 K level, as a consequence of the reduction in heat loads due to synchrotron radiation and image currents. The significant reduction in resistive dissipation, however, is totally offset by the strong rise in beam-gas inelastic scattering, which yields a global increase in the 1.9 K heat load.

Since the detailed design of the superconducting magnets in the insertions has not yet been finalized, their expected heat loads have been assessed by approximate scaling from the better-defined arc magnets. The results, displayed in Table 66, reflect the variations in geometry, layout, functions and operating modes of the different LHC insertions.

Compounding the above results yields the global estimates of heat loads in the octants of the LHC, presented in Table 67 for the three previously defined modes of operation. Clearly octants 1 and 2, which house high-luminosity experiments, are subject to the largest low-temperature heat loads, while octant 3, which features the longest string of cryogenic components in the beam-cleaning insertion, exhibits the largest 50–75 K and 4.5–20 K heat loads. Also evident from Table 67 are the wide ranges of variation of the cooling power requirements at 1.9 K and 4.5–20 K, which the octant cryogenic plants will have to follow during LHC operation.

2.2 Ring cooling system

The essential principles of magnet string cooling have not changed since the Pink Book. The magnets operate in static baths of pressurized superfluid helium, through which heat is transported by conduction to a linear cold source constituted by a heat exchanger tube threading its way through the string, and in which heat is absorbed quasi-isothermally by gradual vaporization of flowing saturated superfluid helium (Fig. 52). This concept is implemented in independent cooling loops, each extending over 51 m, the length of a half-cell of the regular lattice (Fig. 53). With respect to the scheme proposed in the Pink Book, one notices the suppression of the recirculation pump on the saturated superfluid helium circuit, a simplification made possible by letting the liquid fully vaporize and thus allowing local dryout in the heat exchanger tube.

Following exploratory tests conducted at about half-scale [64, 65] this mode of operation has been successfully implemented in a 20 m-long thermohydraulic model loop [66] where the cold mass of the cryomagnets was simulated by 10 m-long cylindrical chambers connected in series, filled with pressurized superfluid helium and cooled by a quasi full-scale corrugated-tube heat exchanger (Fig. 54). The stability of the saturated two-phase flow, as well as the excellent heat transfer characteristics of the heat exchanger tube when wetted along its whole length (Figs. 55 and 56), have indeed permitted the operation of the heat exchanger in partial dryout and thus suppressed the need for liquid recirculation; in this way, advantage is also taken of the longitudinal conduction in the static pressurized superfluid helium to transport heat to the fully wetted stretch of the heat exchanger [67].

Also appearing in Fig. 53 is the hydraulic separation plug between successive half-cells, which prevents the buildup of hydrostatic head in the static pressurized helium circuit due to change in elevation along the half-octant, while leaving a passage for the superconducting electrical bus bars that connect the magnets in series. The normal helium circuits in the half-cell cryogenic flow-scheme show no major change. Still, it is worth noting that Fig. 53 reflects the thermal separation of the 50–75 K supply and return circuits apparent in the standard dipole cross-section (Fig. 9), with supply pipe E intercepting heat on the support posts and return pipe F convection-cooling the shell of the cryostat thermal shield.

2.3 Cryogenic plants

On the basis of the revised heat load estimates for the LHC octants, and allowing for some spare capacity, the refrigeration and liquefaction requirements to be simultaneously fulfilled by the cryogenic plants in each octant are listed in Table 68. With respect to Pink Book values, the main changes concern the 4.5–20 K and the 1.8 K refrigeration capacities as well as the liquefaction duties. The 4.5–20 K non-isothermal refrigeration capacity has been significantly reduced, thus reflecting the marked decrease in beam-induced loads to the beam screens. Conversely, taking into consideration the large power deposited by secondaries in the inner triplet quadrupoles at high-luminosity collision points has raised the 1.8 K refrigeration duty to 3 kW in octants 1 and 2. For all octant cryogenic plants, the precise definition of the powering circuits has significantly increased the number of helium vapour-cooled current leads, and thus the liquefaction requirement, which now represents a large fraction of the total load.

With the possible exception of the high-luminosity collision areas 1 and 2, it appears that the highest entropic load applied to any octant could still be extracted by a cryogenic plant of an equivalent refrigeration capacity of about 18 kW at 4.5 K, i.e. within reach of the upgraded and suitably modified LEP 200 installations [68]. A detailed study involving the manufacturers of these cryogenic plants is under way aiming at assessing their effective capacity in LHC operation and defining the required adaptations and modifications. The general layout of the cryogenic components and their interconnections in a standard octant appear in Fig. 57.

Of particular interest is the special configuration proposed for octant 3, where each half-octant will be served by its own refrigerator. This solution was imposed by siting and geotechnical constraints that forbid any additional large civil engineering construction, either underground or at surface level in the vicinity of interaction point 3 (see Part II, Technical Description, Annex III for details). The octant cryogenic plant is then replaced by two refrigerators of half-capacity, each located in a cavern close to the beginning of the arc, some 250 m away from the interaction point proper. Both refrigerator coldboxes will be fed with high-pressure helium from a compressor station located in the existing service area around PM32.

Preliminary studies have been conducted on the cold compressor systems required in each octant for producing the refrigeration at 1.8 K. In order to cope with the overall pressure ratio exceeding 70, and a dynamic range of 2:1, each system will require five stages of cold centrifugal compressors connected in series [69]. Further work is to be done on the precise definition of the 1.8 K cycle, as well as on technological development of such machines. The start-up and commissioning of the CEBAF cryogenic system [70], which features cold compressors of a type and size comparable with those required for the LHC, in a four-stage configuration, will also provide useful data and precious experience on this key technology.

2.4 Helium inventory

A more precise assessment of the helium inventory in the LHC [71] has led to a total amount of 93 500 kg, mostly in the cold mass of the magnet system. Integrally storing this inventory in conventional form, i.e. gas at 2 MPa and 300 K, will result in large investment costs and siting difficulties due to the high visibility of the 250 m^3 reservoirs envisaged for this purpose [72]. Two complementary lines of action are being pursued in order to reduce the LHC helium storage problem:

- Reduction of the inventory inside the magnet cold mass to the minimum required for thermal buffering of rapid thermal transients and for conductive heat transport in pressurized superfluid helium towards the heat exchanger cold source;
- Partial storage in liquid form in a central storage or in standard 11 000-gallon (about 40 000-litre) industrial containers compatible with liquid helium handling by European distributors.

In any case, a minimum amount of medium-pressure gas storage will need to be installed locally for operational flexibility, allowing in particular the immediate recovery of the helium discharged after the quench of a half-octant (see Fig. 58).

Table 61: Heat loads in dipole cryostats (no contingency)

Source of heat load	Temperature levels		
	50–75 K (W)	4.5–20 K (W)	1.9 K (W)
Heat inleaks			
Cold mass			
Support posts	18.1	1.82	0.14
Thermal shield	65.3		
Radiative insulation		0.27	1.28
Safety valve	0.36		0.40
Instrumentation feedthroughs	0.43		0.24
Interconnection			
Thermal shield	4.3		
Radiative insulation		0.01	0.06
Total	88.5	2.10	2.11
Resistive heating			
Cold mass (7 splices)			0.60
Interconnection (2 splices)			0.17
Total	0	0	0.78
Beam-induced heating			
Synchrotron radiation		11.81	0.20
Image currents		9.92	
Beam-gas scattering			1.68
Total	0	21.73	1.88
Total heat load	88.5	23.84	4.77

Table 62: Heat loads in short straight section (no contingency)

Source of heat load	Temperature levels 50–75 K (W)	4.5–20 K (W)	1.9 K (W)	Liquid helium consumption (mg/s)
Heat inleaks				
Cold mass				
Support posts	12.1	1.21	0.09	
Thermal shield	25.9			
Radiative insulation		0.11	0.42	
Safety valve	0.36		0.40	
Instrumentation feedthroughs	0.43		0.24	
Vacuum barrier	9.78	0.18	0.65	
QSA	4.72	0.14	0.95	
BPM	2.02		0.58	
Dipole corrector feedthroughs				5.4
Interconnection				
Thermal shield	4.33			
Radiative insulation		0.01	0.06	
Beam vacuum feedthroughs	0.91		0.01	
Total	60.5	1.65	3.39	5.4
Resistive heating				
Cold mass (9 splices)			0.78	
Interconnection (2 splices)			0.17	
Dipole corrector feedthroughs				3.6
Total	0	0	0.95	3.6
Beam-induced heating				
Synchrotron radiation		5.89	0.10	
Image currents		4.94		
Beam-gas scattering			0.84	
Total	0	10.83	0.94	0
Total heat load	60.5	12.48	5.28	9.0

Table 63: Heat loads for a half-cell (3 dipoles + 1 short straight section)

Mode	Temperature levels 50–75 K (W)	4.5–20 K (W)	1.9 K (W)	Liquid helium consumption (mg/s)
Normal operation	326	84.0	19.6	9.0
Low beam intensity operation	326	7.96	13.0	9.0
Injection standby	326	7.96	9.73	5.4

Table 64: Heat loads for an arc (48 half-cells +1 mid-arc box)

Mode	Temperature levels 50–75 K (W)	4.5–20 K (W)	1.9 K (W)	Liquid helium consumption (g/s)
Normal operation	15682	4033	941	0.43
Low beam intensity operation	15682	384	626	0.43
Injection standby	15682	384	468	0.26

Table 65: Distributed heat loads in nominal operation in an arc (no contingency)

Source of heat load	Temperature levels 50–75 K (W/m)	4.5–20 K (W/m)	1.9 K (W/m)
Heat inleaks	6.4	0.16	0.19
Resistive heating			0.064
Beam-induced heating		1.49	0.129
Total	6.4	1.65	0.38

Table 66: Heat loads in half-insertions (no contingency)

	Temperature levels				Liquid helium consumption
Source of heat load	50–75 K (W)	4.5–20 K (W)	4.7 K (W)	1.9 K (W)	(g/s)
High luminosity insertions 1 and 2					
Heat inleaks	1798	37.1	2.5	50.9	10.3
Resistive heating			0.5	15.7	6.8
Synchrotron radiation		140.7			
Image currents		118.2	10.2	59.8	
Beam-gas scattering			1.7	30.1	
Secondary particle losses			156.0	325.0	
Total	1798	296.0	170.9	481.4	17.0
Cleaning insertion 3					
Heat inleaks	2647	38.3	20.1	35.8	6.9
Resistive heating			2.2	11.7	4.5
Synchrotron radiation		140.7			
Image currents		118.2	124.1	11.2	
Beam-gas scattering			21.0	21.9	
Total	2647	297.2	167.4	80.5	11.4
Low-beta insertion 4					
Heat inleaks	1798	37.1	102.5	50.9	11.3
Resistive heating			0.5	15.7	6.8
Synchrotron radiation		140.7			
Image currents		118.2	10.2	59.8	
Beam-gas scattering			1.7	30.1	
RF losses			200		
Total	1798	296.0	314.9	156.4	18.0
Beam dump insertion 5					
Heat inleaks	1527	31.5	5.6	40.6	7.2
Resistive heating			0.5	13.4	4.7
Synchrotron radiation		140.7			
Image currents		118.2	13.3	29.0	
Beam-gas scattering			2.2	24.9	
Total	1527	290.4	21.6	107.8	12.0
Empty insertions 6 and 7					
Heat inleaks	1910	34.0	5.2	46.2	6.3
Resistive heating			0.4	14.3	4.1
Synchrotron radiation		140.7			
Image currents		118.2	15.2	54.9	
Beam-gas scattering			3.3	29.3	
Total	1910	292.8	24.1	144.7	10.4
Injection insertion 8					
Heat inleaks	1798	37.1	2.5	50.9	10.3
Resistive heating			0.5	15.7	6.8
Synchrotron radiation		140.7			
Image currents		118.2	10.2	59.8	
Beam-gas scattering			1.7	30.1	
Total	1798	296.0	14.9	156.4	17.0

Table 67: Heat loads in octants (no contingency)

Mode	Temperature levels				Liquid helium consumption
	50–75 K (W)	4.5–20 K (W)	4.7 K (W)	1.9 K (W)	(g/s)
Octants 1 and 2					
Normal operation	19279	4625	342	1935	34.5
Low beam intensity operation	19279	459	6	759	34.5
Injection standby	19279	459	5	569	20.8
Octant 3					
Normal operation	20976	4628	335	1133	23.2
Low beam intensity operation	20976	461	45	721	23.2
Injection standby	20976	461	40	539	14.1
Octant 4					
Normal operation	19279	4625	630	1285	36.5
Low beam intensity operation	19279	459	606	759	36.5
Injection standby	19279	459	205	569	22.8
Octant 5					
Normal operation	18735	4614	43	1188	24.4
Low beam intensity operation	18735	447	12	733	24.4
Injection standby	18735	447	11	549	14.7
Octants 6 and 7					
Normal operation	19503	4619	48	1261	21.2
Low beam intensity operation	19503	452	11	747	21.2
Injection standby	19503	452	10	560	12.8
Octant 8					
Normal operation	19279	4625	30	1285	34.5
Low beam intensity operation	19279	459	6	759	34.5
Injection standby	19279	459	5	569	20.8

Table 68: Installed cryogenic power requirements

Source of heat load	Temperature levels 50–75 K (kW)	4.5–20 K (kW)	4.7 K (kW)	1.9 K (kW)	Liquid helium consumption (g/s)
Octants 1 and 2	30	5.0	0.5	2.4	50
Octant 3*	2 × 16	2 × 2.5	2 × 0.2	2 × 1.0	2 × 17
Octant 4	30	5.0	1.1	2.0	53
Octant 5	30	5.0	0.1	2.0	36
Octants 6 and 7	30	5.0	0.1	2.0	31
Octant 8	30	5.0	0.1	2.0	50

*Two separate cryoplants.

3 Vacuum

The volume inside the magnet cryostat between the outermost wall and the 'cold bore' beam tubes inside the coil assemblies is a thermal insulation vacuum ($< 10^{-5}$ torr), and does not call for special remarks in this section.

The cold bores themselves, being in contact with the pressurized superfluid helium bath at 1.9 K, would reach a negligibly low residual gas density due to the low thermal outgassing and the large cryopumping if it were not for the fact that they would have to absorb the 0.82 W/m synchrotron radiation power (considerable for a 1.9 K cryogenic system) emitted by the beams. It is therefore necessary to introduce inside the cold bore a second tube surrounding the beam, the so-called 'beam screen', cooled to the considerably higher temperature range of 4.5–20 K by a gaseous helium flow. The inner walls of these beam screens, although less efficient, also act as cryopumps with the result that at the beginning of operation, and in the absence of beam, the residual gas density will be very low.

However, the very numerous and energetic photons of the synchrotron radiation from the proton beam will desorb gas molecules from the screen which then will stick again on it due to the cryopumping action. These physisorbed molecules will be exposed to the synchrotron radiation and rather easily re-desorbed (secondary desorption). Progressively more and more desorbed gas builds up on the walls of the screen until, when a monolayer or so of adsorbed hydrogen is exceeded, the thermal vapour pressure increases rapidly. The radiation and ion-induced secondary desorption coefficients also continue to increase.

Without any other measure there would be the risk of the gas density along the beam path exceeding by far the safe operational limit. In order to avoid this, holes will be drilled over a few per cent of the screen surface to permit the excess gas to migrate into the volume between the screen and the cold bore. These gas molecules will then be trapped on the 1.9 K wall of the cold bore without any risk of pressure run-away (very low temperature) or desorption, this tube being shielded from synchrotron irradiation.

3.1 Pressure and beam–gas lifetime

In the Pink Book [1] a beam lifetime of 24 hours given by nuclear scattering on the residual gas was taken as a working criterion to define an upper limit to the acceptable gas density. The beam lifetime is inversely related to the gas density. The corresponding pressure depends on the temperature. With this 24-hour beam–gas lifetime the energy deposition in the superconducting coils, due to beam–gas scattering at a beam current of 53 mA, is one order of magnitude lower than the quench level [6].

The synchrotron-radiation-induced gas desorption yields from unbaked Cu-plated stainless steel have been measured at room temperature and at a critical energy of 63.5 eV. This is close to the 45.4 eV corresponding to the present design energy (7.0 TeV) of the LHC [73, 74]. The resulting desorption yields are shown in Fig. 59 as a function of the photon dose and show a definite clean-up. Note that with a beam current of 0.053 A, the 10 Ah dose indicated in Fig. 59 will be reached after 7.9 days of operation. The desorption yields were very similar to those from bulk Cu.

For critical energies ε below 280 eV it was found that the desorption yields from Cu-plated stainless steel varied on average as $\varepsilon^{1.2}$. Since ε varies with beam energy E as E^3 and the photon flux varies with E, the gas pressure due to synchrotron radiation, which depends on the product of the desorption yield and the photon flux, varies as $E^{4.6}$.

3.1.1 *First-year operation*

The initial commissioning of the machine will be made with beam currents much less than the design value of 0.53 A [75]. It is expected that the LHC would be operated with one-tenth of the design current during the first year of operation, gradually increasing to full current over the following two to four years. We have therefore assumed that the LHC will start up at 7.0 TeV and 0.053 A, and have based our calculations of the behaviour of the vacuum system on these parameters.

The desorption yields measured at room temperature have been extrapolated to the slightly lower critical energy, and the residual gas densities calculated for the LHC with a beam screen at 5 K and the appropriate parameters of energy and initial beam current. The predicted behaviour is shown in Fig. 60. For convenience, all pressure increases due to photon-induced desorption have been expressed in H_2 equivalent gas densities, for example the CO_2 pressure increase has been converted to gas density at 5 K and multiplied by the nuclear scattering cross-section for protons on CO_2 relative to protons on H_2.

At start-up the initial beam–gas lifetime due to nuclear scattering will be about 1330 hours. It is seen that CO_2 followed by CO are the dominant gas species determining the equivalent density and hence the lifetime.

After about 22 Ah of running the desorption yields will have decreased considerably resulting in a lifetime of 4800 hours. However, at this stage the surface will have accumulated about one monolayer of condensed hydrogen and, as a result, the H_2 thermal vapour pressure will start to increase. A transparency of 2% of holes in the beam-screen surface will limit and stabilize the H_2 gas density to an increase of a factor of 50. Adding this to the total gas density would increase the latter by a factor of 2.2 and hence reduce the lifetime to about 2180 hours.

3.1.2 Operation at full intensity

As the operating intensity of the LHC approaches the design level of 0.53 A, the equilibrium pressure to the right-hand side of Fig. 60 will increase by a factor 10 in the absence of further beam cleaning. This would reduce the beam lifetime to a still acceptable 218 hours – a minimum figure in view of the inevitable additional beam cleaning which will occur.

3.2 Secondary desorption

Very recent, and as yet incomplete, measurements made at Novosibirsk [76] seem to confirm our concern that the incident synchrotron radiation will also continually re-desorb H_2 and other gases from the condensed layer which is being progressively built up on the screen by the cryopumping action. Desorption from this layer is called secondary desorption. For H_2 over most of the range for which it has been measured, i.e. almost up to one monolayer at 4.2 K, the effect is greater for a level of the photon flux corresponding to 53 mA than the thermal vapour pressure. The result will be that the H_2 density will start to increase sooner than expected on the basis of thermal vapour pressure alone, i.e. well before the 22 Ah quoted above, but otherwise the behaviour and the final level will be the same. One has substituted photon-induced secondary desorption in place of thermal vapour pressure, but the principle of stabilization by the pumping holes remains the same. Similarly, secondary desorption by ion bombardment [77], which could otherwise lead to a run-away ISR-type pressure bump, will also be stabilized.

A transparency of 2% of holes will also limit to a factor of 50 any increase of the other gas densities by these as yet incompletely quantified secondary desorption mechanisms. A worst case situation involving secondary desorption of all gases would result in a decrease of the beam lifetime during first-year operation and after 22 Ah of beam cleaning to 96 hours – still a comfortable figure.

3.3 Beam-screen treatments

It has been shown [74] that a pretreatment at 300°C under vacuum of the Cu-plated stainless steel test chamber before installation can result in considerable improvements in the desorption yields for certain gases, e.g. a factor of 40 reduction for H_2O. Moreover, since temperatures up to 500°C for 24 hours have little influence on the electrical conductivity of the Cu layer [78] this treatment could further improve the situation.

The effect of an argon glow discharge will also be examined.

3.4 Ongoing experimental programme

It must be stressed that Fig. 60 is very schematic and gives only a simple picture of the situation at 5 K. The desorption yields used were measured at room temperature, when, in reality, the beam screen will be at a temperature between 4.5 K and 20 K, where the Novosibirsk data already indicate that the H_2 desorption yields may be up to a factor of 10 less. In addition, the condensed gas layer will not be pure H_2 but a mixture of gases. How these factors will modify Fig. 60 is not certain, but this will be clarified when the ongoing measurements of adsorption isotherms of gas mixtures at temperatures above 4.2 K and electron- and ion-induced gas desorption from condensed gas layers are completed, and when better data for adsorption yields at low temperature are available.

The adsorption isotherm for pure H_2 at 4.2 K on the same Cu-plated stainless-steel surface has been measured [79] and is shown in Fig. 61. There it can be seen that the gas density (vapour pressure) starts to rise around 2×10^{15} mol/cm^2. It is this figure which is defined as the monolayer coverage and has been used in Fig. 60 to deduce the point of increasing H_2 density at 22 Ah of machine operation.

3.5 Helium leaks

It has only recently been appreciated [80, 81] that a helium leak into the beam vacuum, which has surfaces at 1.9 K, may take many days before it is detected at a vacuum gauge or ion pump at a distance of a half-cell or full cell, even though the leak may already be of such a magnitude as to scatter a number of protons into the magnets to cause a quench. Detection of such local pressure bumps may be possible via external ionization chambers or by running the LHC with an unbunched beam and extracting the electrons coming from ionization of the residual gas and which are trapped by the positive space-charge of the beam. The electron current is proportional to the pressure and may be measured on suitably polarized plates placed at fixed intervals around the machine.

3.6 Beam-screen design

In order to maximize the horizontal and vertical apertures available for the beam, while still leaving some space for the helium cooling tubes, a rectangular cross-section has been proposed. This is shown schematically in Fig. 62 where 43 mm are available in both planes.

To minimize the coupling impedance of the beam screen the interior surface must have a high electrical conductivity. A suitable material would be Cu which can be deposited by electroplating. The test chamber for the synchrotron-radiation-induced gas desorption measurements was electroplated by a special process [82] using a pyrophosphate solution and a pulsed reversed-current technique. Plating consisted of a 0.1 μm Ni layer followed by a 0.2 μm Au layer then a 100 μm Cu layer. The resulting Cu layer was relatively flat and dense [83] and had a thermal outgassing rate similar to that of stainless steel [84]. The adherence of the Cu to the stainless steel still has to be checked.

3.6.1 Pumping holes

The pumping holes in the beam screen represent discontinuities for the image currents of the beam and result in a beam coupling impedance. An additional effect comes in the high-frequency range from the real part of the impedance. Power is coupled through the holes into the coaxial space between the beam screen and the vacuum chamber and propagates in synchronism with the beam, gradually building up in strength and leaking back into the beam screen, further adding to the real part of the coupling impedance [85].

This power is dissipated in both the outer beam-screen wall and the 1.9 K inner vacuum-chamber wall. For example, in the LHC, with both walls in stainless steel, i.e. the same resistivity, for 5% of the surface covered with 2.5 mm diameter holes and 1 mm beam-screen wall thickness the power dissipated per metre in the 1.9 K surface is 0.12 W/m whereas the calculated heat dissipation in the 1.9 K from all other sources is 0.26 W/m. Thus 5% of 2.5 mm diameter holes increase the heat load on the cryogenic system by about 50%. For 5% of 1 mm diameter holes the power dissipation in the 1.9 K surface is negligible.

Possibly more critical is the low-frequency imaginary (inductive) part of the impedance coming from the holes. An advantage may be gained by having short slots rather than round holes. For example, a slot 10 mm × 1 mm has an inductive impedance about a factor of 2 less than 10 holes, each of 1 mm diameter [86].

3.6.2 Stainless steel permeability

The conventional stainless steels such as 304 L and 316 L can have magnetic permeabilities at 4.2 K and 1 T of about 1.02 [87]. It has been shown [88] that the square beam-screen and its two cooling pipes with a permeability of 1.01 create non-negligible field distortion; thus special, low-permeability stainless steels may have to be used and/or four cooling pipes to reduce the effect of the asymmetry.

3.6.3 Quench forces

Recent calculations of the quench forces induced in the beam screen [89] have shown that the resulting stresses in the 100 μm thick Cu layer on the inside of the present square section are excessive in the corners. Solutions include increasing the thickness of the stainless steel or coating with Cu on the flat sides only, avoiding the corners.

3.6.4 Model work

During the manufacture of a 15 m length of beam screen, various operations such as brazing/welding of the cooling pipes and making of the pumping holes may introduce distortions which will have to be removed. Since even the geometrical tolerances which can be provided on 15 m lengths of square section is unknown, it has been decided to order some sufficiently long ($\sim$ 10 m) square-section lengths from industry. These will be measured and subjected to the various manufacturing processes in order to obtain a better understanding of the final geometrical tolerances to be expected in the LHC.

3.7 Sector valves

To increase the reliability of the sector valves, a design with two sealing surfaces has been produced in collaboration with outside industry, and two prototypes for testing have been ordered.

3.8 Conclusion

It has been shown that the proposed design of the LHC beam vacuum with a perforated beam screen is feasible. All possible effects are still not quantified and further research and development will provide the necessary data. The perforated beam screen exploits the unique cryopumping capabilities afforded by the magnet cold bore at 1.9 K and, as argued in the Pink Book, this concept automatically provides a versatile 'safety net' as exemplified by the discussion on the recently confirmed photon-induced secondary desorption.

References

[1] The LHC Study Group, Design Study of the Large Hadron Collider (LHC): a multiparticle collider in the LEP tunnel, CERN 91–03 (1991).

[2] LEP design report, Vol. 1, The LEP injector chain, CERN–LEP–TH/83–29, CERN–PS–DL/83–31, CERN–SPS/83–26 and LAL/RT/83–09 (1983);
LEP design report, Vol. 2, The LEP main ring, CERN–LEP/84–01 (1984).

[3] C. Rufer, LHC version II insertion layout, AC/DI/FA/Note 93–04.

[4] G. Stevenson and K. Potter, Monte Carlo computations (private communications).

[5] K. Eggert and A. Morsch, Particle losses in the LHC interaction regions, CERN–AT/93–17 and LHC Note 229 (1993).

[6] L. Burnod and J.B. Jeanneret, Beam losses and collimation in the LHC: a quantitative approach, CERN–SL/91–39 and LHC Note 167 (1991).

[7] L. Burnod and J.B. Jeanneret, Scenarios for beam losses in LHC, AC/DI/FA/Note 92–05.

[8] L. Burnod and J.B. Jeanneret, Updating the systematic losses, AC/DI/FA Note 93–02 (1993).

[9] L. Burnod and D. Leroy, Influence of beam losses on the LHC magnet, LHC Note 65 (1987).

[10] J.B. Jeanneret, Momentum losses and momentum collimation in LHC, a first approach, CERN–SL/92–44 (EA) and LHC Note 211 (1992).

[11] J.B. Jeanneret, SL/Note 92–65 (EA) (1992).

[12] T. Trenkler, LHC Note 217 (1993).

[13] T. Trenkler, The optimum phase advance in a two-stage collimation system, CERN–SL/92–50 (EA) (1992).

[14] L. Burnod, J.B. Jeanneret and T. Trenkler, The optics and layout of the cleaning insertion of the LHC for a combined betatron and momentum collimation system, SL/Note 93–45 (1993).

[15] P.J. Bryant, N. Galante, E. Klein and T. Taylor, CERN–SL/93–15 (1993).

[16] D. Boussard and V. Rödel, The LHC RF system, Proc. XV Int. Conf. High Energy Acc., Hamburg, July 1992.

[17] T. Bohl and D. Boussard, 400 MHz superconducting cavities in the SPS, CERN–SL–RFS Note/93–47.

[18] D. Boussard and E. Onillon, Damping of phase errors at injection in the LHC, Proc. Part. Acc. Conf., Washington DC, 17–20 May 1993.

[19] E. Brouzet and K.H. Schindl (ed.), Heavy ions in the LHC, CERN–SL/Note 93–60 (AP), PS/DI Note 93–18 (tech.), LHC Note 225.

[20] D. Brandt, E. Brouzet and J. Gareyte, Heavy ions in the SPS–LHC complex, SL/Note 92–47 (AP) and LHC Note 208.

[21] D. Warner (ed.) et al., CERN heavy-ion facility design report, CERN 93–01 (1993).

[22] D. Brandt et al., Production of lead ions for the CERN Large Hadron Collider (to be published).

[23] P. Lefèvre, D. Möhl, A low energy accumulation ring of ions for LHC, LHC Note 237.

[24] The LHC Magnet Team, presented by R. Perin, Status report on the LHC magnets, Proc. 3rd World Congress on Superconductivity, Munich, 1992 (Pergamon Press, 1993), pp. 1487–1502.

[25] M. Bona, D. Leroy, R. Perin, P. Rohmig, B. Szeless and W. Thomi, Design, fabrication variants and results of LHC twin-aperture models, IEEE Trans. Magn. **28**, 338–341 (1992).

[26] D. Leroy et al., Test results on 10 T LHC superconducting one-meter long dipole models, IEEE Trans. Appl. Supercond. **3**, 614–621 (1993).

[27] J.L. Borne, D. Bouichou, D. Leroy and W. Thomi, Manufacturing of a 10 T twin-aperture superconducting dipole magnet for LHC, IEEE Trans. Magn. **28**, 323–326 (1992).

[28] F. Zerobin, D. Leroy and B. Szeless, Fabrication and test of a LHC NbTi model magnet with a split collar system, IEEE Trans. Magn. **28**, 327–330 (1992).

[29] H. Boschman, H.J. Israël, R.L. Dubbeldam, D. Leroy and P. Rohmig, Fabrication and test results of a twin-aperture superconducting dipole model magnet for LHC, IEEE Trans. Appl. Supercond. **3**, 765–768 (1993); LHC Note 203.

[30] A. Yamamoto et al., Development of 10 T dipole magnets for the Large Hadron Collider, IEEE Trans. Appl. Supercond. **3**, 769–772 (1993).

[31] The LHC Machine Group, presented by G. Brianti, LHC progress and status, Proc. Part. Acc. Conf., Washington DC, 17–20 May 1993; LHC Note 221.

[32] The LHC Magnet Team, presented by R. Perin, Status of the Large Hadron Collider magnet development, 13th Int. Conf. on Magnet Technol., Victoria, Canada, 20–24 September 1993; LHC Note 244.

[33] M. Granier, D. Hagedorn, K.N. Henrichsen, Ph. Lebrun, D. Leroy, R. Perin, J. Vlogaert, J. Deregel, P. Genevey, J.P. Jacquemin, F. Kircher and J. Le Bars, Performance of the twin-aperture dipole for the CERN LHC, Proc. EPAC92, Berlin, March 1992; LHC Note 179 (1992).

[34] J.M. Rifflet et al., Status of the fabrication and test of the prototype LHC lattice quadrupole magnet, 13th Int. Conf. on Magnet Technol., Victoria, Canada, 20–24 September 1993.

[35] H. Bidaurrazaga et al., Design and fabrication of the prototype superconducting tuning quadrupole and octupole correction winding for the LHC project, IEEE Trans. Magn. **28**, 342–345 (1992).

[36] A. Ijspeert et al., Development of a superconducting sextupole–dipole corrector magnet, Proc. 11th Int. Conf. on Magnet Technol. (MT11), Tsukuba, Japan, 1989 (Elsevier, London, 1990), Vol. 1, pp. 200–205.

[37] E. Baynham et al., Construction and tests of a model of the LHC superconducting corrector magnet MDSBV, LHC Note 155 (1991).

[38] A. Ijspeert at al., Test results of the prototype combined sextupole–dipole corrector magnet for LHC, LHC Note 201 (1992).

[39] E. Baynham et al., Design of superconducting corrector magnets for LHC, 13th Int. Conf. on Magnet Technol., Victoria, Canada, 20–24 September 1993.

[40] R. Ostojic, T.M. Taylor and G.A. Kirby, Design and construction of a one-metre model of the 70 mm aperture quadrupole for the LHC low-β insertions, 13th Int. Conf. on Magnet Technol., Victoria, Canada, 20–24 September 1993.

[41] B. Baudouy, C. Meuris, M.X. François, D. Leroy, L. Burnod and B. Szeless, Transfert thermique dans l'isolation de câbles supraconducteurs d'accélérateurs refroidis par helium superfluide, 4e Journées d'Aussois, 12–14 Mai 1993.

[42] R. Wolf, Persistent currents in LHC magnets, IEEE Trans. Magn. **28**, 374–377 (1992).

[43] S. Russenschuck and T. Tortschanoff, Optimization of the coil of the LHC main dipole, LHC Note 206;
Estimation of the errors of conductor positioning in the LHC main magnets from a given multipole content, LHC Note 204, papers presented at CEFC Conf. on Electromagn. Field Computation, Claremont, Ca., July 1992.

[44] J.C. Brunet, J. Kerby, Ph. Lebrun, P. Rohmig, B. Szeless and L.R. Williams, Design of the LHC prototype dipole cryostats, Cryogenics, **32** (1992) ICEC Supplement; LHC Note 195 (1992).

[45] M. Blin, H. Danielsson, B. Evans and M. Mathieu, Design, construction and performance of superconducting magnet support posts for the Large Hadron Collider, LHC Note 235 (1993).

[46] E. Menant and J.P. Quesnel, Reference target positioning, CAS Magnetic Measurement and Alignment, Montreux, 16–20 March 1992.

[47] N. Siegel, Strength of LHC tuning quadrupole, Internal Note AT–MA/91–26 (1991).

[48] A. Ballarino and A. Ijspeert, Expected advantages and disadvantages of high-Tc current leads for the Large Hadron Collider, submitted to the Cryogenic Engineering Conf., Albuquerque, USA, 12–16 July 1993.

[49] W. Cameron, B. Jenny, G. Riddone, P. Rohmig and R. van Weelderen, Design and construction of a prototype superfluid helium cryostat for the short straight sections of the CERN Large Hadron Collider (LHC), LHC Note 237 (1993).

[50] T.M. Taylor and R. Ostojic, Conceptual design of a 70 mm aperture quadrupole for LHC insertions, IEEE Trans. Appl. Supercond. **3**, 761–764 (1993).

[51] D. Hagedorn and L. Coull, Radiation resistant quench protection diodes for the LHC, submitted to the Cryogenic Engineering Conf., Albuquerque, USA, 12–16 July 1993, LHC Note 226 (1993).

[52] L. Coull, D. Hagedorn, V. Remondino and F. Rodriguez-Mateos, LHC magnet quench protection system, 13th Int. Conf. on Magnet Technol., Victoria, Canada, 20–24 September 1993.

[53] F. Clari et al., A prototype warm-bore anti-cryostat for LHC magnet measurements, CERN–AT–MA Internal Note 93–73.

[54] D. Leroy et al., Quench observation in LHC superconducting one-metre-long dipole models by field perturbation measurements, IEEE Trans. Appl. Supercond. **3**, March 1993; LHC Note 199.

[55] P. Sievers, Principle of the magnetic measurement of the LHC dipoles, LHC Note 168 (1991).

[56] M. Barranco-Luque, J.P. Dauvergne, W. Erdt, P. Frandsen, D. Güsewell, F. Haug, A. Juillerat, G. Passardi, J. Schmid and G. Winkler, The refrigeration system for the LEP upgrade, Cryogenics, **30**, September Supplement, pp. 136–142 (1990).

[57] L. Tavian, Abaissement de la température de fonctionnement du LHC de 1.9 K à 1.8 K: faisabilité et implications, Note LHC 154 (1991).

[58] G. Riddone, Bilancio termico della semicella prototipo dell'acceleratore di particelle L.H.C., Tesi di Laurea in Ingegnera Nucleare, Politecnico di Torino (1993).

[59] Ph. Lebrun, L. Mazzone, V. Sergo and B. Vullierme, Investigation and qualification of thermal insulation systems between 80 K and 4.2 K, LHC Note 189 (1992).

[60] H. Danielsson, Ph. Lebrun and J.M. Rieubland, Precision heat inleak measurements on cryogenic components at 80 K, 4.2 K and 1.8 K, LHC Note 190 (1992).

[61] M. Granier, Ph. Lebrun and M. Mischiatti, Design and construction of a superfluid helium cryostat for a ten metre long high-field superconducting dipole magnet, Cryogenics, **30**, September Supplement, pp. 98–102 (1990).

[62] J. Deregel, P. Genevey, J.P. Jacquemin, F. Kircher, J. Le Bars, A. Le Coroller, K.N. Henrichsen, Ph. Lebrun and J. Vlogaert, Cryogenic and magnetic tests of the twin-aperture prototype dipole in the Saclay Test facility, IEEE Trans. Appl. Supercond. **3**, No. 1, pp. 777–780 (1993), (Proc. ASC 92, Chicago, 1992).

[63] L. Burnod (private communication).

[64] A. Cyvoct, Ph. Lebrun, M. Marquet, L. Tavian and R. van Weelderen, Heated two-phase flow of saturated helium II over a length of 24 m, LHC Note 169 (1991).

[65] J. Casas, A. Cyvoct, Ph. Lebrun, M. Marquet, L. Tavian and R. van Weelderen, Design concept and first experimental validation of the superfluid helium system for the Large Hadron Collider (LHC) project at CERN, LHC Note 191 (1992).

[66] A. Bézaguet, J. Casas-Cubillos, Ph. Lebrun, M. Marquet, L. Tavian and R. van Weelderen, The superfluid helium model cryoloop for the CERN Large Hadron Collider (LHC), LHC Note 233 (1993).

[67] J. Casas-Cubillos and R. van Weelderen, Modèle de simulation de la dynamique du transfert de chaleur dans une boucle cryogénique d'hélium superfluide, Note LHC 223 (1993).

[68] L. Tavian, Utilisation des réfrigérateurs LEP 200 pour LHC: conditions de fonctionnement et interfaces, Note LHC 164 (1991).

[69] J. Ph. Guignard, Contribution à l'étude de la stabilité de fonctionnement et de l'adaptation de charge des compresseurs centrifuges cryogéniques multiétages, Travail d'option "Machines–Energétique", Ecole des Mines de Paris (1993).

[70] C.H. Rode, D. Arenius, W.C. Chronis, D. Kashy and M. Keesee, 2.0 K CEBAF cryogenics, Adv. Cryog. Eng. **35A**, pp. 275–286 (1990).

[71] L. Tavian, Stockage hélium et interconnexion des différents points du système cryogénique du LHC, Note LHC 198 (1992).

[72] B. Bianchi, A. Dagan, G. Mazzone, R. Principe, A. Scaramelli and L. Tavian, Compte rendu du groupe de travail pour le stockage de l'hélium du LHC (communication privée).

[73] J. Gómez-Goñi, O. Gröbner and A.G. Mathewson, CERN Vacuum Group Technical Note 93–01 (1993).

[74] J. Gómez-Goñi, O. Gröbner and A.G. Mathewson, CERN Vacuum Group Technical Note 93–03 (1993).

[75] This publication, Part II, Technical Description, Section 14.3.

[76] V. Anashin, Budker Institute of Nuclear Physics, Novosibirsk, Russia (private communication).

[77] N. Hilleret and R. Calder, Proc. 7th Int. Vac. Congress, Vienna, Sept. 1977.

[78] J.M. Dalin and J. Hague, CERN MT Division Internal Report MT–SM–Mi/92–128/JMD/cl No. MT–SM/93–06 (1993).

[79] Erik Wallén (private communication).

[80] D. Edwards, Jr. and P. Limon, J. Vac. Sci. Technol. **15**, 1186 (1978).

[81] J.P. Hobson and K. M. Welch, Brookhaven National Laboratory Report, BNL–47434, AD/RHIC–111 (1992).

[82] J.C. Puippe and W. Saxer, Werner Flühmann AG, Ringstrasse 9, Dübendorf 1, CH-8600, Switzerland, XV Int. Conf. on High Energy Accelerators, Hamburg, 1992, Supercollider 4, Ed. J. Nonte (Plenum Press, New York, 1992).

[83] J.M. Dalin, CERN MT Division Internal Report MT–SM–MI/93–109/JMD/cl No. 93/03/30 (1993).

[84] Anne-Heidi Mokal Evensen, CERN Vacuum Group Technical Note 92–08 (1992).

[85] F. Caspers, E. Jensen and F. Ruggiero, Third European Particle Accelerator Conference, Berlin, 1992 (Editions Frontières, Gif-sur-Yvette, 1992), p. 889.

[86] E. Ruiz, L. Walling, Y. Goren and N. Spayd, CAP 93, Pleasanton, 22–26 February, 1993.

[87] J. Billan and T. Tortschanoff, CERN AT Division Magnet Group Internal Report 91–38 (1991).

[88] T. Tortschanoff, CERN AT Division Magnet Group Internal Report 93–76 (1993).

[89] R. Maleyron and R. Valbuena, CERN MT Division Technical Note MT–ESI/93–03 (1993).

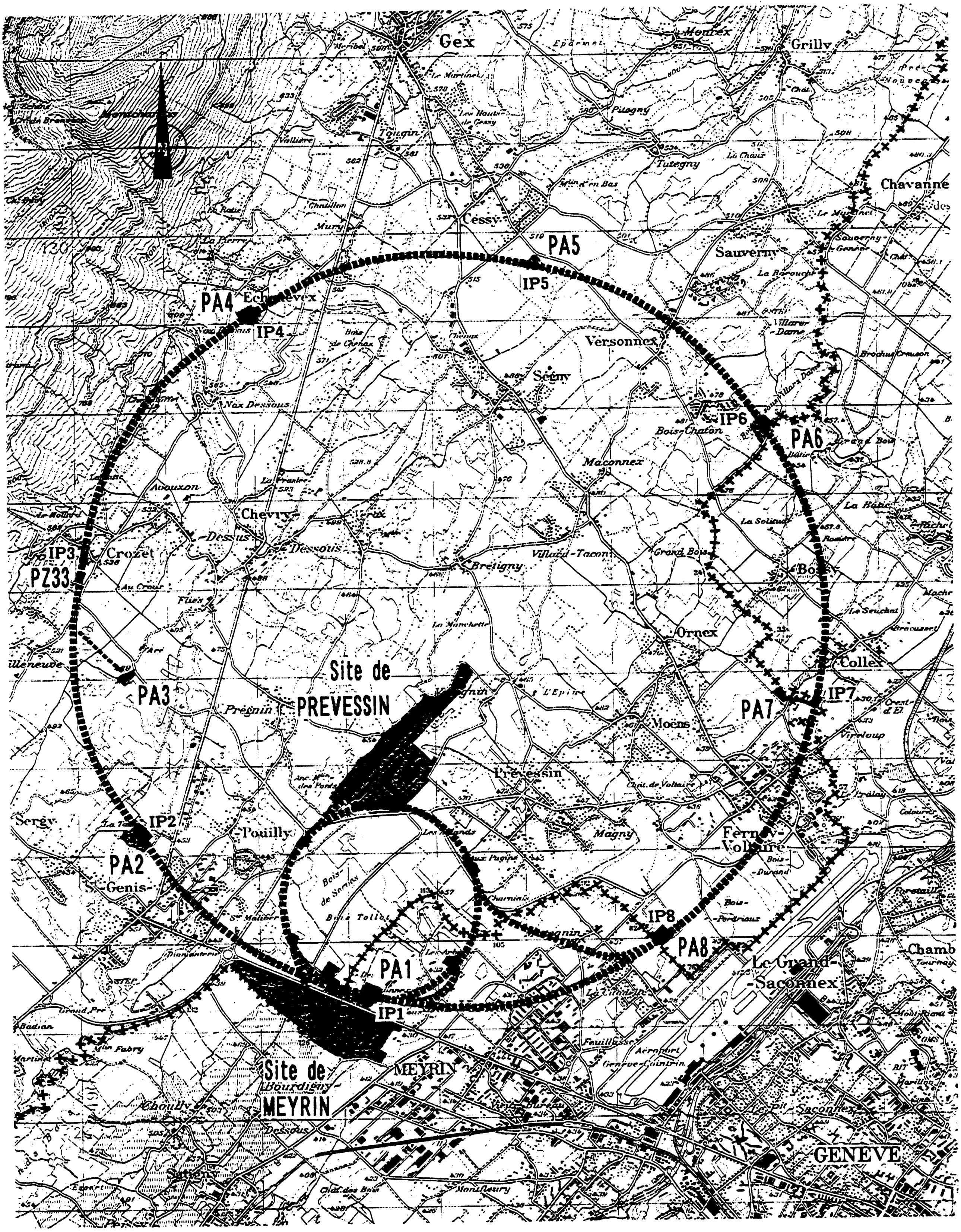

Figure 1: The LEP tunnel implantation

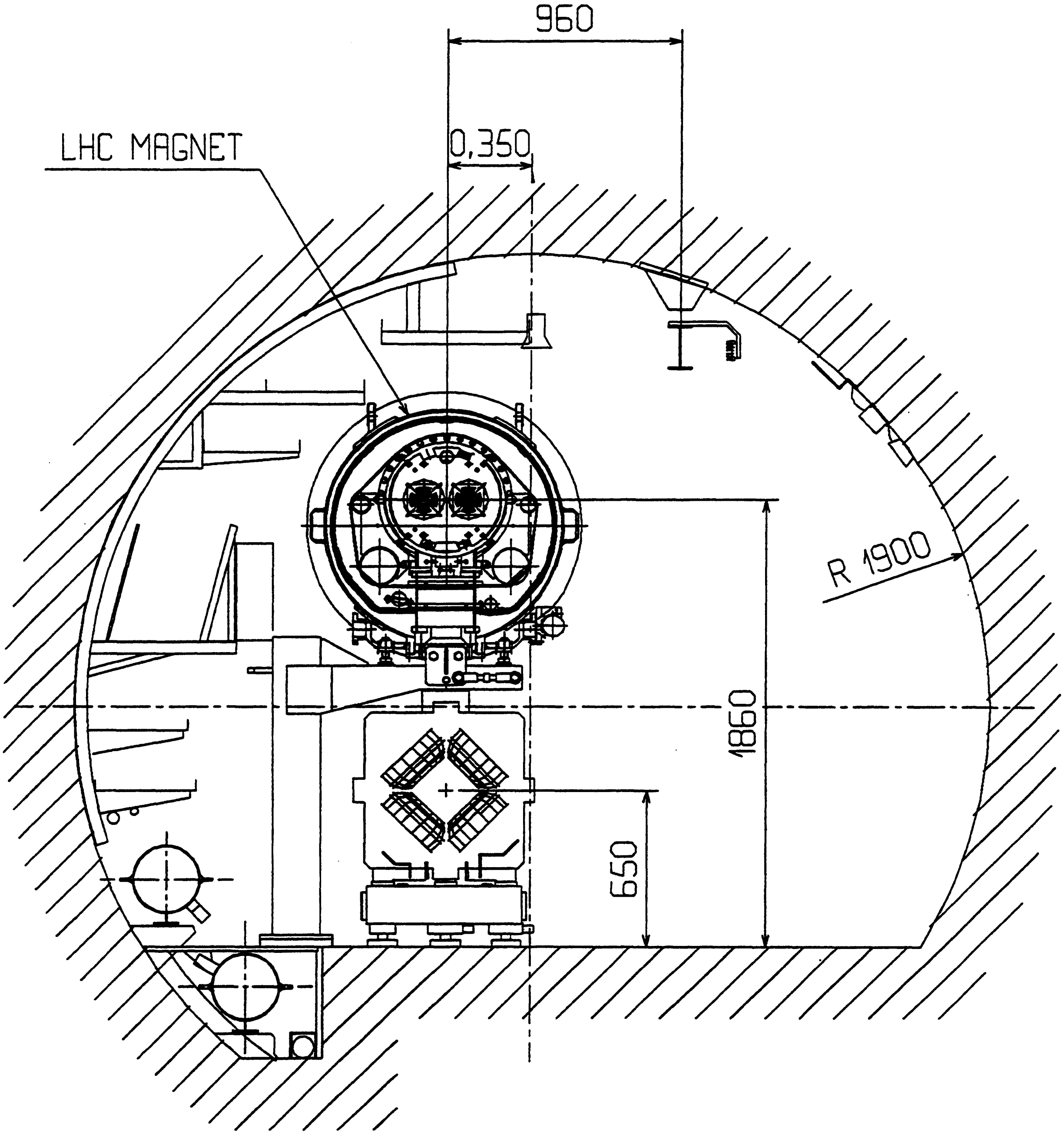

Figure 2: The LEP tunnel cross-section

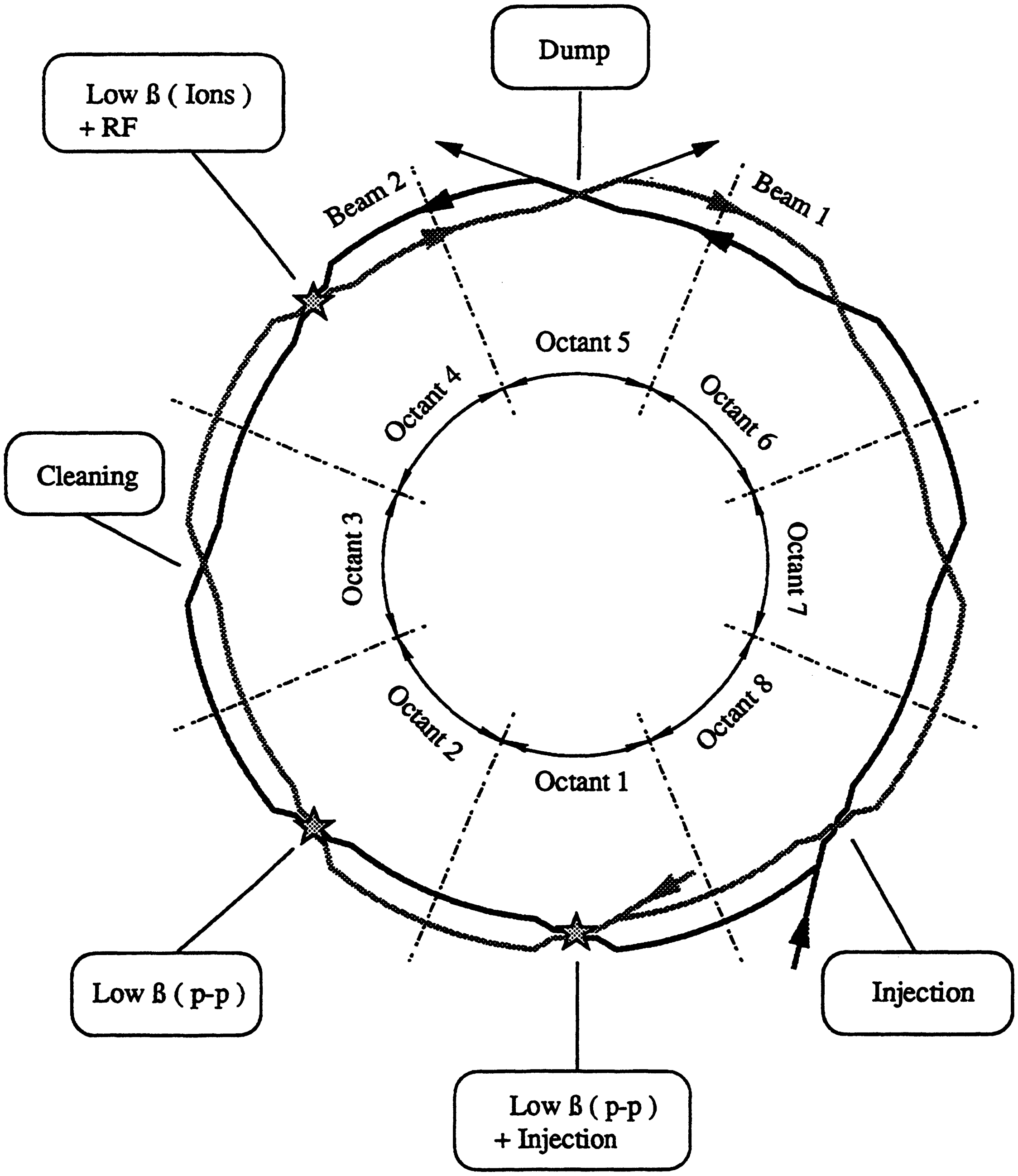

Figure 3: The LHC schematic layout

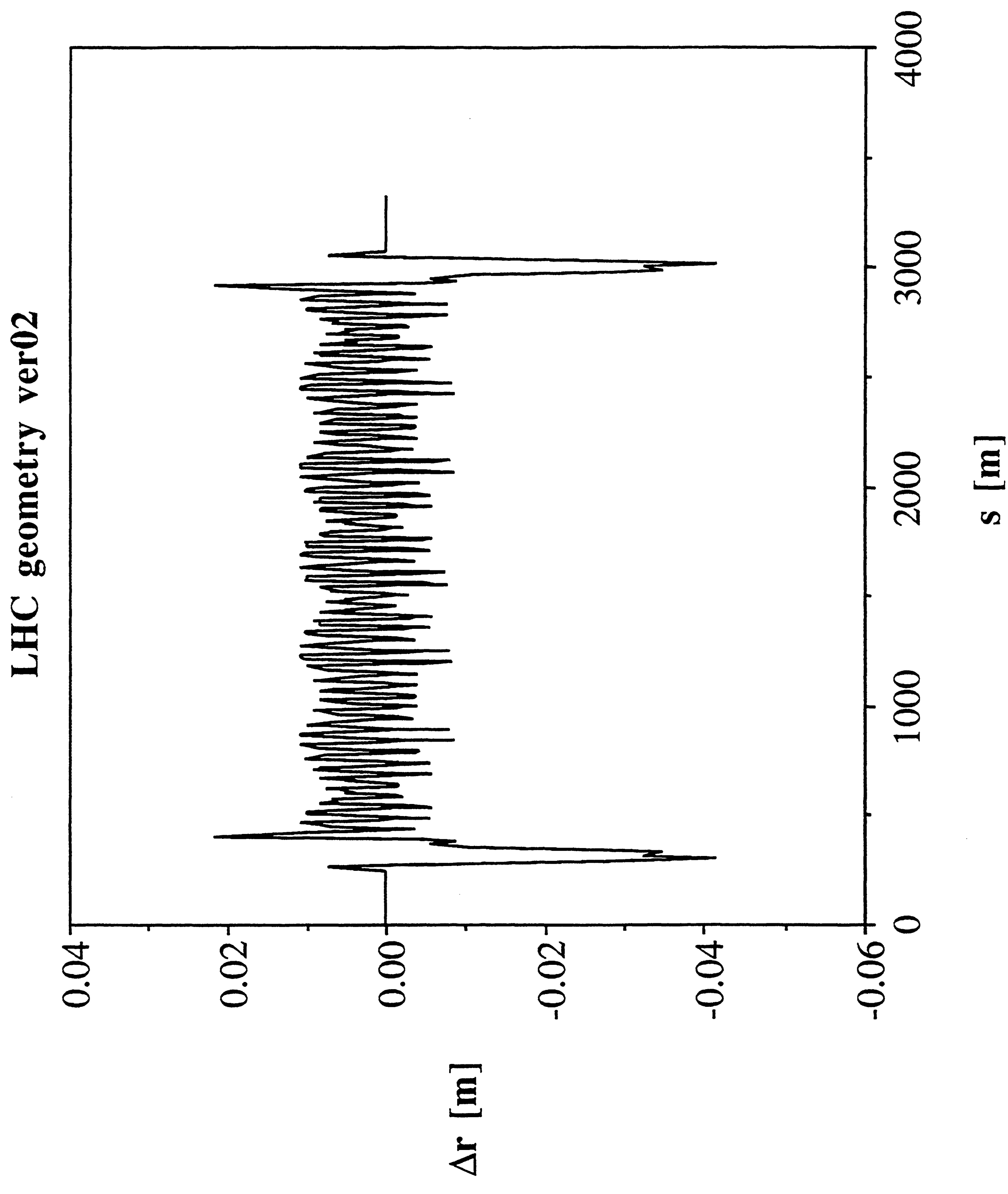

Figure 4: Radial difference between LEP and LHC

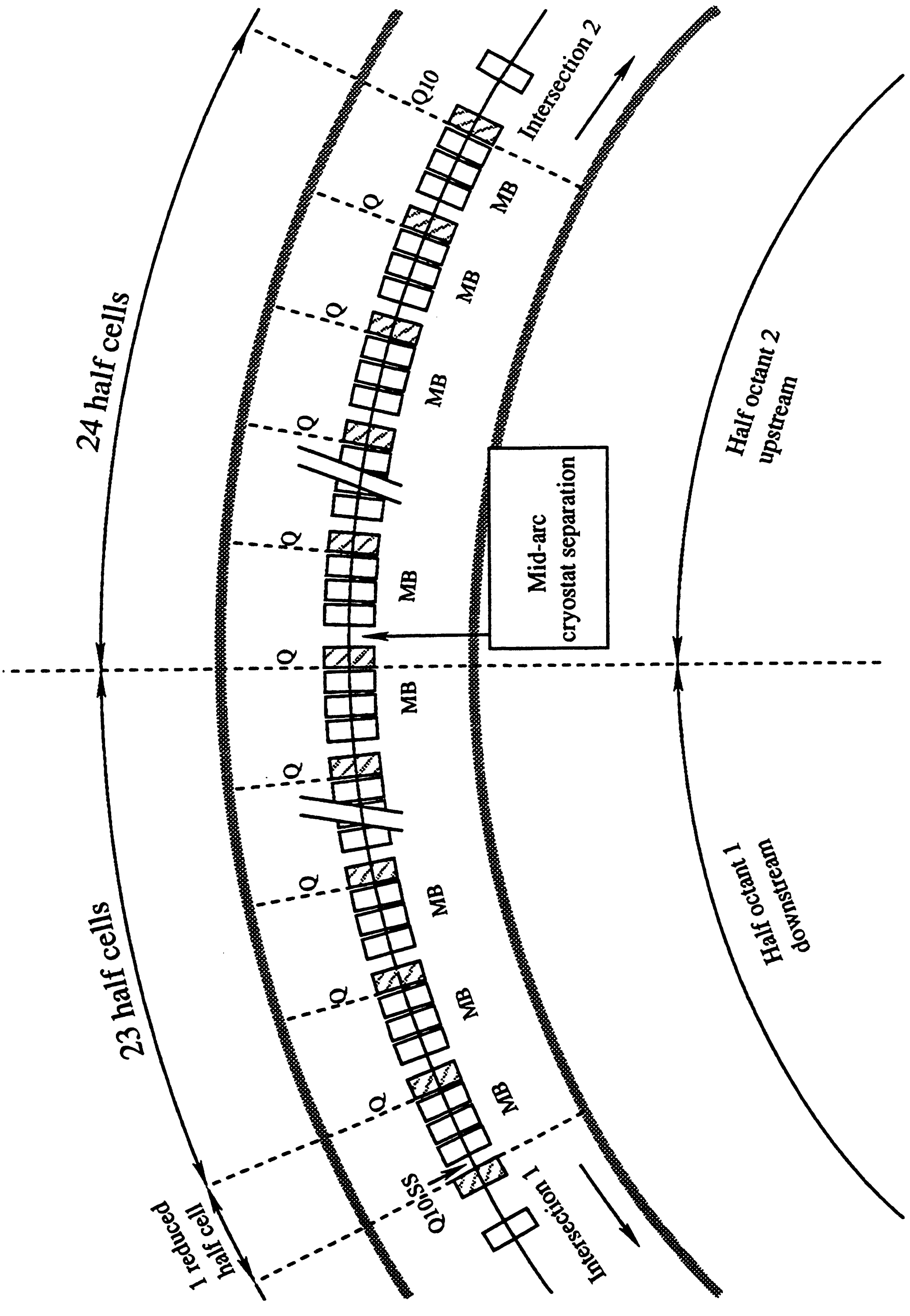

Figure 5: (a) Schematic representation of arcs (even sectors)

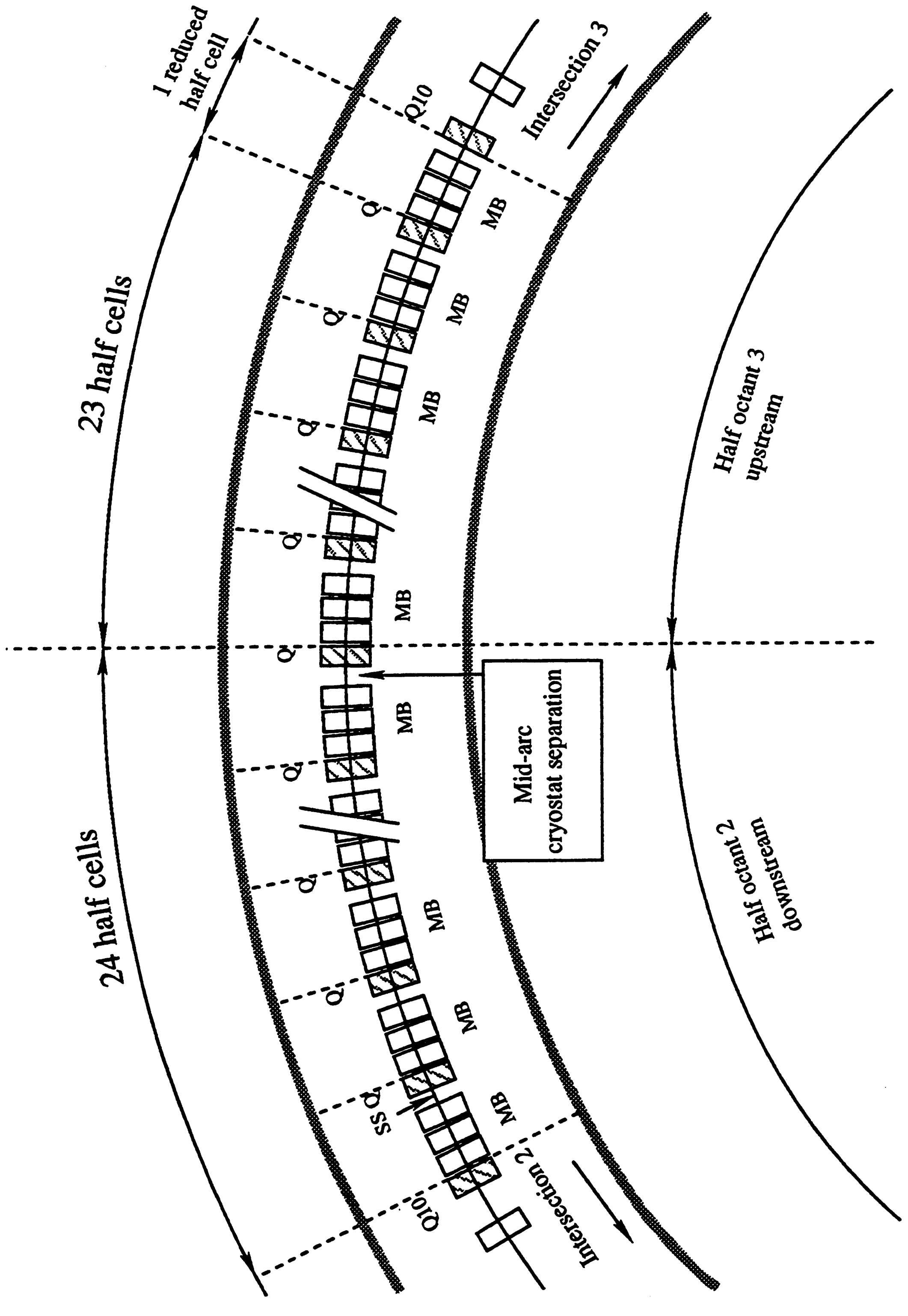

Figure 5: (b) Schematic representation of arcs (odd sectors)

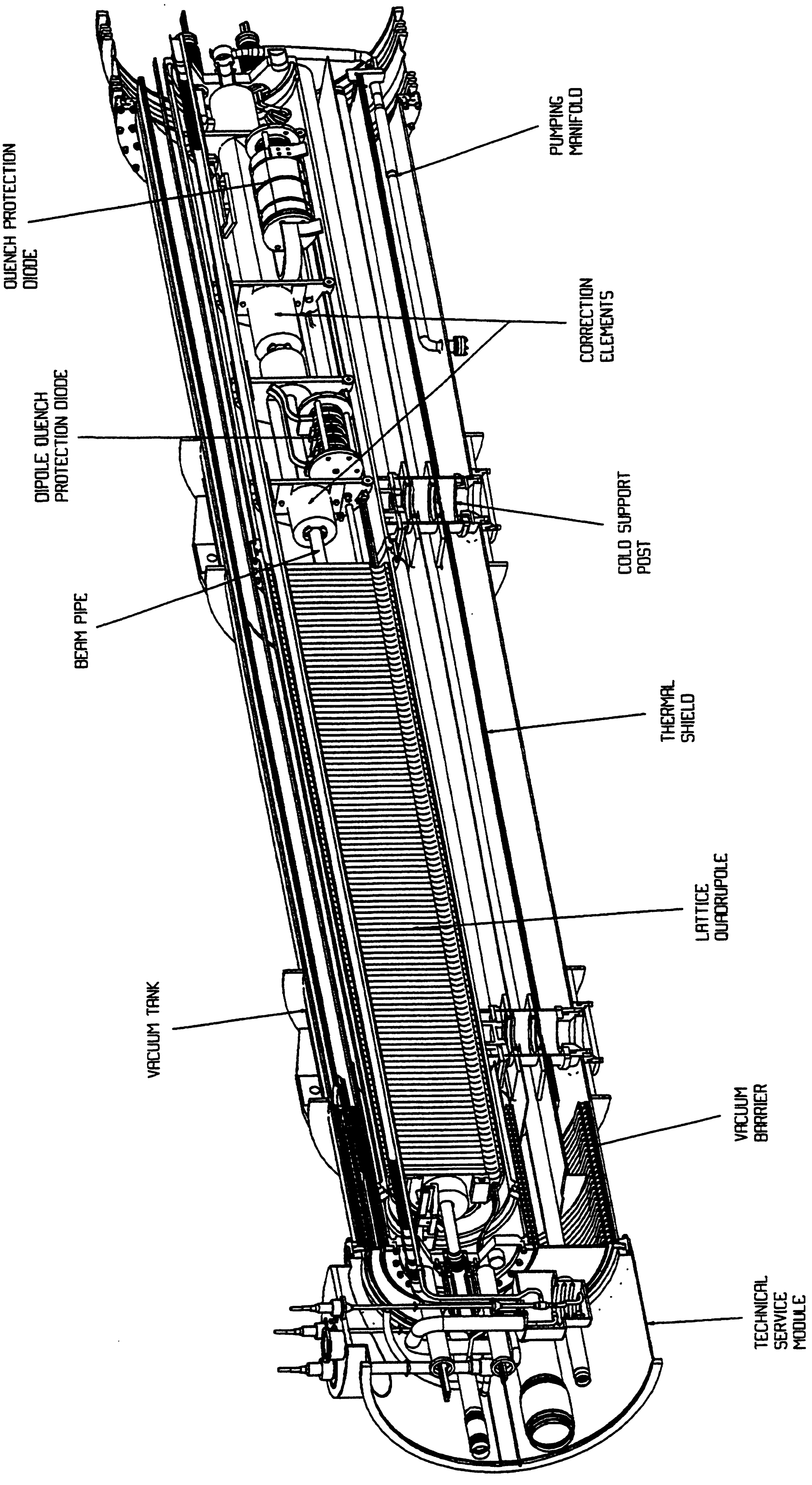

Figure 6: The LHC short straight section

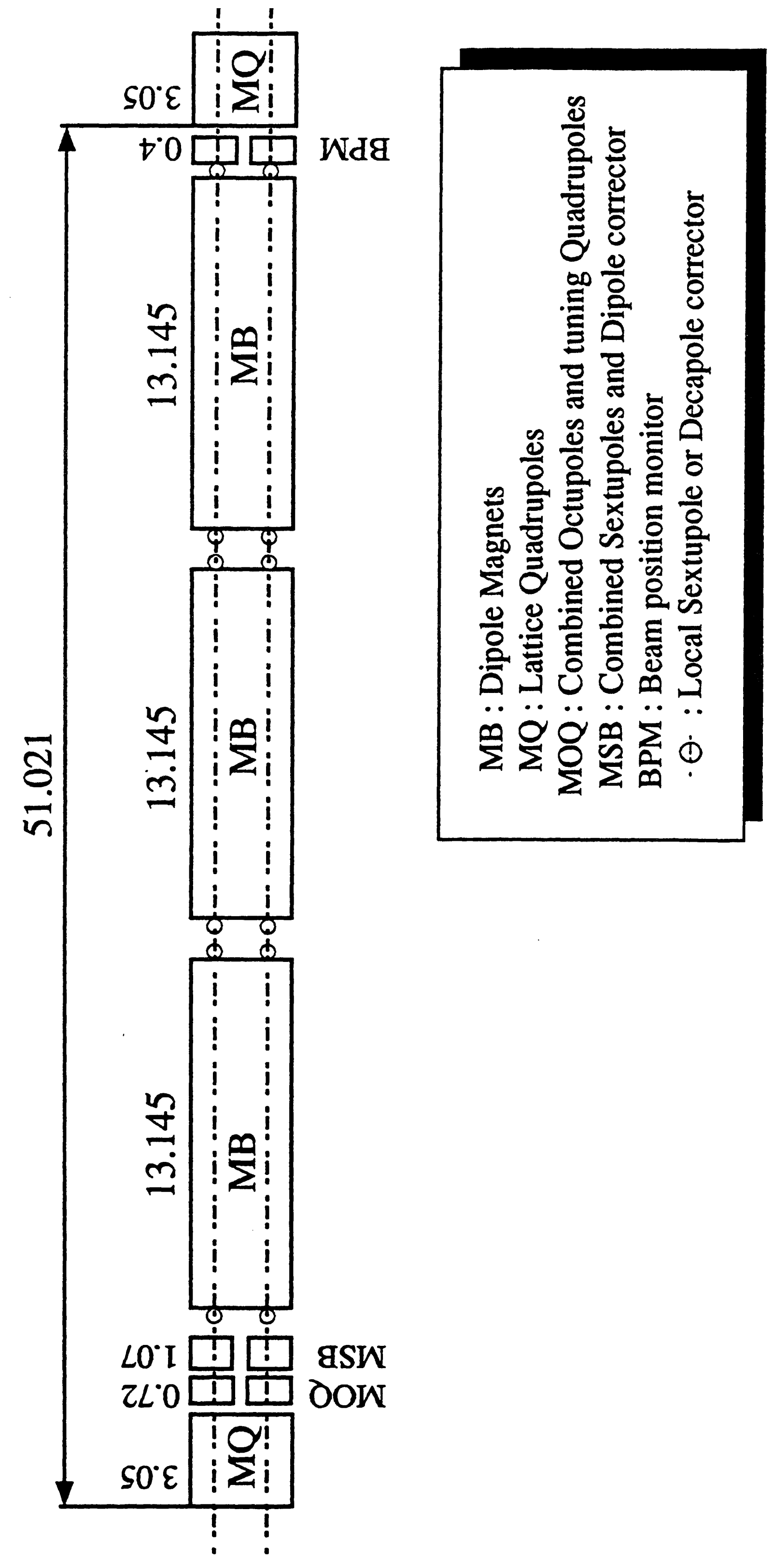

Figure 7: Schematic representation of a half-cell (even sector)

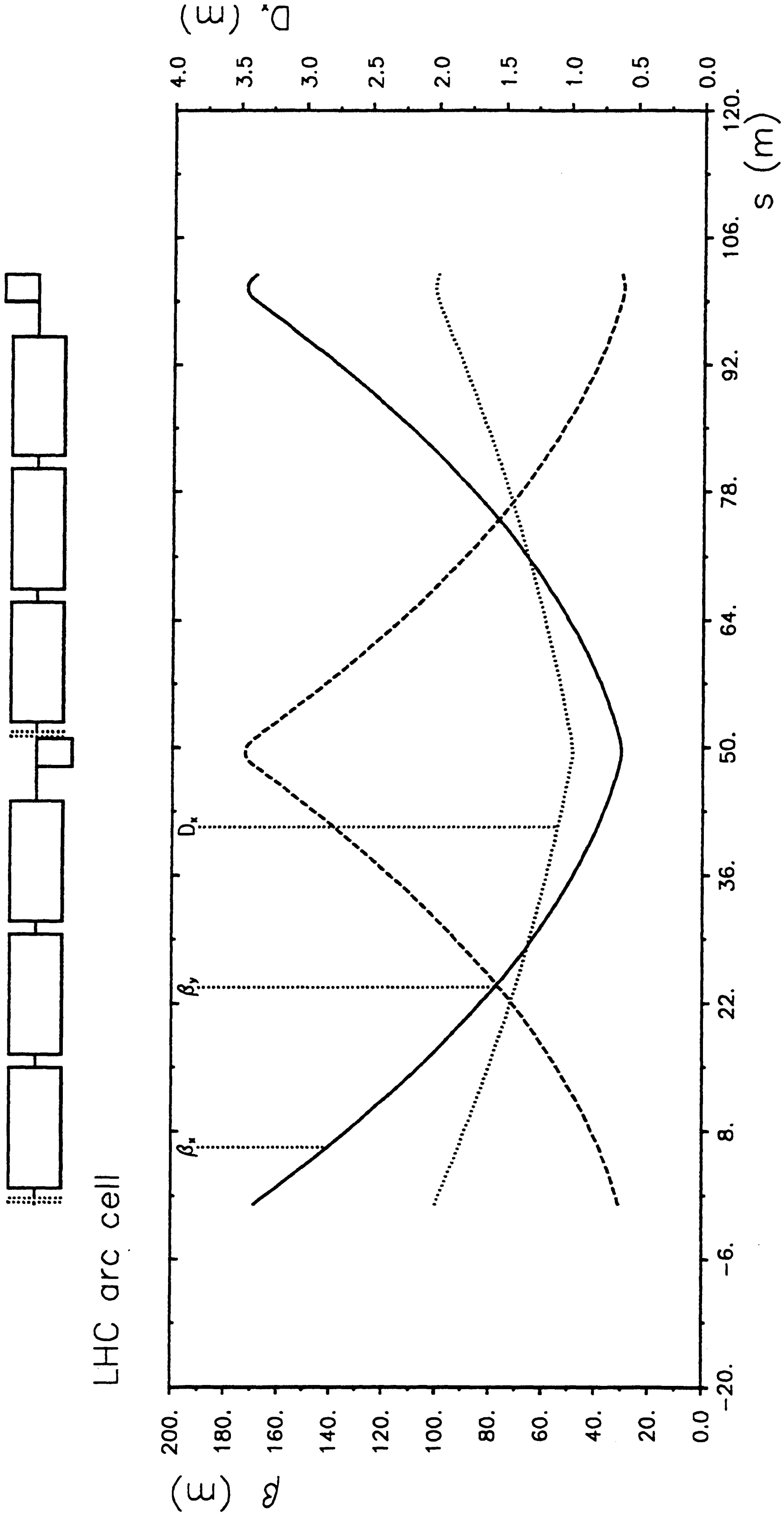

Figure 8: Optics functions of the regular half-cell

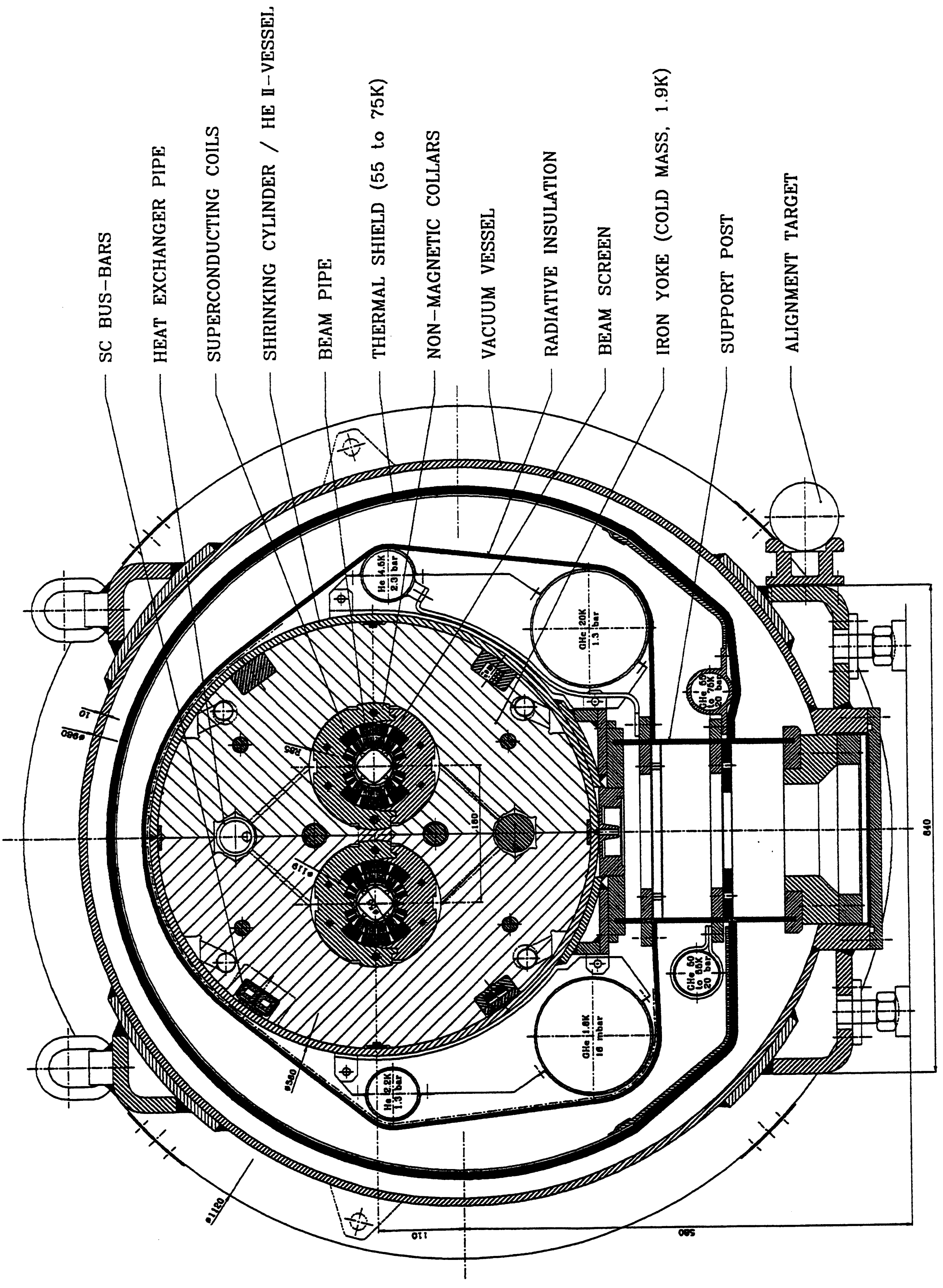

Figure 9: Magnet dipole cross-section

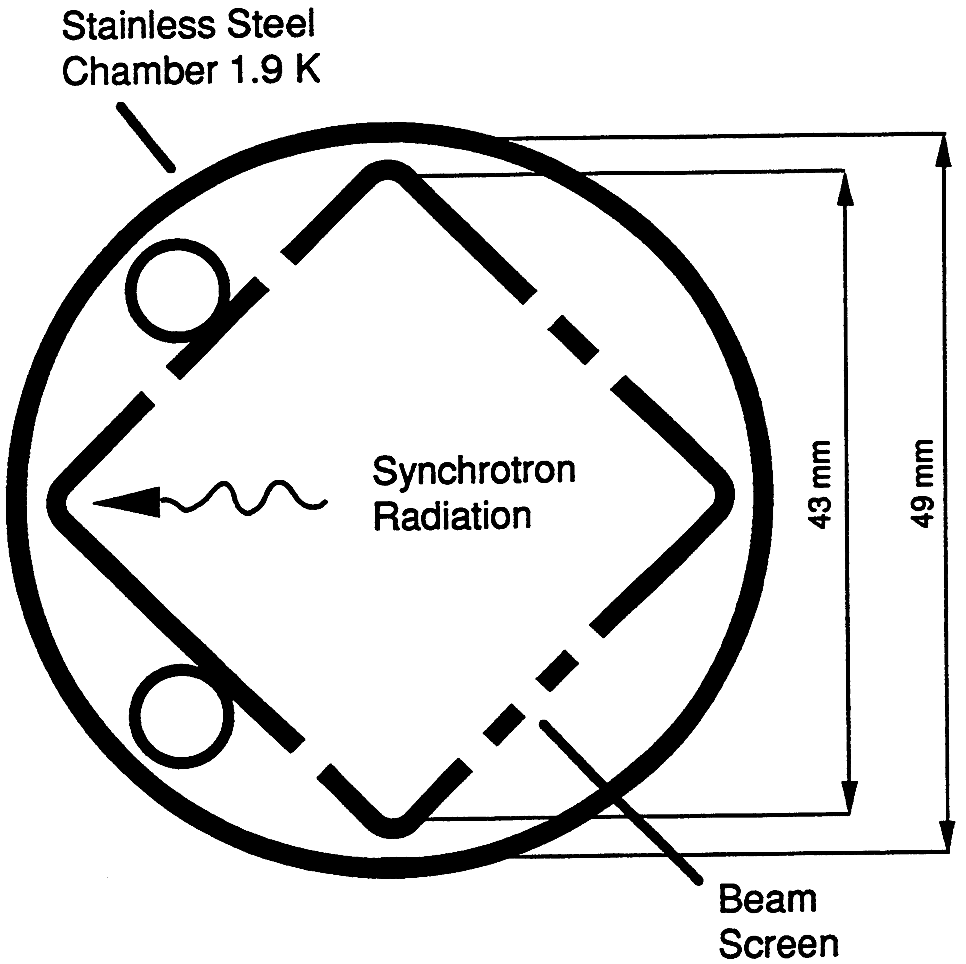

Figure 10: Beam screen and vacuum chamber

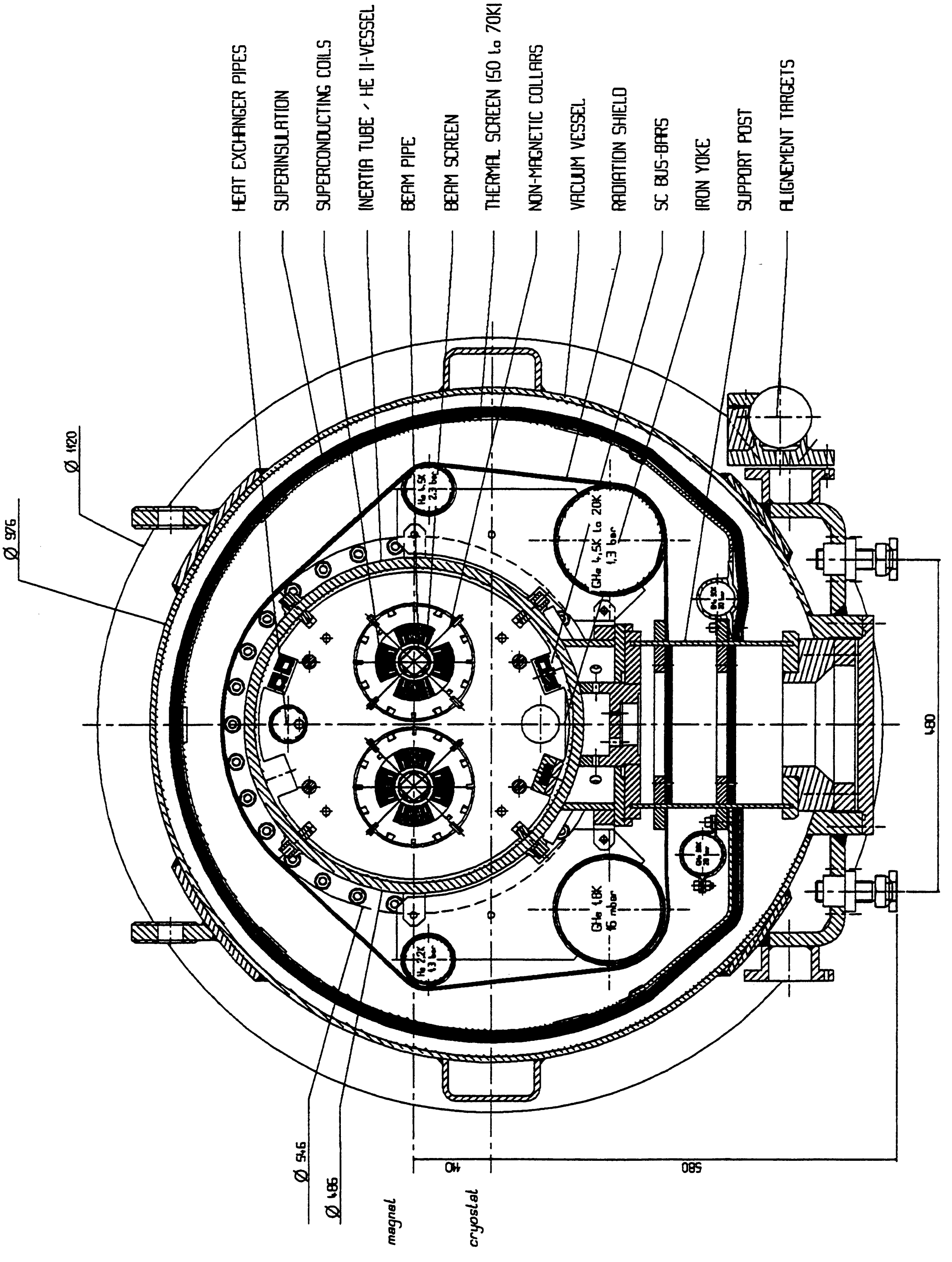

Figure 11: Schematic cross-section of the quadrupole

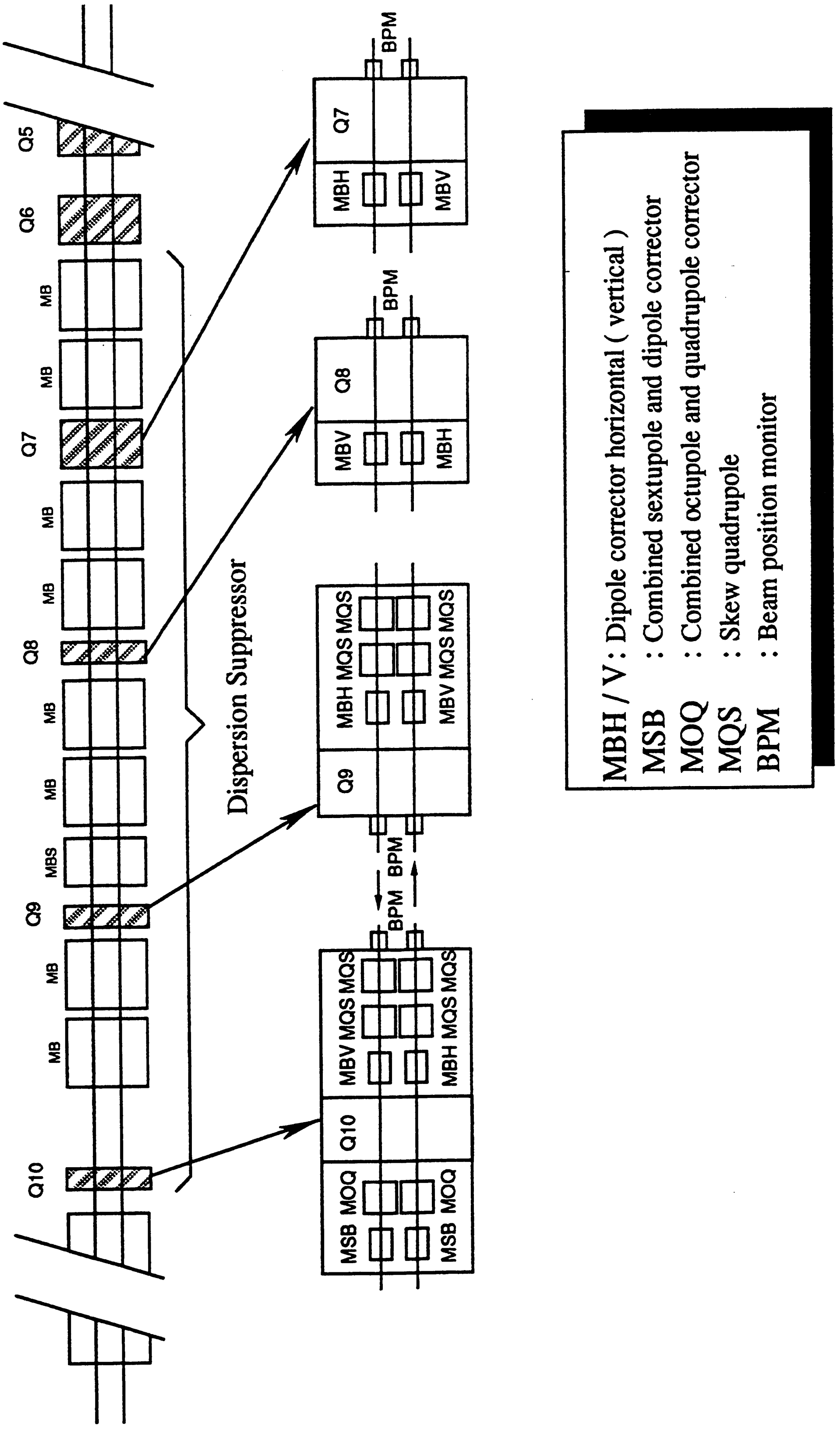

Figure 12: Schematic layout of the dispersion supressor

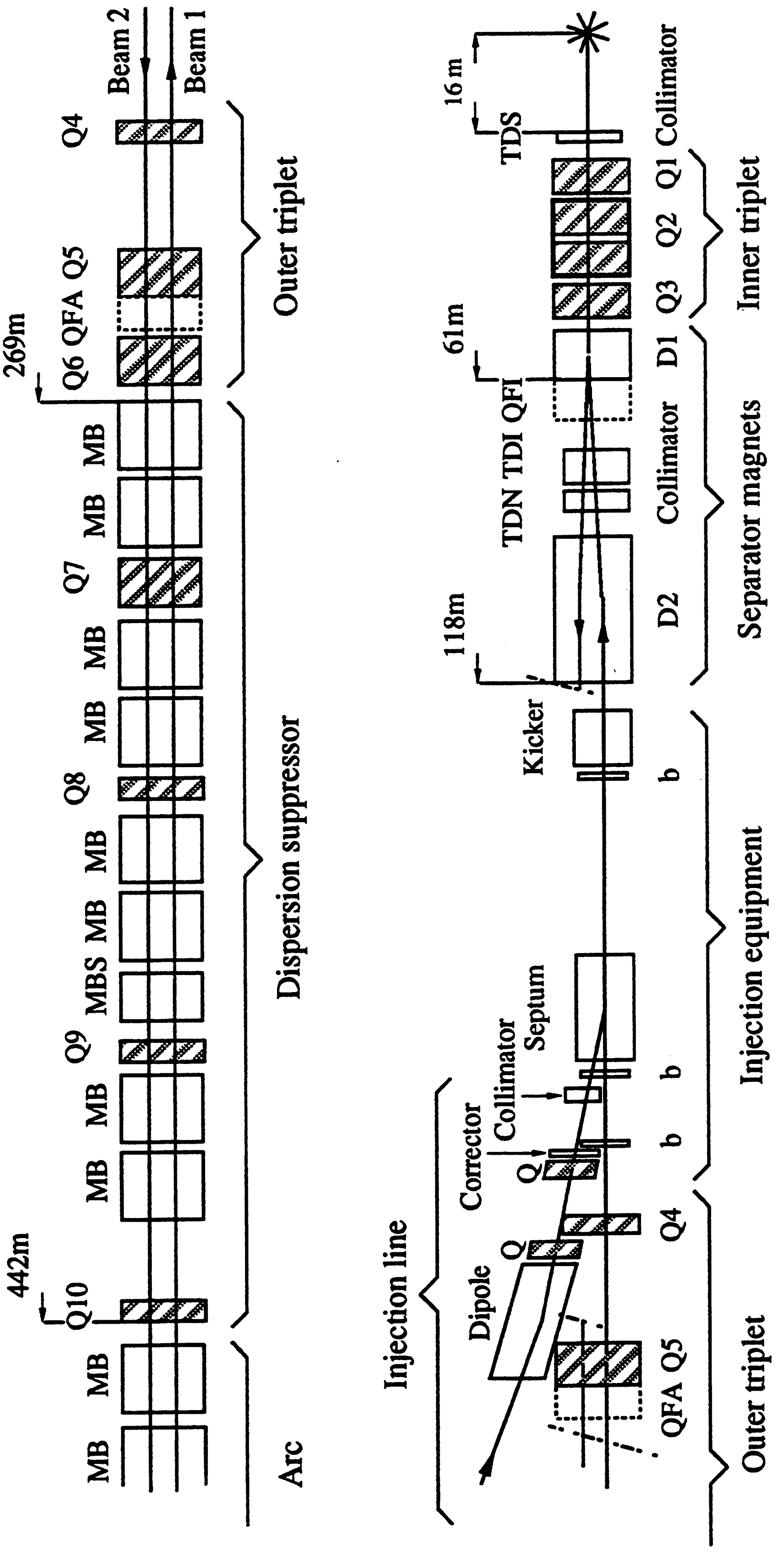

Figure 13: Insertion 1 upstream layout

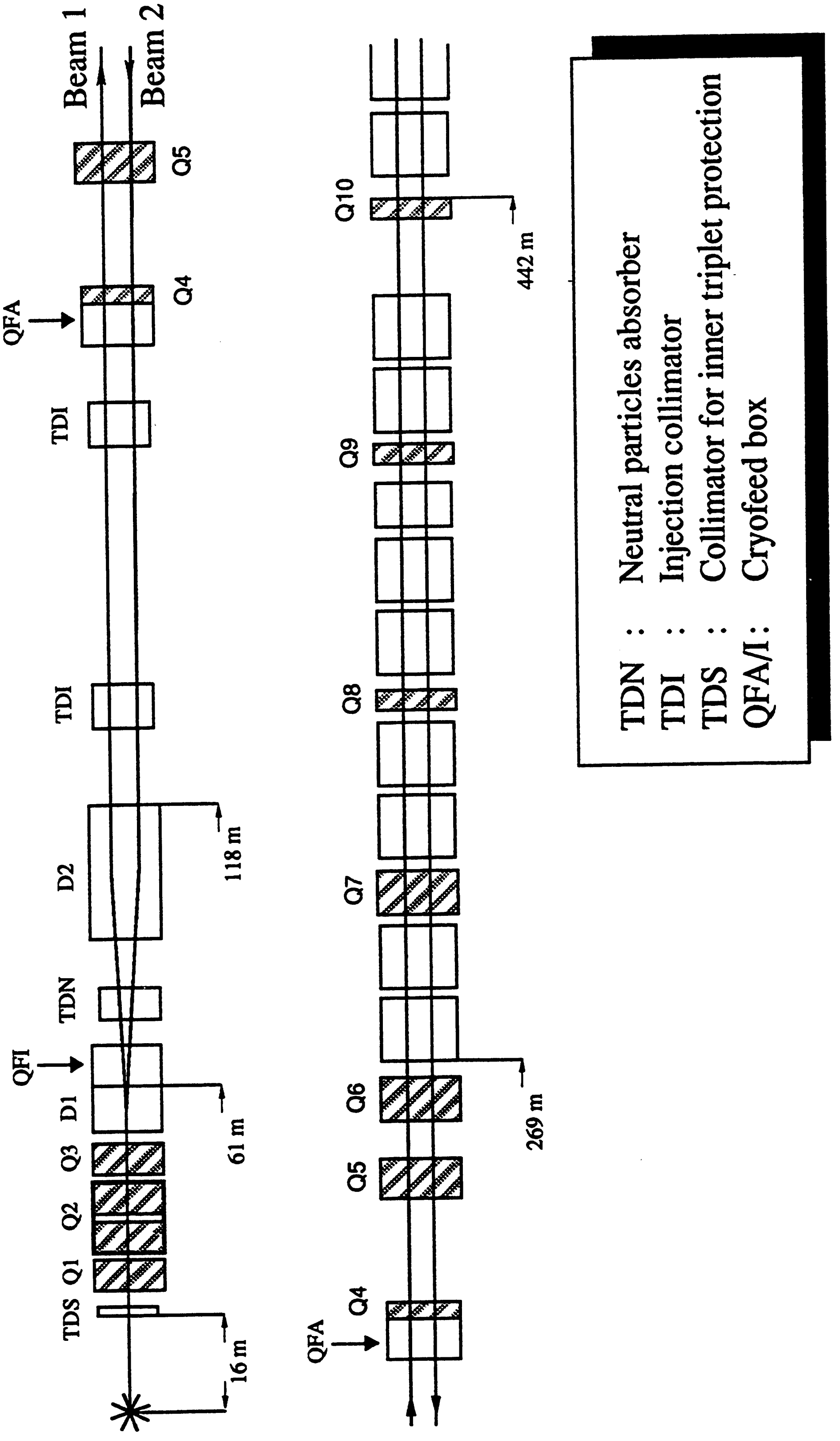

Figure 14: Insertion 1 downstream layout

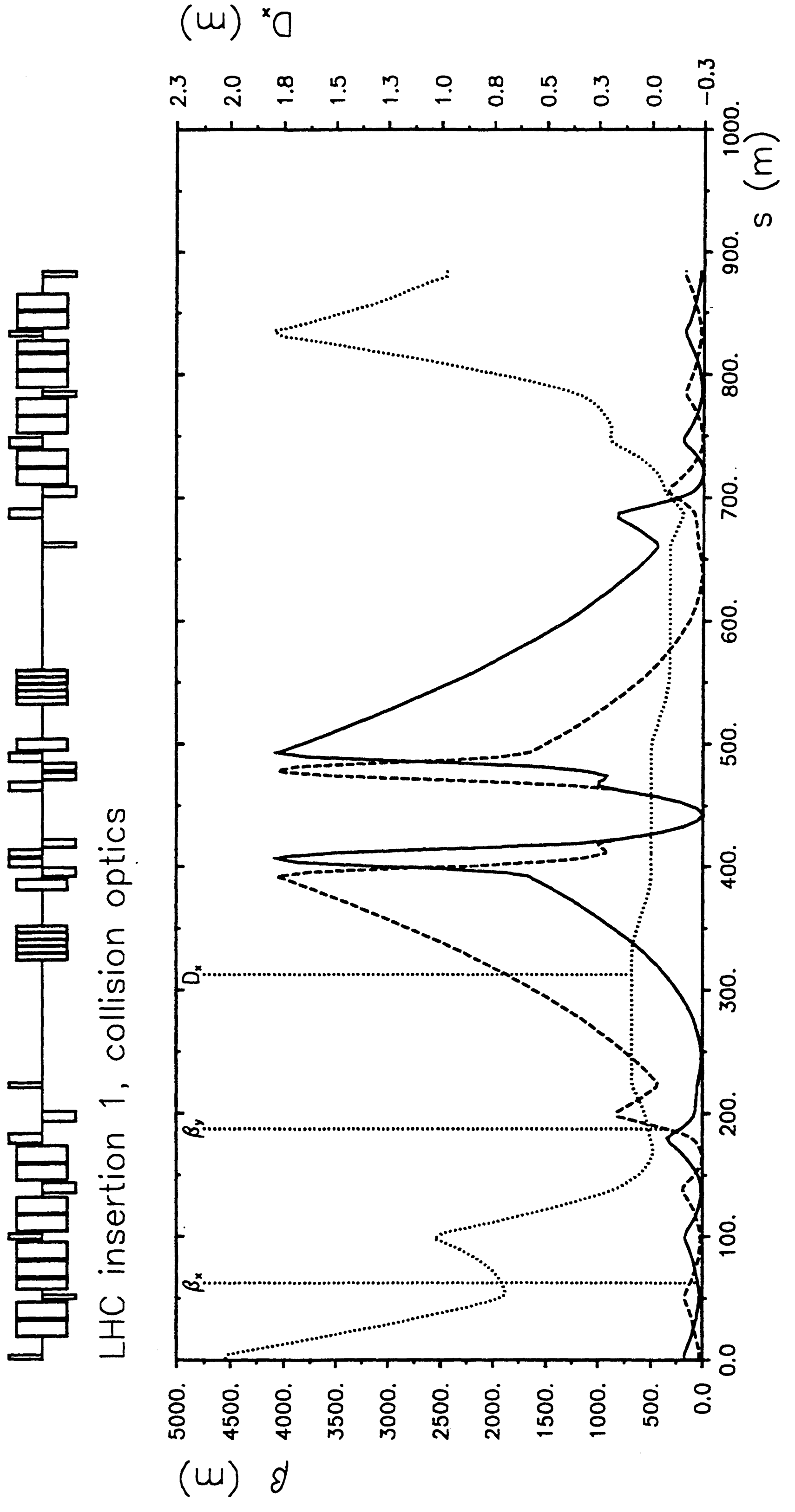

Figure 15: Optics functions of insertion 1 (tuned low-beta)

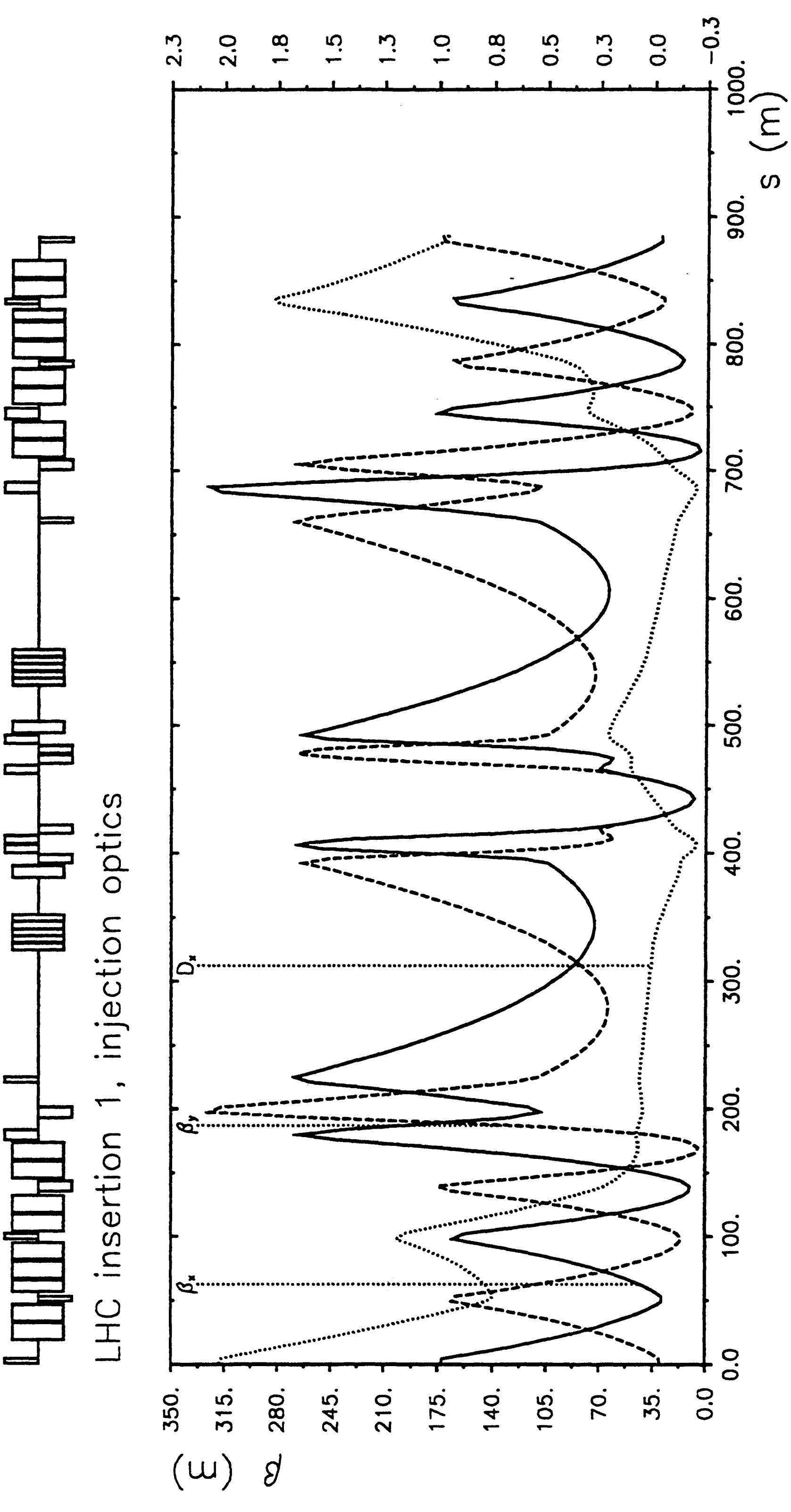

Figure 16: Optics functions of insertion 1 (detuned low-beta)

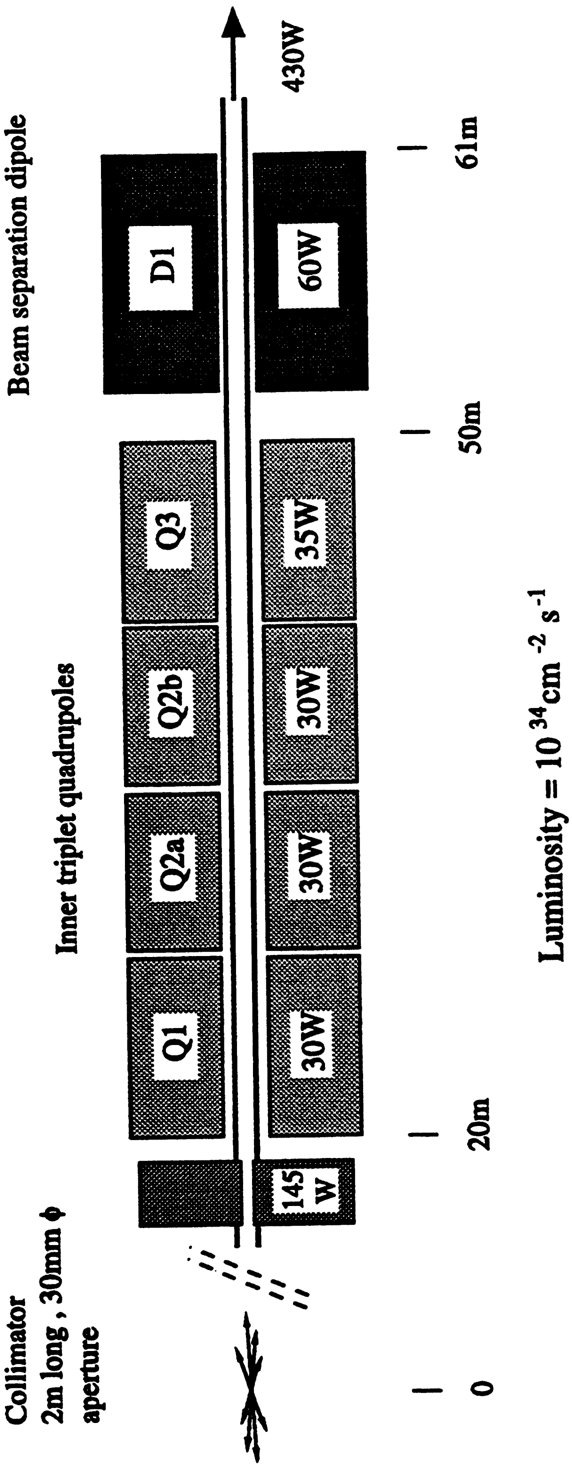

Figure 17: Power deposited in machine elements near a high-luminosity IP

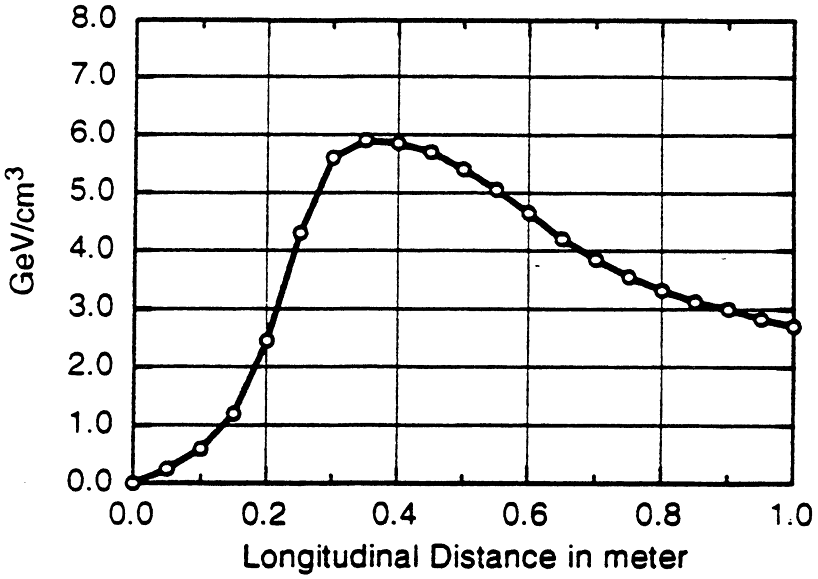

Figure 18: Density of energy deposited by a 7.3 TeV proton in the most exposed cable of the dipole coil

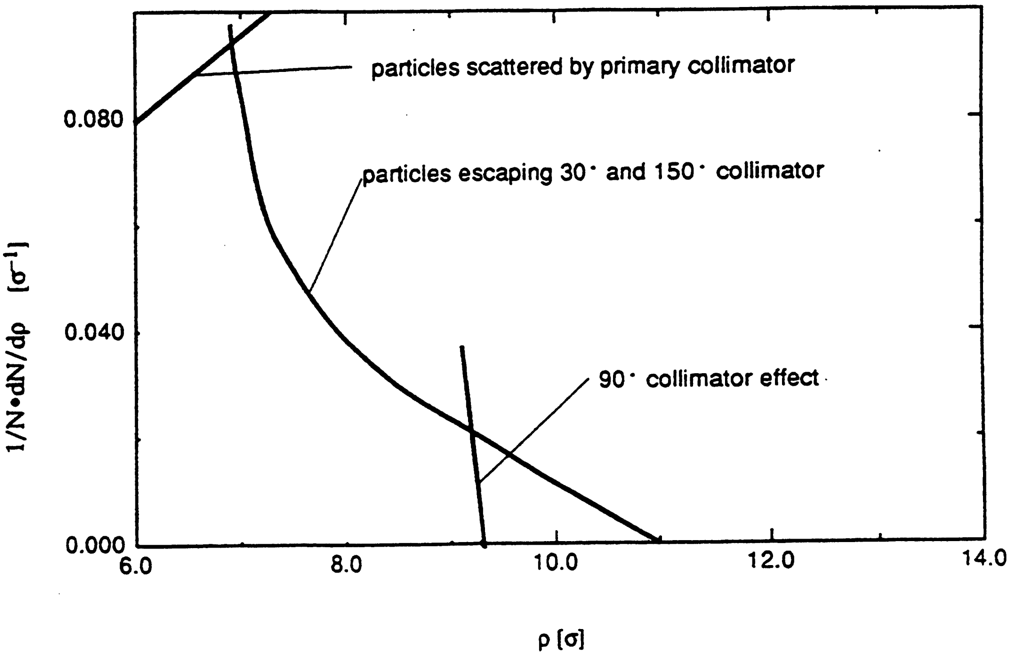

Figure 19: Amplitude distribution of particles escaping from collimators

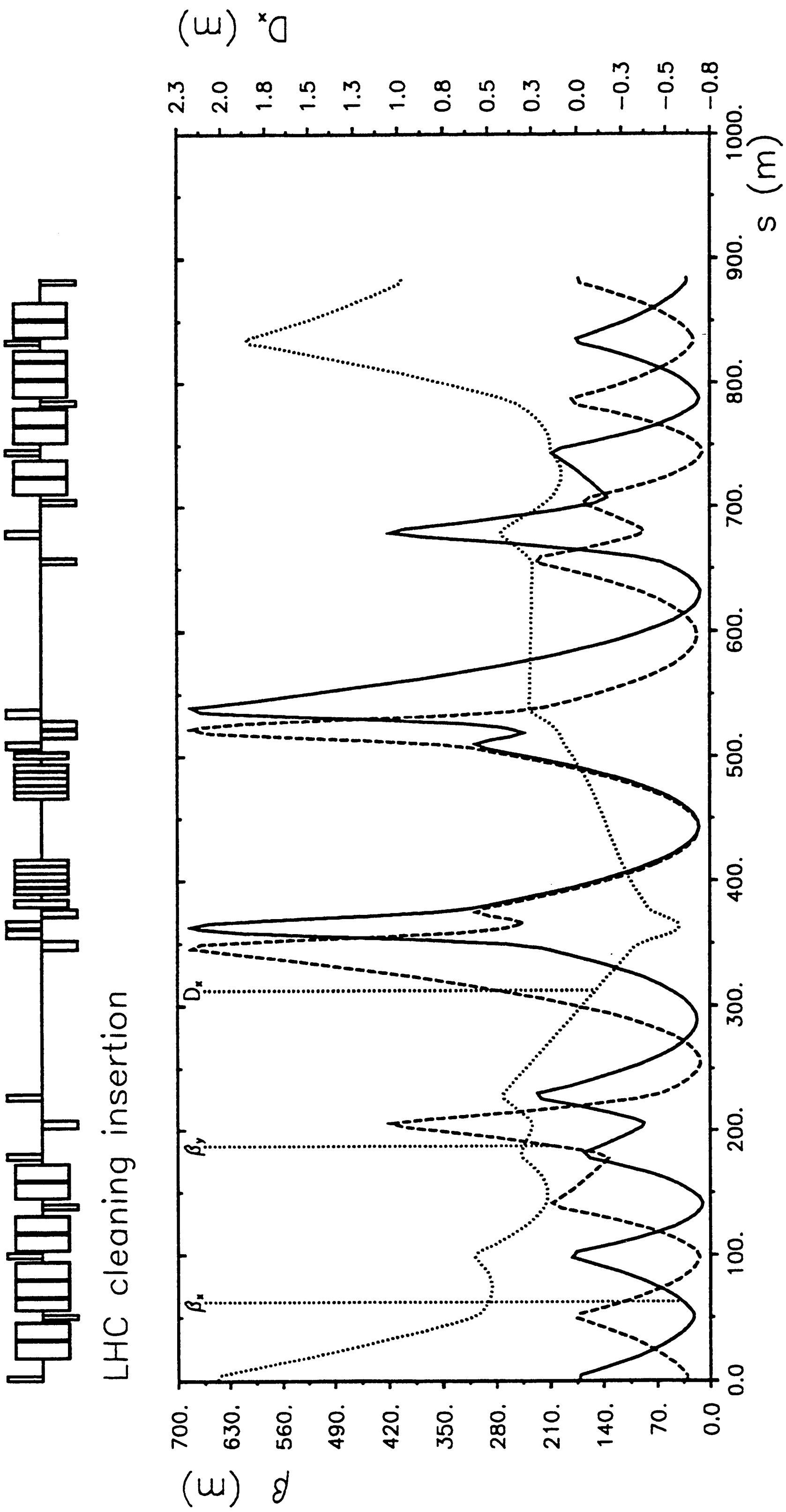

Figure 20: Optics functions in insertion 3

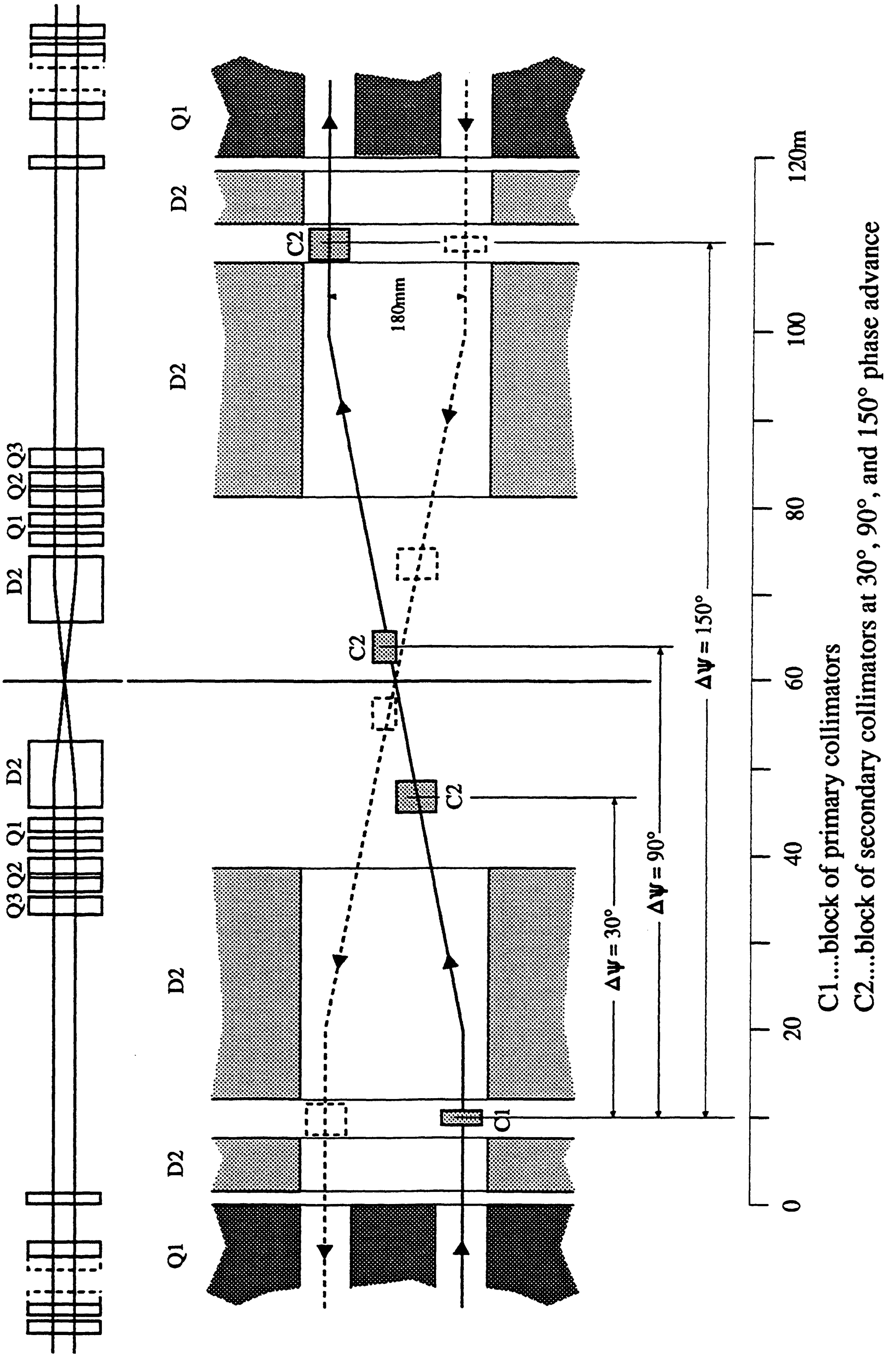

Figure 21: Schematic layout of SS 3 (cleaning insertion)

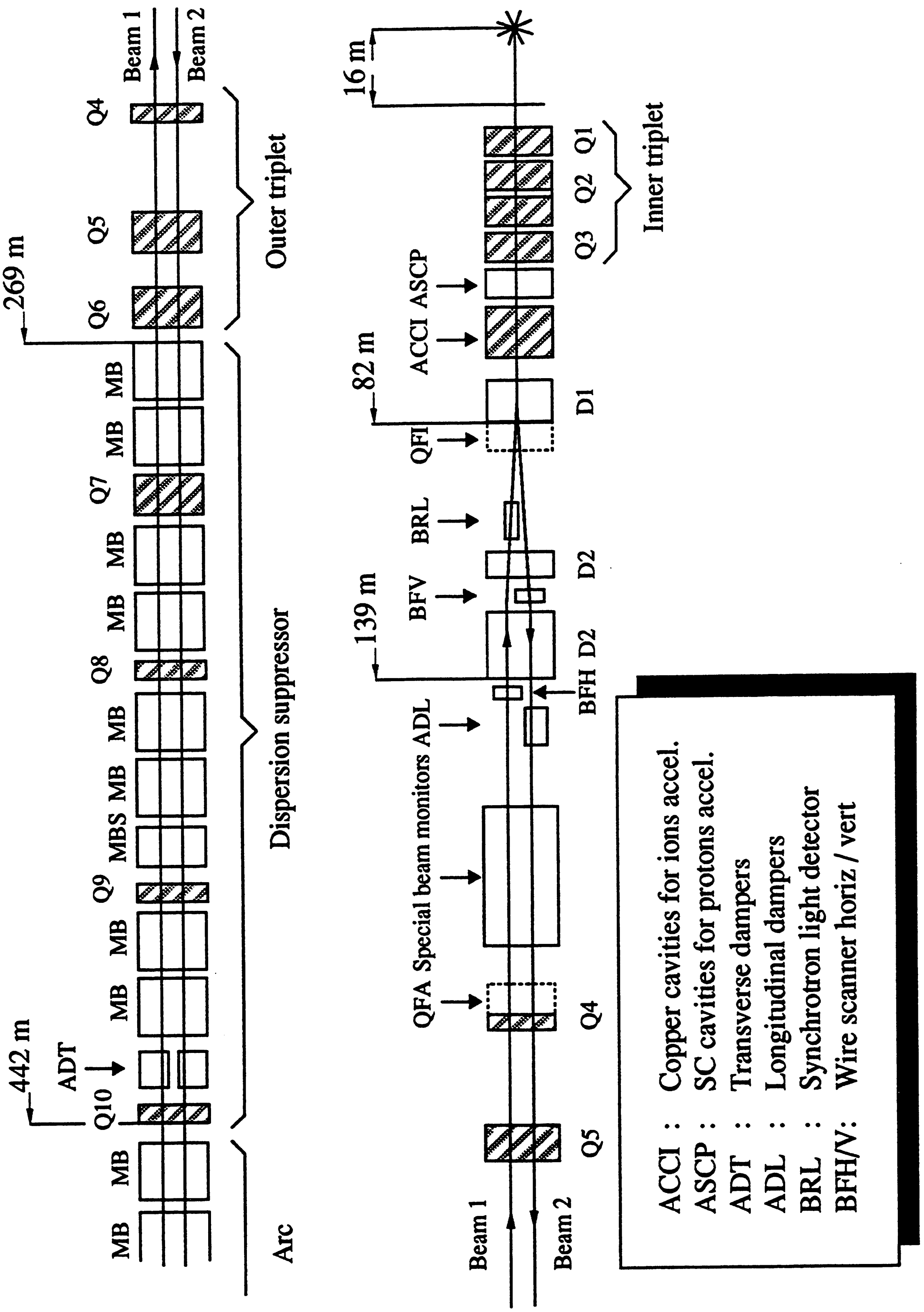

Figure 22: Insertion 4 layout

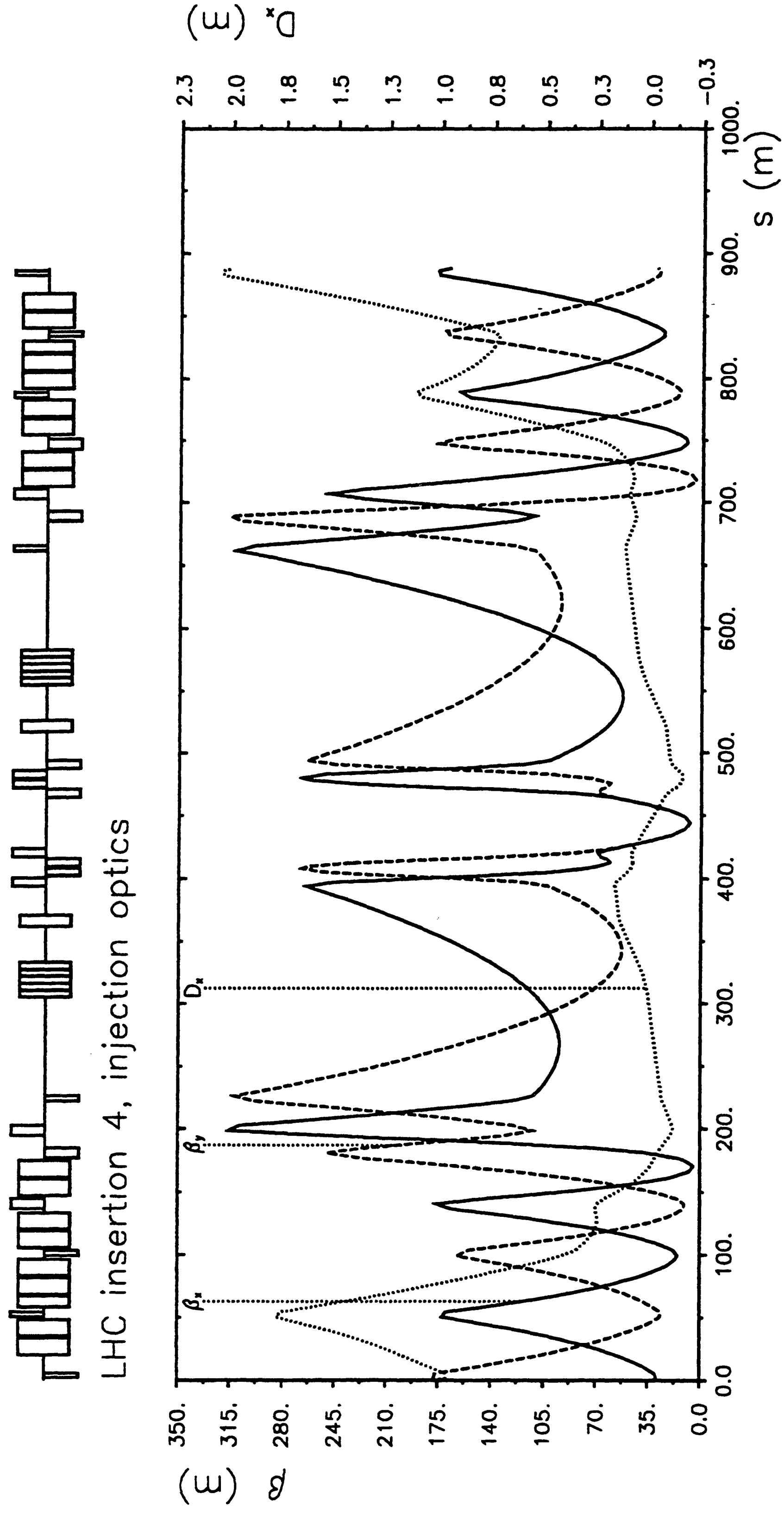

Figure 23: Optics functions in SS 4

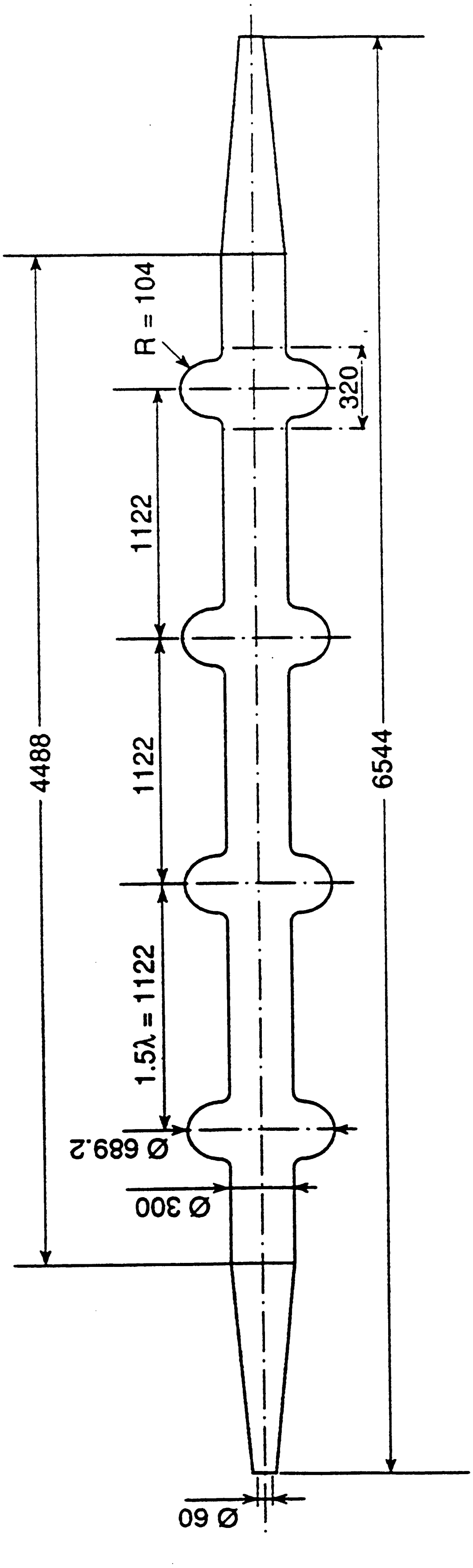

Figure 24: Proton accelerating cavities

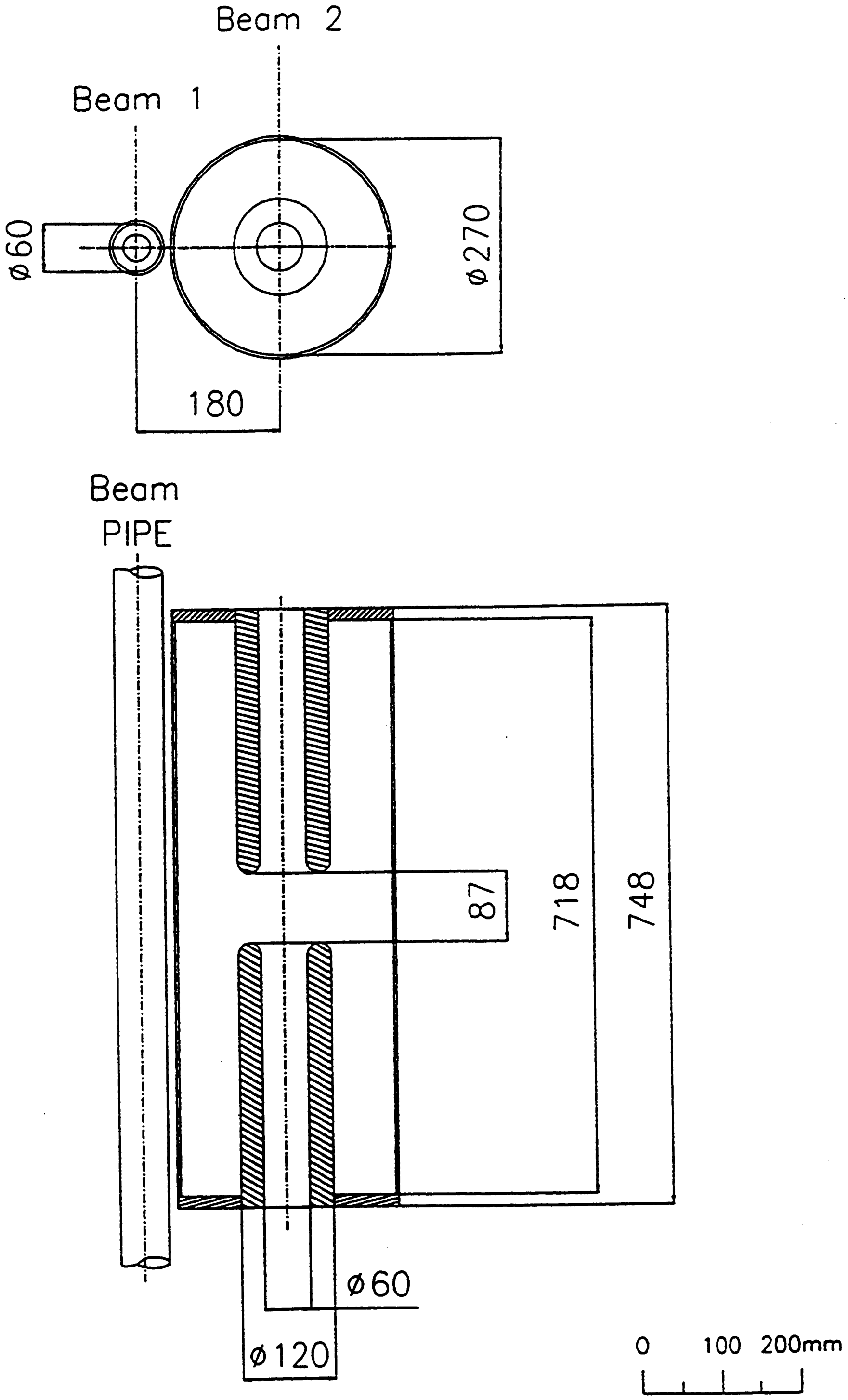

Figure 25: Longitudinal damper cavity

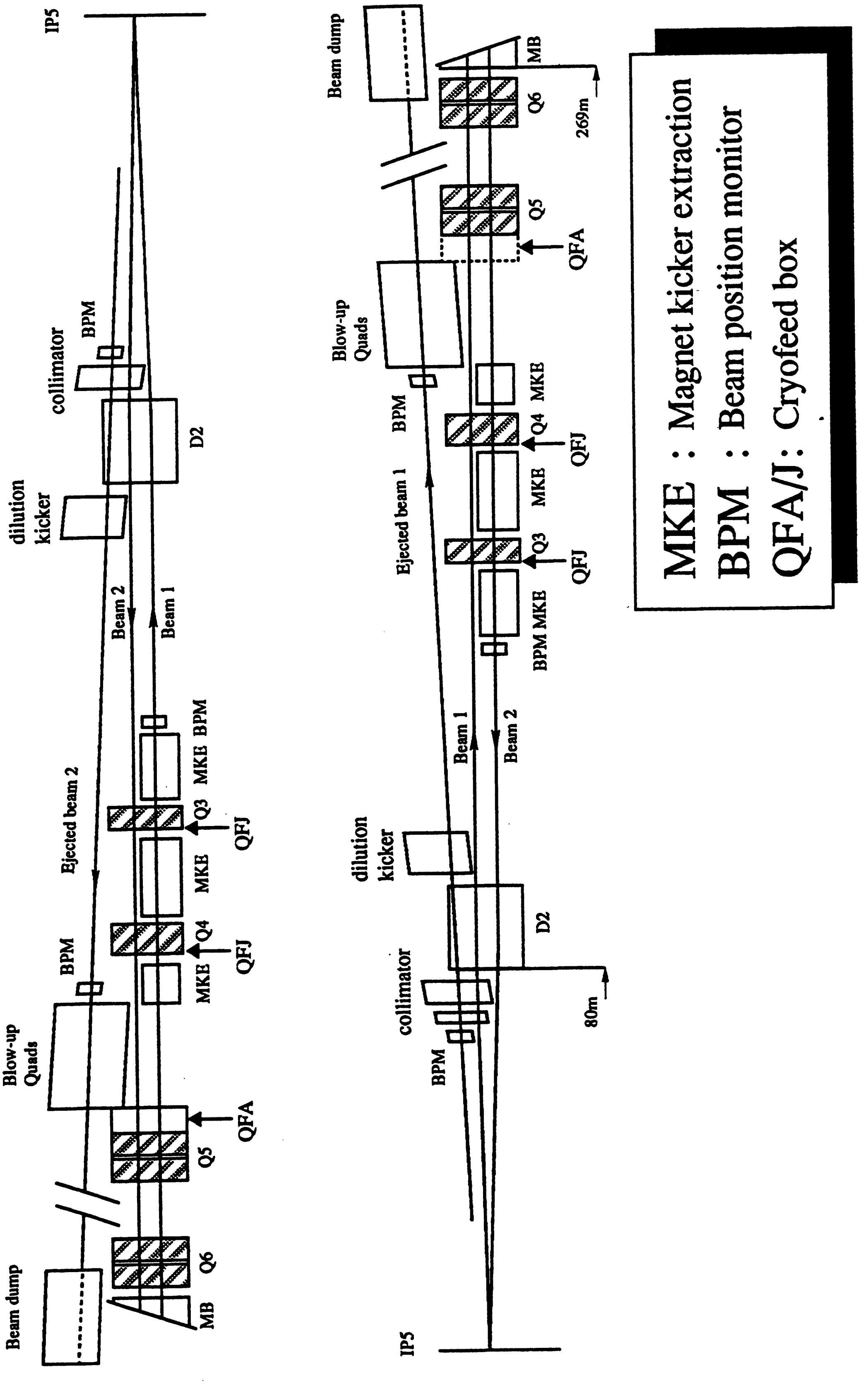

Figure 26: The SS 5 insertion layout (beam dump)

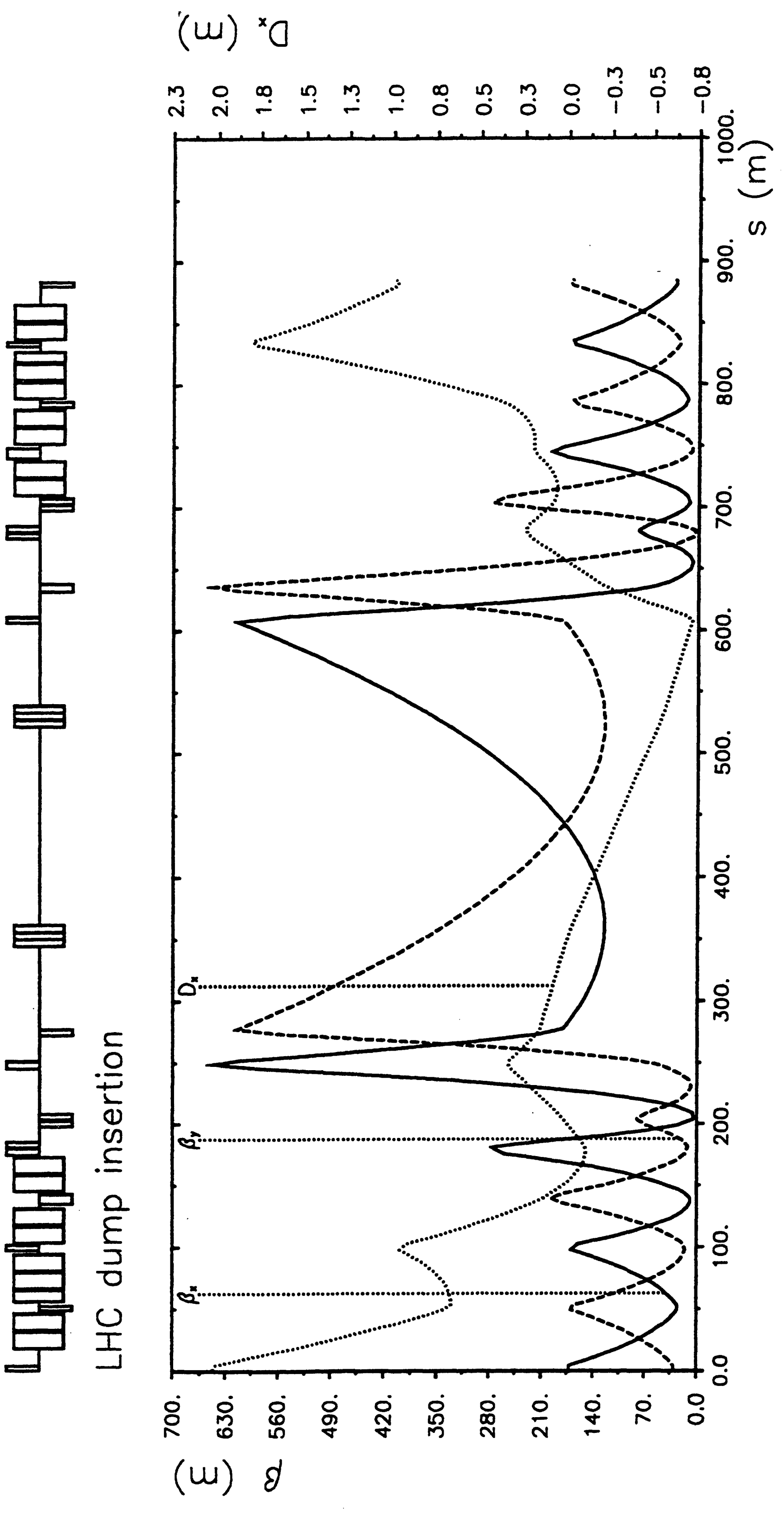

Figure 27: Optics functions in SS 5 (beam dump)

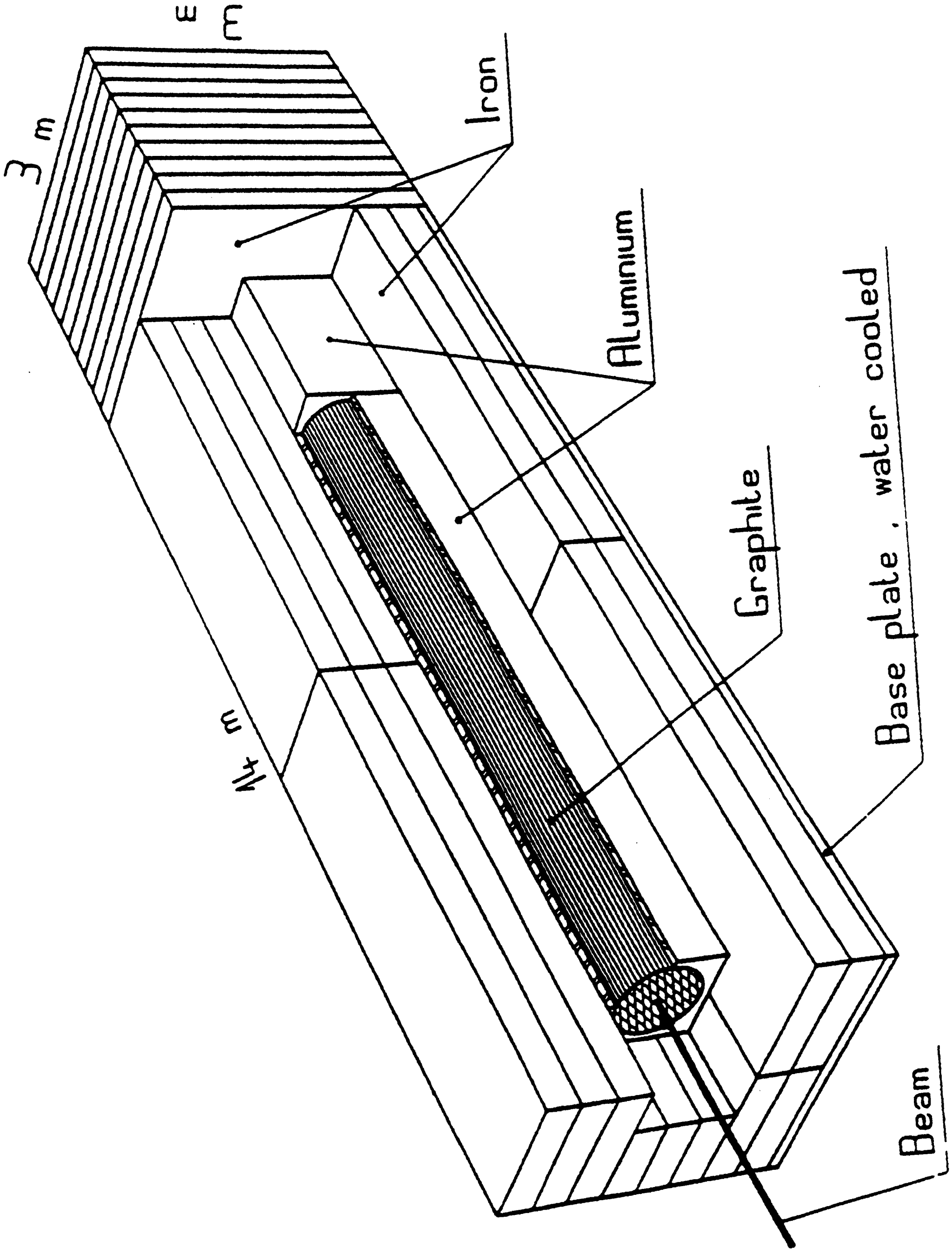

Figure 28: Beam-dump mechanical structure

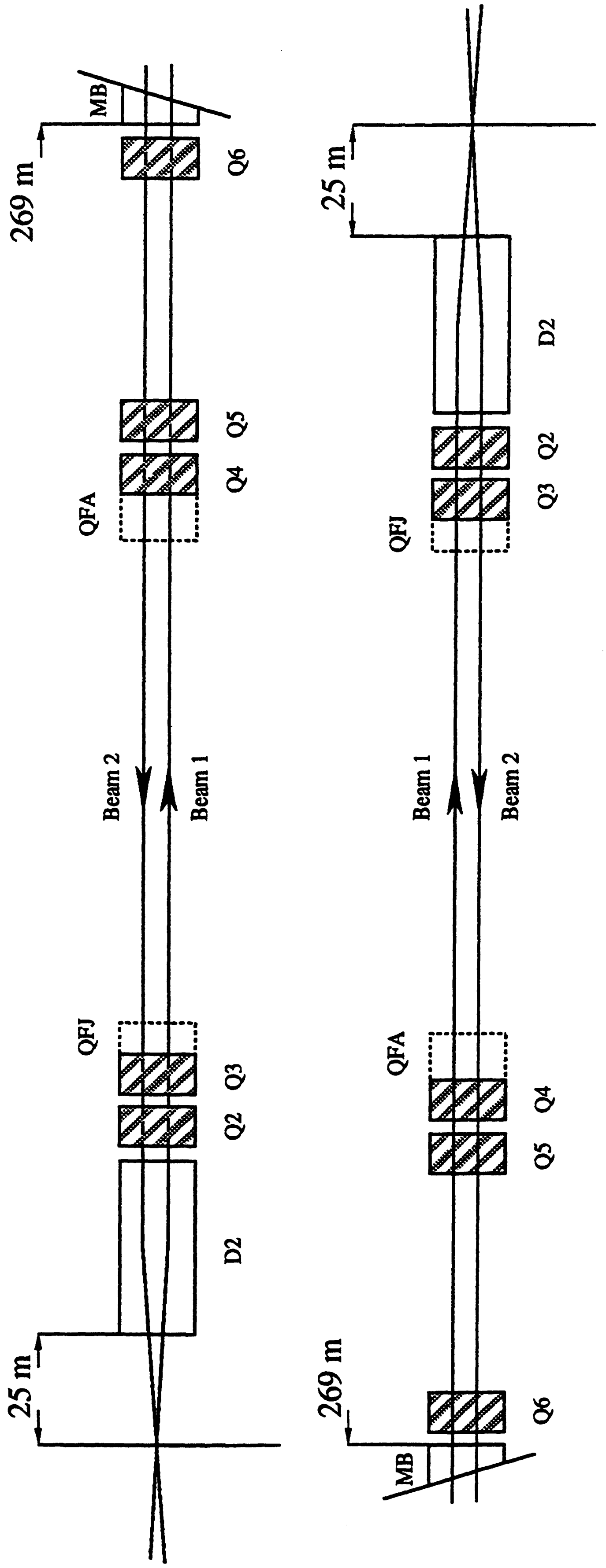

Figure 29: Simple insertion layout

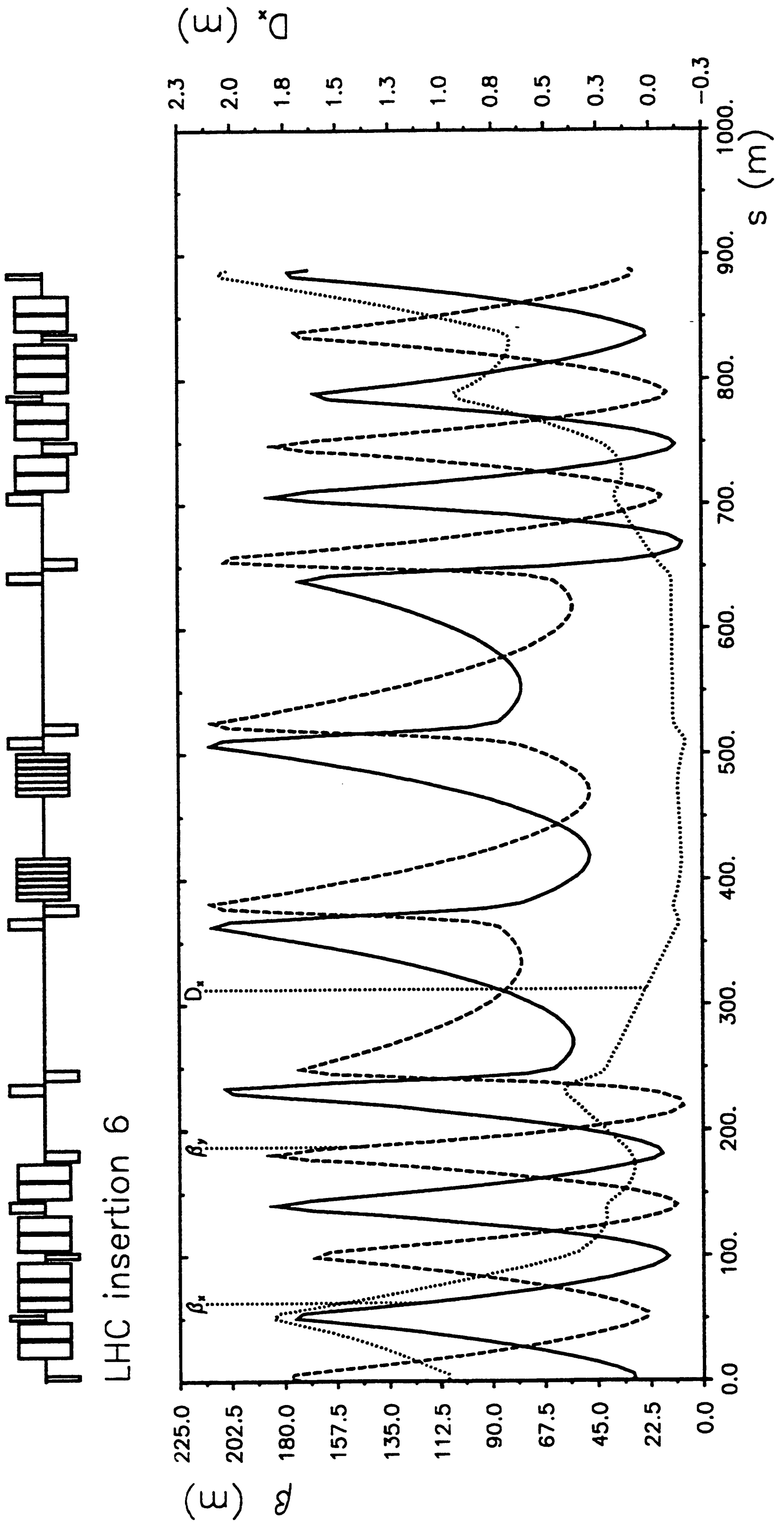

Figure 30: Simple insertion lattice functions

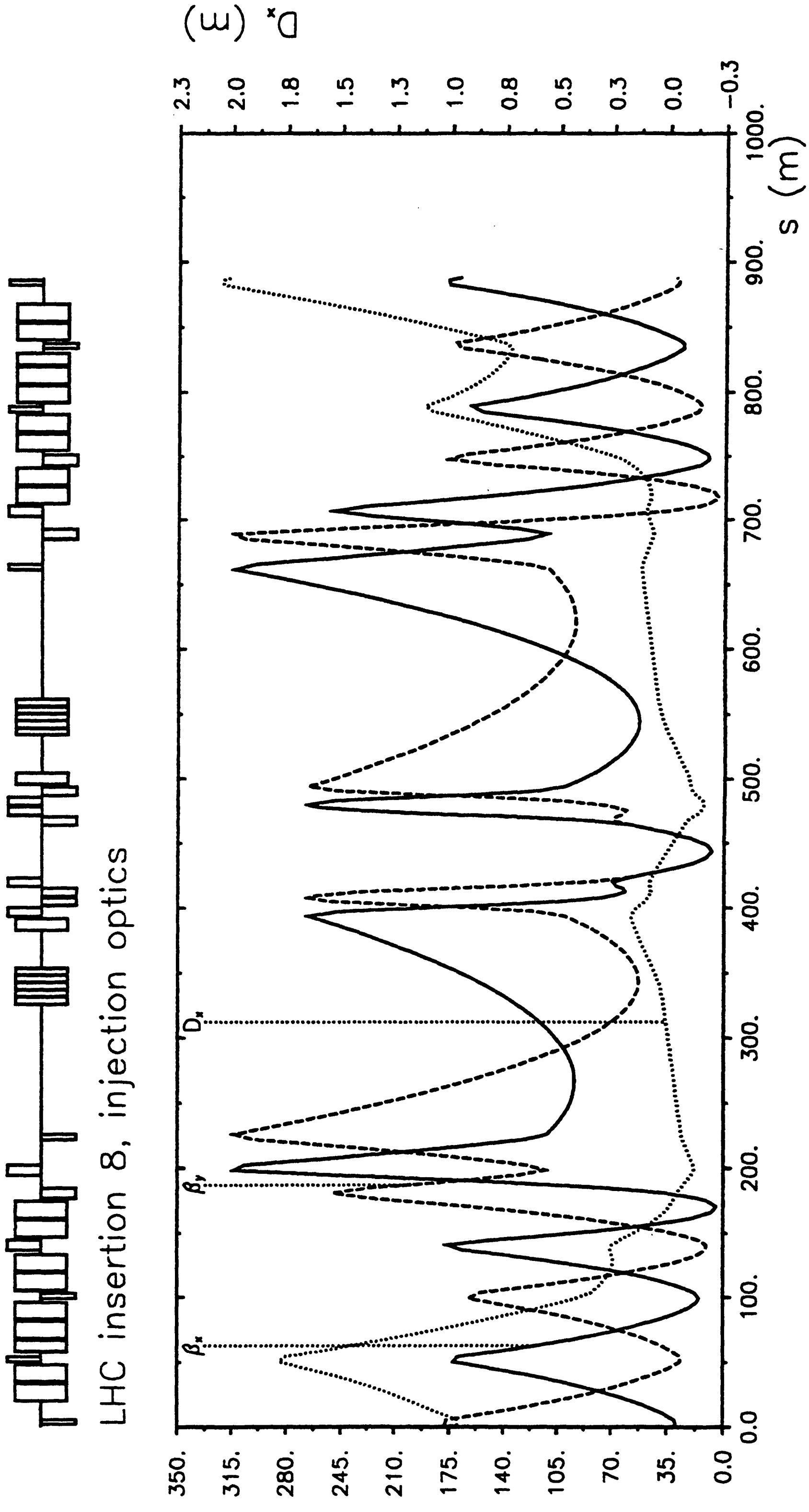

Figure 31: The SS 8 insertion lattice functions

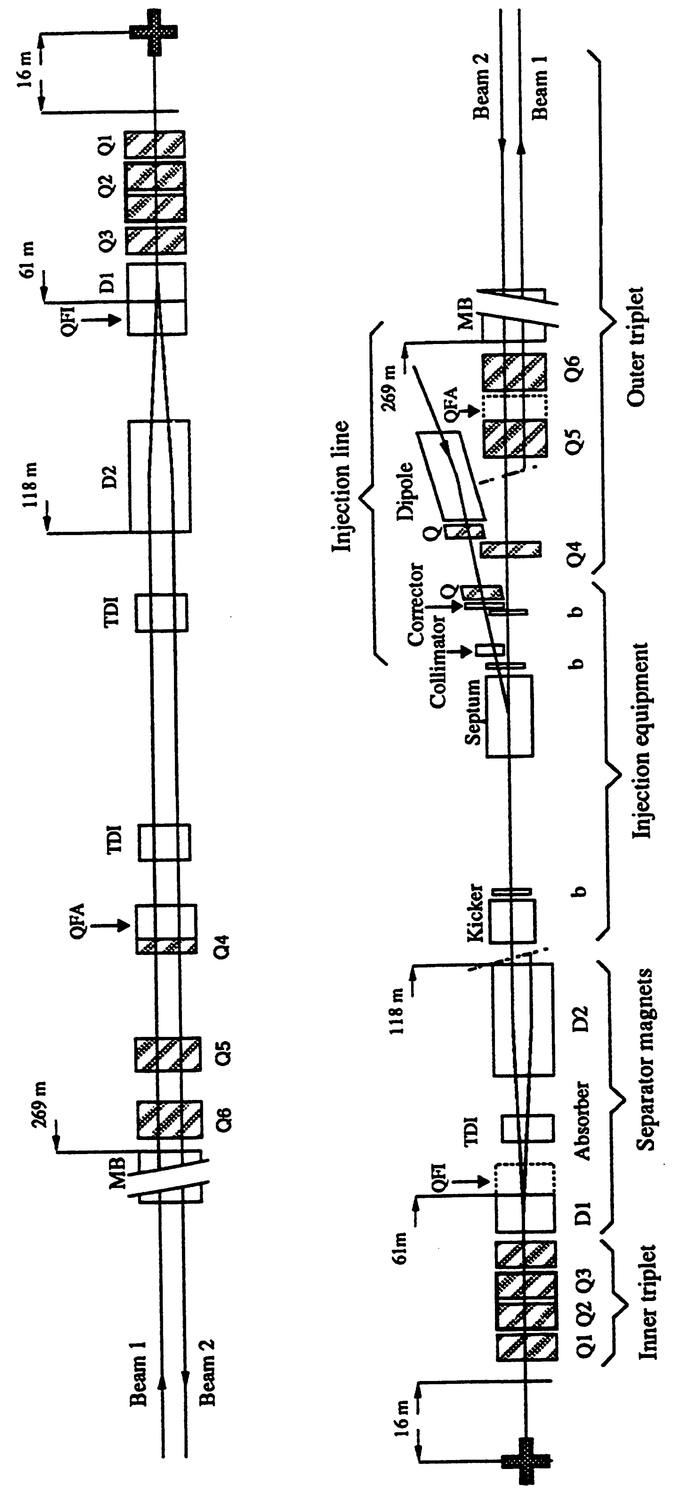

Figure 32: Schematic layout of SS 8

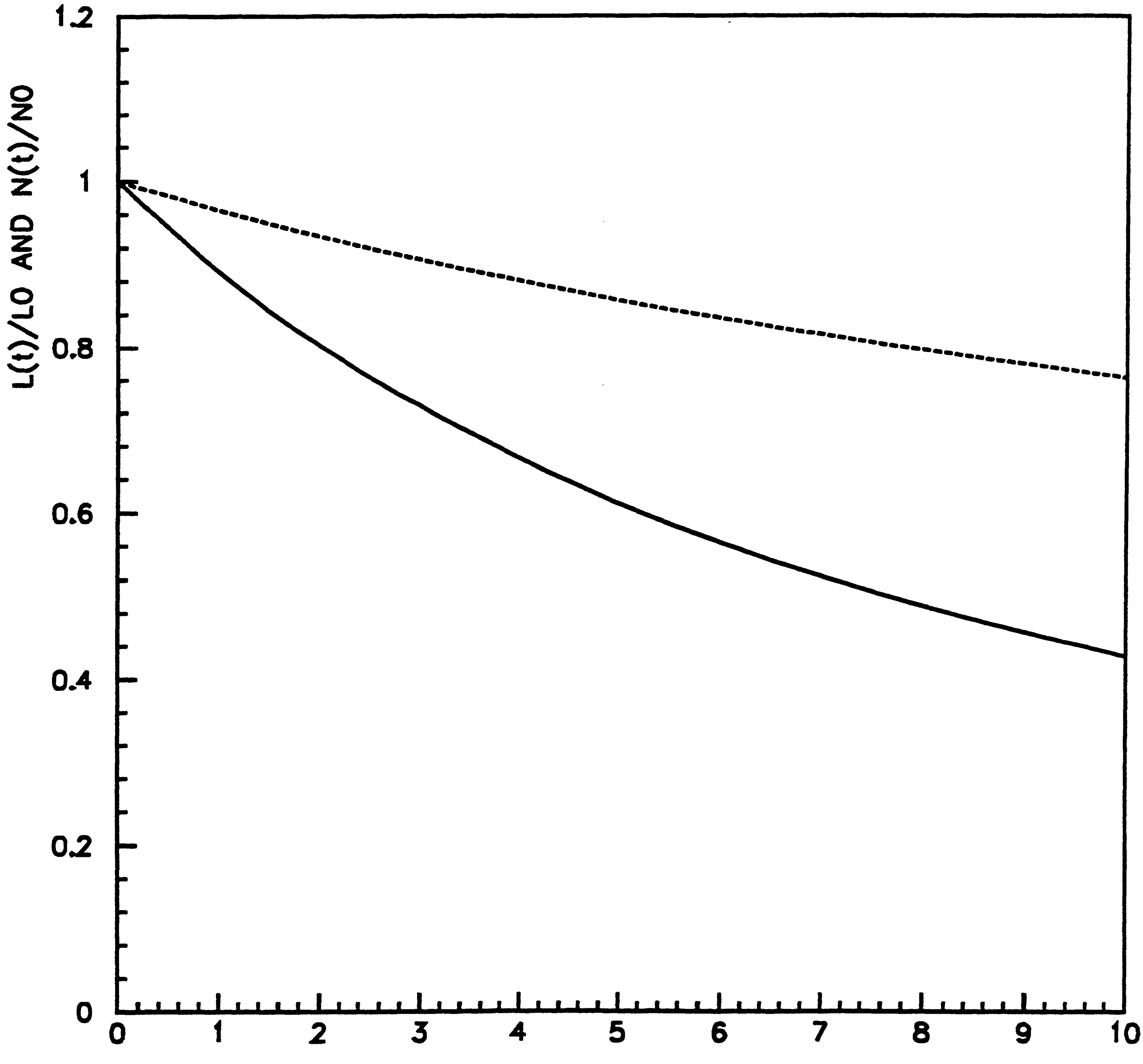

Figure 33: Lead ions: luminosity versus time

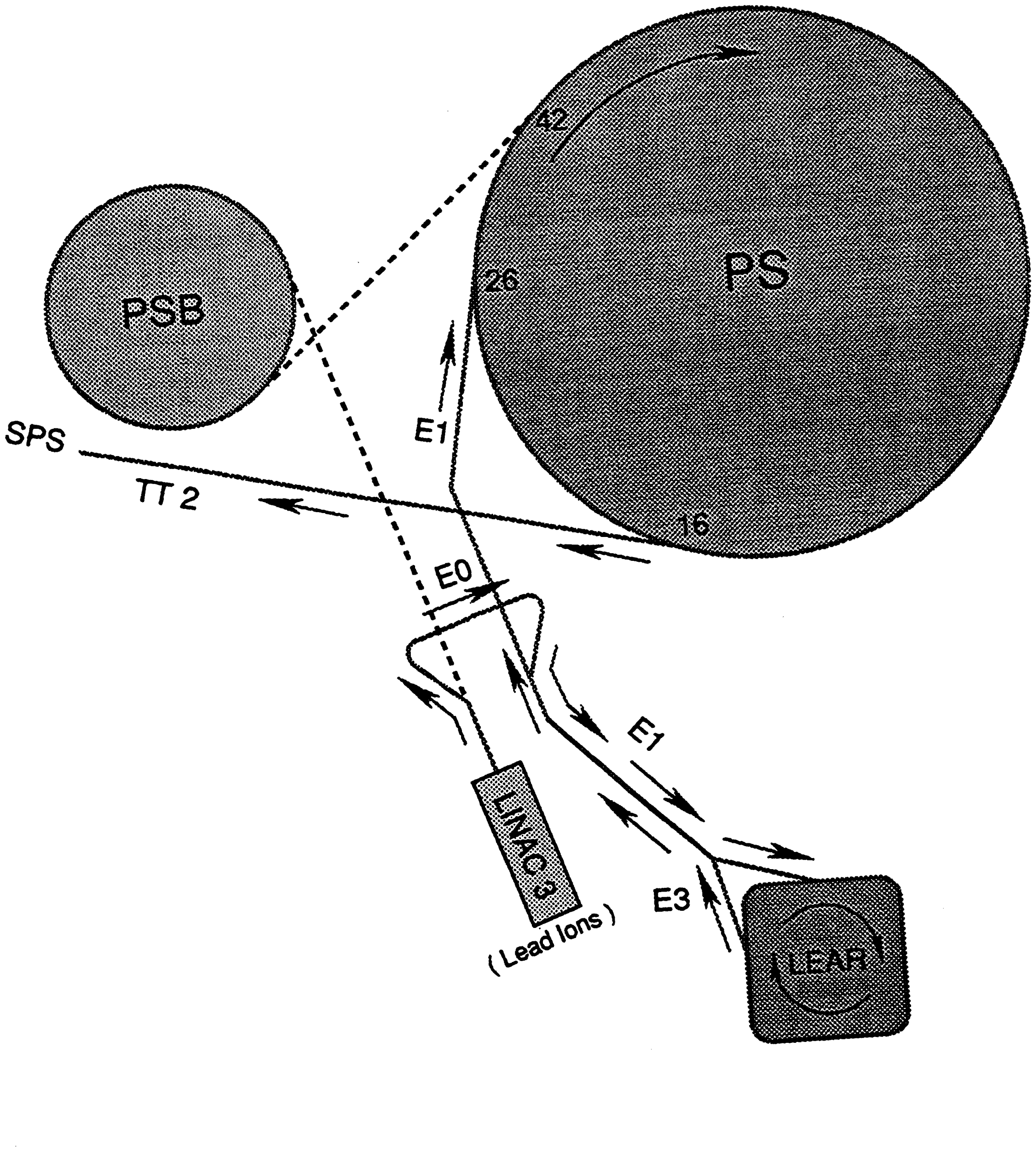

Figure 34: Lead ions: injector layout

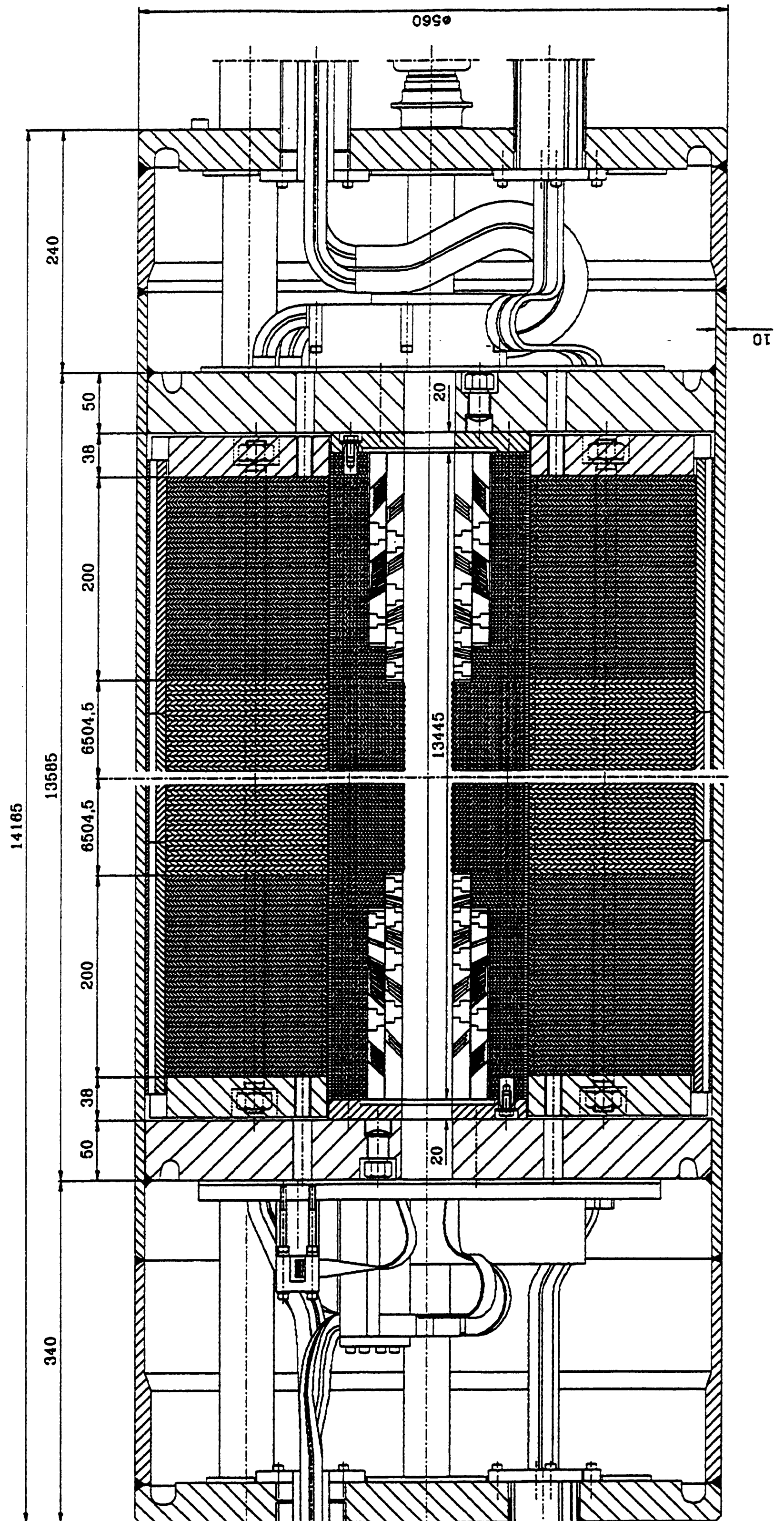

Figure 35: LHC dipole – longitudinal cross-section

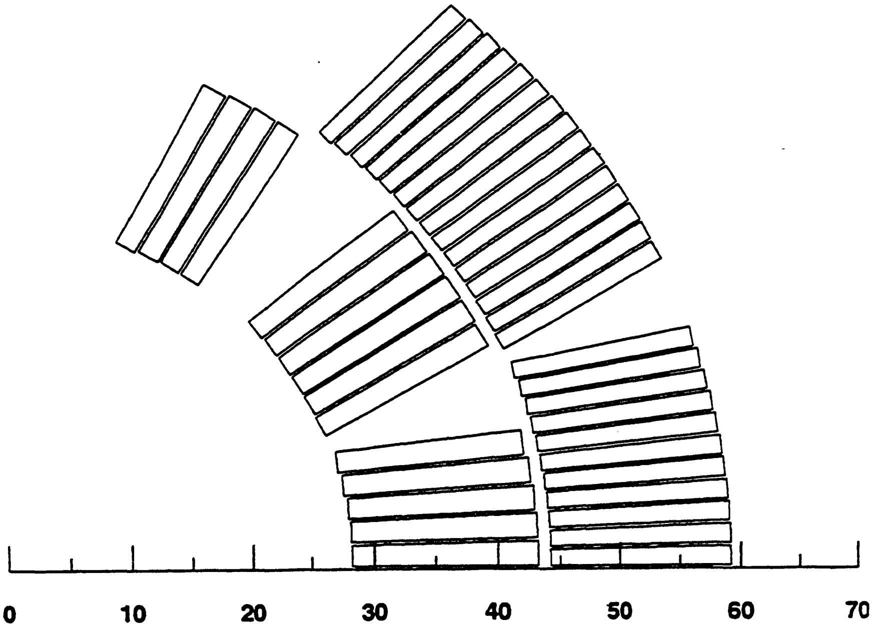

Figure 36: Conductor distribution in the dipole coil cross-section

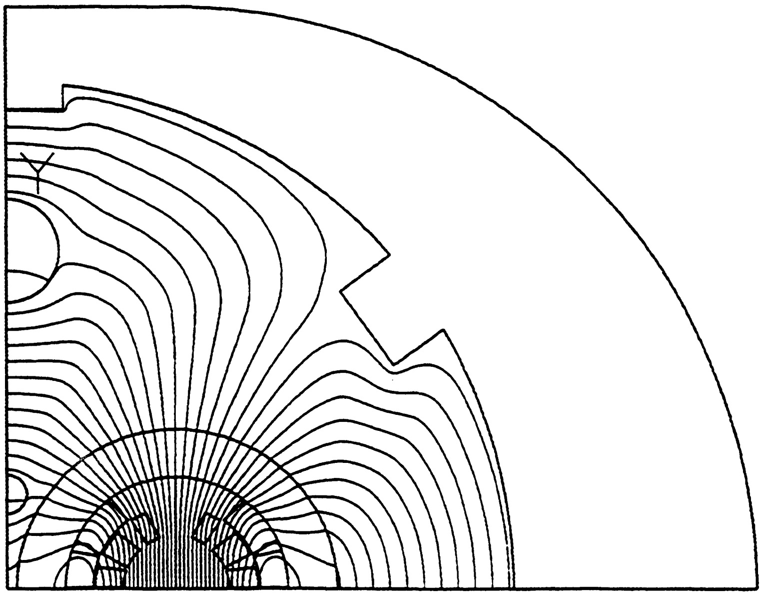

Figure 37: Dipole magnet flux plot

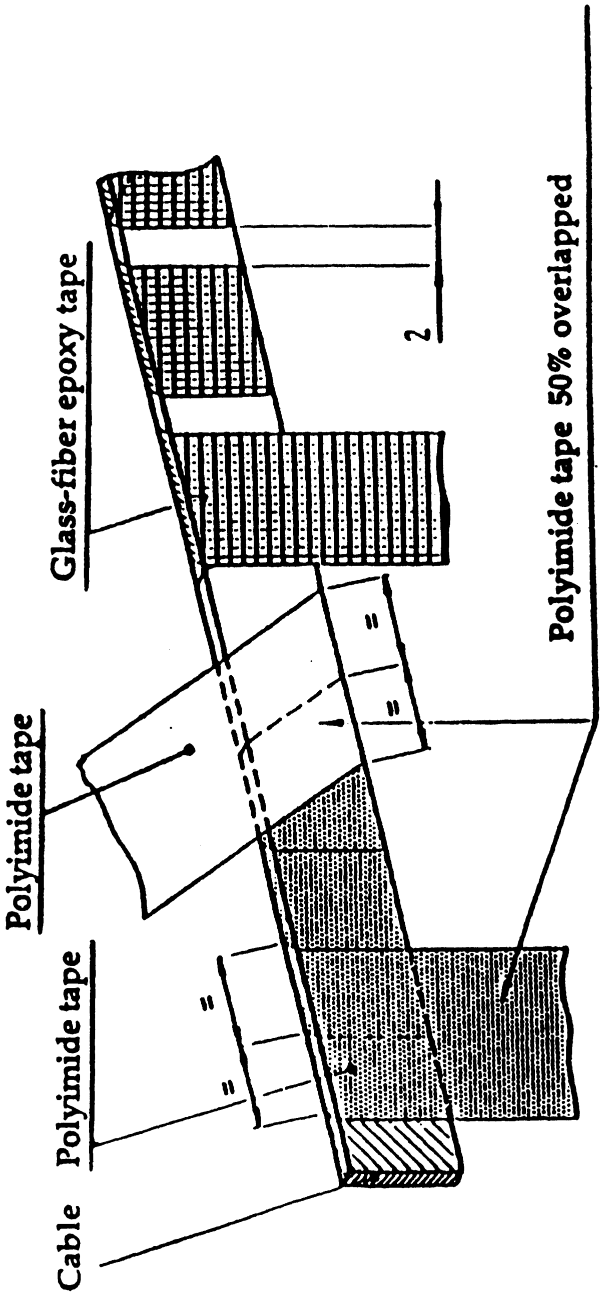

Figure 38: Conductor insulation

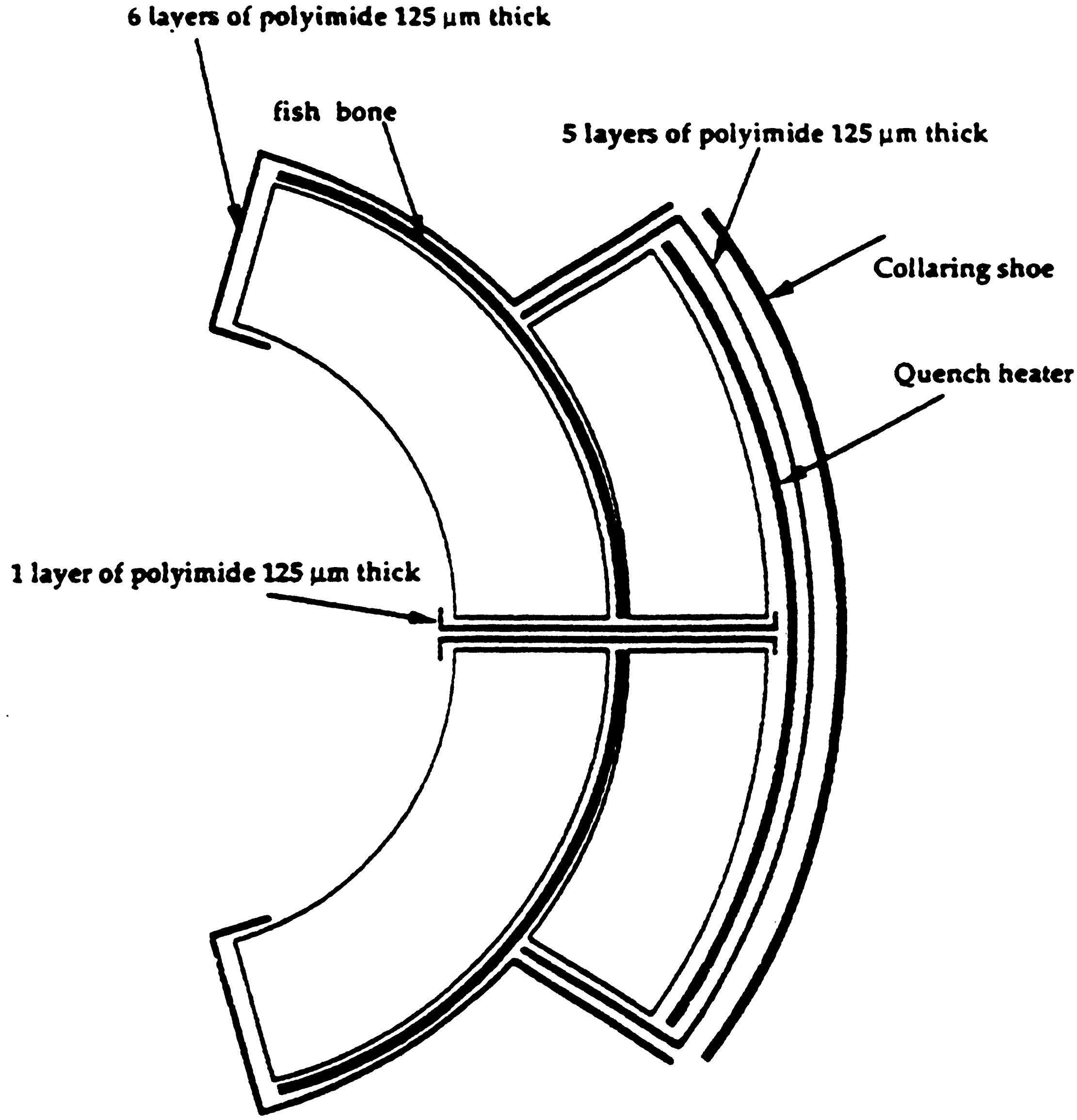

Figure 39: Ground insulation

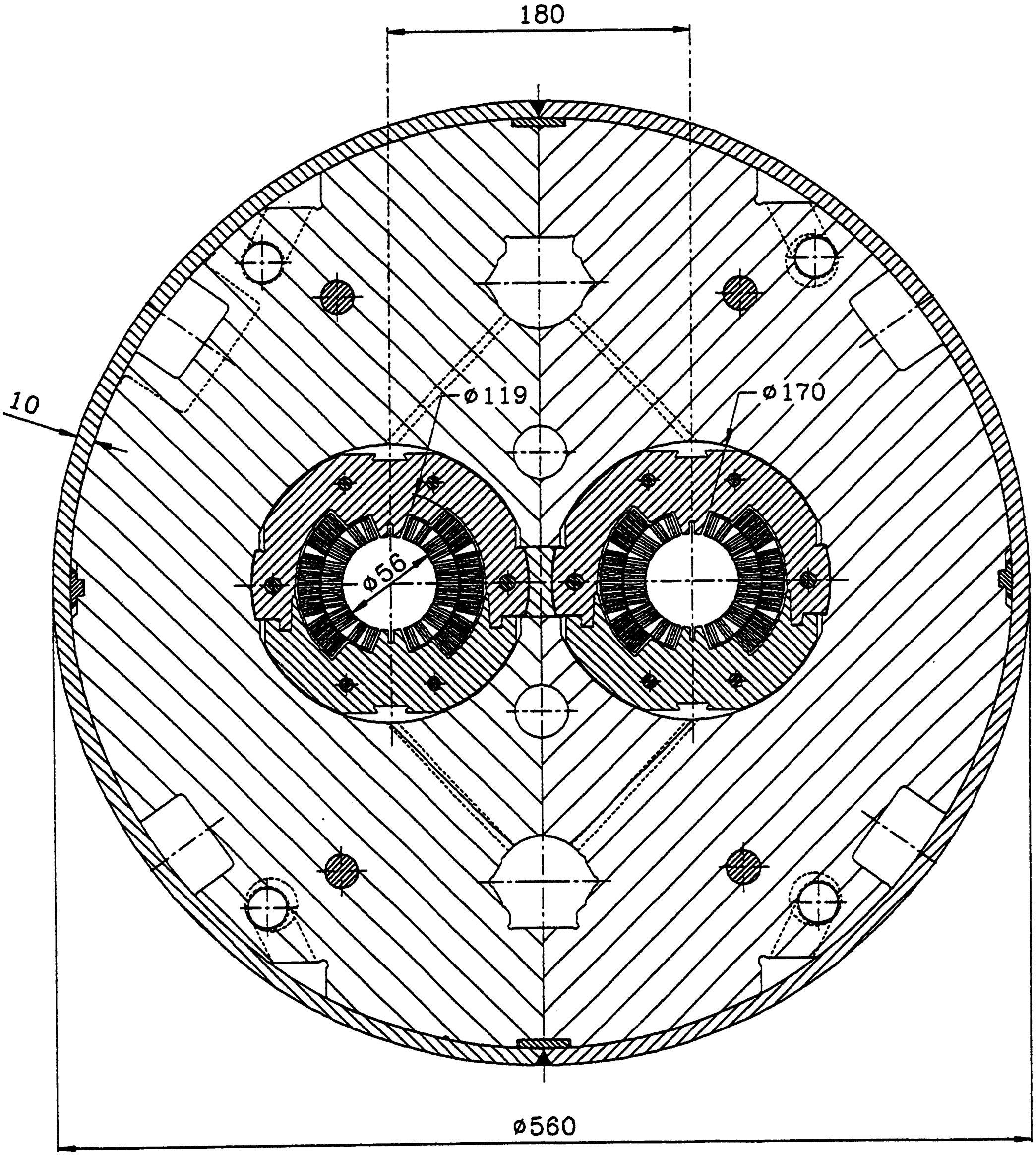

Figure 40: Dipole cold mass cross-section with a vertical gap

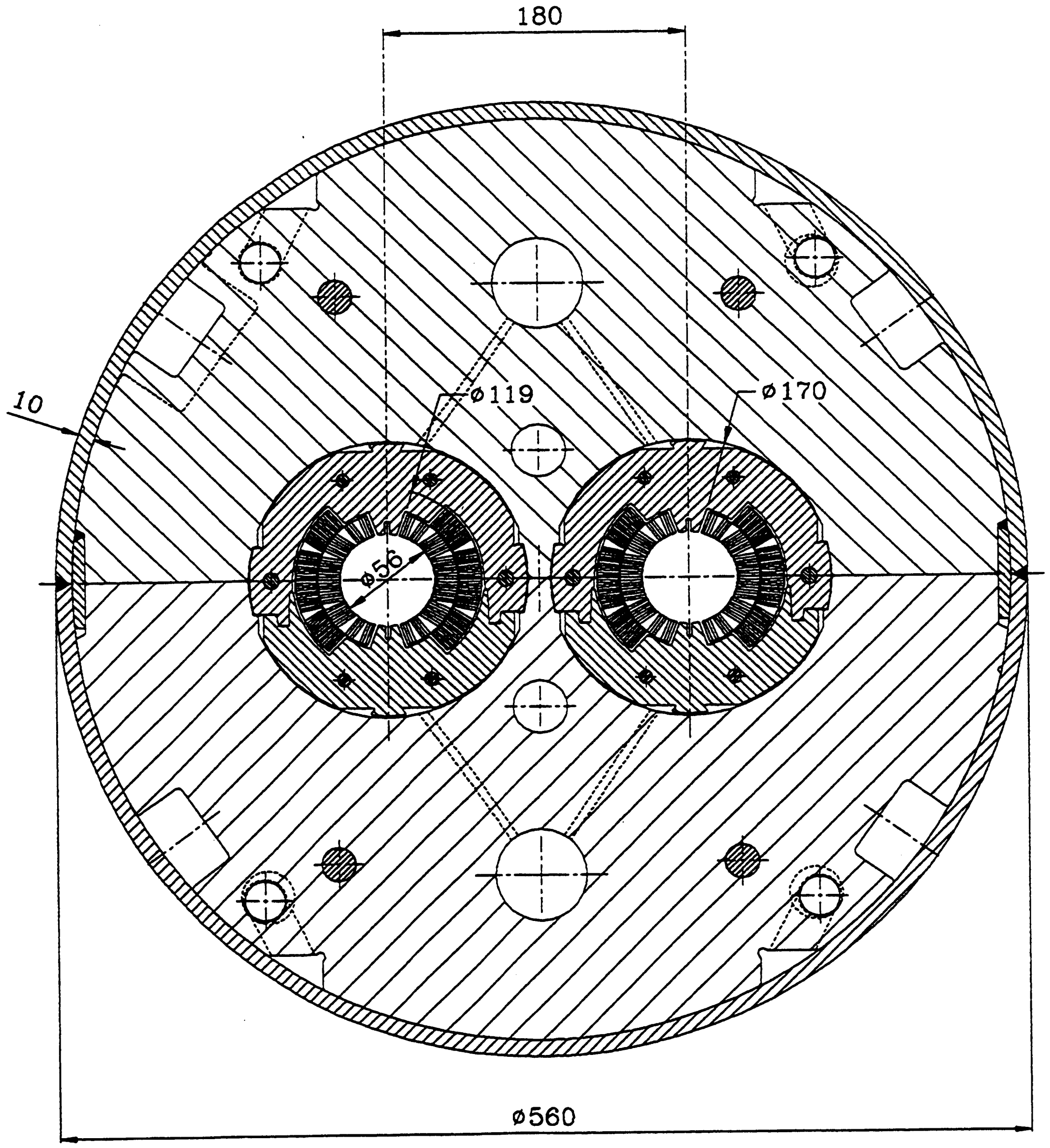

Figure 41: Dipole cold mass cross-section with a horizontal gap

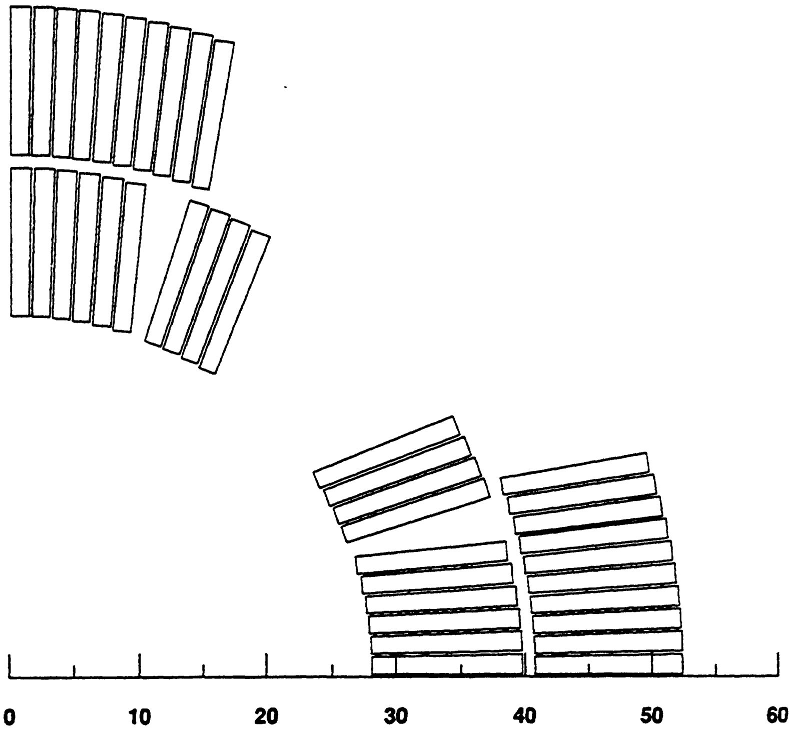

Figure 42: Conductor distribution in the quadrupole cross-section

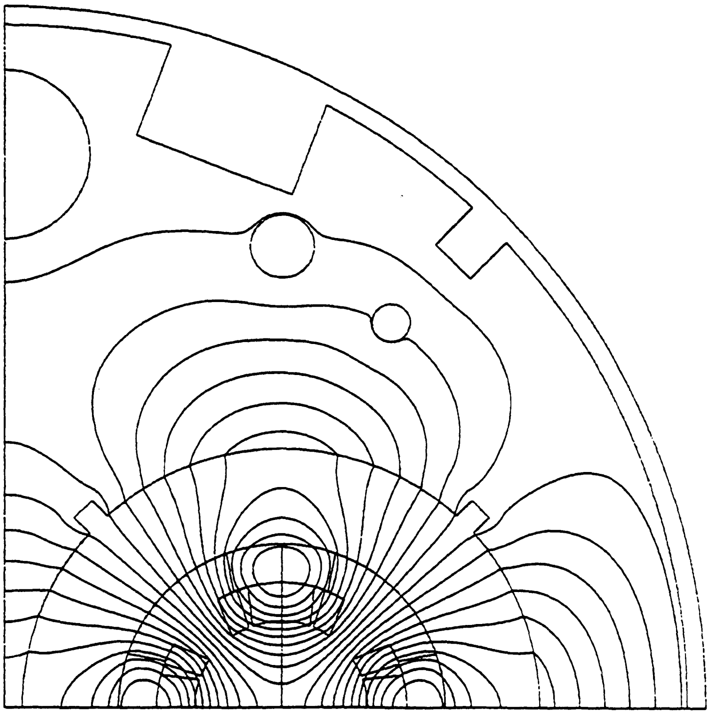

Figure 43: Quadrupole magnet flux plot

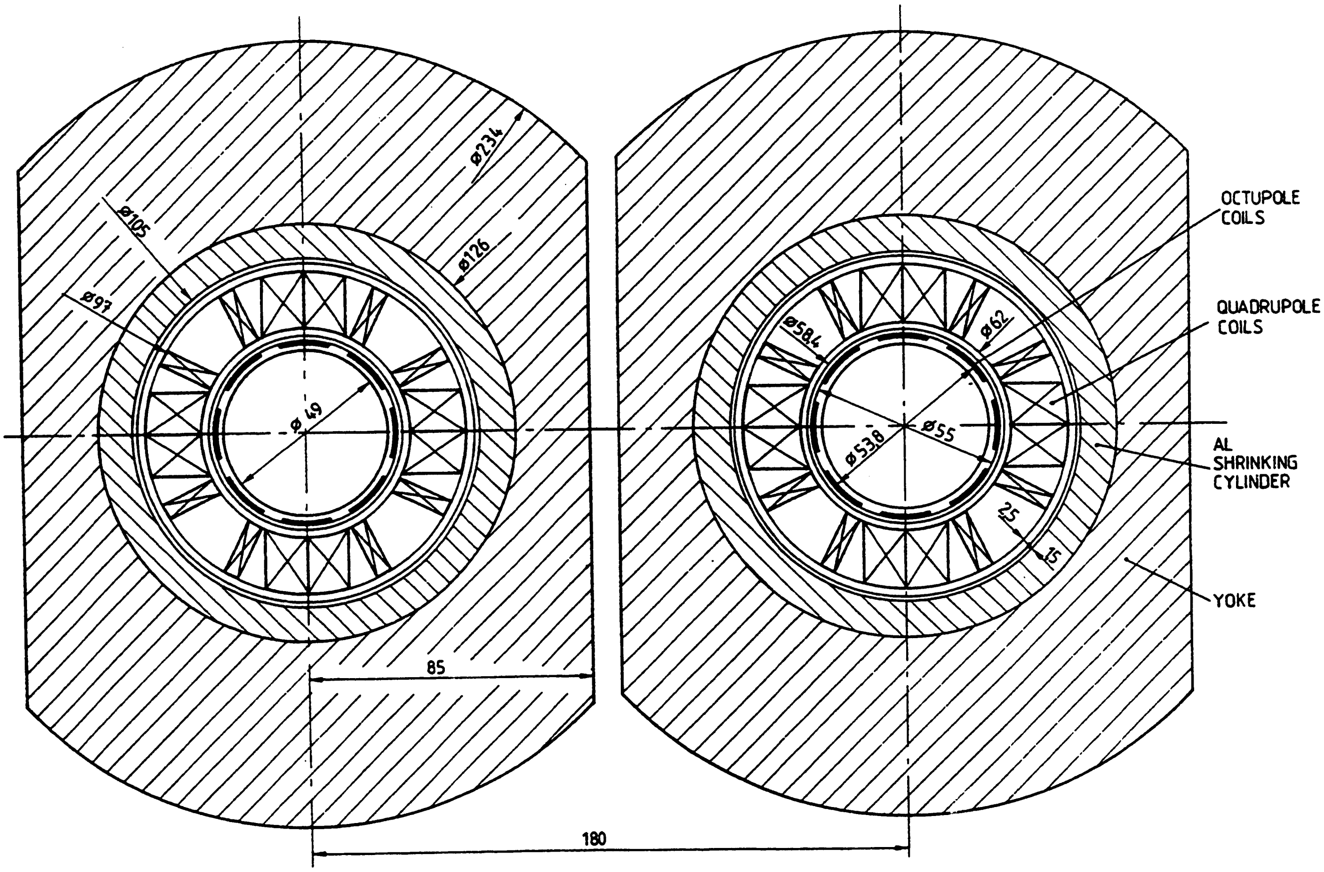

Figure 44: Combined tuning quadrupole and octupole

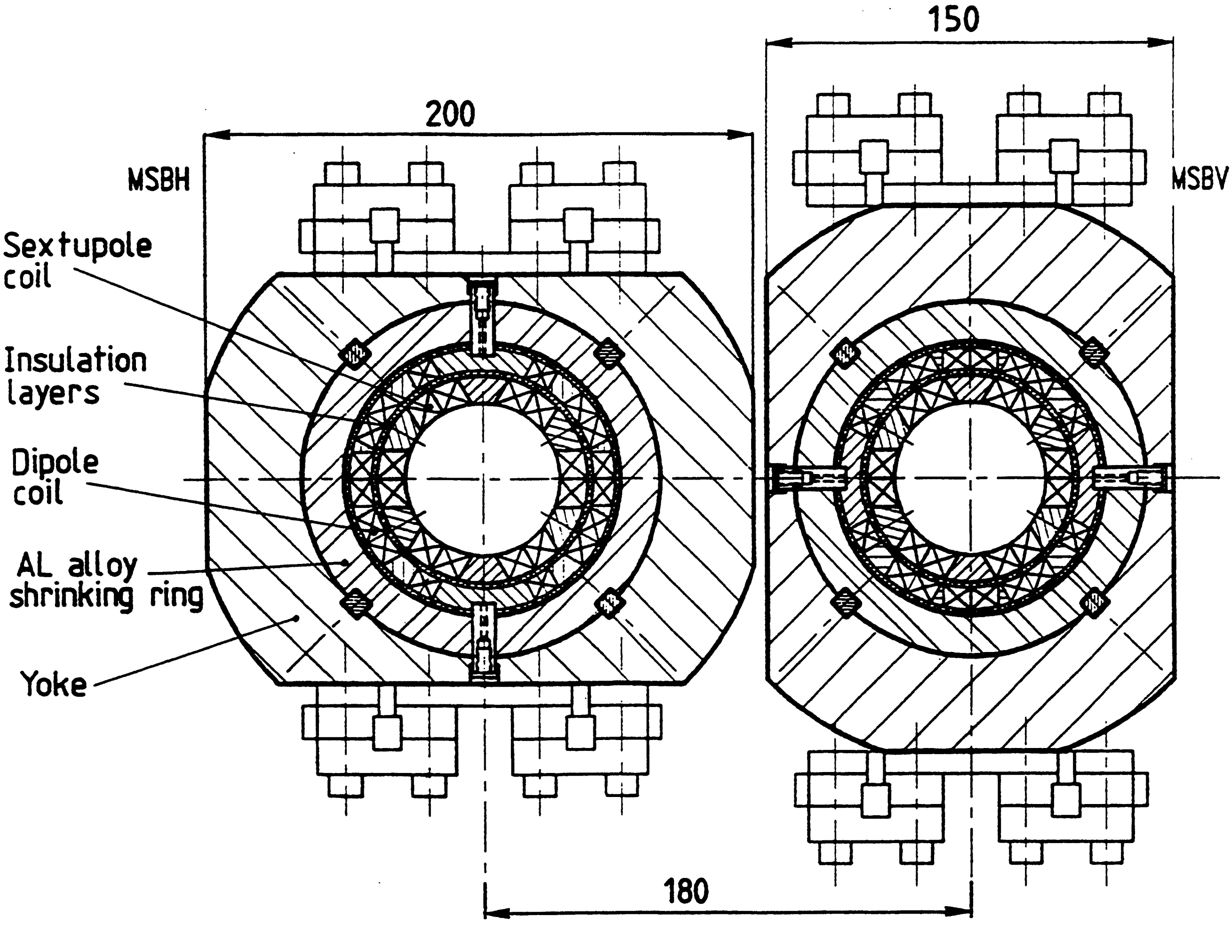

Figure 45: Cross-section of MSBH & MSBV corrector

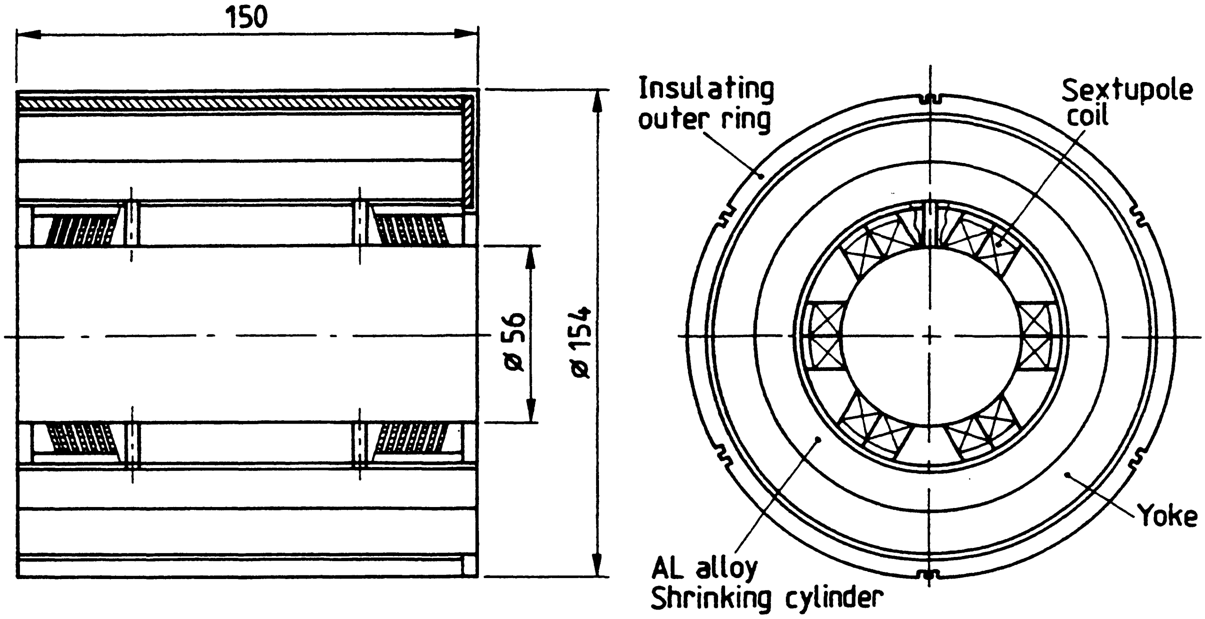

Figure 46: Cross-section of sextupole (MSC) spool-piece corrector magnet

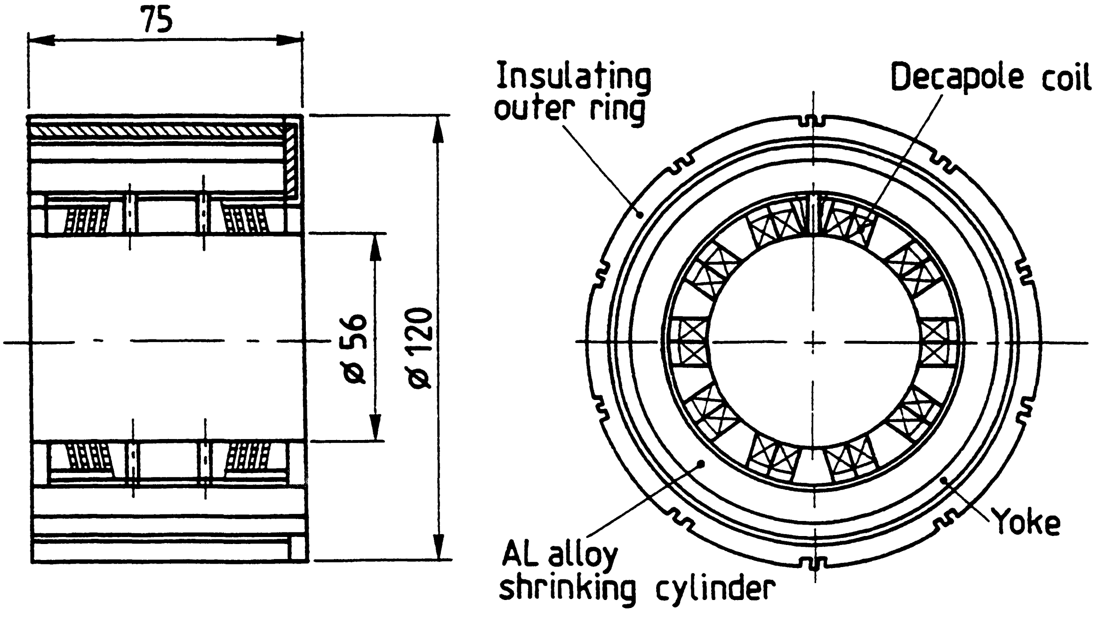

Figure 47: Cross-section of decapole (MDC) spool-piece corrector magnet

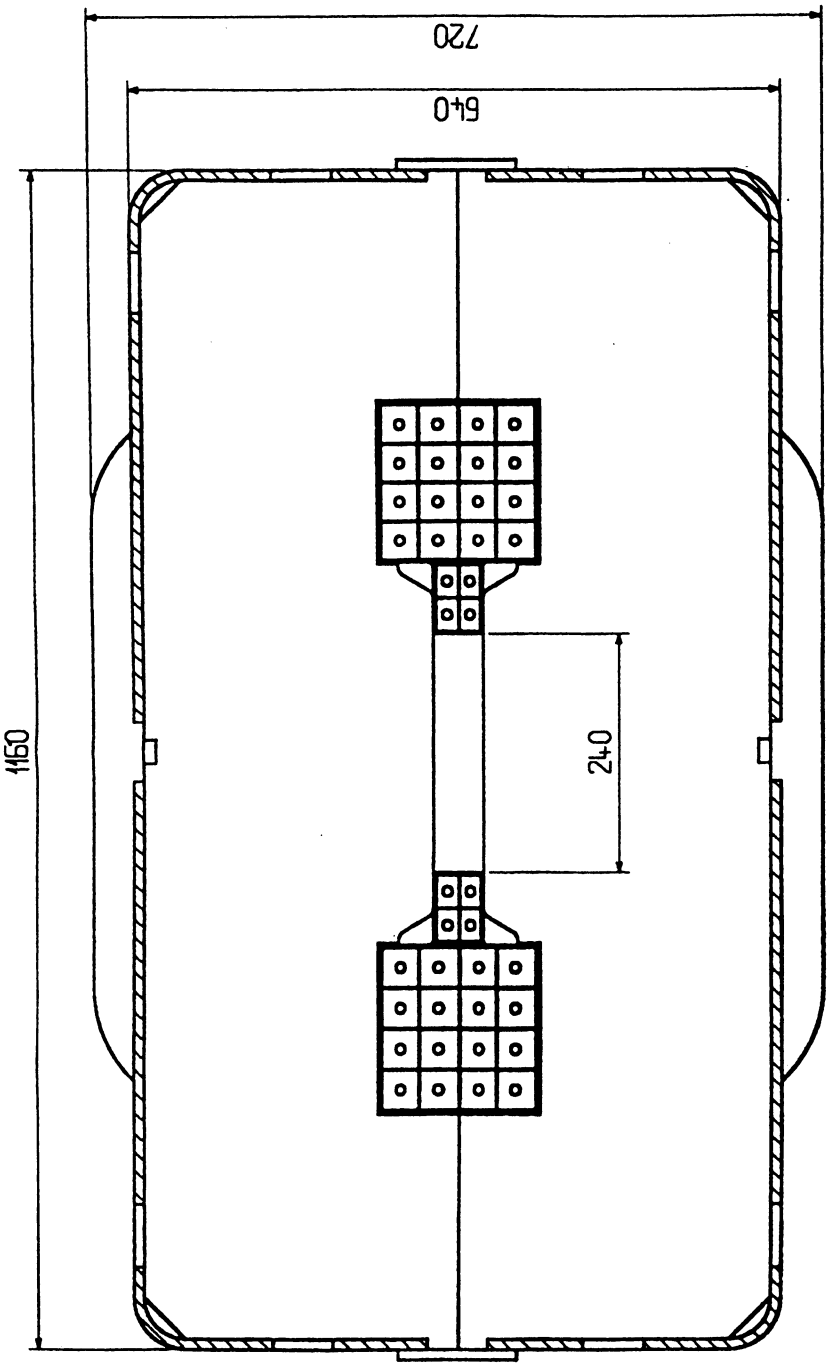

Figure 48: Cross-section of D2 separation dipole

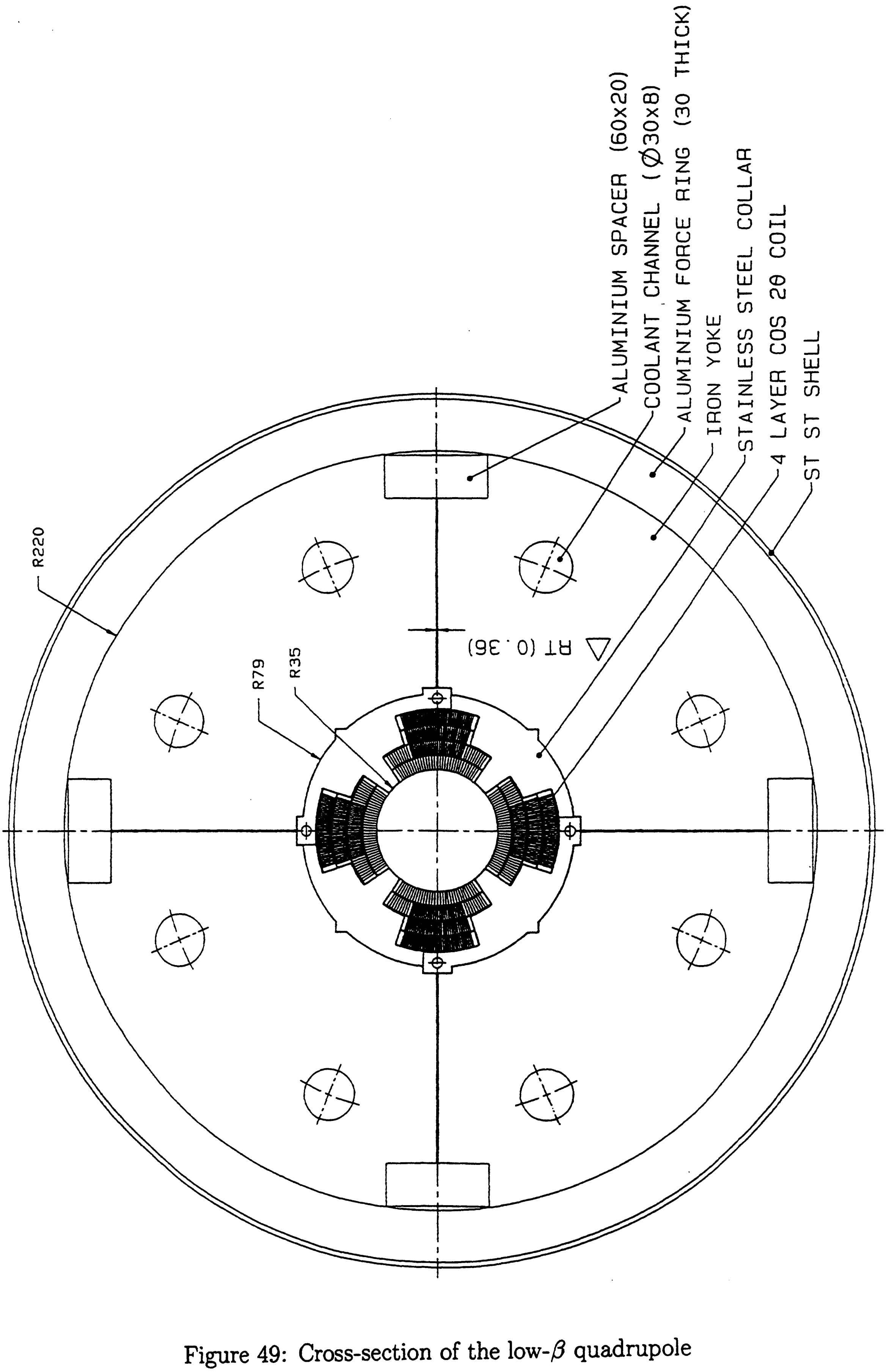

Figure 49: Cross-section of the low-β quadrupole

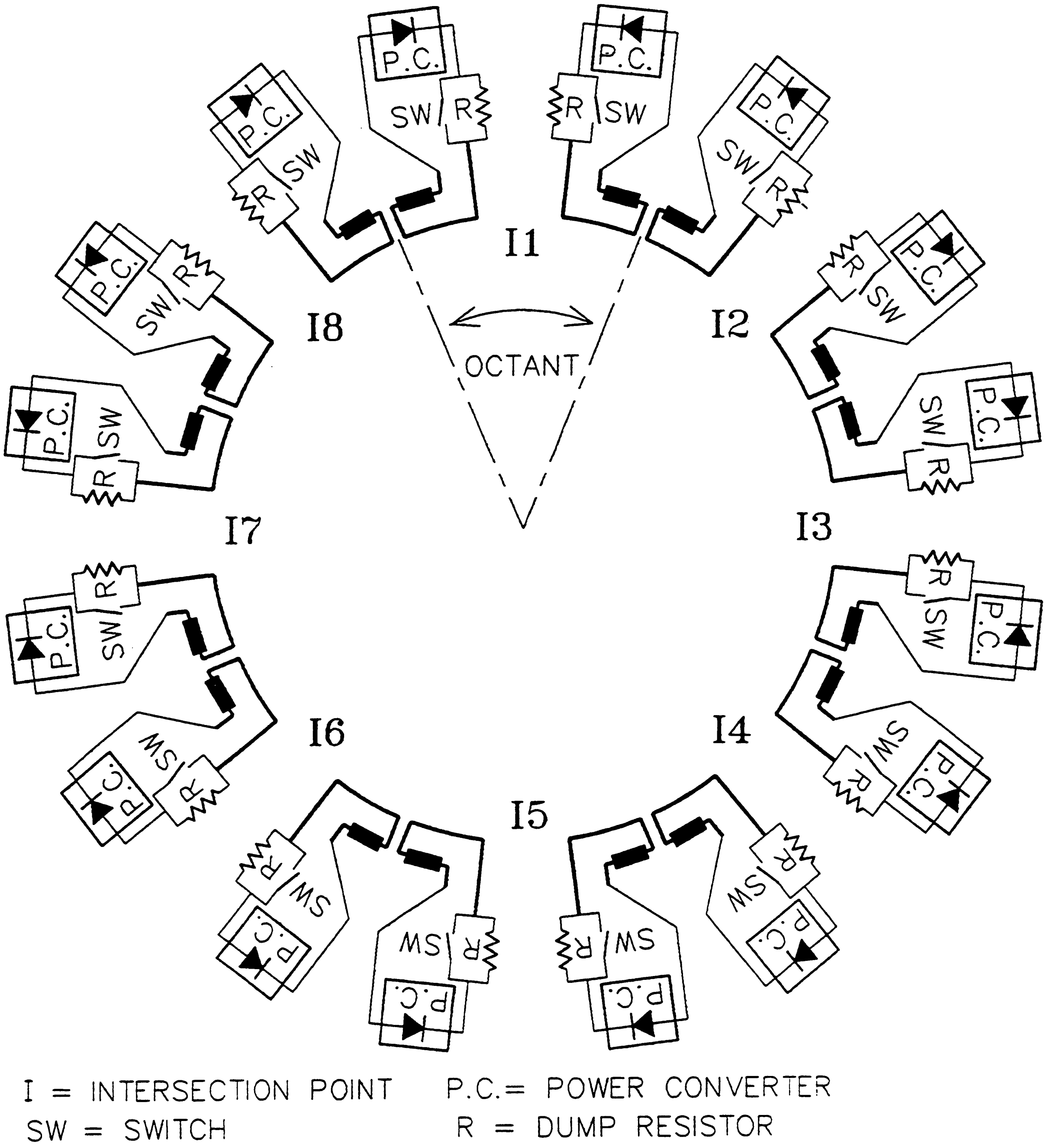

Figure 50: LHC powering

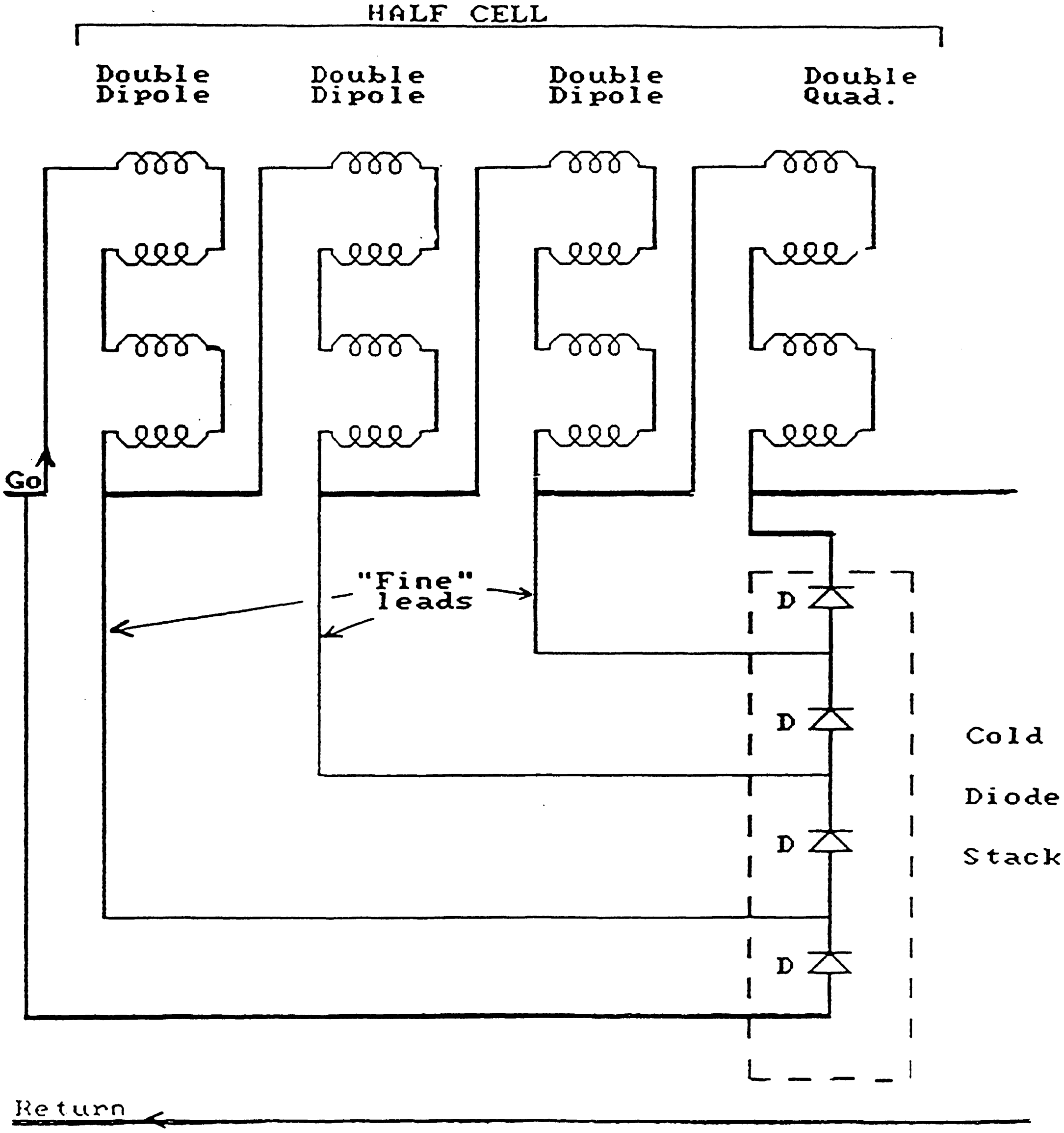

Figure 51: LHC half-cell quench protection scheme, with diodes

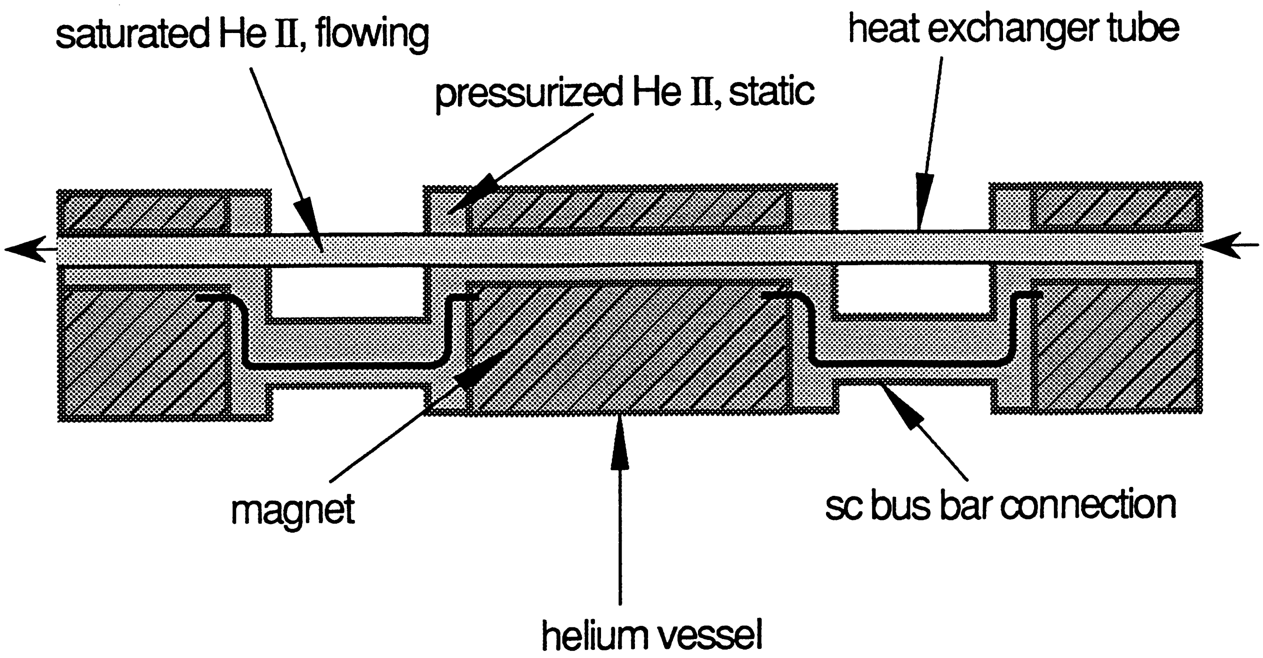

Figure 52: The LHC superfluid helium cooling scheme

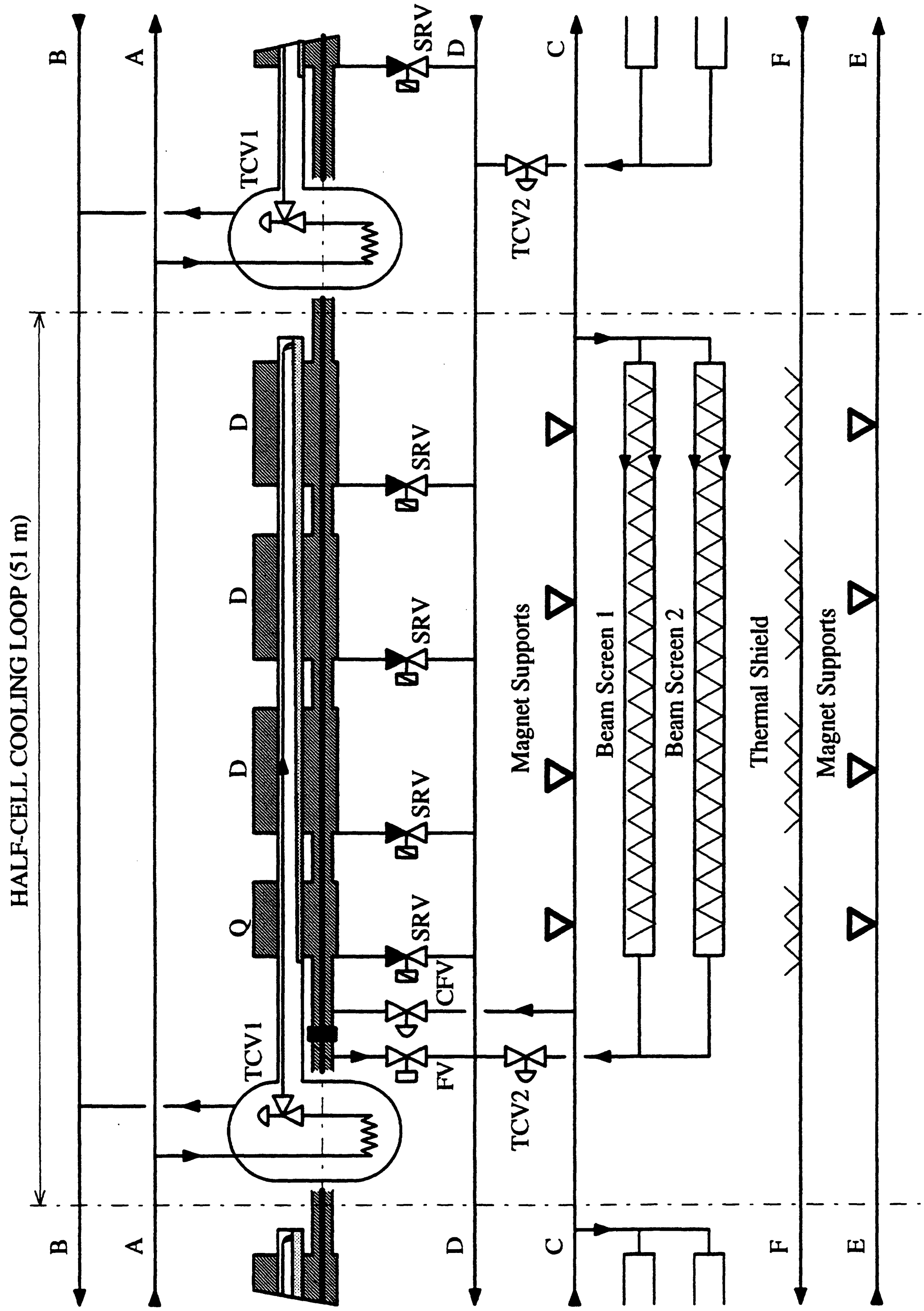

Figure 53: Cryogenic flow scheme of half-cell

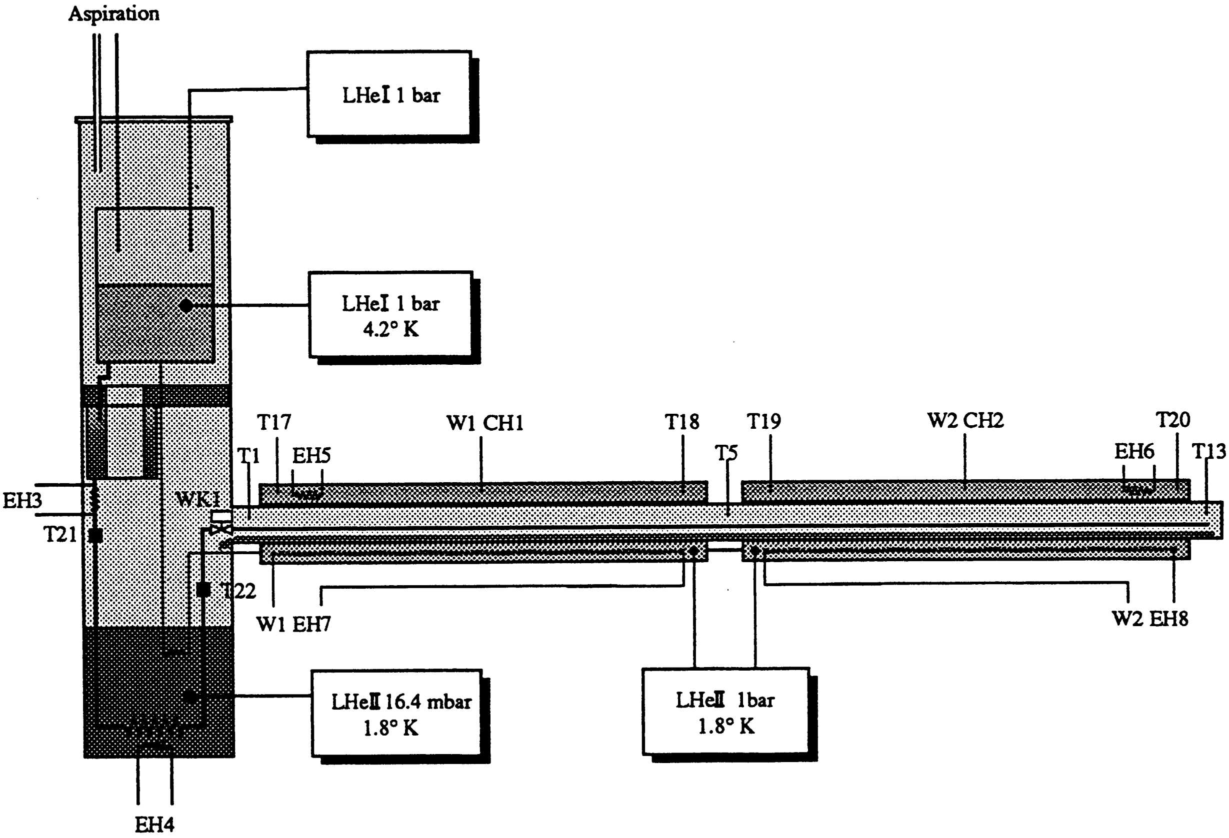

Figure 54: Flow scheme of superfluid helium model cryoloop

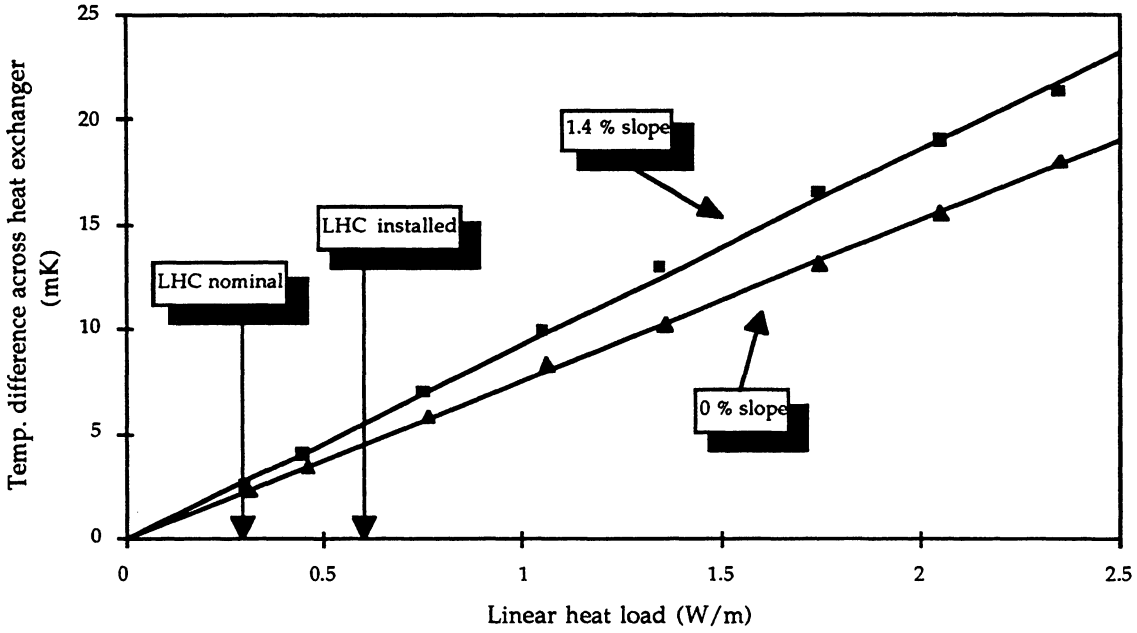

Figure 55: Measured heat transfer across the superfluid helium heat-exchanger tube

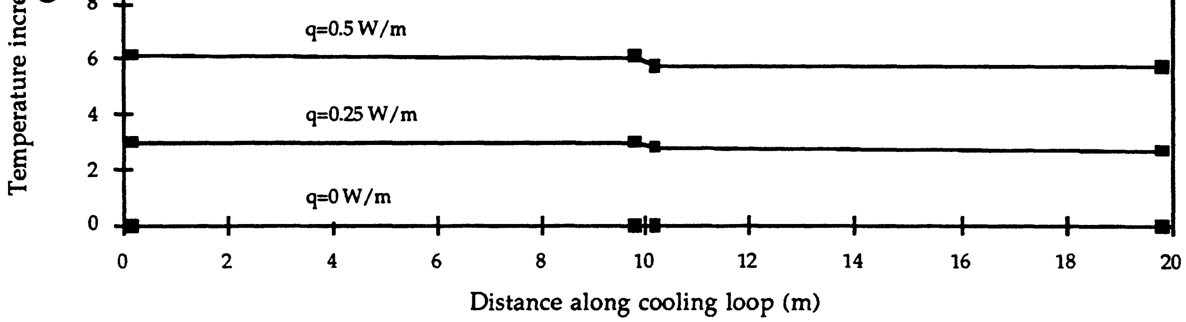

Figure 56: Measured heat-transfer profile in the static pressurized superfluid helium as a function of applied heat load

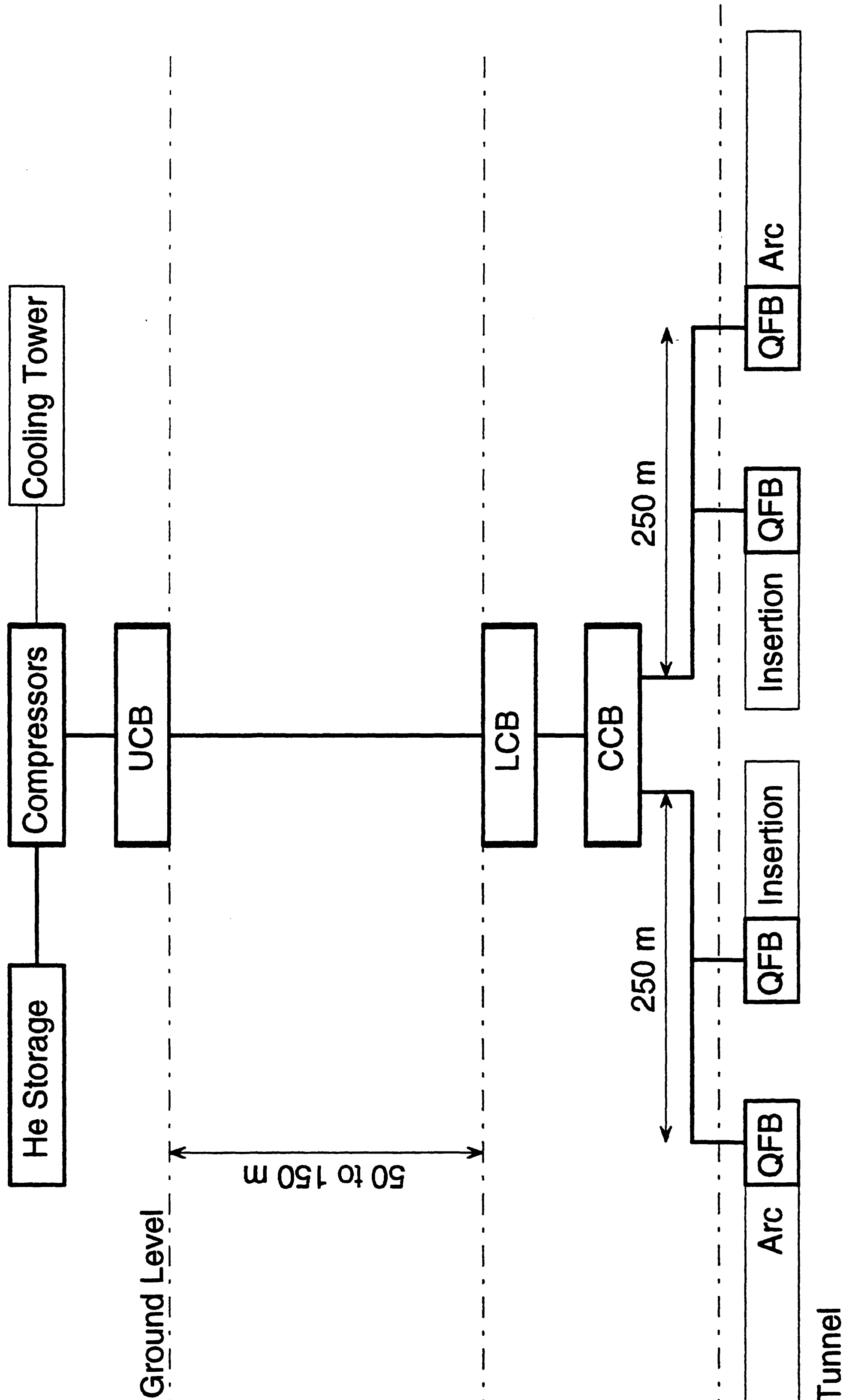

Figure 57: Block diagram of cryogenics for standard LHC octant

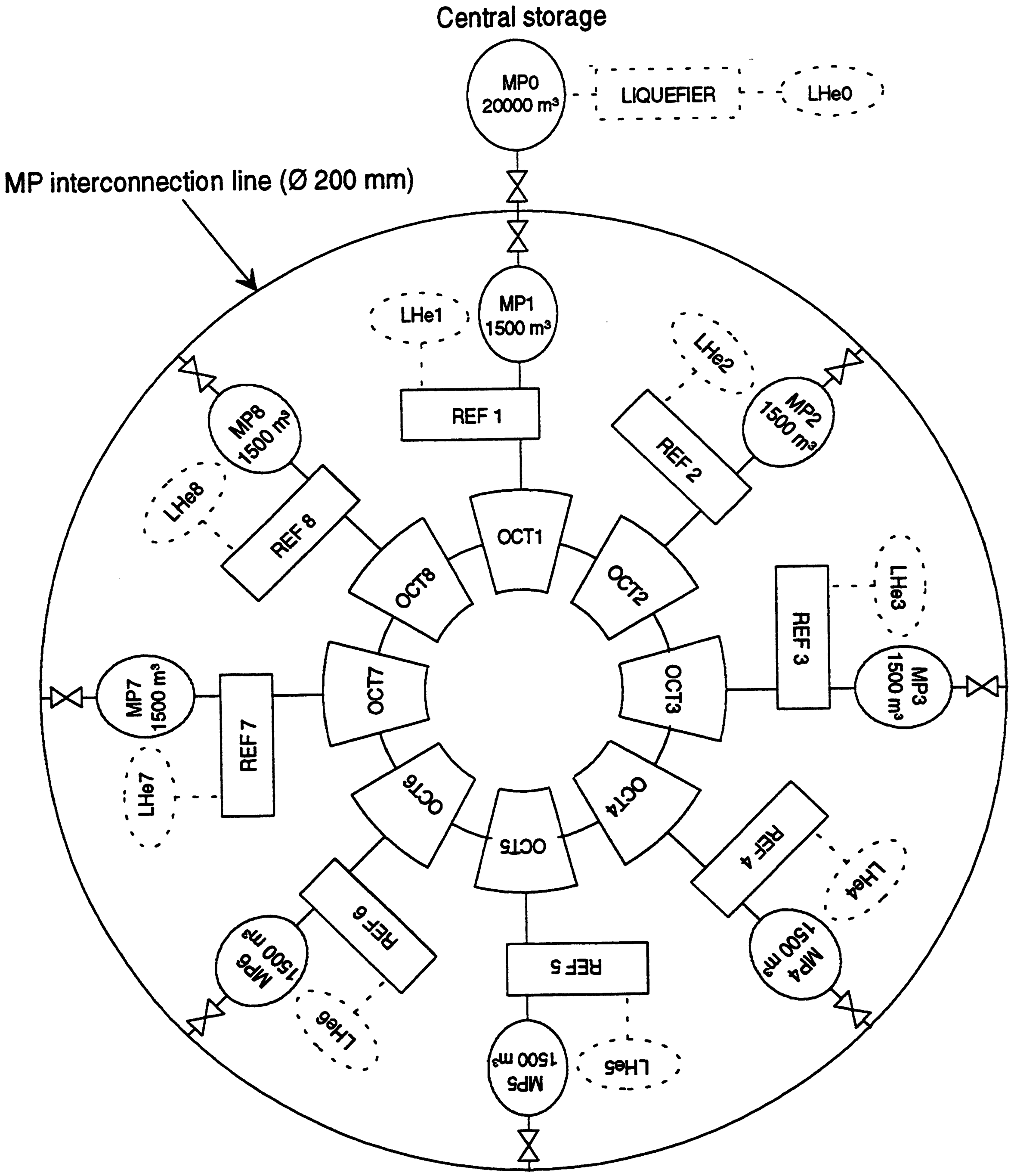

Figure 58: Storage and management of the LHC helium inventory

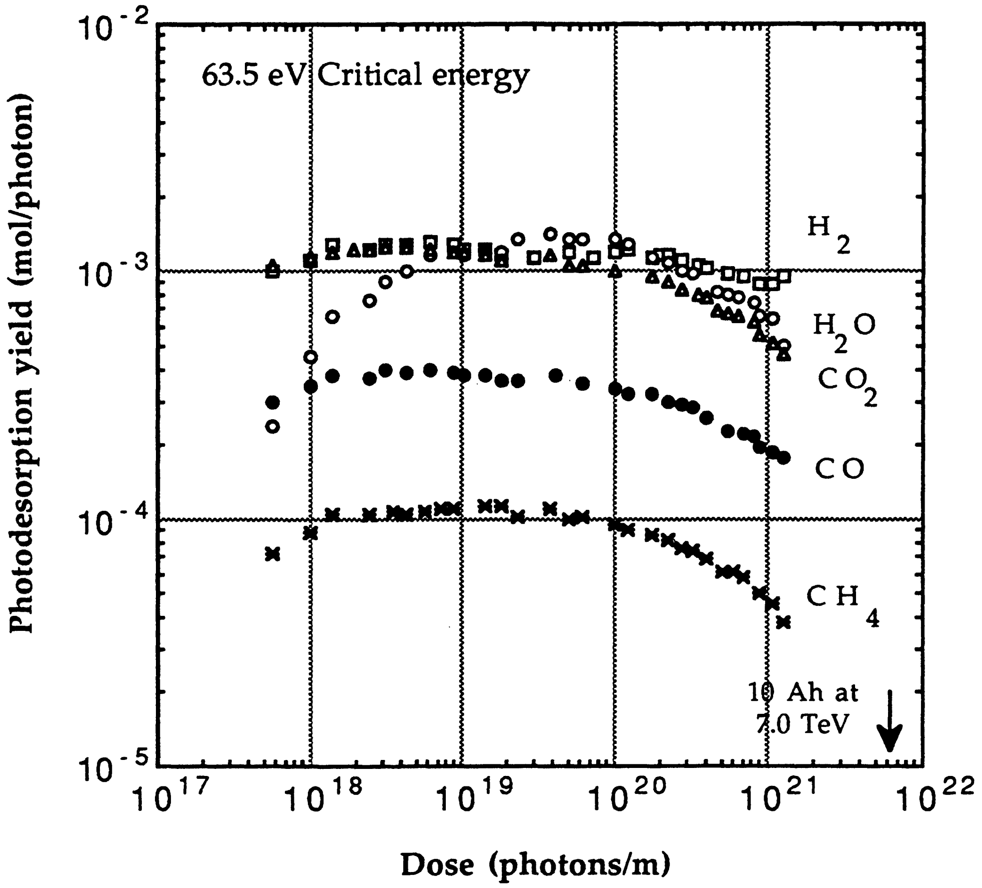

Figure 59: The synchrotron-radiation-induced desorption yields at 63.5 eV critical energy for unbaked Cu-plated stainless steel at room temperature as a function of the photon dose

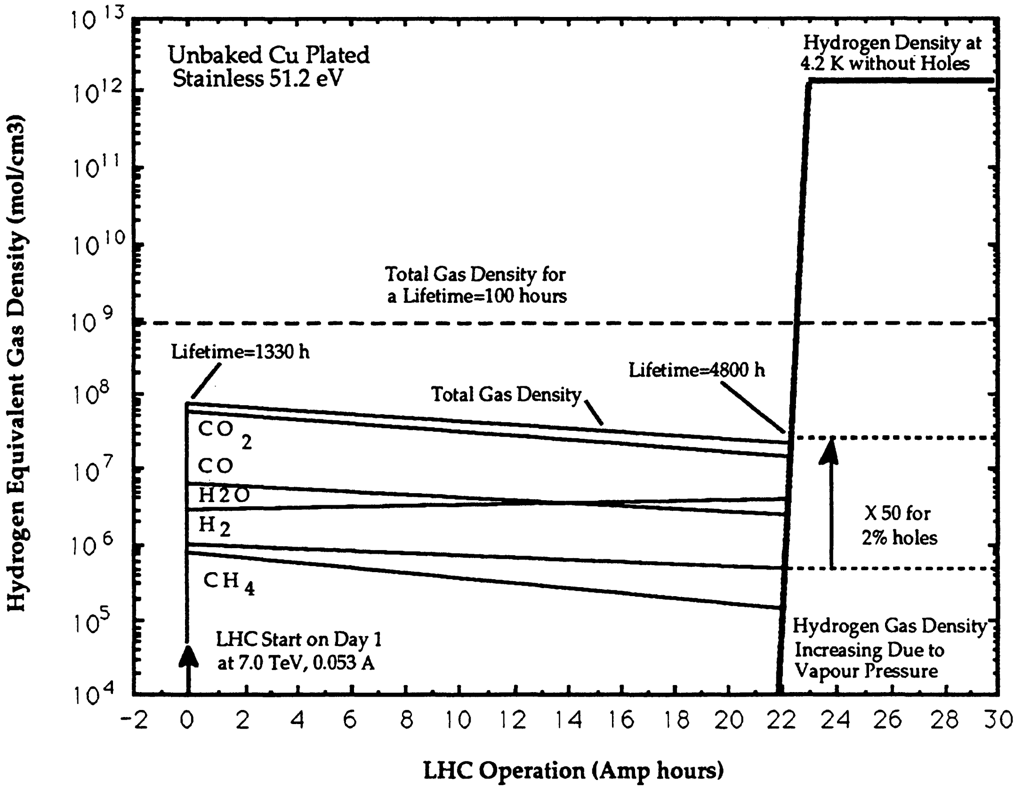

Figure 60: The hydrogen-equivalent gas density at the first start-up of the LHC with the design parameters, and the variation during operation

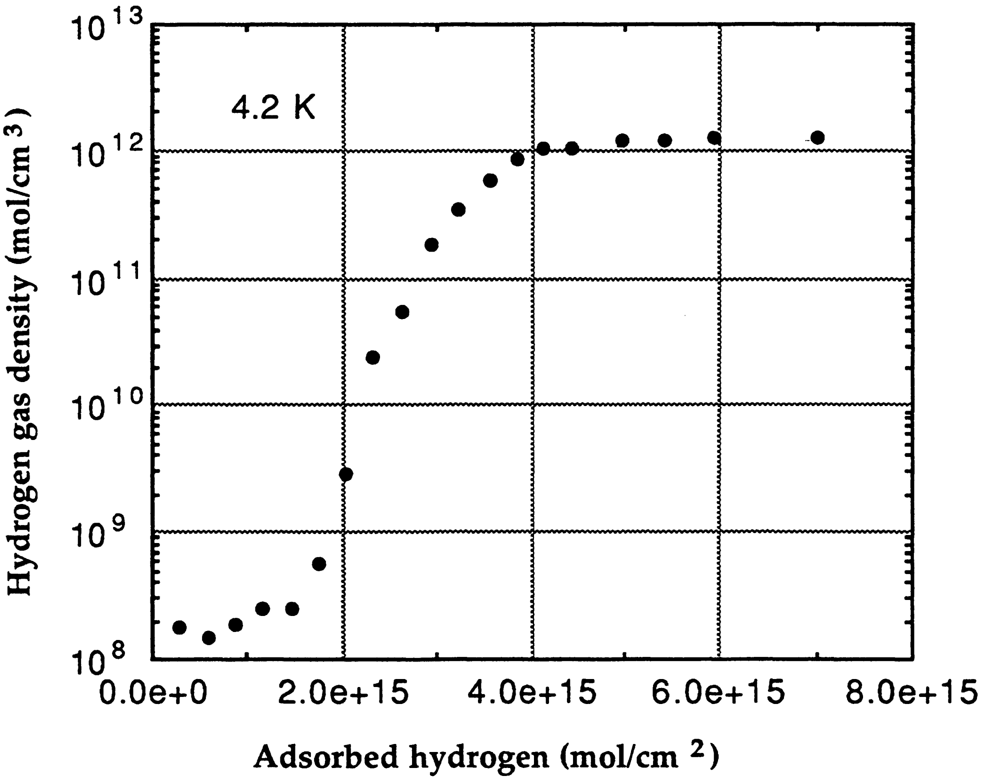

Figure 61: The H_2 adsorption isotherm at 4.2 K on the stainless-steel Cu-plated surface

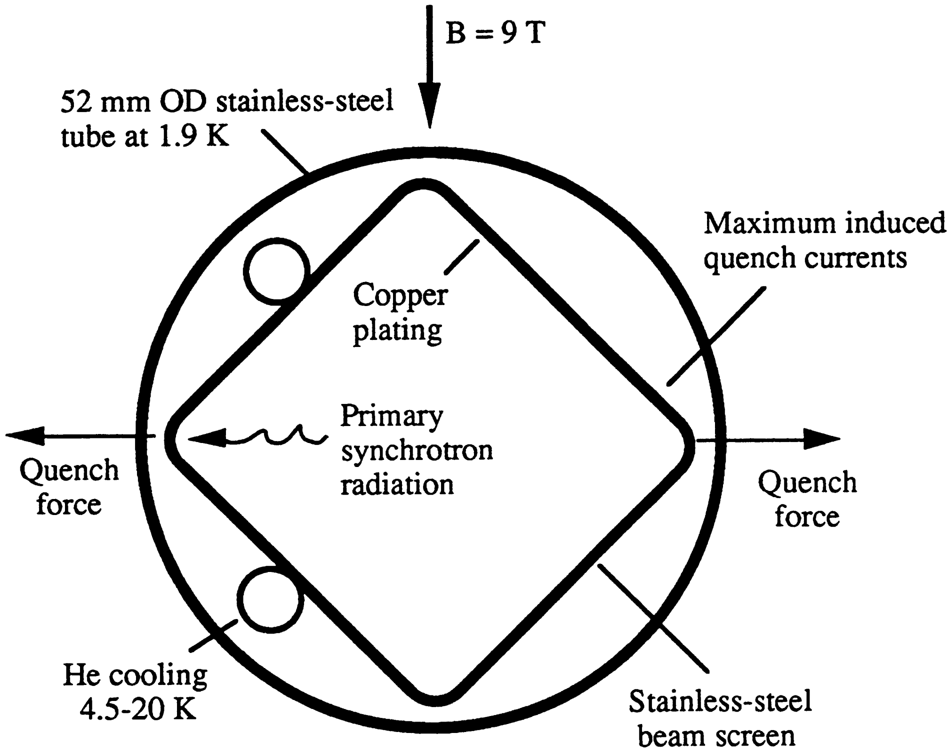

Figure 62: A schematic diagram of the square-section beam screen